



**UNIVERSITÉ
DE GENÈVE**

**The construction of the Insertable B-Layer and the b -tagging
performance at high- p_T of the ATLAS experiment**

Thèse

Présentée à la Faculté des Sciences de l'Université de Genève pour obtenir le
grade de docteur ès Sciences, mention Physique.

Par
Antonio Miucci

Thèse N° 4902

Genève
2016



**UNIVERSITÉ
DE GENÈVE**

FACULTÉ DES SCIENCES

***Doctorat ès sciences
Mention physique***

Thèse de *Monsieur Antonio MIUCCI*

intitulée :

**"The Construction of the Insertable B-Layer and the b-tagging
Performance at High-PT of the ATLAS Experiment"**

La Faculté des sciences, sur le préavis de Monsieur G. IACOBUCCI, professeur ordinaire et directeur de thèse (Département de physique nucléaire et corpusculaire), Monsieur M. POHL, professeur ordinaire (Département de physique nucléaire et corpusculaire), Madame T. MONTARULI, professeure ordinaire (Département de physique nucléaire et corpusculaire) et Monsieur S. GRINSTEIN, professeur (Institut de Física d'Altes Energies, Universitat Autònoma de Barcelona, España), autorise l'impression de la présente thèse, sans exprimer d'opinion sur les propositions qui y sont énoncées.

Genève, le 24 février 2016

Thèse - 4902 -

Le Doyen

N.B. - La thèse doit porter la déclaration précédente et remplir les conditions énumérées dans les "Informations relatives aux thèses de doctorat à l'Université de Genève".

Abstract

Although the recent discovery of the Higgs boson by the LHC experiments represented a major success of the Standard Model theory, several questions need still to be answered. The search of new physics particles beyond the Standard Model will require the LHC to collect a large amount of data. To achieve this goal the LHC collider went through a long shutdown, increasing both the energy and the luminosity. In particular the increase of luminosity will require the ATLAS Inner Detector to operate in a more track-dense environment, which mainly affects the ATLAS Pixel Detector. In order to cope with the high pile-up expected with the increase of luminosity the Pixel detector was then upgraded during the long shutdown with the insertion of a fourth innermost layer, the Insertable B-Layer (IBL). This thesis focuses on the construction of the IBL. This includes the loading of silicon pixel detector modules on the support staves, the quality assurance of these instrumented staves and the commissioning after the integration around the support structure. The energy upgrade of the LHC will increase the sensitivity to new particles with high mass, whose decay can produce b -quarks with a very high transverse momentum. An optimization of the impact parameters (d_0 and z_0) of the ATLAS b -tagging algorithm is presented in the last Chapter of this thesis.

Alors que la récente découverte du boson de Higgs par les expériences du LHC représente un succès majeur de la théorie du Modèle Standard, plusieurs questions sont encore sans réponse. La recherche de nouvelles particules de la physique au-delà du modèle standard nécessitera du LHC de recueillir une grande quantité de données. Pour atteindre cet objectif, le collisionneur LHC a traversé une période d'arrêt de deux ans, augmentant à la fois son énergie et sa luminosité. En particulier, l'augmentation de la luminosité, requièrera du détecteur interne d'ATLAS de fonctionner dans un environnement avec une plus haute densité de traces, ce qui affecte principalement le détecteur Pixel d'ATLAS. Afin de faire face au "pile-up" élevé, attendu avec une telle augmentation de luminosité, le détecteur Pixel a ensuite été mis à jour au cours de la période d'arrêt avec l'insertion d'une quatrième couche, la plus interne, le Insertable B-Layer (IBL). Cette thèse porte sur la construction de l'IBL. Ceci inclut le chargement des modules de pixels sur les planches de support, l'assurance de qualité de ces instruments et la mise en service après l'intégration autour de la structure de support. La mise à niveau de l'énergie du LHC va augmenter la sensibilité à de nouvelles particules de hautes masses, dont la décomposition peut produire des quarks b avec une impulsion transversal très élevé. Une optimisation des paramètres d'impact (d_0 et z_0) de l'algorithme de b -tagging d'ATLAS est présentée dans le dernier chapitre de cette thèse.

Contents

Abstract	2
Introduction	7
1 The Large Hadron Collider and the ATLAS experiment	9
1.1 Physics at the LHC	9
1.1.1 The Standard Model	9
1.1.2 Physics beyond the Standard Model	11
1.2 The Large Hadron Collider	12
1.2.1 The advantages and challenges of hadron colliders	12
1.2.2 The LHC design	13
1.3 The ATLAS experiment	15
1.3.1 The magnet system	17
1.3.2 Inner Detector	17
1.3.3 Calorimeter	22
1.3.4 Muon System	26
1.3.5 Trigger System	27
1.4 The ATLAS data taking until 2015	27
1.5 The LHC upgrade program	30
2 Track reconstruction with pixel detectors	32
2.1 Particle interaction with matter	32
2.1.1 Interaction of charged particles	33
2.1.2 Particle scattering	35
2.1.3 Interaction of neutral particles	35
2.2 Properties of pixel silicon detector	37
2.2.1 Signal generation in silicon sensors	38
2.2.2 Amplification and digitization of the signal	41
2.2.3 Spatial resolution	43
2.2.4 Radiation damage of the silicon bulk	44
2.2.5 Radiation damage of the electronic read-out	46
2.3 Tracking with the Inner Detector	48
2.3.1 Tracking in magnetic field	48
2.3.2 Impact parameter resolution	49
2.3.3 Momentum resolution	50
3 The ATLAS Pixel upgrade for the LHC Run 2	52
3.1 Refurbishment and consolidation of the Pixel Detector	53
3.2 Motivation for the ATLAS IBL detector	53

3.2.1	Track reconstruction performance	53
3.2.2	b -tagging performance	54
3.3	IBL Layout Overview	58
3.4	Module Layout	62
3.4.1	The FE-I4 redout chip	62
3.4.2	Sensors	66
3.4.3	Module Flex Hybrid	70
3.4.4	Dressed modules	71
3.5	Stave Layout	72
3.5.1	The support stave	72
3.5.2	Stave Flex	75
4	The IBL construction	77
4.1	Module electrical test	77
4.2	FE-I4 production and QA	80
4.3	Sensor Production	82
4.4	Module assembly and QA	84
4.4.1	Module assembly	84
4.4.2	Module QA	85
4.4.3	Production Yield	89
4.5	Bare stave and flex assembly	89
4.6	Stave Loading	91
4.6.1	Module reception tests	92
4.6.2	Module loading procedure	94
4.6.3	Stave quality check at the loading site	98
4.7	Stave Quality Assurance at the IBL integration site	102
4.7.1	Reception tests	102
4.7.2	Calibration and radioactive-source scan	103
4.7.3	Pixel defects	104
4.7.4	Stave ranking	106
4.7.5	Wire bond corrosion issue	107
4.8	Summary of the IBL construction	110
5	The IBL commissioning	112
5.1	The IBL on-surface testing	112
5.1.1	The IBL system test	112
5.1.2	The IBL stave-connectivity test	115
5.2	Detector calibration after insertion in ATLAS	117
5.2.1	Charge calibration	117
5.2.2	Timing optimization	120
5.3	The IBL mechanical stability	124
5.3.1	Measurement of the bowing and thermal stability	125
5.3.2	Effect on the performance	129
5.4	Measurement of the Lorentz angle	130

6	The b-tagging performance in Run II	134
6.1	Physics motivation	134
6.2	The Run 2 b -tagging algorithm for the ATLAS experiment	136
6.2.1	Track Selection	136
6.2.2	Impact Parameter based Algorithms: IP2D, IP3D	136
6.2.3	Secondary-vertex reconstruction of b -jets	141
6.2.4	The secondary vertex finding algorithm: SV	141
6.2.5	The JetFitter algorithm	142
6.2.6	Multivariate Algorithm: MV2	143
6.3	The b -tagging performance	144
6.4	Optimization of the IP3D tagger at high- p_T	147
6.4.1	Tuning over a mixed sample	149
6.4.2	New track selection	152
6.4.3	Next steps	161
	Conclusions	162
	References	164

Introduction

The continuous attempt to answer the questions posed by nature has led the human being to amazing and exciting discoveries, giving to curiosity a remarkable role in the progress of science. One of the most fascinating open points is the comprehension of the elementary objects of nature (elementary particles) and the way they interact with each other.

In particular the Standard Model, developed in the last century, provided a description of the elementary particles and three, out of four, fundamental interactions. All particles predicted by the Standard Model were observed in experiments. Despite of the great success of the theory, the Standard Model still leaves important questions unanswered, e.g. the mass of the neutrinos, the Dark Matter, the way the gravitation force acts at the particle level. New theories emerged in the last years and all of them foresee new particles.

Since 2008, the LHC experiments are taking data, which are used to verify the Standard Model and look for new particles to emerge in proton-proton collision. The discovery of the Higgs Boson, announced in July 2012, confirmed the strong predictive power of the Standard Model.

After the discovery of the Higgs boson the LHC underwent a first long shutdown period, from February 2013 to April 2015, after which the second phase of the LHC started, also known as Run 2, in which new particles are expected to be observed. During this shutdown an upgrade of the magnets was performed, allowing a higher center of mass energy ($\sqrt{s} = 13$ TeV and eventually the design energy of 14 TeV) and a higher peak instantaneous luminosity ($10^{34} \text{ cm}^{-2} \text{ s}^{-2}$) with respect to previous run at 8 TeV and 75 % of the design peak luminosity. The Run 2 phase is planned to last until the end of 2018.

The upgrade poses new challenges for the LHC experiments, in particular the high instantaneous luminosity results in additional soft proton-proton collisions, the so called pile-up interactions, that overlap with the interesting hard collisions.

The ATLAS collaboration made a significant effort to cope with the LHC luminosity without affecting its performance. In particular a new innermost layer of silicon pixel detector was built and installed, the Insertable B-Layer (IBL). This new layer ensures robustness of the charged-particle tracking, prevents from inefficiencies due to the expected high pile-up and improves the tracking performance.

Since many interesting physical phenomena include a b -quark in the final state, it is then of outstanding importance to be able to discriminate b -quark jets from the other jets. The most powerful discriminant is the b -quarks lifetime and therefore the presence of a secondary vertex to which tracks with large impact parameter belong. The IBL is of extreme importance for b -tagging, since, being close to the interaction point of the beams, it provides a significantly better reconstruction of the longitudinal and transverse track-impact-parameters and leads to a factor of 4 improvement in the rejection of light jets at a b -tagging efficiency of 70%.

In this Ph.D. thesis the construction of the IBL is described. A description of the LHC and the ATLAS detector is given in Chapter 1, while an introduction to the pixel detectors and the tracking techniques is provided in Chapter 2. The IBL layout and the expected performance are given in Chapter 3. The construction and characterization of the IBL components are described in Chapter 4. A particular emphasis is given to the assembly of the IBL staves and the qualification of the detector functionality, since I took part of the team responsible for the electrical and mechanical characterizations and the main developer of the analysis software. The commissioning phase of the IBL detector, describing the test around the mechanical support structure, the cosmic ray data-taking period and the first operation with beam in the ATLAS detector are described in Chapter 5. During this commissioning phase, I was the developer of the software for the tuning of the readout-chip electronics and I studied the impact of the detector misalignment on the performance of the b -tagging algorithm. I developed a control system for the IBL temperature monitoring and I took part in the preparation of the IBL detector for the data-taking with cosmic rays and proton collisions.

The high center of mass energy leads to the production of b -hadrons with high- p_T (more than few hundreds GeV). Those particles can travel for some centimeters before decaying, resulting in a decay vertex located beyond the IBL. In general b -hadrons at high- p_T will have different track topologies than the ones with a p_T lower than few hundreds GeV. A description of the ATLAS b -tagging tools is given in Chapter 6, where my work on the optimization of the impact parameter b -tagging algorithm for high transverse momentum is also presented.

Chapter 1

The Large Hadron Collider and the ATLAS experiment

This Chapter provides a brief introduction to the physics investigated at the Large Hadron Collider (LHC)[1], the design of the LHC and of the ATLAS experiment [2, 3].

1.1 Physics at the LHC

The LHC goal is the study of basic laws governing interactions and forces among the elementary particles to answer some of the fundamental open questions in particle-physics.

The discovery of the Higgs boson and the study of its properties were one of the principal targets of the LHC, the last missing particle of the Standard Model theory[4–6]. Several theories predict new physics beyond the Standard Model, which should emerge at the TeV scale, reachable by the LHC.

1.1.1 The Standard Model

The Standard Model (SM) of particle physics attempts to describe, at the most basic level, the particle structure of matter and its interaction via the fundamental forces. The SM theoretical construct contains three of the four fundamental forces (electromagnetic, weak and strong) in terms of a quantum field theory in which the Lagrangian is invariant under a continuous group of local transformations, a gauge theory [7]. As a gauge theory, the SM describes all the particle to be massless, it is then needed to introduce a symmetry-breaking mechanism to justify the experimentally observed masses of the particle. This mechanism is also known as Higgs mechanism, which led to the introduction of a scalar field in the theory. In the SM all matter consists of a finite set of elementary spin- $\frac{1}{2}$ particles denoted as fermions that interact via the exchange of bosons, particles with an integer spin. Two different types of bosons are present in the SM, gauge vector bosons and the scalar Higgs boson.

The fermions are subdivided into leptons and quarks, the first interacting electrically and weakly, the second also strongly. Leptons are observed to exist with integer or null electric charge as defined in units of the charge of the electron. There are three flavors of leptons forming a progressive mass hierarchy in a doublet weak isospin structure

$$\begin{pmatrix} e \\ \nu_e \end{pmatrix}_L \quad \begin{pmatrix} \mu \\ \nu_\mu \end{pmatrix}_L \quad \begin{pmatrix} \tau \\ \nu_\tau \end{pmatrix}_L \quad (1.1)$$

Lepton	Mass	Charge $[Q/ e]$	L_e	L_μ	L_τ
e^-	0.51 MeV	-1	1	0	0
μ^-	105.65 MeV	-1	0	1	0
τ^-	1777.03 MeV	-1	0	0	1
ν_e	< 2 eV	0	1	0	0
ν_μ		0	0	1	0
ν_τ		0	0	0	1

Table 1.1: Lepton Properties [8]. Since the neutrino eigenstates of flavor do not coincide with the eigenstates of mass only the lower limit on neutrino mass is reported on the table. This limit is derived by tritium decay measurements.

whereby each charged lepton is associated with a neutrally-charged lepton called neutrino. The three charged leptons, the electron, the muon, and the tau (e^- , μ^- and τ^-) each with negative charge are taken as the particles states, while their charge-parity conjugates are denoted as their anti-particles states. Within the SM there exists no mechanism that, in a direct way, provides for oscillation between the lepton families; as a result members of each family are assigned a quantum number L_ℓ corresponding to the lepton flavor of the particle. Table 1.1 summarizes the SM lepton properties, the measured mass for the charged leptons and the experimental limit on the mass for the neutrinos. In the context of SM neutrinos are described as massless also after the application of the Higgs mechanism. Neutrinos are observed to oscillate between different flavors. This leads to the idea that the flavor eigenstates of neutrinos are linear combination of different mass eigenstates, so that neutrinos have to be massive [9].

The distinguishing feature of the leptons is that they do not experience a direct interaction with the strong nuclear force and all lepton interactions occur through the electro-weak couplings. In contrast to leptons, quarks are distinguished by their interactions with the strong nuclear force and their fractional electric charge. Strong force binding and confinement lead quarks to form the fundamental substructure for all hadronic matter. Two types of structures are allowed¹, either color neutral three-quark bound states that form the common baryons such as the proton and the neutron, or quark-antiquark color-neutral bound state mesons such as the π , K , η , and ρ . Free quarks are not accessible due to the requirements of color neutrality, which require a stable state to have no net color charge, leading to the so called color confinement.

Similarly to the leptons, there exists a hierarchy of distinct quark flavor doublets with respect to the weak isospin, based on the masses of each quark and their associated quantum properties. Each generation consists of two quarks each with electric charges equal to $-\frac{1}{3}$ and $\frac{2}{3}$ of the electron charge. Three quark generations exists, whose associated quarks we label as up, down, charm, strange, top and bottom. They are arranged in flavor doublets:

$$\begin{pmatrix} u \\ d \end{pmatrix}_L \quad \begin{pmatrix} c \\ s \end{pmatrix}_L \quad \begin{pmatrix} t \\ b \end{pmatrix}_L \quad (1.2)$$

The mass hierarchy of the quark doublets is shown in Table 1.2. As with the leptons, each quark has a corresponding anti-particle state. Unlike the lepton sector, the weak interaction

¹other structures, as penta-quarks, are not forbidden by the SM and have recently been observed [10]

Quark	Mass [GeV/ c^2]	Charge [Q/ e]
u	0.001 – 0.005	2/3
d	0.003 – 0.009	-1/3
c	1.15 – 1.35	2/3
s	75 – 170	-1/3
t	≈ 174	2/3
b	4.0 – 4.4	-1/3

Table 1.2: Quark Properties

vertex can mix quark flavors between generations leading to $s \rightarrow u$ like processes arising via weak currents.

Also integer spin bosons have a fundamental role. Two types of bosons are present in the SM: the gauge bosons (or vector bosons) and the scalar Higgs boson. Gauge bosons are distinguished by their spin-1, they are the carriers of the fundamental interactions. Photons transmit the electromagnetic interaction, the W^\pm and the Z carry the weak interaction while the gluons, which can have 8 different color states, transmit the strong interaction. Photons and gluons are massless while W^\pm and Z have respectively a mass of (80.403 ± 0.029) GeV[8] and (91.1876 ± 0.021) GeV[8]; due to their mass, the range of interaction of the weak force is short: typically $\sim 10^{-18}$ m. The strong force has as well a short interaction distance, the typical range of the strong interaction is $\sim 10^{-15}$ m, due to the confinement property of Quantum Chromo Dynamics (QCD). Photons are massless, so that the interaction distance of the electromagnetic force is not limited.

The only fundamental scalar boson present in the SM is the Higgs boson. The role of the Higgs boson is strictly connected to the mass of the elementary particles, which is generated in the SM by the introduction of a scalar field in the SM Lagrangian. The Higgs boson discovery was announced on the 4th of July 2012 by the ATLAS and CMS experiments at LHC and it is measured to have a mass of $m_H = 125.09 \pm 0.21(stat.) \pm 0.11(syst.)$ GeV [11].

1.1.2 Physics beyond the Standard Model

Even though the SM has proven to give a precise description of particle physics up to the TeV scale, there are several question that are unanswered:

- The SM does not provide any prediction of fundamental particle quantities (couplings, spin ...).
- The SM cannot explain the very large difference between the electroweak energy scale and the Planck scale. This is called the hierarchy problem. In the SM the Higgs field vacuum expectation value can be calculated using a perturbative theory approach, leading to divergent contributions to the Higgs mass.
- Cosmological observations point out the need to include the so called Dark Matter (DM) in the description of the universe. A successful DM candidate must be stable, electrically neutral, weakly interacting and massive: this excludes any known Standard Model particle.

- As a gauge theory the SM describes particles as massless. Thanks to Higgs mechanism it is possible to justify the mass of the bosons, the quarks and the charged leptons but not of the neutrinos, which are described as massless. However the experimentally established phenomenon of neutrino oscillations, which mixes neutrino flavor states with neutrino mass states, requires neutrinos to have masses.
- The SM does not provide any description of the observed matter-antimatter asymmetry in the universe.

On top of these open points, the SM does not provide a description of the gravitational force. All these open questions lead to the idea that the SM is an effective theory that works fine at the electroweak scale, but is the approximation of a more complex theory at high scales. Several theoretical models have been developed to overcome these issues: they all predict a set of new particles. One of these theories is Supersymmetry (SUSY) in which each SM particle is associated with a new particle, known as its super-partner, the spin of which differs by a half-unit. There are other theories which extend the SM making other hypothesis (compositeness, extra-dimensions). They all predict the existence of new fundamental particles.

The experiments at the LHC are investigating the possibility of these new particles to be produced at the energy scale of the TeV. The LHC is investigating, as well, the asymmetry in matter-antimatter by studying CP violation and looking for potential candidates forming the Dark Matter.

1.2 The Large Hadron Collider

The Large Hadron Collider (LHC)[1] is a two-ring-hadron accelerator and collider which is located at CERN². The LHC project started in the early '90s of the last century with the aim of building a collider able to deliver collisions at a center of mass energy of 14 TeV, an order of magnitude higher than the already existing hadronic collider (Tevatron) and two order of magnitude greater than the leptonic one (LEP). The LHC is a hadronic collider that is used for proton-proton, heavy ions and proton-heavy ion collisions. Only proton-proton collisions are considered in the work presented in this thesis.

1.2.1 The advantages and challenges of hadron colliders

The main motivation to use a hadron instead of electron-positron circular collider, as was LEP, is the much higher achievable center of mass energy. Circular colliders which accelerate electrons are limited in energy due to synchrotron radiation, the electromagnetic radiation generated by the acceleration of charged particles when they are accelerated radially. In circular colliders the main contribution to the synchrotron radiation is from the dipoles used to bend the charge particles trajectory. The energy loss due to synchrotron radiation in circular colliders is:

$$\frac{dE}{dt} \propto \frac{E^4}{m^4 R} \quad (1.3)$$

where E is the energy of the beam particles, m the mass, and R the bending radius. There are other families of lepton colliders, the electron linear collider, e.g. the Stanford

²CERN: the European Organization for Nuclear Research

Linear Collider, and the muon circular colliders, the latter at the moment is still at R&D stage. In principle one can minimize the energy loss by synchrotron radiation by using linear colliders instead of circular ones. At the moment two linear colliders are considered for the future, the International Linear Collider (ILC)[12] and the Compact Linear Collider (CLIC)[13]. Both aim to accelerate electron and positron at energy higher than 0.5 TeV thanks to an accelerator facility of few dozens kilometer length. Even though the energy is lower than the one delivered from LHC, this has not to be shared within the different partons in the protons, but it will be the energy of a single elementary object. The other option is to use muon circular colliders. A muon is ~ 200 times lighter than an electron, this means that a muon collider would have an energy loss of a factor $\sim 10^9$ lower with respect to an electron collider, keeping both the energy and the radius constant, as it can be seen in Equation 1.3. The challenge of muon colliders is represented by the limited lifetime of a muon at rest, $\sim 2.2 \mu\text{s}$, which will be extended to few micro-seconds for muons at TeV energy, so that the system has to deal with a beam with a limited lifetime.

Hadron circular colliders have a minimal energy leakage from synchrotron radiation at the TeV scale and they use stable particles, so that there are no time constraints in the preparation of the beam before the collisions.

The choice of a hadron collider, instead of a leptonic, brings features related to the composite structure of the hadrons. In hadron colliders the partonic center of mass energy is assigned by the parton distribution function and is only a fraction of the total center of mass energy. This allows to scan a wide energy range without changing the beam configuration, differently from leptonic colliders. Moreover the cross section for hard collisions, which have a large momentum transferred, is smaller than the one for soft collisions. So that for collecting a large statistics of these events of interest a hadronic machine has to operate with high collision rate, which is 40 MHz for the LHC.

At the LHC the hard scattering events of interest will originate from a single proton-proton interaction out of the collision of two bunches of $\sim 10^{11}$ protons. While it is extremely unlikely that more than one colliding proton pair will produce a high transverse momentum, high- p_T , hard scattering event when the two bunches cross, in general several additional low- p_T interactions will take place among other protons in the same bunches. These are usually called pile-up collisions and they are completely independent from the hard scattering process. In addition to the in-time pile-up, where low- p_T events come from interaction in the same bunch, also out-of-time pile-up events have to be considered. Indeed the time interval between two consecutive collisions is 25 ns, which is shorter than the average time response of many of the detectors subsystems. Finally the underlying event is defined as the outcome of additional parton interactions taking place among components of the same protons which give rise to the hard scattering process of interest, so that in each high- p_T event there is a low- p_T component resulting from the hadronization of the other quarks.

1.2.2 The LHC design

The LHC consists of two rings with counter-rotating beams for hosting and accelerating hadrons, i.e. proton and lead nuclei. Due to the limited size of the hosting tunnel, a two-in-one design was chosen for the superconducting magnets so that a unique magnet provides a magnetic field in opposite directions for the two rings. The acceleration chain of the LHC is embedded in the CERN accelerator facility that is shown in Figure 1.1 and consists of several stages. Starting from hydrogen gas, an electric field is used to strip hydrogen atoms of their

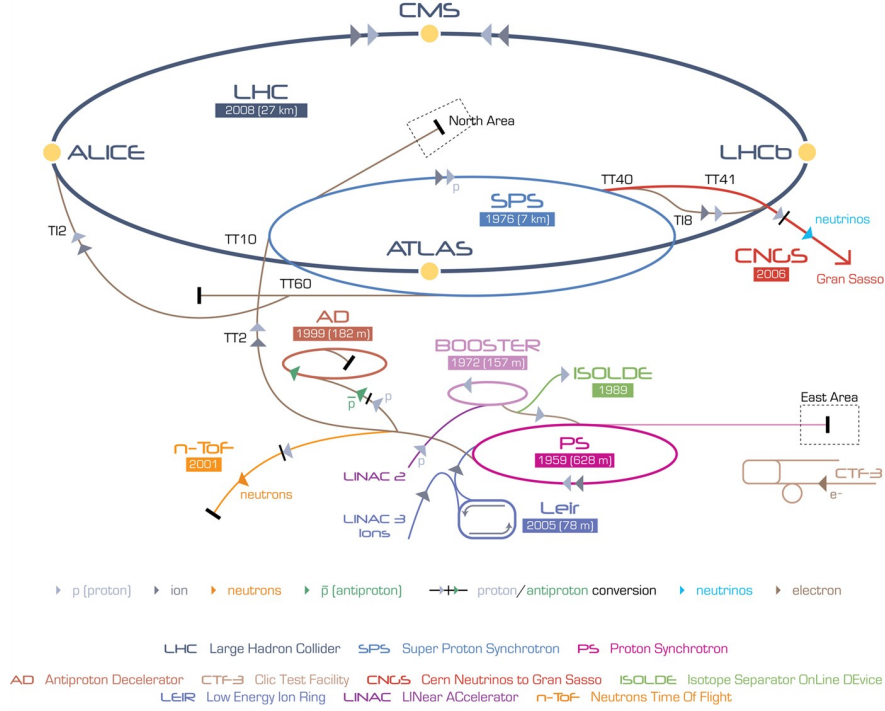


Figure 1.1: Accelerator facility at CERN, in particular it can be appreciated the LHC injection chain.

electrons to yield protons. Linac 2, the first accelerator in the chain, accelerates the protons to the energy of 50 MeV. The beam is then injected into the Proton Synchrotron Booster (PSB), which accelerates the protons to 1.4 GeV, followed by the Proton Synchrotron (PS), which pushes the beam to 25 GeV. Protons are then sent to the Super Proton Synchrotron (SPS) where they are accelerated to 450 GeV. The protons are finally transferred to the two beam pipes of the LHC. The beam in one pipe circulates clockwise while the beam in the other pipe circulates anticlock-wise. It takes 4 minutes and 20 seconds to fill each LHC ring, and 20 minutes for the protons to reach their maximum energy. Beams circulate for many hours inside the LHC beam pipes, then, when the population of proton decreases, the beam is dumped and a new fill of protons is injected. The two beams are brought into collision inside four detectors: ALICE, ATLAS, CMS and LHCb.

Lead ions for the LHC start from a source of vaporized lead and enter Linac 3 before being collected and accelerated in the Low Energy Ion Ring (LEIR). Those then follow the same route to maximum energy as the protons.

In the case of protons, the design maximum beam energy that the LHC can deliver is 7 TeV and it results from a nominal magnetic field of 8.33 T of the bending dipole magnets. Therefore the maximum energy in the center of mass is $\sqrt{s} = 14$ TeV.

Another important parameter of particles colliders is the luminosity, defined as the ratio of the number of events detected (N) in a certain time (t) to the interaction cross-section (σ):

$$L = \frac{1}{\sigma} \frac{dN}{dt} = f \frac{n_1 n_2}{A_{eff}} \quad (1.4)$$

where n_1 and n_2 are the number of particles contained in the two opposite orbiting bunches, f is the collision frequency and A_{eff} is the effective collision area. The size of the collision

	Injection	Collision
Energy	450 GeV	7 TeV
Luminosity		$10^{34} \text{ cm}^{-2} \text{ s}^{-1}$
Number of bunches		2808
Bunch spacing		25 50 ns
Number of particles per bunch		$\simeq 2 \times 10^{11}$
Beam current		0.58 A
Transverse emittance	3.5 μm	3.75 μm
Longitudinal emittance	1.0 eV	2.5 eV
synchrotron radiation loss per turn	$\sim 0 \text{ keV}$	7 keV
Bunch length (4σ)	1.7 ns	1.0 ns
Relativistic gamma	479.6	7461
β^*	18 m	0.55 m
θ_c	$\pm 320 \mu\text{rad}$	$\pm 285 \mu\text{rad}$
Geometrical reduction factor F	-	0.836
RMS bunch length	11.24 cm	7.55 cm
RMS beam size	375.2 μm	16.7 μm

Table 1.3: Main parameters of the LHC collider for the proton collision mode

area depends on the beam width in the horizontal (σ_x) and vertical (σ_y) axes. Under the assumption of gaussian beams $A_{eff} = 4\pi\sigma_x\sigma_y$. Luminosity can be also expressed in terms of the geometrical characteristics of the colliding bunches and of the machine parameters as:

$$L = \frac{N_b^2 n_b f \gamma_r}{4\pi\epsilon_n \beta^*} F \quad (1.5)$$

where N_b is the number of particles per bunch, n_b is the number of bunches per beam, f is the revolution frequency, γ_r is the relativistic gamma factor, ϵ_n is the normalized transverse beam emittance, β^* is the distance from the interaction point at which the beam is twice as wide as the focus point and F is the geometrical reduction factor due to the crossing angle at the interaction point:

$$F = \frac{1}{\sqrt{1 + \left(\frac{\theta_c \sigma_z}{2\sigma^*}\right)^2}} \quad (1.6)$$

where θ_c is the full crossing angle at the interaction point, σ_z is the RMS of the bunch length and σ^* is the RMS of the transverse beam size at the interaction point.

The main accelerator parameters in the proton-proton operation mode are reported in Table 1.3, where the parameters are shown for injections and collisions.

1.3 The ATLAS experiment

ATLAS (A Toroidal LHC ApparatuS)[2, 3] is one of the seven particle detector experiments (ALICE, ATLAS, CMS, TOTEM, LHCb, LHCf and MoEDAL) constructed at the LHC. ATLAS and CMS are the two general-purpose detectors, designed to exploit the LHC physics scenario. ATLAS is 46 meters long, 25 meters in diameter, and weighs about 7000 tonnes.

The high-energy and luminosity delivered by the LHC produce collisions in the ATLAS detector at high interaction rate, with very high radiation doses, in particular in proximity of the interaction region. The search for the Higgs boson and for new physics phenomena imposed the following requirements:

- large geometrical acceptance with almost full azimuthal angle coverage;
- good charged particle momentum resolution and reconstruction efficiency;
- good impact parameter resolution for identification of jets coming from b-quarks and τ leptons, which requires a vertex detector close to the interaction region despite the high radiation doses;
- a very good electromagnetic calorimeter for electron and photon identification and measurement, complemented by a full-coverage hadronic calorimeter for accurate jet and missing transverse energy measurements;
- a precise muon identification and momentum resolution over a wide range of momenta;
- a flexible and fast trigger system to select interesting events, even in the presence of low transverse-momentum particles and large background from uninteresting events.

In ATLAS, the nominal interaction point is defined as the origin of the coordinate system, the beam direction defines the z axis. The positive x direction is defined as pointing from the interaction point to the centre of the LHC ring. The azimuthal angle ϕ is measured around the beam axis, while the polar angle θ is the angle from the beam axis. Usually the angle θ is more conveniently expressed in terms of the pseudo-rapidity $\eta = -\ln(\tan(\theta/2))$, which can be as well expressed in terms of momentum:

$$\eta = \frac{1}{2} \ln\left(\frac{|\vec{p}| + p_L}{|\vec{p}| - p_L}\right). \quad (1.7)$$

In the limit of ultra relativistic particles the pseudorapidity is close to the rapidity y defined as:

$$y = \frac{1}{2} \ln\left(\frac{E + p_L}{E - p_L}\right). \quad (1.8)$$

A useful feature of rapidity is that differences of rapidity are invariant under Lorentz boost along the beam axis, so that the angular description can be provided in terms of y and ϕ . In such coordinates the angular separation of two events is invariant with respect to boosts along the beam axis. Since rapidity requires both the energy and the momentum, a simpler description is provided by pseudorapidity, given the relation $y \simeq \eta$ for relativistic particles. Another advantage of this description is that the production of particles at colliders is flat in rapidity and so it is approximately flat in pseudorapidity.

The overall ATLAS detector layout is shown in Figure 1.2. The main sub-detectors extend radially starting from the interaction point. The detector closest to the interaction point is the Inner Detector formed by pixel and strip silicon detectors and by transition radiation detectors. The Inner Detector is immersed in a 2T solenoidal field which has a coverage up to $|\eta| \leq 2.5$. Outside the Inner Detector, the electromagnetic calorimeter,

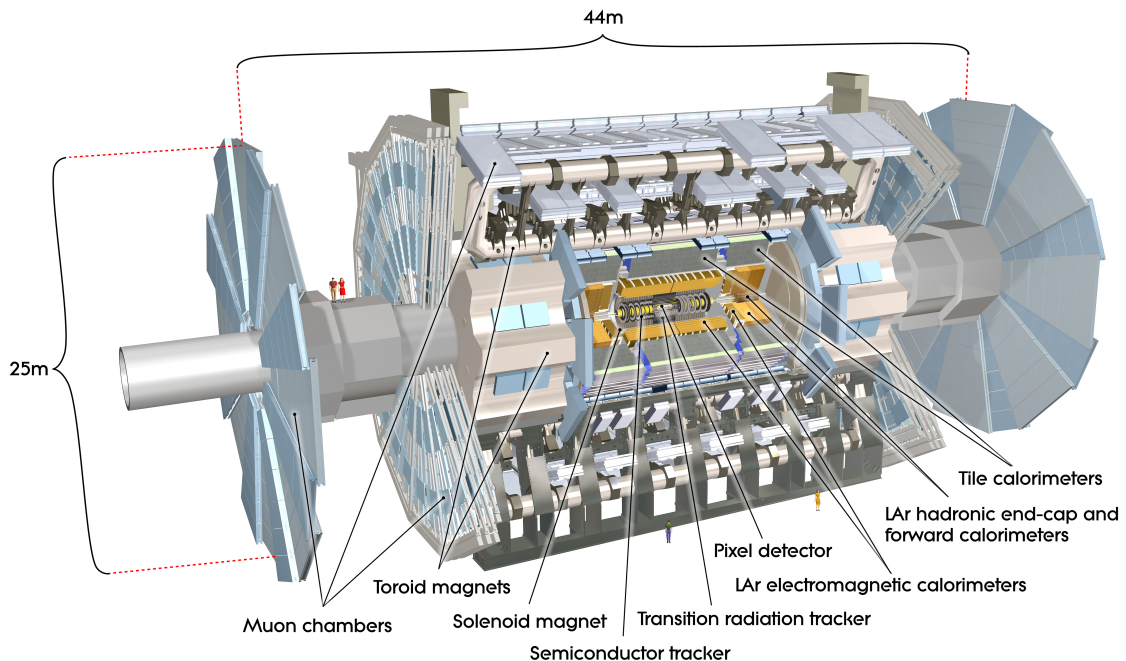


Figure 1.2: A three-dimensional view of the ATLAS detector

based on LAr technology, covers the pseudo-rapidity range up to $|\eta| \leq 3.2$. Behind it, the hadronic calorimetry is provided by the scintillator-tile calorimeter in $|\eta| \leq 1.5$ and by the LAr calorimeter up to $|\eta| \leq 4.9$. The muon spectrometer surrounds the calorimeter and has three layers of high precision tracking chambers, which extend up to $|\eta| \leq 2.7$.

1.3.1 The magnet system

The ATLAS magnet system[14] comprises a thin superconducting solenoid surrounding the Inner Detector and three large superconducting toroids (one barrel and two end-caps), arranged with an eight-fold azimuthal symmetry around the calorimeters, which provides bending power for the muon spectrometer. The solenoid has its field axis matching the beam direction. It is made of a single-layer aluminum coil wound by a NbTi conductor, optimizing thus its thickness in order to have a small impact on the energy measurement in the calorimeters. The solenoid has an inner radius of 1.23 m and a total length of 5.8 m. A magnetic field of 2 T is produced in the central region of the the Inner Detector. The external toroidal magnets use coils consisting of a conductor made of aluminum, niobium, titanium and copper, and they extend the magnet system to a total of 26 m length and 20 m diameter. This configuration provides a magnetic field for the muon spectrometer of 0.5 T and 1 T in the barrel and end-caps, respectively.

1.3.2 Inner Detector

The ATLAS Inner Detector[15, 16] (ID) is the detector system close to the interaction point which is composed of three sub-detectors: a Pixel Silicon Detector (Pixel), a Silicon Micro-Strip Detector (SCT) and a Transition Radiation Tracker (TRT). Aim of the ID is

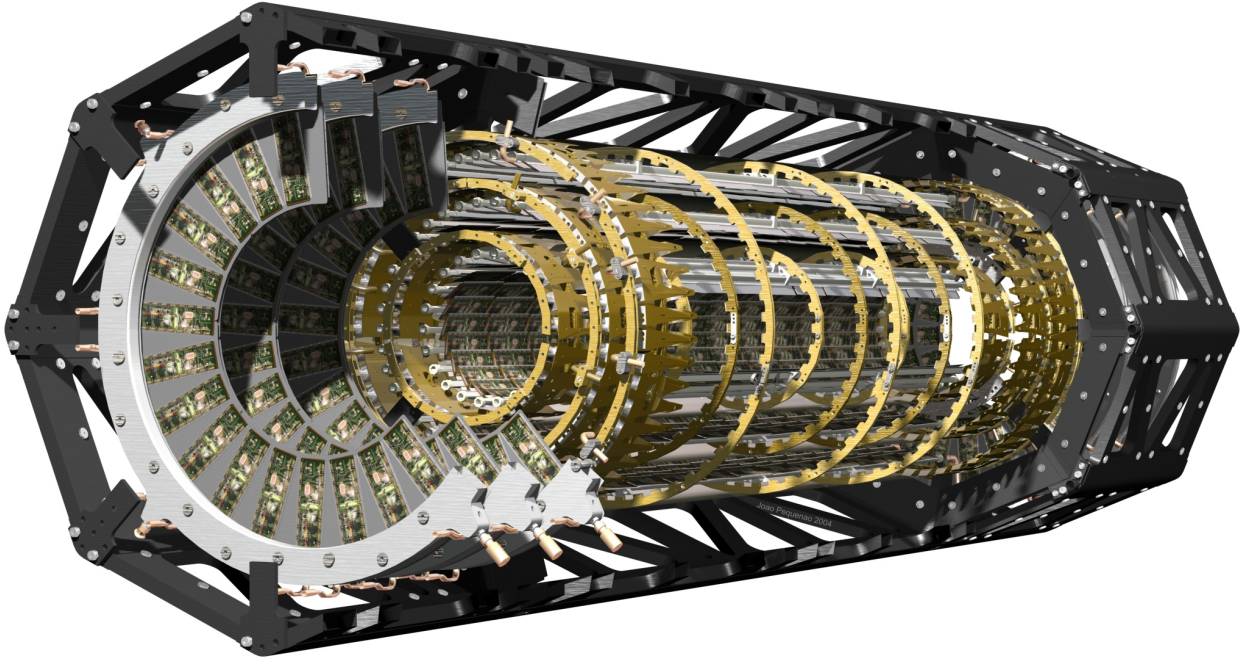


Figure 1.3: Engineering drawing of the Pixel Detector.

the reconstruction of charged tracks, in terms of momentum and impact parameters. This reconstruction is achieved by combining the energy deposited in each of its sub-detector layers. The layout of the ID is illustrated in Figure 1.5.

The Pixel Detector: The ATLAS Pixel Detector consisted of three barrel layers during Run 1, located at 50.5, 88.5 and 122.5 mm, and three disks on either side in the forward direction at a distance of 495, 580 and 650 mm from the interaction point (IP); a drawing of the layout is shown in Figure 1.3. The Pixel Detector has a full coverage for the ϕ angle and up to ± 2.5 in pseudo-rapidity with respect to the interaction point.

During the first long shutdown of the LHC machine the Pixel detector was upgraded with the insertion of an innermost barrel layer, the Insertable B-Layer (IBL), which is located at 32.5 mm from the interaction point. The IBL is the main subject of this work of thesis and it will be described in Chapter 3. The three outermost barrel layers are equipped with 1744 identical sensor-chip-hybrid modules, mounted on carbon support structure (staves). This structure guarantees good mechanical and position stability of the modules during operation while the amount of material was kept to a minimum. At the same time it has to provide cooling to remove the heat load of typically 4 W from each module and maintain the sensors at a low temperature to keep the radiation damage low. The cooling is provided by a evaporative fluorocarbon system[17]. The total material budget of the entire barrel is approximately $10.7\% X_0$ for particle crossing the detector at $\eta = 0$. A pixel module (Figure 1.4) consists of a single silicon sensor, with an area of approximately $2 \times 6 \text{ cm}^2$ and a thickness of $250 \mu\text{m}$. To provide a high space-point resolution of $14.4 \mu\text{m}$ in the $R\phi$ plane and $\sim 115 \mu\text{m}$ along the beam pipe direction, each sensor is subdivided in a pixel matrix. The pixel matrix presents two categories of pixels, the standard one which is $50 \mu\text{m}$ long in the $R\phi$ direction and $400 \mu\text{m}$ in z , and the long one which has the same length in $R\phi$

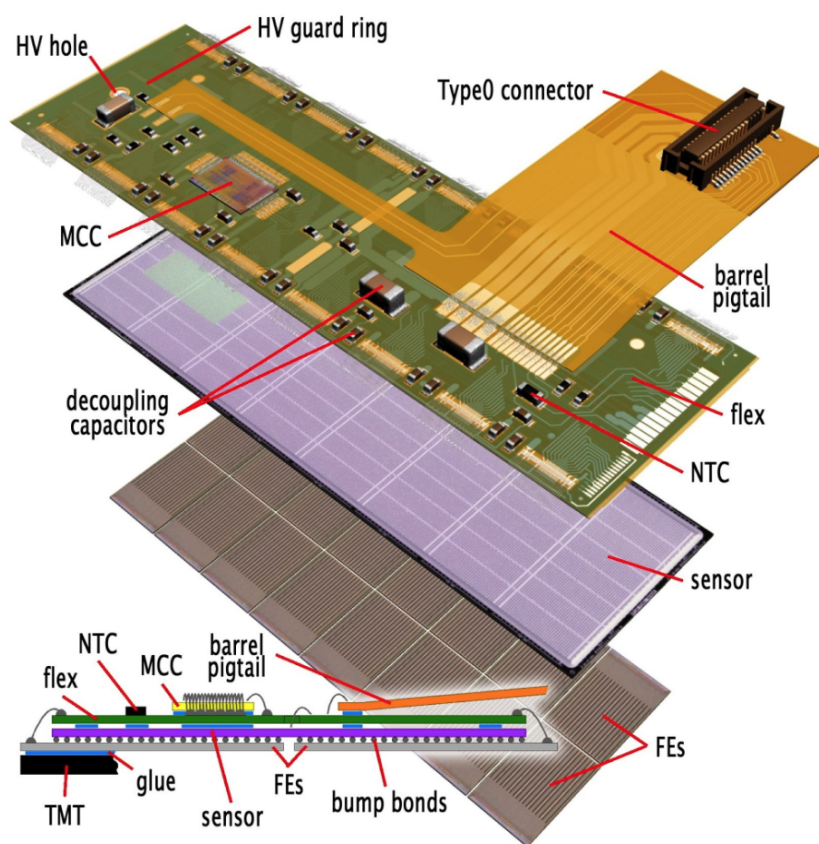


Figure 1.4: Schematic view of the FEI3 pixel module

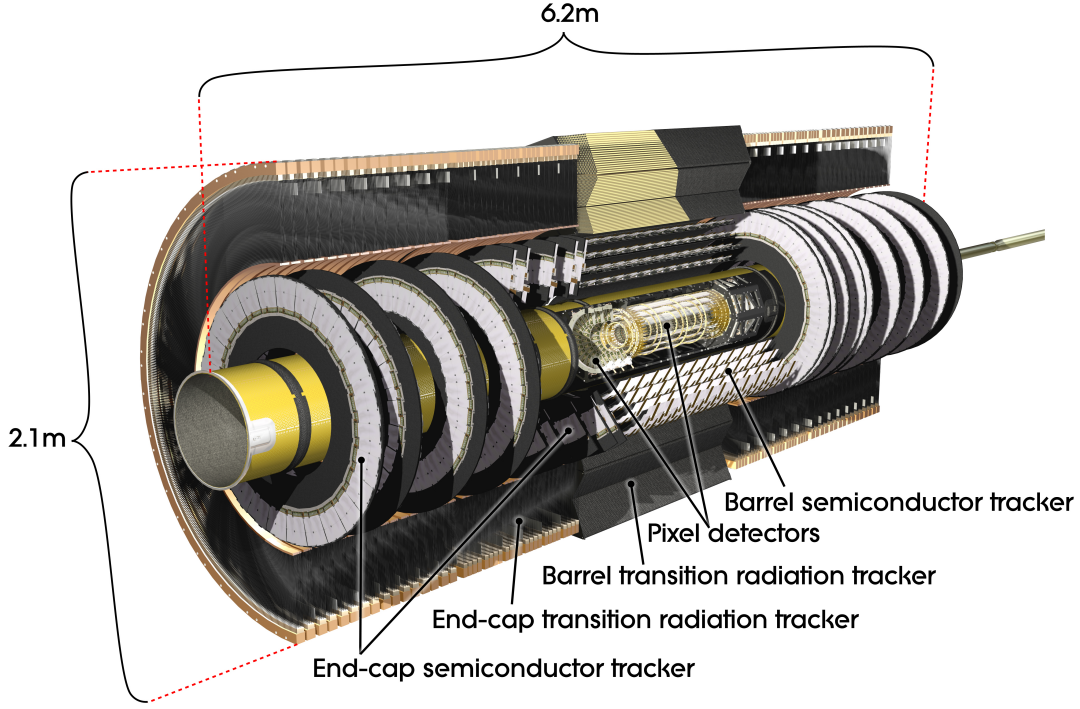


Figure 1.5: Cut-away view of the ATLAS Inner Detector

but is $600\text{ }\mu\text{m}$ in the z direction. For each sensor there are 41984 standard pixels and 5248 long ones. The long pixels are located at the edge of the module to cover the gaps between adjacent front-ends.

Each sensor is individually connected to 16 front-end chips (FE-I3)[18]) using bump-bondings for each pixel. The front-end provides pulse height measurements by means of the Time over Threshold (ToT) with zero suppression on chip. These front-end chips are connected via wire-bonds to a kapton-flex hybrid glued onto the back-side of the sensor. A module-control chip is mounted on top of the flex-hybrid and combines the individual events from the front-end chips and distributes trigger and command signal. The module-control chip is responsible of the communication with the off-detector electronics via optical link. In order to keep the material budget low, both the front-end and the module control-chip are thinned to below $200\text{ }\mu\text{m}$.

Silicon microstrip detector: The SCT[19] consists of four nested cylindrical barrels in the centre and nine disks in each of the two end-caps. The barrels cover a region from 300 to 520 mm in radius and have an active length of 1530 mm, centered around the interaction point. The barrel layers are fully covered by 32, 40, 48 and 56 rows of twelve identical modules, overlapping in a tile-structure in order to ensure full coverage, making a total of 2112 modules. The end-caps consist of nine disks each placed in z from 835 to 2788 mm and radii ranging from 259 to 560 mm, with the modules being placed in three rings overlapping azimuthally, two on one side, one on the other, in order to achieve full coverage. The SCT barrel modules are made of four sensors, glued in pairs on either side of a thermally conductive baseboard. The sensors are approximately $6\times 6\text{ cm}^2$ p-in-n silicon wafers of approximately $300\text{ }\mu\text{m}$ thickness. Each sensor has 768 strips with $80\text{ }\mu\text{m}$ pitch. The end-cap

modules are made of two or four wedge-shaped sensors of varying size depending on their position on the end-caps rings. The strip pitch varies from $57\text{ }\mu\text{m}$ on the inner edge of the innermost sensors to $94\text{ }\mu\text{m}$ on the outer edge of the outermost sensors. The top and bottom sensors are rotated by a stereo angle of 40 mrad with respect to each other in order to obtain two-dimensional position information while keeping the number of ghost hits small. The strips in the barrel are oriented in z -direction and radially in the end-caps in order to obtain the best position resolution in the azimuthal direction. The intrinsic accuracy in the barrel region is $17\text{ }\mu\text{m}$ ($R - \phi$) and $580\text{ }\mu\text{m}$ (z). The total number of readout channels of the SCT is approximately 6.3 million.

Transition radiation tracker The TRT[20] is composed of 1.43 m long cylindrical barrel layer ranging from 56 to 108 cm in radius and two end-caps ranging from 0.84 m to 2.71 m in z and 64 cm to 103 cm in radius. Both parts contain similar carbon-polyimide straw tubes of 4 mm in diameter which are aluminium-coated on their inner surface to form a cathode and contain a gold-plated tungsten wire of $30\text{ }\mu\text{m}$ in diameter that is used as anode. The straws are filled with 70% Xe, 27% CO_2 and 3% O_2 , the first component being the main gas in which ionisation occurs and the latter had to be added to avoid etching problems with the glass joins that holds the wires. The straws are operated in proportional mode with the electrodes being on $\sim 1500\text{ V}$ bias. The 52544 straws in the barrel are 144 cm long and form modules in which they are embedded in polypropylene radiator foils. Relativistic particles emit transition radiation when crossing the boundary of radiator foils which is subsequently detected in the straw tubes. Since the intensity of the emitted radiation depends on the $\gamma = E/m$ of the particle, light particles will emit more transition radiation than heavier particles which is used in the TRT to distinguish electrons from other particles such as π -mesons. While the intrinsic resolution of the TRT cannot compete with the resolution of the silicon-based technology, the high number of measurements and the long lever arm with respect to the measurements in the silicon layers makes the TRT significantly contribute to the momentum resolution. In addition, the low detector granularity is compensated by the larger radial positions of the straw tubes, so that a standalone pattern recognition is still possible for instantaneous luminosities up to and not beyond the nominal luminosity of $10^{34}\text{ cm}^{-2}\text{ s}^{-1}$.

Impact of detector material The material budget of the tracking system must be kept to a minimum in order to limit disturbing effects from multiple scattering and undesired interactions. This material has been accurately mapped and introduced in the ATLAS simulation since the impact on ATLAS performance is expected to be large:

- a significant fraction of low energy pions will undergo inelastic hadronic interaction inside the inner detector volume;
- approximately 40% of the photons will convert into an electron-positron pair before reaching the LAr cryostat and the electromagnetic calorimeter;
- many electrons will lose a good part of their energy through bremsstrahlung before reaching the calorimeter.

The first two effects will be an important factor limiting the b -jet identification performance, described in Chapter 6, which relies indeed on distinguishing higher impact parameter

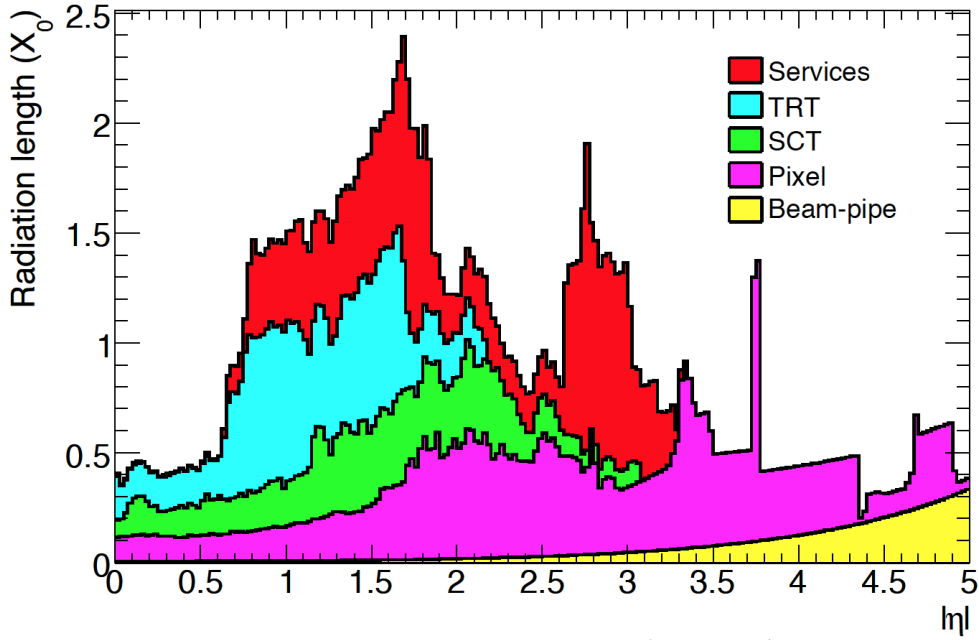


Figure 1.6: Material distribution (X_0) at the exit of the ID envelope, including the services and thermal enclosures. The distribution is shown as a function of η and averaged over ϕ . The breakdown indicates the contributions of external services and of individual sub-detectors, including services in their active volume.

tracks (from b -decays) from prompt tracks. A description of material budget can be given in term of radiation length, X_0 . This is a characteristic of a material, related to the energy loss of high energy, electromagnetically-interacting particles. The definition of X_0 is the length (in cm) to reduce the average energy of an electron by a factor e . The X_0 can be calculated given the characteristics of the material:

$$X_0 = \frac{716.4 \cdot A}{Z(Z+1) \ln \frac{287}{\sqrt{Z}}} g \cdot cm^{-2} \quad (1.9)$$

where Z is the atomic number and A is a mass number of the nucleus. Figure 1.6 shows the estimation of the X_0 obtained in simulation by the probability to create a photo-conversion $\gamma \rightarrow e^-e^+$ interacting with the ID material. The large contribution of the services to X_0 is a result of the need to have cooling, services and electronics inside the detector volume in order to cope with the finely granulated tracking detector elements.

1.3.3 Calorimeter

The requirement of hermeticity, which is a necessary condition to achieve good resolution of the measurement of the missing transverse momentum, is one of the key design components of the ATLAS calorimeter, which indeed has a coverage up to $|\eta| = 4.9$. Different technologies are used across different regions in pseudo-rapidity for the different calorimeter sub-detectors as Figure 1.7 shows. In particular the ATLAS Calorimeter is mainly divided in two types of Calorimeters, the Electro-Magnetic (EM) Calorimeter and the Hadronic Calorimeter.

Going radially from the interaction point to the outermost layer of the ATLAS experiment, the EM Calorimeter is located soon after the TRT. Over the $|\eta|$ range where the

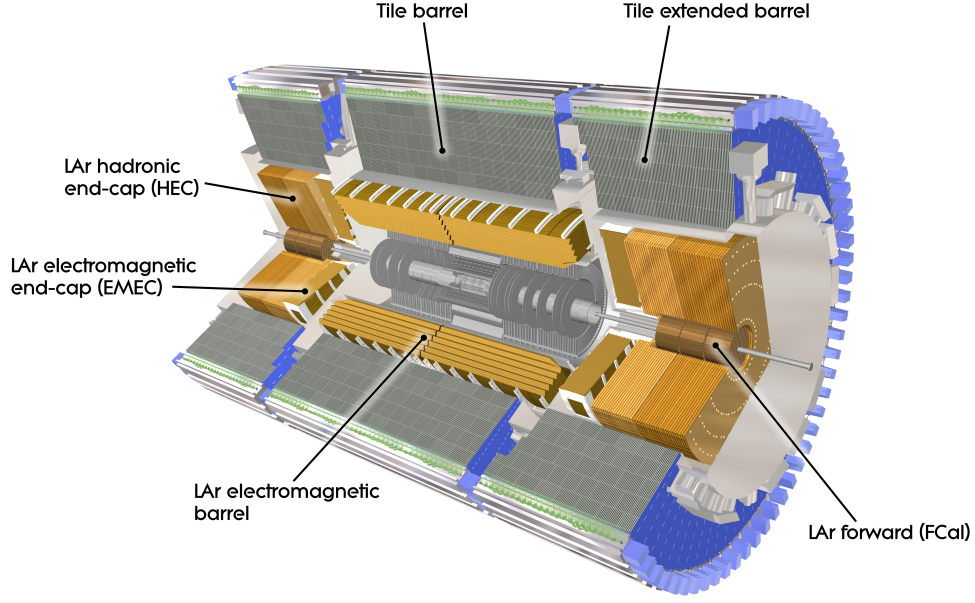


Figure 1.7: Cut-away view of the ATLAS calorimeter system

calorimeter is surrounding the ID, the EM calorimeter is finely segmented for precision measurements of electrons and photons. Those interact via bremsstrahlung process with the calorimeter material, generating a shower of electrons and positrons, detected in liquid Ar. As the EM Calorimeter needs to provide the energy measurement with good resolution, it needs to have enough material to let the electron-positron shower be fully contained in the EM volume.

The hadronic calorimeter is located at outer radius with respect to the EM one and it is segmented more coarsely since it is mainly aimed at reconstructing jets and at measuring the missing transverse momentum.

An important design criterion came from the need of containing both the electromagnetic and hadronic showers of particles of energies around the TeV scale, since energy escaping the calorimeter results both in a significantly reduced energy resolution and in punch-through into the muon system. For the hadronic interactions the description is provided in terms of the absorption length λ . λ is defined as the distance that a particle spent into a material at which the probability of not being absorbed has dropped to $1/e$.

The approximately 10 absorption length both in the barrel and in the end-caps are sufficient to provide very good resolution for high energy jets. The total thickness, including the outer support, is 11λ at $|\eta|=0$; this has been shown by simulation and confirmed by test beam data to be sufficient to reduce punch-through into the muon system well below the irreducible level of prompt or in-flight decays into muons. The pseudo-rapidity coverage, granularity and segmentation in depth of the calorimeters are summarized in Table 1.4.

Electromagnetic Calorimeter The Electromagnetic Calorimeter is divided into a barrel ($|\eta| < 1.475$) and two end-caps ($1.375 < |\eta| < 3.2$). Each end-cap calorimeter is mechanically divided in two coaxial wheels: an outer wheel covering the region $1.375 < |\eta| < 2.5$ and an inner wheel covering $2.5 < |\eta| < 3.2$. The EM calorimeter is based on a lead-LAr detector

	η coverage		Granularity ($\Delta\eta \times \Delta\phi$)
EM calorimeter	barrel	end-cap	
Presampler	$ \eta < 1.54$	$1.5 < \eta < 1.8$	0.025×0.1
Sampling 1	$ \eta < 1.475$	$1.375 < \eta < 3.2$	0.003×0.1^a 0.025×0.025^b $0.003 - 0.025 \times 0.1^c$ 0.1×0.1^d
Sampling 2	$ \eta < 1.475$	$1.375 < \eta < 3.2$	0.025×0.025 0.075×0.025^b 0.1×0.1^d
Sampling 3	$ \eta < 1.35$	$1.5 < \eta < 2.5$	0.05×0.025
Tile calorimeter	barrel	extended barrel	
Sampling 1-2	$ \eta < 1.0$	$0.8 < \eta < 1.7$	0.1×0.1
Sampling 3	$ \eta < 1.0$	$0.8 < \eta < 1.7$	0.2×0.1
Hadronic end-cap			
Sampling 1-4	$1.5 < \eta < 3.2$		0.1×0.1^e 0.2×0.2^d
Forward			
Sampling 1-3	$3.1 < \eta < 4.9$		0.2×0.2

^a $|\eta| < 1.4$, ^b $1.4 < |\eta| < 1.475$, ^c $1.375 < |\eta| < 2.5$, ^d $2.5 < |\eta| < 3.2$, ^e $1.5 < |\eta| < 2.5$

Table 1.4: Pseudo-rapidity coverage, longitudinal segmentation and granularity of the ATLAS calorimeters.

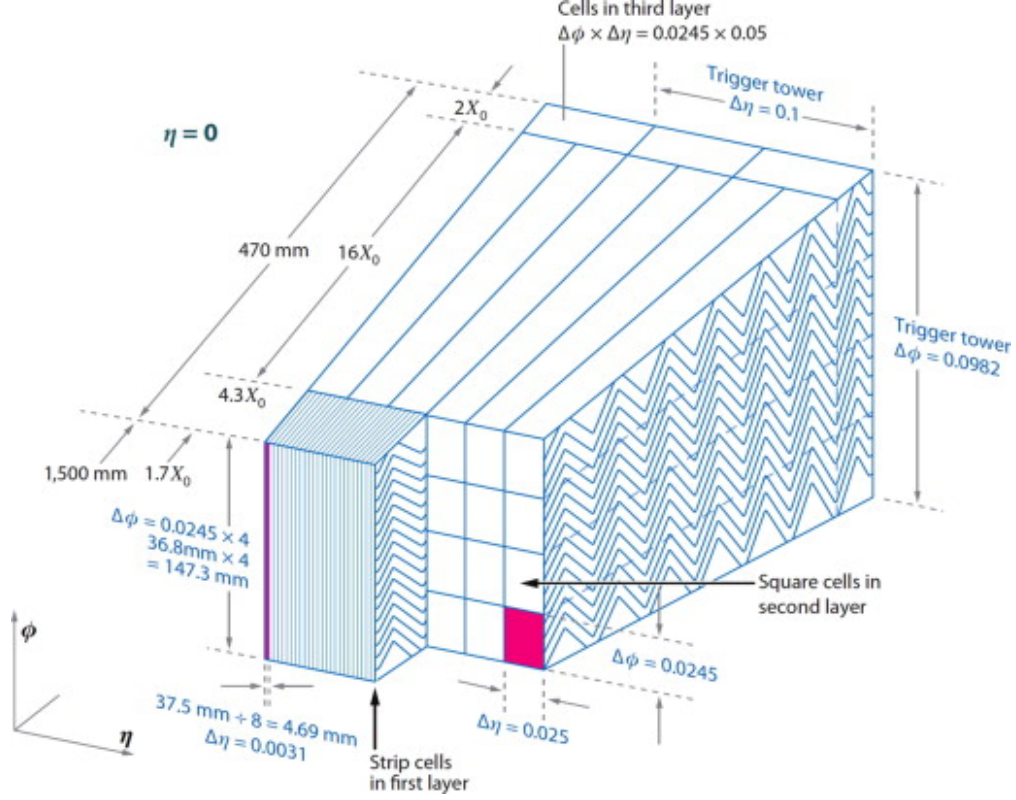


Figure 1.8: A schematic of the barrel Electromagnetic calorimeter. The three layers of the calorimeter and the accordion layout of the lead absorbers and electrodes are shown. Each layer presents a different granularity as summarized in Table 1.4

with accordion-shaped kapton electrodes and lead absorption plates over its full coverage. The liquid argon was chosen as an active medium because of its intrinsic radiation hardness and good energy resolution. The advantage of the accordion geometry is that it provides complete ϕ symmetry without azimuthal cracks. Over the region which is intended to be used for precision physics ($|\eta| < 2.5$) the EM calorimeter is segmented in depth in three sections. In addition, a presampler is used to recover the energy lost in dead material in front of the calorimeter. The total thickness of the EM calorimeter is $22 X_0$ in the barrel and $24 X_0$ in the end-caps. The layout of the barrel is shown in Figure 1.8.

The first layer of the calorimeter, called the η -strip layer, is finely granulated in η in order to allow for a better separation between photons (which results in a single energy deposition) and neutral pions (which results into two very close deposits of energy from the $\pi^0 \rightarrow \gamma\gamma$ decay).

The resolution achievable in the barrel EM calorimeter, according to test beam data, is:

$$\frac{\sigma(E)}{E} = \frac{10\%}{\sqrt{E(\text{GeV})}} \oplus 0.17\% \quad (1.10)$$

where 10% is the stochastic term and 0.17% is the constant term. The energy response is also linear within $\pm 0.1\%$. Similar results have been obtained for the end-cap EM calorimeters. At the transition between the barrel and the end-cap calorimeters, at the boundary between the two cryostats, the amount of material in front of the calorimeter reaches a localized maximum of about $7 X_0$. For this reason, the region $1.37 < |\eta| < 1.52$ is not used for

precision measurements involving photons and electrons.

Hadronic Calorimeters The hadronic calorimeters are subdivided in the tile calorimeter, whose barrel covers the region $|\eta| < 1.0$ and whose extended barrels cover the region $0.8 < |\eta| < 1.7$, in the LAr hadronic end-cap calorimeters, which extend from $|\eta| = 1.5$ up to $|\eta| = 3.1$ and finally the LAr forward calorimeter, which covers the pseudorapidity range up to $|\eta| = 4.9$. The tile calorimeter uses steel as the absorber and scintillating tiles as active material. Two sides of the scintillating tiles are read out by wavelength shifting fibres into two separate photomultiplier tubes. The energy response to isolated charged pions of the combined LAr and tile calorimeter was measured with test beams and turns out to be:

$$\frac{\sigma(E)}{E} = \frac{52\%}{\sqrt{E(\text{GeV})}} \oplus 3\% \quad (1.11)$$

For the end-cap hadronic calorimeters LAr technology is used, as the EM calorimeter in the barrel region, but copper is used instead of lead as a passive material and a flat-plate geometry was chosen. The energy response to isolated pions can be condensed in the energy resolution:

$$\frac{\sigma(E)}{E} = \frac{71\%}{\sqrt{E(\text{GeV})}} \oplus 1.5\% \quad (1.12)$$

Finally, the forward calorimeter is based again on LAr active material and uses copper as passive absorber material for the first layer and tungsten for the second and third layers. As a result of test beams, the energy response to isolated pions is expressed by:

$$\frac{\sigma(E)}{E} = \frac{94\%}{\sqrt{E(\text{GeV})}} \oplus 7.5\% \quad (1.13)$$

1.3.4 Muon System

The detection of muons in ATLAS can count on a dedicated sub-detector. Muons are among the most important signatures for interesting processes at the LHC and have a clear advantage that they are the only charged particles which are not stopped in the calorimeter (apart from rare cases of punch-through) and they are detected in the muon system. The muon detector is based on two kinds of sub-detectors, one for precision measurements, which is needed to determine the muon momenta with high precision, and another for the online trigger of muon events, which requires very fast sub-detectors to uniquely associate the muons to a certain bunch crossing. The precision measurements are performed by the Monitored Drift Tubes (MDT), which cover the pseudorapidity region up to 2.7, and in the forward region ($2 < |\eta| < 2.7$) by the Cathode-Strip Chambers (CSC), which are used in the innermost layer due to their capability of working at very high rate. The MDT chambers only constrain the muon track in the bending plane (z -coordinates), with a precision of $35\text{ }\mu\text{m}$, while the CSC, being multi-wire proportional chambers with cathode planes segmented into strips in orthogonal direction, provide a measurement both in the R direction of $40\text{ }\mu\text{m}$ precision and in the ϕ direction of 10 mm . These chambers are complemented (both for the measurement of the missing ϕ in case of the MDT and for the online event selection) in the barrel region ($|\eta| < 1.05$) by Resistive Plate Chamber (RPC) and in the end-cap ($1.05 < |\eta| < 2.4$) by Thin

Gap Chambers (TGC). The intrinsic time resolution of these detectors components (1.5 ns for RPC and 4 ns for TGC) is appropriate for triggering and permits to identify the correct bunch crossing.

Given the three chambers layout of the muon system, the momentum measured of a high- p_T track will depend on the resolution by which its sagitta (determined in the $R - z$ plane in the middle chamber with respect to a straight line) can be determined. For a high- p_T track of 1 TeV, this sagitta will be about 500 μm . The muon chamber resolution provided in ϕ by the MDTs allows to reach a precision better than 10% in the momentum measurements of muons up to 1 TeV, which corresponds to the design goals of ATLAS. For the measurements of low- p_T muons, the measurements in the muon system typically need to be complemented by measurements in the ID, since in general the outermost layer of the muon detectors will not be reached due to the stronger bending of low- p_T particles in the magnetic field.

1.3.5 Trigger System

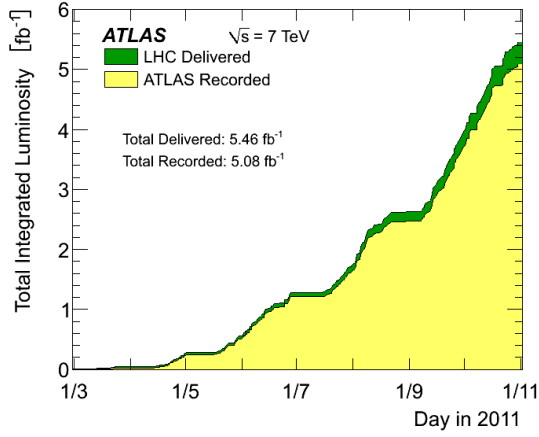
The ATLAS experiment uses a two staged trigger system to identify collisions of interest. The first stage, called Level-1 trigger, reduces the event rate from 40 MHz to 100 kHz, since a decision must be taken every 25 ns. Since the transit and processing time is around 2.5 μs , the detector data must be time stamped and held in the buffers of the front-end circuit. The Level-1 trigger uses information from dedicated muon trigger and from the calorimeters. The only signatures which can be selected in the L1 trigger are high- p_T muons, electrons/photons, jets, τ -lepton decaying into hadrons and missing transverse energy. No information coming from the tracking devices can be used at L1, so, for example, it is not possible to select b-jets at this level.

The second stage of the trigger system reduces the event rate further to a level of 0.5 kHz to 1 kHz. It is software based and uses offline-like reconstruction algorithms, utilizing informations from all sub-detectors in regions of interest around the Level-1 objects in full granularity. The regions of interest are areas of the detector which the L1 trigger has identified as interesting. The use of regions of interest allows to have a fast execution time keeping high the selection efficiency.

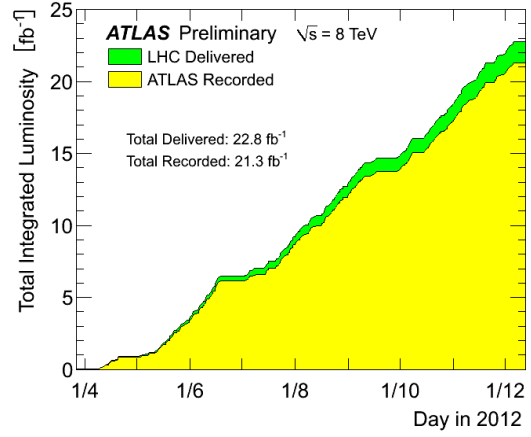
1.4 The ATLAS data taking until 2015

The LHC machine and the related experiments showed excellent performance. The data-taking was so far divided in two main period, Run 1 which took place in between 2010 and 2012, and Run 2 which started in June of 2015. So far the LHC delivered 32.5 fb^{-1} to the ATLAS and CMS experiments, as shown in Figures 1.9a, 1.9b and 1.9c. The ATLAS experiment was able to record 93% of the delivered luminosity as shown in Figure 1.9 for what concerns the proton-proton collisions.

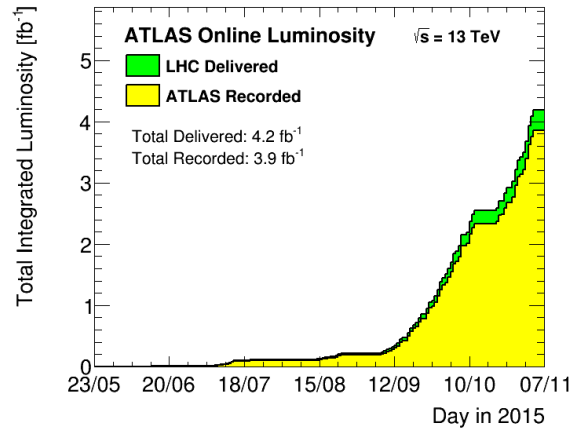
Detailed measurements of well-known SM processes were performed and used to calibrate the detector. Figure 1.10 shows the measured production cross section for several SM processes with their theoretical prediction.



(a) 2011 Luminosity



(b) 2012 Luminosity



(c) 2015 Luminosity

Figure 1.9: Cumulative luminosity versus day, in green the amount of luminosity delivered to ATLAS and in yellow the recorded one. This assume stable beam configuration for proton-proton collisions.

Standard Model Total Production Cross Section Measurements

Status:
Nov 2015

$\int \mathcal{L} dt$
[fb⁻¹]

Reference

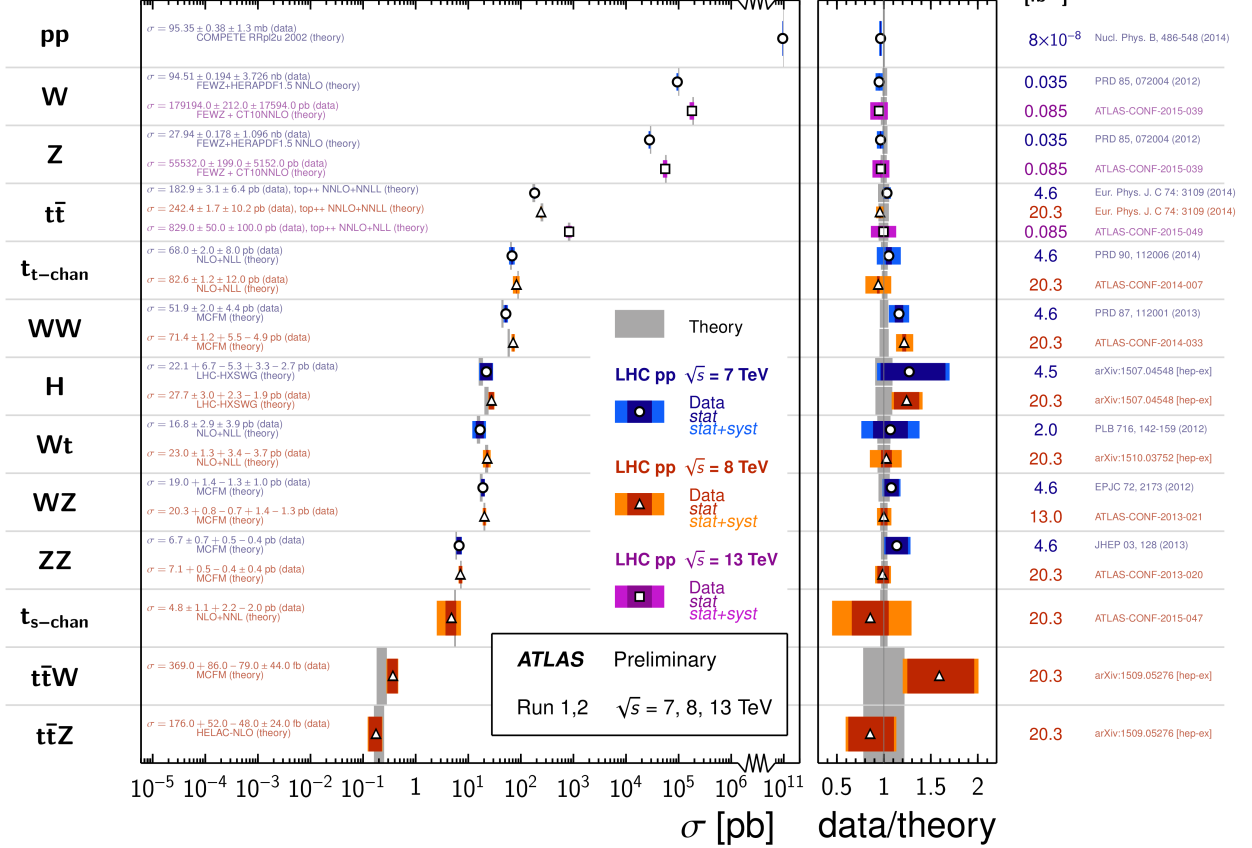


Figure 1.10: Summary of several Standard Model total production cross section measurements, corrected for leptonic branching fractions, compared to the corresponding theoretical expectations. All theoretical expectations were calculated at NLO or higher order. The W and Z vector-boson inclusive cross sections were measured with 35 pb⁻¹ of integrated luminosity from the 2010 dataset. All other measurements were performed using the 2011 dataset, the 2012 dataset, or the 2015 partial dataset. The dark-color error bar represents the statistical uncertainty. The lighter-color error bar represents the full uncertainty, including systematics and luminosity uncertainties. The data/theory ratio, luminosity used and reference for each measurement are also shown. Uncertainties for the theoretical predictions are quoted from the original ATLAS papers. They were not always evaluated using the same prescriptions for PDFs and scales.

1.5 The LHC upgrade program

The success of the discovery of the Higgs Boson was just one of the impressive results achieved by LHC experiments during the first period of data-taking. Figure 1.11 summarizes the upgrade steps of the LHC machine. A first long shutdown happened from February 2013 to April 2015 to consolidate the magnet inter-connects of the LHC machine. This upgrade was needed to run the LHC at the design energy of 7 TeV per beam and at the design luminosity of $10^{34} \text{ cm}^{-2} \text{ s}^{-1}$. The period after this upgrade of the LHC is usually referred to as Run 2, and it should last from 2015 to 2019, aiming to collect 100 fb^{-1} of data. The Run 2 has begun in the spring of 2015, with a 13 TeV center of mass energy, which will be increased to 14 TeV in next years. A second shutdown with machine development is foreseen in 2019, where the luminosity should be upgraded to twice times the nominal value, targeting an integrated luminosity of about 300 fb^{-1} . Detailed investigation of the Higgs boson properties and searches for new physics phenomena will require to collect more data than the 300 fb^{-1} foreseen in the present LHC schedule. Therefore an extension of the LHC data-taking is currently under investigation. The LHC plan is to record about 3000 fb^{-1} during the entire LHC data-taking campaign. A third shutdown is foreseen in 2024, where the luminosity should be upgraded to more than five times the current LHC nominal value. This major upgrade will require an optimization of the detectors, in particular, the higher luminosity will have an impact on the radiation performance of the Inner Detector, which will need to stand higher doses than the current one.

The first long shutdown was used for an upgrade of the ATLAS pixel detector as it will be discussed in Chapter 3 of this thesis. While no upgrade of the ATLAS Pixel detector is foreseen in the second long shutdown a complete redesign will be needed after the third long shutdown. The new system should in particular sustain the harsh radiation environment and provide fast information for the new track based trigger system.

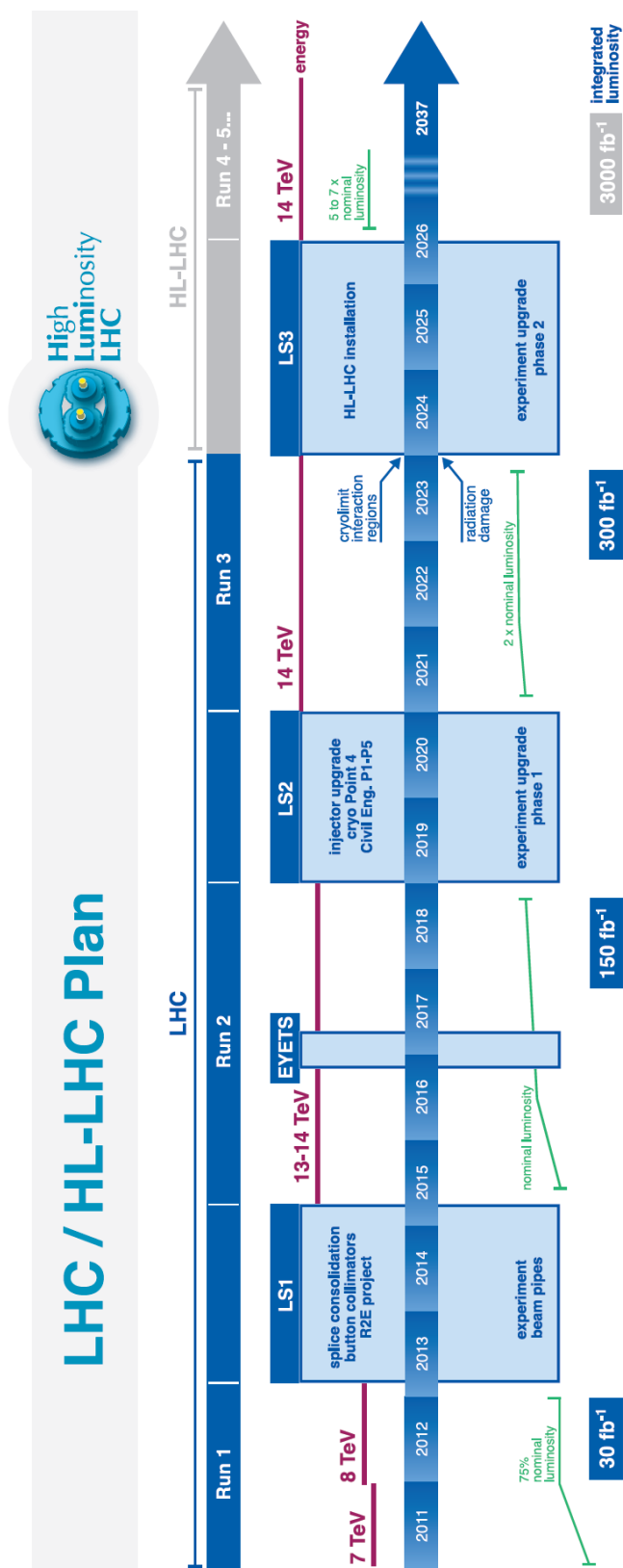


Figure 1.11: Time schedule for the long LHC shutdowns and the run phases

Chapter 2

Track reconstruction with pixel detectors

Precise tracking is a fundamental tool for any collider experiment. An efficient identification of electrons and muons, based on tracking, is a key factor for a correct reconstruction of the final states of collision events.

It is important to determine the position of the interaction point, the primary vertex, moreover some particles do not decay promptly after the production and they neither live enough to transverse the full detector, i.e. hadrons containing b and c-quarks and the τ -lepton. All these particles have in common that they decay inside or close to the innermost detector layer, but on average live long enough to have their decay detected by measuring the position of their decay vertex, the secondary vertex.

Pixel detectors play a fundamental role in tracking and vertex identification thanks to their high granularity, good time resolution and the high radiation hardness. The high density of channel lead to a high spatial resolution, a feature extremely important to be able to distinguish each of the tracks in a dense environment, so that pixel detectors can be used for pattern recognition purposes. The high rate of collision of the LHC requires also detectors to be very fast, and operate at the typical 40 MHz rate. Pixel detectors meet this requirement thanks to fast transistors with dimension of the order of 200 nm. This detection technique is ideal for operating close to the interaction point (IP) due to its radiation hardness performance. In this chapter the mechanism of charged particles detection, tracking in magnetic field and vertices discrimination will be covered.

2.1 Particle interaction with matter

A particle that is crossing some material could interact with it either losing some of its own energy or deflecting its trajectory. Those properties are used to detect particles at high energy physics experiments. The energy loss could happen either via electromagnetic or nuclear interactions, involving the atom's electrons and nuclei. Particles detectors are mainly distinguished by the mechanism they use to reveal the particles and the type of particles they are devoted to detect, i.e. tracking detectors normally detect charged particles via ionization interaction. In this section a brief description of the main interaction processes in tracking detectors will be presented.

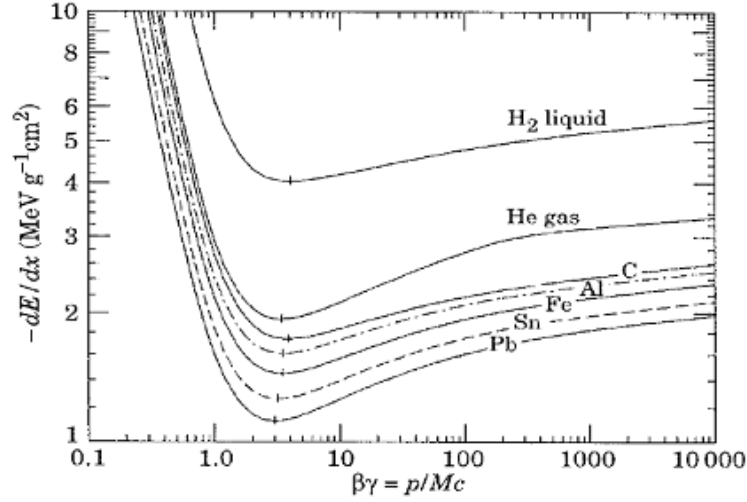


Figure 2.1: The Bethe-Bloch equation solved for several materials in case of a particle with electric charge 1.

2.1.1 Interaction of charged particles

The description of the energy loss of a charged particle through ionization is provided by the Bethe-Block formula[21], a quantum-mechanical correction to the Bohr formula which uses a classical electro-dynamic approach. The mean energy loss per unit length is:

$$-\left\langle \frac{dE}{dx} \right\rangle = \frac{4\pi r_e^2 m_e c^2 N_A Z z^2 \rho}{A \beta^2} \left(\frac{1}{2} \ln \left(\frac{2m_e c^2 \beta^2 \gamma^2 T_{max}}{I^2} - \beta^2 - \frac{\delta(\beta\gamma)}{2} \right) - \frac{C}{Z} \right) \quad (2.1)$$

where Z and A are the atomic and the mass number of the material, ρ is the material density, N_A is the Avogadro constant and $r_e = 2.8$ fm is the classical electron radius, z is the charge of the incident particle in unity of electrons, $\beta = \frac{v}{c}$ and $\gamma = \frac{1}{\sqrt{1-\beta^2}}$, where c is the speed of light. The mean excitation energy of the material $I \simeq I_0 Z$ with $I_0 \simeq 12$ eV when $Z < 13$. T_{max} is the maximum kinetic energy which can be transferred to a free electron in a single collision. C is the shell correction. The density correction δ is an effect which becomes important at high energy, when the incident particle polarizes the material while crossing it. This produces a screening effect on atoms far from the particle, reducing the energy loss. As a function of $\beta\gamma$ the energy loss has no dependency on the mass of the incident particle. The Bethe-Block formula is valid in the $\beta\gamma$ range from 0.05 and 500, outside this range other processes than ionization are dominant.

Figure 2.1 shows the mean energy loss of a particle crossing a material as a function of its $\beta\gamma$. Due to the small increase above the minimum, all the particles with $\beta\gamma > 3$ and up to 500 are commonly called Minimum Ionizing Particles, for $\beta\gamma > 500$ radiative effects becomes dominant with respect to ionization. This condition is typical of the collision products of the LHC. The calculation of energy loss depends on the width of the absorber media. For a thick absorber the distribution of energy loss is gaussian, given the high number of interactions. For a thin absorber the number of interactions is low and the energy loss distribution is not gaussian. A theoretical calculation was provided by Landau[22], Symon and Vavilov based on the parameter $\kappa = \frac{\bar{\Delta}}{W_{max}}$, where $\bar{\Delta}$ is mean energy transferred in a single scattering and W_{max} is the maximum energy that can be trasferred in a single scattering process. The Landau theory is valid for $\kappa \leq 0.01$ and it assumes that $W_{max} \rightarrow \infty$, the trasferred energy is

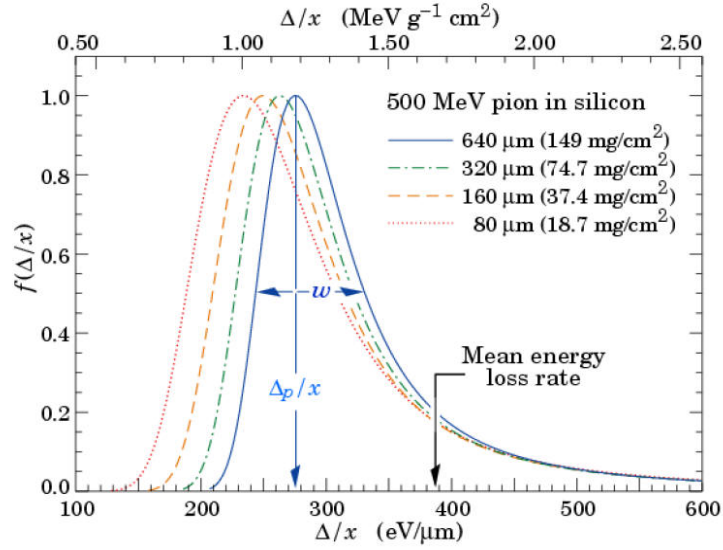


Figure 2.2: Landau functions in silicon for 500 MeV pions, normalized to unity at the most probable value Δ/x . The Landau distribution is shown for different widths of silicon layers.

high enough that the electrons could be considered as free, the speed of the incident particle remains constant in the scattering process. The integral transport equation can be solved under these hypothesis.

$$\frac{df}{dx}(x, \Delta) = \int_0^\infty W(E)[f(x, \Delta - E) - f(x, \Delta)]dE \quad (2.2)$$

Here $f(x, \Delta)$ represents the distribution probability that the incident particle will lose an amount Δ of energy on traversing a layer of thickness x . $W(E)dE$ denotes the probability per unit path length of a collision transferring energy E to an electron in the material. The function $W(E)dE$ is not generally known, an approximate solution by using the free electron (Rutherford) cross section that matches with the hypothesis:

$$W(E) = \frac{\xi}{x} \frac{1}{E^2} \quad \& \quad \xi = 0.1535x \frac{z^2 Z \rho}{A \beta^2} [\text{MeV}] \quad (2.3)$$

The Landau distribution is therefore given by:

$$f_L(x, \Delta) = \frac{\phi(\lambda)}{\xi} \quad \& \quad \phi(\lambda) = \frac{1}{\pi} \int_0^\infty e^{-t \ln(t) - \lambda t} \sin(\pi t) dt \quad (2.4)$$

$$\lambda = \frac{\Delta - \bar{\Delta}}{\bar{\Delta}} - \ln\left(\frac{\bar{\Delta} 2mc^2 \beta^2}{(1 - \beta^2) I^2}\right) - 1 + C_E$$

where $C_E = 0.5772$ is the Euler constant. The Landau distribution, $f_L(x, \Delta)$, is asymmetric with a tail extending to E_{max} . This tail is mainly due to fast emitted δ -rays, electrons with enough energy to escape a significant distance away from the primary radiation beam and produce further ionization. The energy loss corresponding to the maximum of the function $f_L(x, \Delta)$ is the most probable energy loss. Figure 2.2 shows the typical Landau distribution for different widths of silicon layers for an incoming 500 MeV pion.

2.1.2 Particle scattering

In addition to inelastic collisions with the atomic electrons, particles passing through matter undergo repeated elastic scattering from nuclei although with a smaller probability. Considering that usually nuclei have mass greater than the incoming particle, the energy transfer is negligible but each scattering centre adds a small deviation to the incoming particle trajectory. Even if this deflection is small, the sum of all the contribution adds a random component to the particles path which proceeds with a zig-zag path. As result, particles show a deviation from the incoming trajectory after having crossed a material. Three possibility can be considered:

- Single scattering. When the thickness is extremely small and the probability to have more than one interaction is negligible. In this case the situation is well described by the Rutherford formula[23]:

$$\frac{d\sigma}{d\Omega} = \left(\frac{1}{4\pi\epsilon_0}\right) \frac{z_1^2 z_2^2 e^4}{M^2 c^4 \beta^4} \frac{1}{\sin^4(\frac{\theta}{2})} \quad (2.5)$$

- Plural scattering. When the number of Coulomb scattering increases but remains under few tens. This is the most difficult case to deal with, several works have been published by different authors[24].
- Multiple scattering[25]. When the thickness increases and the number of interactions become high the angular dispersion can be modeled as Gaussian.

Multiple scattering is the most common situation. The angular dispersion can be calculated as:

$$\sigma_{\Theta_0} = \frac{13.6 MeV}{\beta c p} z \sqrt{\frac{x}{X_0}} [1 + 0.038 \ln(\frac{x}{X_0})] \quad (2.6)$$

where p is the momentum, z is the charge of the incident particle and $\frac{x}{X_0}$ is the path in radiation lengths in the absorber material. Multiple scattering contributes to the uncertainty on the track reconstruction. Reducing the detector thickness and using material with larger X_0 decreases the standard deviation of the scattering angle distribution.

2.1.3 Interaction of neutral particles

Charged particles are not the only ones contributing to energy release in matter, since also the release of energy from zero electric charge particles needs to be considered. Significant contributions come from photons and from neutrons. The two type of particles interact in a very different way and have different impact on tracking performance. Photons can interact in many ways with the material via electromagnetic interactions. The type of interaction depends on the atomic number Z of the material and of the energy of the photons themselves. Figure 2.3 shows the probability of photon absorption for 300 μm silicon as function of the photon energy and the contribution from different processes. Several types of photon interaction with matter are possible, the most probable are:

- Photoelectric effect: which is the most probable interaction for energy lower than 0.1 MeV

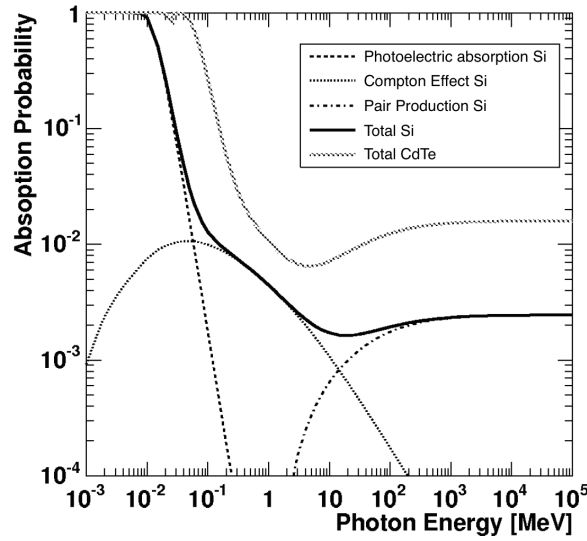


Figure 2.3: Probability of photon absorption for 300 μm silicon as function of the photon energy. Contributions from different processes are indicated. The total absorption probability for 300 μm CdTe is also given for comparison.

- Compton effect: which is the most probable interaction in the energy range 0.1 MeV to 100 MeV
- Pair production via bremsstrahlung: which is the most probable interaction for energy higher than 100 MeV

In the LHC environment photons are typically energetic and the pair production mechanism, which is the dominant one, will be taken in consideration in the following text. Although pair production is the key-process for photon identification in the calorimetry, it is a background phenomenon that could lead to fake reconstructed tracks and vertices in the Inner Detector. In this process the photon interacts with an electron or a nucleus producing a positron-electron pair. In order to produce the pair the photon must have at least an energy of 1.022 MeV.

Neutron can interact with matter by strong interactions with nuclei. In general strong interactions could happen also with charged hadrons, as protons, but they are rare with respect to electromagnetic interactions. Nevertheless, with the high fluences of LHC hadronic interactions cause radiation damage to the device so that it needs to be well monitored. The type of neutron interaction will depend upon the energy of the neutron and the mass number of the material itself. Here follows a list of the most important phenomena:

- Elastic scattering, which is dominant in the MeV region;
- Inelastic scattering, in which the nucleus is excited and then decays with the production of γ . This phenomenon has a energy threshold of about 1 MeV;
- Neutron capture, corresponding to the process $n + (Z, A) \rightarrow \gamma + (Z, A + 1)$, which is dominant for low energy neutrons (eV-keV);
- Other nuclear reactions, which typically happen for low energy neutrons (eV-keV);

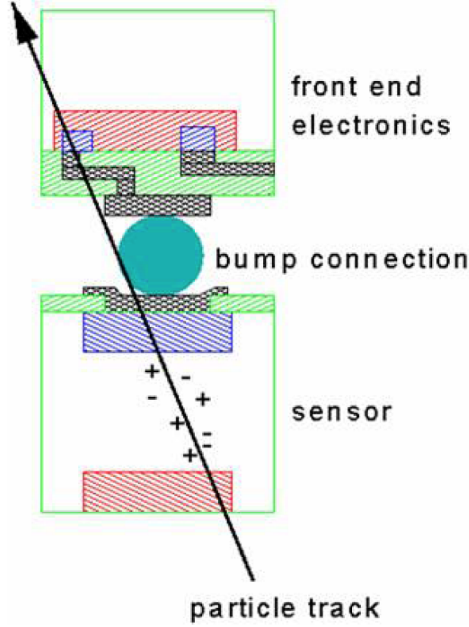


Figure 2.4: Cross section of hybrid pixel readout channel. The sensor, at the bottom, provides the electric signal, the bump, in the middle, provides the interconnection and the readout chip, at the top, takes care of the signal amplification and the data processing.

- Production of hadronic showers, for very high energy neutrons ($\simeq 100$ MeV)

The cross section of neutron interaction is inversely proportional to the velocity of the neutron itself. This means that the most interacting neutrons are the low energetic ones, which are then the most dangerous for devices that needs to operate in a radioactive environment. Details about the radiation damage will be treated later in this thesis work.

2.2 Properties of pixel silicon detector

The main tasks of the pixel detector is the pattern recognition and the reconstruction of the impact parameters of the tracks. Additionally, pixel detectors contribute to the resolution of the secondary vertices measurements. Pixel detectors are made of silicon sensors. The choice of silicon as a bulk material is motivated by the radiation hardness, the possibility to achieve fine segmentation, good time resolution and high availability that provides a relatively low cost. A brief description of the main properties and the most important aspects that need to be considered in silicon detectors is given in the following.

There are two possible options for pixel silicon sensors, either the readout electronics is integrated on the sensor itself (monolithic sensor) or the readout electronic is integrated in an external chip, connected to each pixel of the sensor (hybrid sensor).

The working principle of hybrid sensors is shown in Figure 2.4, the signal is created in the silicon sensor and then transmitted to the readout chip connected to the sensor via a metallic bump.

2.2.1 Signal generation in silicon sensors

Silicon is a semiconductor, this means that electrons that are bounded to the silicon atoms can be freed when a relatively small amount of energy is transferred to them. This principle is well described in the band theory [26] with the concept of energy gap, which is the minimum energy that an electron requires to move freely in the structure of the material. In silicon the energy gap is ~ 1.1 eV, this mean in average 3.6 eV are needed to free an electron from a silicon atom, because most of the energy is lost within the lattice structure. The electron is then free to move around the silicon lattice and it contributes to the electrical conductivity of the material.

The lack of an electron in the crystal bounds is as well participating to the electrical conductivity. Indeed in the lattice electrons from other atoms could fill the vacancy, and those electrons will be affected by any external field applied to the silicon, taking part to the electrical conductivity. This phenomenon could be schematized thinking the vacancy of an electron in the silicon crystal acting as a positive charge, also called hole. The electrical conductivity can be then described in terms of electrons, referring to the contribution of free electrons inside the lattice, and holes, referring to the contribution of bounded electrons of the lattice.

As previously said, when a ionizing particle crosses a material, it transfers energy to the material by ionization. In semiconductors this energy is high enough to let an electron leave the atom and so to create an electron-hole pair. The same happens in metals, but without an energy threshold, so that thermal effects dominate and the creation of the signal cannot be distinguished.

Another property that makes silicon a good material for particle detection is the possibility of doping it to modify its electrical properties. Doping is a process in which impurities are diffused in the silicon, with local modification of the lattice structure. Doping can be p-type, where boron atoms replace some of the silicon atoms in the lattice structure, or n-type where phosphorus atoms are used instead. In the p-type silicon, given the 3 valence electrons of the boron instead of the 4 of the silicon, one of the bounds of the boron with the surrounding silicon atoms is made by a single electron, instead of a couple. The net effect of p-type boron is to increase the number of holes in the lattice structure. In the n-type silicon, phosphorus atoms have 5 valence electrons, 4 of them are used to create bounds with the surrounding silicon atoms and one is free to move in the crystal.

Doping is widely used in electronics to create p-n junction non-linear devices as diodes and transistors. A diode is a p-n junction, a device in which the silicon is doped with two different dopings. In a p-n junction the two different types of doping are made next one to each other in a silicon crystal. Since the two doped materials have different concentrations of electrons and holes, free electrons from n-type side will diffuse in the p-type region and free holes of p-type will go in the n-type one. This process will create a region depleted by free charge and in which there is a built-in electrical field due to the charge of the ions (boron and phosphorus), the depletion region, as shown in Figure 2.5.

Silicon sensors are simple diodes where the collecting electrodes, made of heavily doped silicon (typically the concentration of doping centers is higher than $10^{15}/\text{cm}^3$), are implanted on a poorly doped bulk (doping concentration in the range $10^{12}/\text{cm}^3$ to $10^{14}/\text{cm}^3$). Two types of electrodes are present in silicon detectors, one with an opposite-type doping with respect to the bulk and another with same-type doping but higher concentration. The first forms the p-n junction with respect to the bulk, while the second is used as ohmic contact.

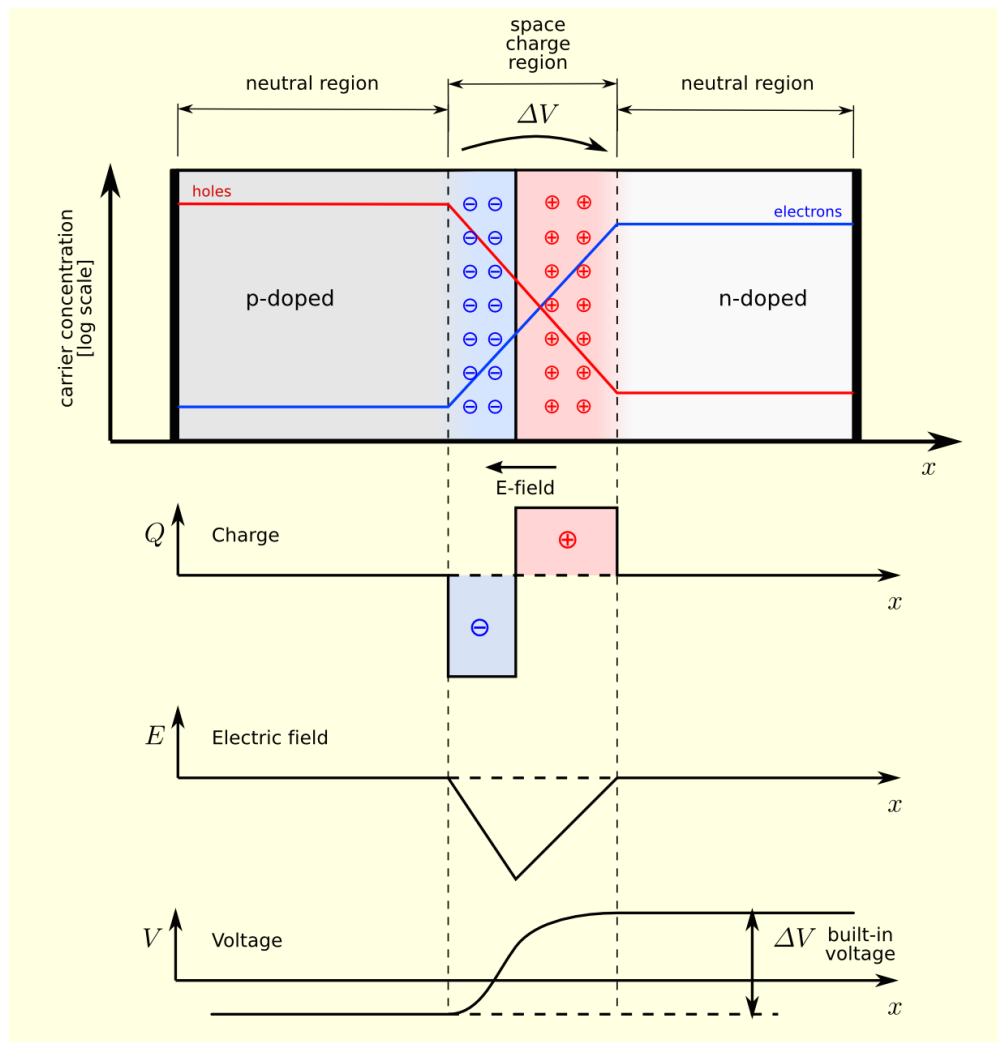


Figure 2.5: Schematic view of a p-n junction

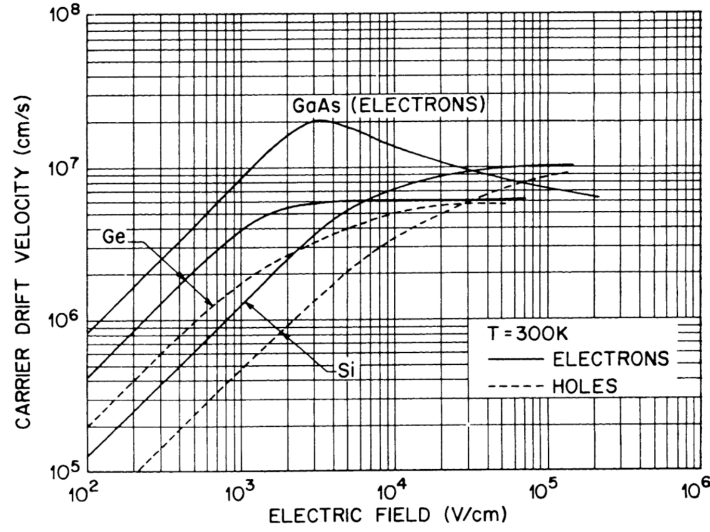


Figure 2.6: Drift velocity as function of the electric field for different material at room temperature. [27]

Metal is not used to create an ohmic contact with the bulk because of the higher fermi level, which would effect in an additional current source in the device.

The depletion region is crucial in silicon detectors. When an ionizing particle is passing through the depletion region it generates holes and electrons that drift towards the electrodes because of the electric field, so that the possibility of recombination of the electron-hole pair is drastically reduced. The depletion region can be enhanced applying a reverse bias to the diode, up to the entire volume of the sensor. The maximum voltage that one can impose while keeping the current across the diode low is called breakdown voltage. Silicon sensors are typically operated below the breakdown voltage, in order to limit the leakage current. The speed of electrons and holes is directly proportional to the electric field;

$$\vec{v}_{h,e} = \mu_{h,e}(|\vec{E}|)\vec{E} \quad (2.7)$$

where $\mu_{h,e}$ is the mobility, which depends on material impurities and temperature. Figure 2.6 shows the drift velocity as function of the applied electric field for silicon devices at room temperature. Drift is not the only type of movement for holes and electrons in the silicon, since thermal diffusion is acting as well as predicted from diffusion theory. The diffusion mechanism spreads the cloud of electron-hole pairs generated with a gaussian distribution around the generation point. The standard deviation of this gaussian is:

$$\sigma_{h,e} = \sqrt{2D_{h,e}t_{h,e}} \quad (2.8)$$

where $D_{h,e}$ is the diffusion coefficient and $t_{h,e}$ is the lifetime for holes and electrons. Holes and electrons turn out to have roughly the same σ , because $D_{h,e} \propto \mu_{h,e}$ and $t_{h,e} \propto 1/\mu_{h,e}$. Typical values are $\sigma \simeq 10 \mu\text{m}$. Given the Bethe-Block equation, a singly charged minimum ionizing particle releases $1.66 \text{ MeVcm}^2/\text{g}$ in silicon, which means that for a $200 \mu\text{m}$ thick device 14000 electron-hole pairs are generated. Those numbers are very important to choose the proper threshold in the electronics. The signal seen by the electrodes is an induced signal, the movement of each single electron is contributing to the current at the electrode even when the charges are far from it. The typical signal duration depends on the applied voltage, the resistivity of the silicon and the thickness of device. Typically this is of the order of $\sim 10 \text{ ns}$.

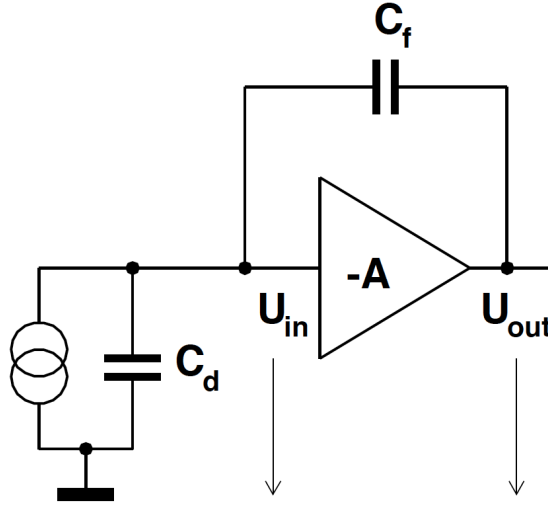


Figure 2.7: Principle of a charge-sensitive amplifier [27]

2.2.2 Amplification and digitization of the signal

The signal coming from the silicon sensor needs to be amplified and digitized to be transmitted to the data-acquisition system. These operations are performed at the level of the read-out chip, which is typically divided in a analog circuitry, responsible for the amplification and the digitization, and a digital circuitry, responsible for the delivering of the signal to the data-acquisition system.

The analog part of the circuitry faces directly the silicon sensors and it can use several techniques for the conversion of the signal in an amplified and square one. In the following the details about a charge sensitive amplifier will be given, since this is the strategy used for the read-out chip considered in this thesis.

The principle of a charge sensitive amplifier is shown in Figure 2.7. The silicon sensor can be schematized as a current source in parallel with a capacitor, describing the capacitance of the sensor pad. The induced charge from the silicon sensor results in a voltage U_{in} at the amplifier input that is amplified to $U_{out} = -AU_{in}$. Ideally no current flows at the amplifier input and then the charge Q_f on the feed-back capacitor C_f and the charge Q_d remaining on the detector capacity must add to the signal charge Q_{coll} . The voltage on C_f is the difference between input and output voltage and thus:

$$Q_{coll} = Q_f + Q_d = U_{out} \cdot \left(C_f \frac{A+1}{A} - C_d \frac{1}{A} \right) \quad (2.9)$$

which yields the output voltage as function of induced charge:

$$U_{out} = \frac{Q_{coll}}{C_f \frac{A+1}{A} + \frac{C_d}{A}} \xrightarrow{A \rightarrow \infty} \frac{Q_{coll}}{C_f} \quad (2.10)$$

so that the charge gain is easily controlled by only one parameter (C_f) in case of large amplification. The feed-back capacitor of the charge sensitive amplifier needs to be reset after a signal from the silicon sensor has been processed. This is achieved by either adding a resistor or a constant current source in parallel to C_f . It is often necessary to modify the

shape of the signal pulse produced by the charge sensitive amplifier, combining a low-pass and a high-pass filter to the amplifier; this is usually referred as shaper. The limiting frequency range that can pass the charge sensitive amplifier circuit is used to limit the bandwidth for noise to pass through the read-out circuit. Noise in electronic devices has three main origins:

- Thermal noise: caused by thermal fluctuations in the charge carrier distribution of any conductors; its power spectrum is constant in frequency and proportional to the temperature.
- Shot noise: caused by fluctuations in the number of charge carriers when a boundary (e.g. a p-n junction) is crossed; its power spectrum is constant in frequency and proportional to the current crossing the boundary.
- Low frequency noise: has a large variety of sources, e.g. charge trapping and release in semiconductors. The power spectrum is proportional to $f^{-\alpha}$, where f is the noise frequency and $\alpha = 0.5...2$.

A more detailed treatment of noise can be found in [28]. The noise as seen after the analog part of the readout system is described by the variance of the amplitude of the output signal $< U_{out}^2 >$ which is directly proportional to the noise power spectrum. The noise contribution from the silicon sensor comes from shot noise of the leakage current I_{leak} , while the noise that comes from the amplifier transistors corresponds to voltage fluctuations on the amplifier input, composed of low frequency and thermal noise. The noise could be estimated as the charge needed on the read-out input in order to create an output signal of the same amplitude as:

$$Q_{noise}^2 = C_f^2 \cdot < U_{out}^2 > = c'_1(C_d + C_f)^2 \frac{1}{\tau} + c'_2(C_d + C_f)^2 + c'_3 I_{leak} \tau \quad (2.11)$$

where τ is the time constant of the shaper. In most of the vertex detectors the amount of information and channels is large enough to require the analog signal to be digitized already on the detector electronics, turning signal information into a digital bit-stream. A discriminator is used to decide if a signal is sufficiently large to have been created by a particle hit, thus discarding a fraction of noise hits. The discriminator information can be used to limit further processing only to those signals that have a hit reported (zero-suppression), thereby reducing the amount of data that has to be handled.

If the shape of the signal at the discriminator input is well controlled and the falling edge is significantly larger than the rise-time, the time that the signal remains above threshold (time-over-threshold, ToT) is related to the height of the signal and then proportional to the charge released in the silicon detector. The ToT is measured by detecting the rising and falling edges of the discriminator output and determining the time difference between them. In case of a linearly falling edge of the amplifier signal, the signal height is approximately proportional to the measured ToT . When a hit is to be measured by a discriminator, *time – walk* may be of concern: due to a finite amplifier rise time, which is controlled by the amplifier supply current, the time at which the discriminator goes to the logical on depends on the height of the signal itself, i.e. on the charge at the amplifier input. If the time-walk is too large, a hit with low charge might be detected too late and be wrongly associated to the next bunch-crossing. The setting of the amplifier supply current is therefore a compromise between power consumption and thus heat dissipation and the need to keep the time-walk as low as possible.

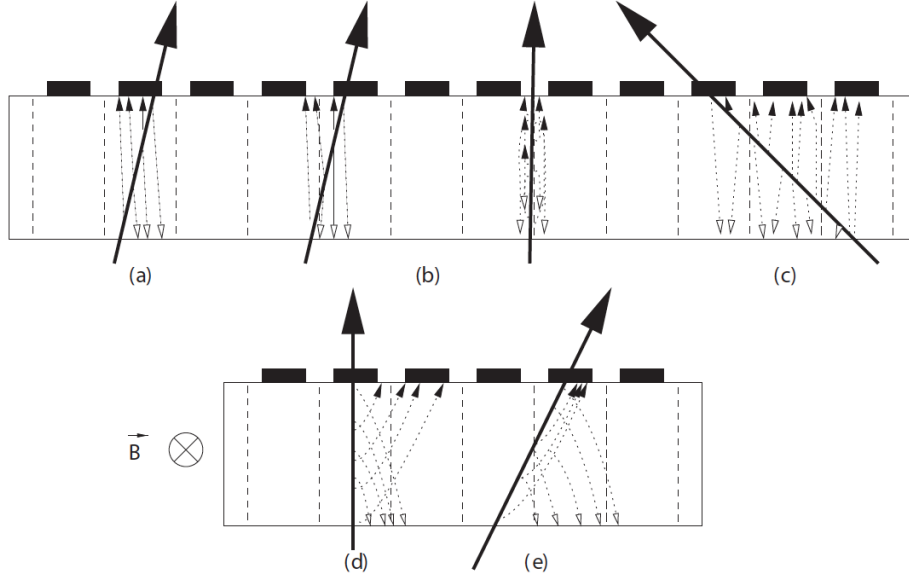


Figure 2.8: The formation of clusters in a silicon detector [27]. The different types of arrows denote the polarity of the charge carriers while the big arrow indicates the particle direction. Clusters are determined by the position and angle of the track. The presence of a magnetic field (see d and e) leads to a shift of the carriers path (Lorentz angle) in the silicon.

2.2.3 Spatial resolution

The spatial resolution across a given direction is determined by the dimensions of the pixel and the charge sharing between neighboring pixels. The minimum spatial resolution is obtained when a single pixel is collecting all the signal and so the charge is not shared among different pixels. The resolution in this case can be calculated assuming a uniform particle occupancy across the pixel width. The error on the position measurement is thus the standard deviation σ of the distribution probability, which is:

$$\sigma = \sqrt{\frac{\int x^2 f(x) dx}{\int f(x) dx}} = \sqrt{\frac{\int_{-\frac{d}{2}}^{\frac{d}{2}} x^2 dx}{\int_{-\frac{d}{2}}^{\frac{d}{2}} dx}} = \frac{d}{\sqrt{12}} \quad (2.12)$$

where d is the pixel size across the considered direction.

When a particle crosses the detector there is the possibility that more than one pixel detects it. The different possibilities are shown in Figure 2.8. In particular a particle could pass in between the pixels (Figure 2.8(b)) or crossing the silicon detector with a large angle so that charge is released in several pixels (Figure 2.8(c)). Another effect is the spread of the electron-holes cloud, but this contribution is limited by the strong electric field applied to the silicon sensors and typically the spread is in the order of few μm , small if compared to the pixel size. In case more than one pixel fires at the passage of a particle the information provided by each of them is treated together as a single object, called cluster. The cluster is defined by its size, which is the number of firing pixel, its position, which is the weighted center of charges of all the pixel, and its total charge. When the cluster size is greater than

one, the resolution improves, because the position of the particle can be determined by the calculation of the "centre of gravity" of the charge. In ATLAS the reconstruction of the cluster is performed with neural network algorithms [29]. In case only an electric field is applied to separate the charge carriers, they drift along the direction of this field. If an additional magnetic field is present, as it is the case of most tracking detectors, the path of the charge carriers deviates off the direction of the electric field due to the additional Lorentz force acting on the carriers (Figure 2.8(d)). The effective angle of this deviation, the Lorentz angle θ_L , is [27]:

$$\tan\theta_L = \mu_{Hall}B_{\perp} \quad (2.13)$$

where B_{\perp} is the magnetic field perpendicular to the drift direction and μ_{Hall} is the Hall mobility, which is closely related to the mobility previously discussed. The effect of the magnetic field is illustrated in Figure 2.8(d). It leads to a systematic shift of the detected hit position. The Lorentz angle may partially be compensated by inclining the detector with respect to normal particle incidence, as indicated in Figure 2.8(e). For strong electric fields, the dependency of the mobility μ on the field strength becomes important, also changing the Lorentz angle. This is an issue for silicon detectors after irradiation due to the increased depletion voltage necessary to operate them with high electric field. While charge sharing is in general beneficial for the precision of the reconstruction of the track position, it also reduces the signal seen on each electrode which may be below the detection threshold of the read-out electronics. The design of a silicon detector, in particular the inclination of the silicon sensors with respect to the expected particle direction, is therefore a compromise: the position resolution by charge sharing must be optimized while maintaining an efficient detection of signals.

2.2.4 Radiation damage of the silicon bulk

Silicon detectors suffer from radiation damage due to the particles produced in the collisions, an issue which is particularly relevant for the LHC experiments due to the high doses delivered to the tracking systems. Incident particles at the LHC have sufficient energy to remove a silicon atom from the lattice. These collisions are mediated by the Coulomb interaction in case of charged particles and by nuclear forces in case of neutral particles, in particular neutrons. Silicon atoms that are removed and get a sufficient amount of kinetic energy can remove other atoms from the lattice, resulting in a cascade of interactions. Radiation-induced lattice damage is classified into point and cluster defects. Typically defects in the lattice are unstable and an interstitial atom is mobile and can fill a vacancy in another position.

The defects are of importance to the detector properties because they can create additional energy levels in the gap between valence and conduction bands. Levels in the middle of the gap act mainly as generation and recombination centers given the similar distance to either band and thus similar access probability for electrons and holes. In contrast, levels close to the valence or conduction band act as trapping centers, i.e. electrons or holes are captured from the respective bands and released with a delay. The trapping modifies the effective doping since free charge carriers are removed from the material. In a similar way acts the combination of donor or acceptor atoms with vacancies or interstitial into stable defects. This has an effect on the depletion zone and on the bias needed for the full depletion. For large radiation doses, the depletion voltage may change from 100 V to 1000 V. The charge trapping has also a consequence for the signal that is measured; the trapped charge carriers

are released with a delay of the order of μs which is too long for the released electron (or hole) to be detected in the data-taking time window. The net signal measured is therefore smaller than for unirradiated devices, reducing detector performance. The trapping is usually characterized by a trapping constant τ^+ . The observed charge signal from a minimum ionized particle is reduced by ΔQ due to trapping for an originally created amount of charge carriers Q according to [30]:

$$\frac{\Delta Q}{Q} = \frac{1}{3} \left(\frac{t_e}{\tau_e^+} + \frac{t_h}{\tau_h^+} \right) \quad (2.14)$$

where $t_{e,h}$ are the time for electrons or holes to reach the electrodes, respectively. The inverse of the trapping time constant is proportional to the particle fluence Φ :

$$\frac{1}{\tau^+(\Phi)} = \frac{1}{\tau^+(0)} + \gamma\Phi \quad (2.15)$$

with $\tau^+(0) \sim 0.51 \cdot 10^6 \text{s}^{-1}$ for both electrons and holes. For low fluences, the proportionality constant γ is approximately the same for electrons and holes ($\gamma \sim 0.24 \text{cm}^2/\text{s}$), however electrons show a stronger increase of $\frac{1}{\tau^+}$ above fluences of $\sim 10^{14} \text{cm}^2/\text{s}$ normalized to 1 MeV neutrons [30]. The generation-recombination centers lead to a additionally free electrons-hole pairs, that lead to an increase of leakage current I_{vol} related to the applied reverse bias voltage V as: $\Delta I_{vol} = \alpha\Phi V$, with $\alpha \sim 8 \cdot 10^{-14} \text{A/cm}$ for silicon at a temperature of 20°C [30]. Another phenomenon that occurs after high radiation fluence is the change of properties of the bulk material, that led to an increase of the full depletion voltage. The increase of the depletion voltage results in, the increase of the operation voltage of the device, with the subsequent increase in power consumption and a significant heat load to the device. If the heat load is not carried away effectively, the exponential dependency of I_{vol} on the temperature will lead to an avalanche effect between increase of temperature and leakage current, also known as thermal runaway. Therefore sufficient cooling must be provided, with low temperature in order to reduce α and thus the extent of the radiation damage.

The radiation induced defects in the silicon crystal structure that cause this degradation are most often not stable and consequently lead to a change of the sensor properties within time. The mobility of defects in silicon or their transformation is a process known as annealing and it is usually accelerated exponentially with temperature [31]. Two stages are generally identified in the annealing process. In the first stage, known as beneficial annealing, part of the negative space charge generated by the defects is neutralized. Following this stage, the reverse annealing takes place, during which additional negative space charge is created in the sensor bulk [31].

The behavior of a silicon detector with respect to irradiation depends on the bulk doping of the silicon. N-type bulk undergoes to a phenomenon known as type inversion, that leads the concentration of p-type defects to increase with radiation, so that, at some point, the number of p-type defects becomes larger than the n-type ones. The net effect is the migration of the p-n junction from the p^+ electrodes to the n^+ , which needs to be considered in the design.

Three main field were investigated in order to reduce the contribution of leakage current and to keep high performance even after high radiation doses: the defect engineering of silicon, the device engineering and the study of new materials.

Defect engineering of silicon consists in the deliberate incorporation of impurities or defects into the silicon bulk to improve the radiation tolerance of detectors. This is usually done enriching the silicon with oxygen during the production of the silicon lattice.

Device engineering consists in the optimization of the design of the device. Several concepts have been developed so far. As already introduced p-doping is the best choice for device that have to stand high radiation doses, this translates in n^+ -in-p devices, where the junction electrodes are made of heavily doped n-type silicon and the bulk is p-type silicon. Another choice is n^+ -in-n device, in which the bulk is of n-type; in this device the junction is initially located to the electrodes not connected to the front-end readout chip, while after irradiation migrate to the front-end side. This was the baseline choice for the ATLAS Pixel Detector. Another example of device engineering regards the geometry of the electrodes; for example making columnar electrodes that penetrate the silicon bulk can lower the full depletion voltage and makes the charge collection faster. This is the working principle of the 3D technology, described in detail in Chapter 3.

2.2.5 Radiation damage of the electronic read-out

The electronic read-out is subject to radiation damage as well as the silicon bulk. A brief description of radiation damage for MOSFET (metal-oxide-semiconductor field effect transistor) technology [32] follows, since this was the employed technology used for the IBL. In MOSFET technology the conduction is based on the flow of majority carriers below the SiO_2 -Si interface. This region does not extend deeply into the bulk and so the net effect of radiation damages coming from displacement of silicon atoms is negligible up to 10^{15} particles/cm².

The main source of radiation damage is the ionization, generated by charged particles and photons. When ionizing radiation goes through a MOSFET, electron-holes pairs are generated. Those charges quickly disappear in the gate metal contact and in the substrate, which have poor resistivity. The silicon dioxide used beneath the gate contact behaves differently because it is an insulator. Figure 2.9 illustrates the effect of ionizing radiation in a MOSFET device for positive gate bias. A fraction of the electron-hole pairs generated by the ionizing particles will recombine each other, the rest of them will drift towards the gate because of its field. While the electrons will leave the oxide easily, hole can get trapped in the silicon defects due to the much smaller mobility, which can be from five to twelve orders of magnitude lower. The latter phenomenon lead to a change of properties of the device with irradiation. A first effect is the change of the threshold voltage of the device, which is the minimum gate-to-source voltage difference that is needed to create the conductive path between the source and the drain terminals. The oxide trapped charge gives origin to a threshold voltage shift proportional to the density of trapped holes and to the position of the charge distribution in the oxide with respect to the SiO_2 -Si interface: the closer the charge to the SiO_2 -Si interface, the bigger is the threshold voltage shifts. Hence, the threshold voltage of a NMOS¹ transistor decreases because of the positive bias applied to the gate, whilst the one of a PMOS² increases (in absolute value).

Another effect is the increase of leakage current after irradiation. Leakage current in a MOSFET is defined as the current which flows from drain to source when $V_{gs}=0$ V and $V_{ds}=V_{dd}$, and it is referred as leakage current. Only NMOS transistors undergo an increase in the off-state current after irradiation. Two effects lead to this increase: the increase of the sub-

¹MOSFET obtained in n-type silicon bulk

²MOSFET obtained in p-type silicon bulk

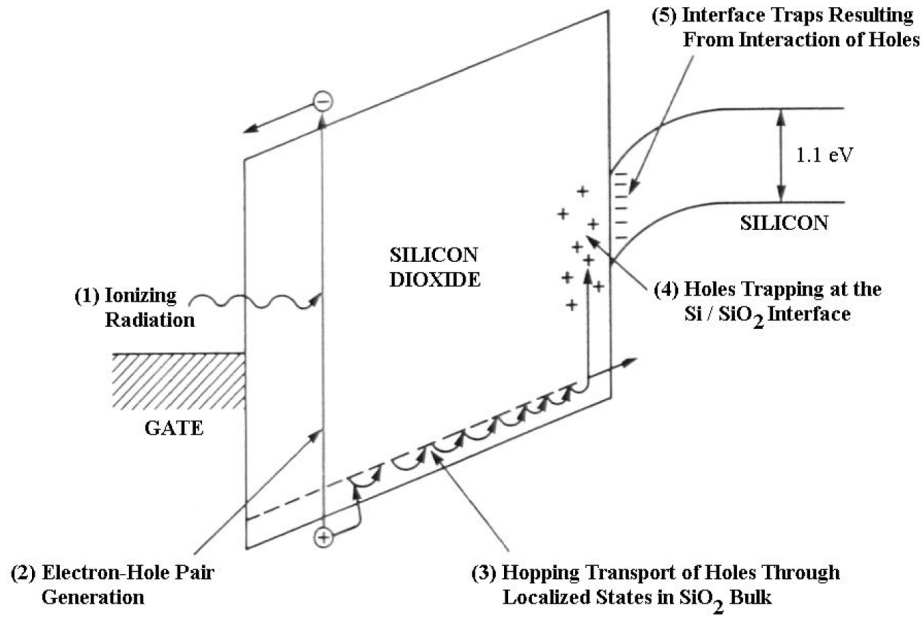


Figure 2.9: Schematic illustration of the effects induced by ionizing radiation in a positively biased MOSFET device.

threshold current and the generation of parasitic currents.

The decrease of the transistor threshold and the consequently increase of the leakage current are compensated by a counter-mechanism after few Mrad of Total Ionizing Dose (TID). At higher TID interface states start to appear in the silicon dioxide. The negative charge trapped in the interface states (in the case of NMOS transistors) only starts to compete with the oxide-trapped charge with some delay, giving origin to the rebound effect. From this point on the interface states contribute significantly to the charge balance at the transistor edge, increasing the threshold voltage of the parasitic lateral transistor and hence decreasing the leakage.

In addition to the changes of threshold voltage and leakage current, ionizing radiation affects other transistor parameters. The build-up of interface traps degrades the mobility of the carriers in the transistor channels. The trapping and releasing of the carriers increase the noise of the device. The quantitative effects of the radiation on the device depends upon its design. Radiation tolerance can be improved by several techniques as the reduction of the gate dimensions or using special layouts and architectures in the design phase. Transistors at LHC needs to stand a high level of TID; in particular for the innermost layer of the Pixel Detector the requirement is to stand 300 Mrad.

Radiation can lead not only to permanent damages of the devices, but as well to transient effects that come with a high linear energy transfer from charged heavy particles. These particles, in particular ions created in hadronic interactions, can change the state of the transistor hitting the depleted gate region. This effect is called Single Event Upset and it can lead to wrong information stored in or transmitted by the chip. A technique to correct for this effect is the replication of the memory cells combined with a majority vote logic.

2.3 Tracking with the Inner Detector

2.3.1 Tracking in magnetic field

The trajectory of a charged particle of momentum p and charge q in a static magnetic field is given by:

$$\frac{d^2 \vec{r}}{ds^2} = \frac{q}{p} \frac{d\vec{r}}{ds} \times \vec{B}(\vec{r}) \quad (2.16)$$

where $ds = vdt$ is the distance along the trajectory. The vector $\frac{d^2 \vec{r}}{ds^2}$ is perpendicular to the trajectory and its length is $1/R$, where $R(s)$ is the curvature radius of the trajectory; the vector $\frac{d\vec{r}}{ds}$ is tangent to trajectory and it has unit length. The integral

$$\int d\alpha = \int \frac{ds}{R} = \int \left| \frac{d^2 \vec{r}}{ds^2} \right| ds = \frac{q}{p} \int \left| \frac{d\vec{r}}{ds} \times \vec{B}(\vec{r}) \right| ds \quad (2.17)$$

provides the bending angle of a charged particle in a magnetic field environment. The transverse displacement δ of a particle after a path length ℓ perpendicular to the magnetic field is $\delta = \ell\alpha/2$, for $\ell \ll R$. The reconstructed cluster from the detectors are analyzed by a pattern recognition program that associates coordinates measurements to tracks. At large momentum the trajectory can be approximated with a straight line $Y = a + bZ$ in the plane containing the magnetic field and with a parabola $Y = a + bX + (c/2)X^2$ in bending plane perpendicular to the magnetic field. The parameter of the quadratic term is related to the momentum of the particle in the bending plane p_t through the radius of the circumference $c = -R^{-1}$. The most popular approach to track finding is the combinatorial Kalman filter where the full knowledge of the tracks parameters at each detector layer is used to find compatible measurements in the next detector layer, forming combinatorial tree of track candidates. A Kalman filter is usually applied to linear dynamic systems, which at every step k are described by a state vector \vec{r} [33]. The evolution of the state vector from step $k - 1$ to step k is described by the linear transformation:

$$\vec{r}_k = F_{k-1} \cdot \vec{r}_{k-1} + \vec{w}_{k-1} \quad (2.18)$$

where F_{k-1} is the propagation matrix and \vec{w}_{k-1} is a random noise contribution to the system during the propagation step. At every step a new measurement constrains the system, where the measurements \vec{m}_k needs to be described as a linear function of the state vector \vec{x}_k with associated Gaussian noise $\vec{\epsilon}_k$;

$$\vec{m}_k = H_k \vec{x}_k + \vec{\epsilon}_k \quad (2.19)$$

Given such a linear dynamic system, the Kalman filter provides:

- Filtering: the optimal recursive estimator of the present state vector \vec{x}_k given all previous measurements
- Prediction: the optimal estimation of the state vector at a future time, given all past measurements.
- Smoothing: an improved estimation of the state vector at some time in the past, given all measurements up to the present time.

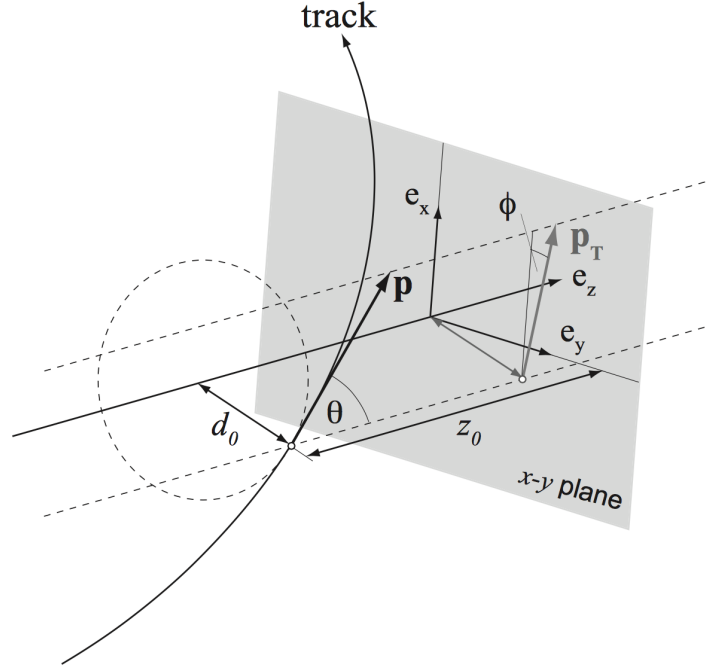


Figure 2.10: Illustration of helix parameters of a charged tracks defined in the ATLAS convention[34]

In the case of track fitting, the various steps k need to be interpreted as the various clusters to be added to a track along the track path: at each step k the track helix is propagated to a new layer of the detector, through the propagation matrix F_k and adding both the noise due to the multiple scattering and eventual energy losses due to radiation and the new measurement is added in linearized form, according to the linearization matrix H_k .

Kalman filter is used as well for the calculation of the vertex position. The determination of the vertex position is a well defined task: it consists in taking N input tracks and in determining their intersection, which results in the estimation of the vertex position and its related error. There are several methods that could be used for this task. The easiest way is to minimize the χ^2 , but in general this approach is rather slow due to the size of the covariance matrix that grows with the number of tracks. A significantly faster method is the application of the Kalman filter, firstly applied in vertex fitting in [33]. In the case of vertexing the application of a Kalman filter each step k is interpreted as the addition of a track to the vertex. The state vector is given by the vertex position and the track momentum corresponding to the track added at step k : $\vec{x}_k = (\vec{r}, \vec{p}_k)$. After all the track have been included in the fit, the Kalman filter provides the estimation of the vertex and related covariance matrix corresponding to the minimization of the vertex χ^2 .

2.3.2 Impact parameter resolution

A set of five helix parameters $(d_0, z_0, \phi, \cot(\theta), \frac{Q}{p_T})$ can describe a track in the solenoidal magnetic field B , as shown in Figure 2.10. In particular the first two parameters are referred as transverse impact parameter (d_0) and longitudinal impact parameter (z_0). The d_0 is defined as the distance of closest approach to the beam-line, while z_0 as the value of z of the point on the track that determines d_0 . Because the errors on the five track parameters are not

independent, they are described by a 5×5 covariance matrix C . Because in a very good approximation the variables in the (x, y) plane and the (r, z) plane are independent, only 2×4 covariances are not zero: $cov(Q/p, \phi)$, $cov(Q/p, d_0)$, $cov(\phi, d_0)$ and $cov(cot(\theta), z_0)$. Covariance matrices are always symmetric, invertible and positive definite. The errors of the impact parameters are derived from the covariance matrix and they depends on the geometrical characteristics of the detector and on the multiple scattering. A simple example to evaluate the basic tracking performance is based on equally spaced detector. For the plane containing the magnetic field, a detector made by $N + 1$ layers, each one having a measurement error σ , has an error on the z_0 measurement given by:

$$\sigma_{z_0}^2 = \sigma_a^2 + \sigma_b^2 Z_c^2 = \frac{\sigma^2}{N+1} + \frac{\sigma^2}{N+1} \frac{12N}{N+2} \frac{Z_c^2}{L^2} \quad (2.20)$$

where the formula is calculated choosing a reference frame with the origin at the center of the track, and $L = Z_N - Z_0$, $Z_c = (Z_N + Z_0)/2$ and the error on track parameters (σ_a and σ_b) are not correlated. The above formula shows how the error of z_0 depends on the error of the slope of the track (σ_b) and on the distance of the center of the spectrometer from the interaction point (Z_c). The impact parameter resolution is also affected by multiple scattering so that a more precise calculation is given by:

$$\sigma_{z_0} = \sqrt{\frac{\sigma^2}{N+1} + \frac{\sigma^2}{N+1} \frac{12N}{N+2} \frac{Z_c^2}{L^2}} \oplus \frac{k}{p_T} \quad (2.21)$$

where k is derived the contribution of the multiple scattering. The calculation of the transverse impact parameter is similar but it contains additional terms that depends on the magnetic field; to minimize the error on the impact parameter the following characteristics are required:

- excellent spatial resolution σ is needed;
- make the spectrometer as long as possible to reduce the error on the slope;
- place the innermost layer as close as possible to the interaction point.
- minimize the material since the impact of multiple scattering is important at low energy

2.3.3 Momentum resolution

Momentum resolution could be calculated studying the case of the plane transverse to the magnetic field, considering a spectrometer placed at the position X_0, \dots, X_N . The spectrometer length is $L = X_N - X_0$. The error on the coefficient of the quadratic term of the parabola fit is:

$$\sigma_c^2 = \frac{\sigma^2}{L^4} A_N, \quad A_N = \frac{720N^3}{(N-1)(N+1)(N+2)(N+3)} \quad (2.22)$$

Since $c = -R^{-1}$ the error on the transverse momentum p_t is given by:

$$\frac{\delta p_t}{p_t} = \frac{p_t}{q} \frac{\sigma}{BL^2} \sqrt{A_N} = p \frac{\sigma}{0.3BL^2} \sqrt{A_N} \quad (2.23)$$

in units of GeV, Tesla and metres. The formula illustrates the basic features of the momentum measurement with a magnetic spectrometer:

- the relative transverse momentum resolution is proportional to the transverse momentum;
- the dependence on the square of the spectrometer length L calls for large detectors to achieve good momentum resolution;
- the transverse momentum resolution is inversely proportional to the magnetic field;
- the dependence on the number of measured coordinates is weak; however the number of coordinates is important for the robustness of the pattern recognition.

Chapter 3

The ATLAS Pixel upgrade for the LHC Run 2

The ATLAS Pixel Detector[35] was upgraded during the first long shutdown of the LHC in 2013-2014. The major upgrade was the installation of a new innermost pixel layer, the Insertable B-layer (IBL) [36], with a new Be beam pipe. A refurbishment and consolidation of the 3 layer Pixel operating in Run 1 was performed, with the implementation of a new service quarter panel (nSQP). A description of the Pixel Detector and its upgrade before the Run 2 of the LHC is given in this chapter.

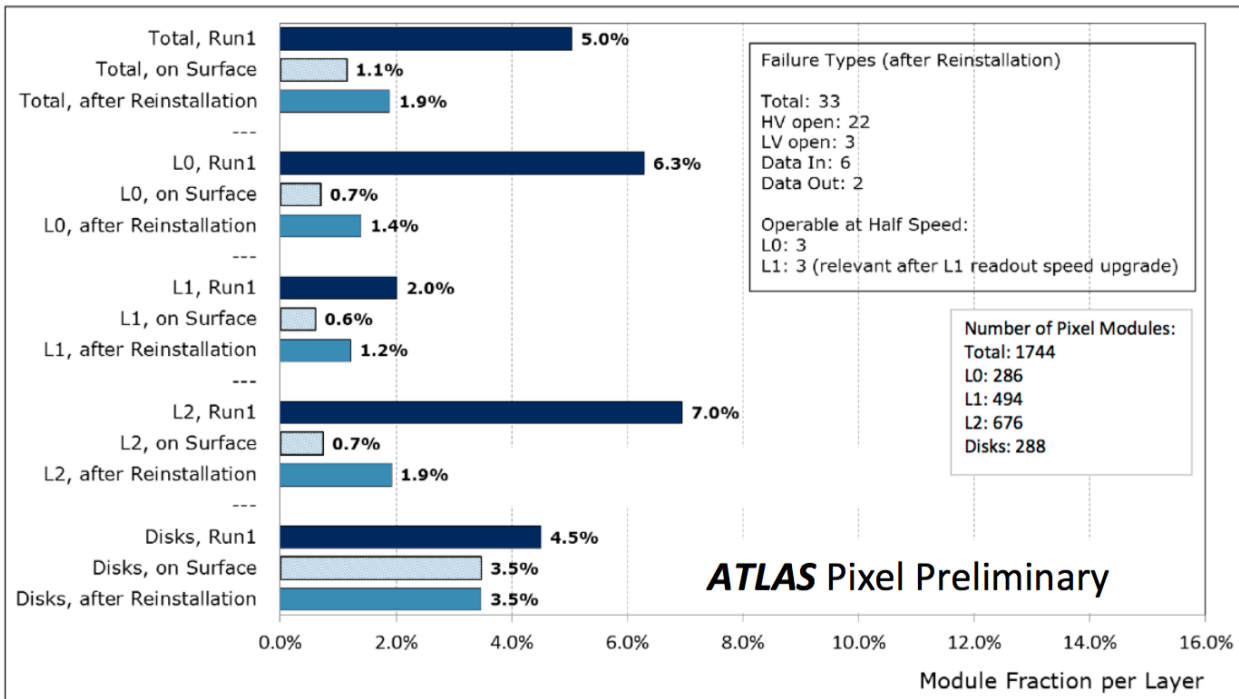


Figure 3.1: Operational status of pixel module at the end of Run 1 and after the intervention before the start of Run 2

3.1 Refurbishment and consolidation of the Pixel Detector

During the Run 1 some of the lasers in the off-detector system of the Pixel Detector started to fail, those were the transmitters plugin of the data-acquisition board, located 80 m away from the ATLAS volume. The same type of laser were also present in the on-detector system (Optoboards) and they cannot be accessed without removing the Pixel Detector from ATLAS. To prevent any risk in the future it was then decided to build new service quarter panels (nSQP) locating the Optoboards into the accessible area. The readout speed of the second layer was also upgraded to 160Mbit/s, as for the innermost layer.

At the end of Run 1 95% of the pixel module was correctly operating. An investigation was performed for the modules which were failing in the operation, and wherever it was possible, faulty modules were fixed. In May 2014 the Pixel detector has been re-installed in the ATLAS experiment, all the services were connected and after having retested the detector 98% of the modules was fully functional. Figure 3.1 shows the details about the module recovery.

3.2 Motivation for the ATLAS IBL detector

The first long shutdown of the LHC was the opportunity for the ATLAS collaboration to improve the ATLAS Inner Detector performance with the addition of a fourth innermost layer of silicon pixel detectors, the IBL.

The ATLAS Pixel Detector will be operational until the third long-shutdown of the LHC machine, foreseen at the end of the year 2023. In this long period some module are expected to fail, without the opportunity of performing any intervention or substitution of those.

In particular a loss of data in the Pixel B-layer would seriously deteriorate the impact parameter resolution, directly affecting the b-tagging capabilities. The addition of a fourth layer, close to the beam-pipe, not only ensures that the b-tagging capabilities will not deteriorate in time but improves the b-tagging performance being located closer to the interaction point with respect to the Pixel B-layer.

During the Run 2 collisions happen each 25 ns, instead of the 50 ns interval used during Run 1, the peak luminosity was increased. These upgrade led to the increase of the pile-up. The higher pile-up environment requires redundancy in the measurement of tracks in order to control the fake rate arising from random combinations of clusters.

Since the existing envelope allowed only 8.5 mm of radial free space, too small for the insertion of a new layer, the existing beam pipe has also been replaced by a new pipe of a reduced diameter allowing the insertion of an additional layer. The new Be beam pipe allows the reduction of material budget close to the interaction point.

The improvement of the Pixel Detector performance with the addition of the IBL was carefully evaluated with studies on tracking and b-tagging that will be presented in the following two sections.

3.2.1 Track reconstruction performance

The impact parameter performance has been evaluated by parametrizing the observed p_T dependence by the $A + \frac{B}{p_T}$ model, for which the A term describes the intrinsic resolution of the detec-

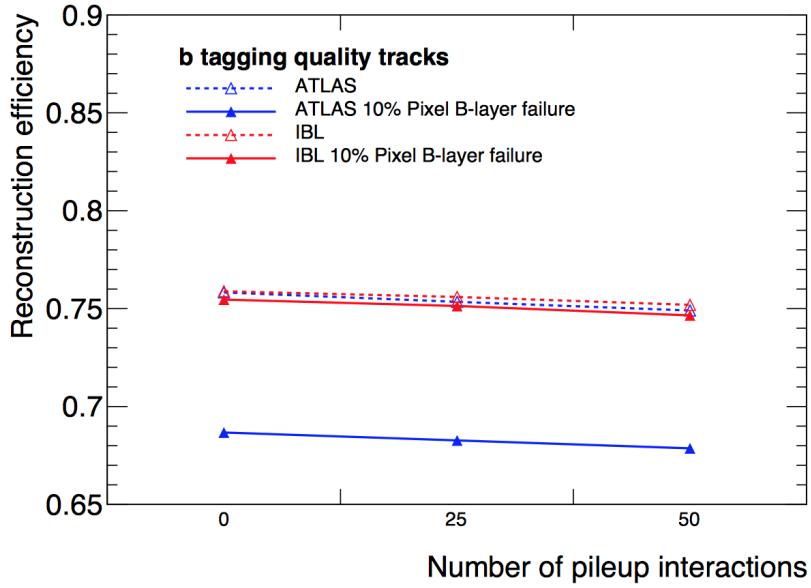


Figure 3.2: Efficiency for reconstructing primary tracks ($p_T > 1$ GeV) with and without IBL in $t\bar{t}$ events as a function of the average number pileup events (μ). This study was performed for the IBL Technical Design Report [36]

tor visible at high p_T , while the B term describes the effect of multiple scattering in the detector material dominant at low p_T . The IBL improves A by a factor of 1.2 in d_0 and a factor of 1.7 in $z_0 \times \sin\theta$, driven by the change in the z pitch between IBL and current Pixel detectors. The multiple scattering term B improves by a factor of 1.8 in d_0 and by a factor of 1.8 in $z_0 \times \sin\theta$. As a consequence of the improved resolution on the impact parameters, the IBL improves the primary vertex resolution and reconstruction, secondary vertex finding, b -tagging performance, hence extending the reach of the physics analysis. To assess the direct contribution of IBL, selected Monte Carlo samples have been generated to compare the performance of the track detector at the end of Run 1 with that obtained at the start of Run 2, using the same boundary conditions (e.g. disabled pixel modules, pile-up and collision energy). Figure 3.2 shows the tracking reconstruction efficiency with and without the IBL. At the end of Run 2 a 10% inefficiency of the B-layer is expected due to degradation with radiation and occupancy.

3.2.2 b -tagging performance

Thanks to the significantly improved impact parameter resolution, the IBL has a major impact on the b -tagging performance. In this section a comparison is presented between the b -tagging performance expected after the addition of IBL and what was achieved at the end of Run 1. The performance was evaluated with the use of the new digitization model and reconstruction algorithms, which were both improved for the Run 2 [29]. The latter include a refined neural network clustering algorithm, a new tracking setup which improves the treatment of shared clusters in the core of a dense jet environment [29] and a new b -tagging algorithm.

All results presented here are based on fully simulated top-pair production events. The

average level of pile-up in this study is ≈ 20 , reflecting the Run 1 luminosity profile. The dependence on pile-up is studied separately. Jets are reconstructed with the AntiKt algorithm [37] with radius $R = 0.4$. The discrimination of the b -jets is performed in ATLAS thanks to a boosted decision tree which combines the outcome of three basic algorithms:

- Impact parameter track reconstruction
- Inclusive secondary vertex reconstruction
- Decay chain multi-vertex reconstruction

The impact parameter based algorithm relies on the impact parameter significance and lifetime sign of the single tracks matched to the jet, which are then combined in a single likelihood discriminator. The secondary vertex based algorithm exploits explicitly the presence of a secondary vertex within the jet and of its properties, including mass, energy fraction and charged decay multiplicity. Finally, the multi-vertex fitting algorithm tries to reconstruct the primary vertex (PV) $\rightarrow b \rightarrow c$ -hadron decay chain expected in most of the b -jets, exploiting its topology and properties. A detailed description of the basic algorithms can be found in Chapter 7.

The input variables obtained from the three basic algorithms are then combined making use of a boosted decision tree algorithm to discriminate b -jets from either light (u, d, s -quark or gluon jets) or c -jets. Results in this section are presented for the MV2c20 algorithm, for which the training is performed on a set of at least 5 million top pair events, using the b -jets as signal and a mixture of 80% light-jets and 20% c -jets as background. In order to perform a fair comparison, the algorithms have been re-trained separately for the ATLAS Run 1 geometry, without IBL, and the ATLAS Run 2 geometry, which includes the IBL.

The inclusive b -tagging performance for top pair events, after a very basic jet selection ($p_T > 20$ GeV and $|\eta| < 2.5^\circ$), is shown in Figure 3.3. The additional of IBL improves the b -tagging performance in terms of light-jet rejection between a factor of 3 or 4 for b -jet tagging efficiencies up to 85%. The improvement in c -jet rejection is smaller and ranges approximately from 80% to 20% for b -jet tagging efficiencies from 50 to 75%. Physics analyses will most often profit from the improved performance by re-tuning their b -tagging requirements in such a way to keep the background rejection the same but have an increased signal efficiency. This is shown in Table 3.1. As an example, adding the IBL allows to keep the light-jet rejection rate at 100 while improving the b -jet tagging efficiency from 72% to 79%, with a relative improvement of 10% on the b -tagging efficiency for each tagged jet in the event.

The b -tagging performance depends strongly on jet transverse momentum (p_T), following the variation in underlying impact parameter resolution and tracking efficiency. The dependence of the performance on jet p_T is shown in Figure 3.4. The largest improvements are seen at low p_T , where the closeness of the IBL to the interaction region allows to reduce significantly the impact of multiple scattering. As an example, the improvement in light-jet rejection ranges from a factor of 3-4 up to $p_T = 100$ GeV, a factor of 2 at $p_T = 150$ GeV, leveling to only a very slight improvement for jet p_T above 250 GeV. At very high jet p_T the tracking efficiency and resolutions are limited by shared clusters from collimated tracks produced in the core of high p_T jets, a problem which becomes more severe with the insertion of IBL, which moves the radial distance of the closest pixel layer to the interaction region from ≈ 5 to ≈ 3.3 cm. The optimization of the tracking and pixel clustering algorithms to

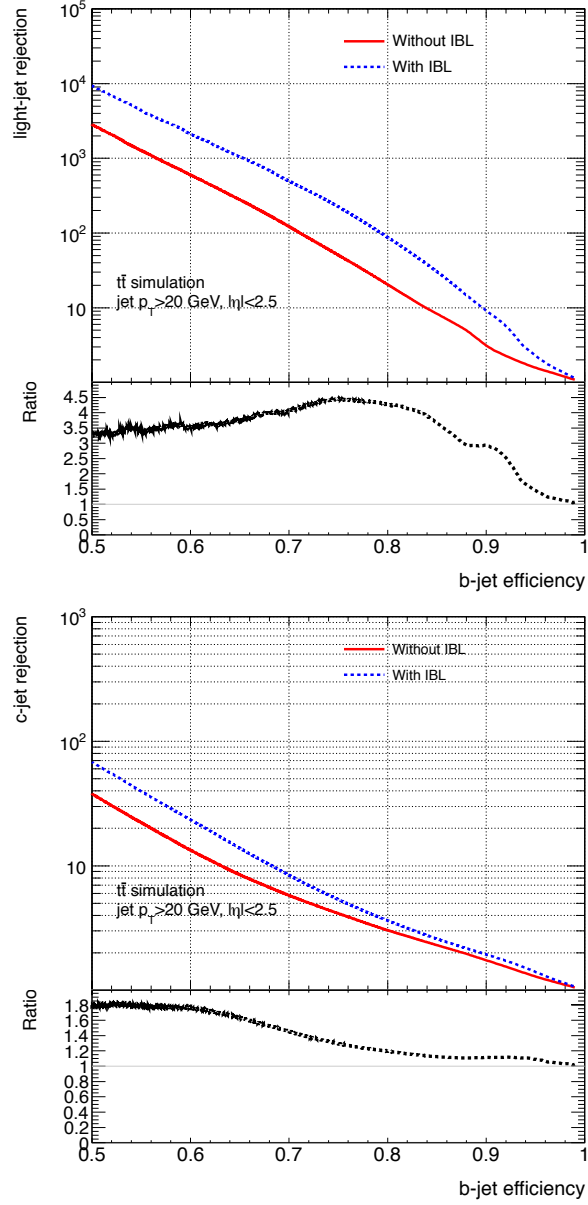


Figure 3.3: Performance of the b -tagging algorithm MV2c20 expressed in terms of light (on the left) or c -jet (on the right) rejection as a function of b -tagging efficiency, obtained by scanning the boosted decision three discriminant. The algorithm is applied to jets from top pair events. The performance of the Run 1 and Run 2 detector layouts are compared, where the latter includes IBL. The rejection is defined as the inverse of the tagging efficiency.

Light-jet rejection	b -jet efficiency w/o IBL	b -jet efficiency with IBL
1000	57%	65%
100	71%	79%
10	84%	90%
Constant c -jet rejection	b -jet efficiency w/o IBL	b -jet efficiency with IBL
20	56%	62%
10	63%	68%
5	72%	76%

Table 3.1: b -jet tagging performance expressed in terms of b -jet efficiency for a fixed light- or c -jet rejection, comparing the Run 1 and Run 2 detector layouts, where the latter includes IBL. The prediction are derived from jets from top pair production, which pass the $p_T > 20$ GeV and $|\eta| < 2.5$ selection requirements.

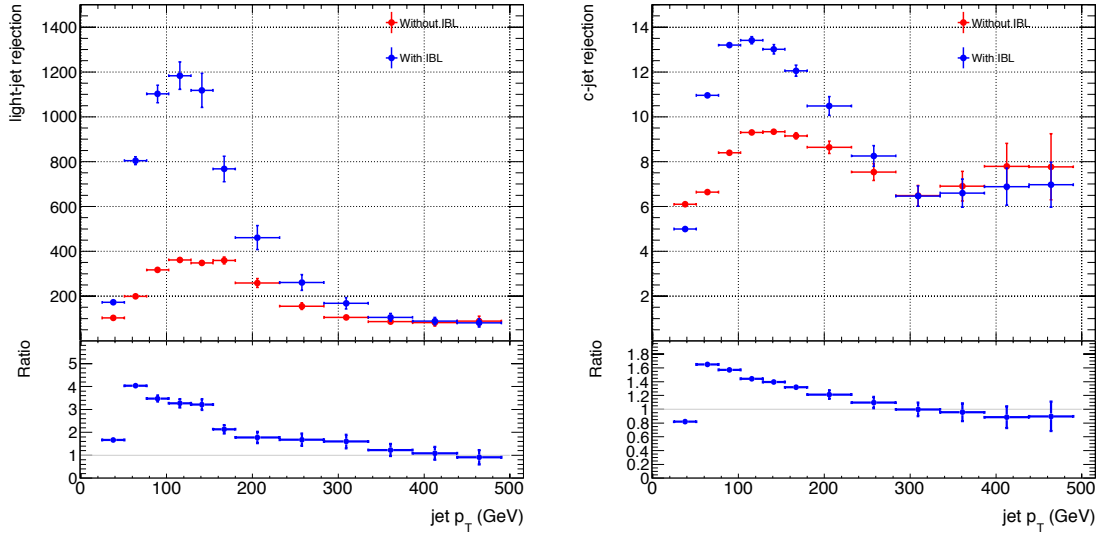


Figure 3.4: Performance of the b -tagging algorithm MV2c20 expressed in terms of light (on the left) or c -jet (on the right) rejection as a function of jet transverse momentum (p_T), while keeping the b -tagging efficiency fixed at 70% in each p_T bin. The performance of the Run 1 and Run 2 detector layouts are compared, where the latter includes IBL. The rejection is defined as the inverse of the tagging efficiency.

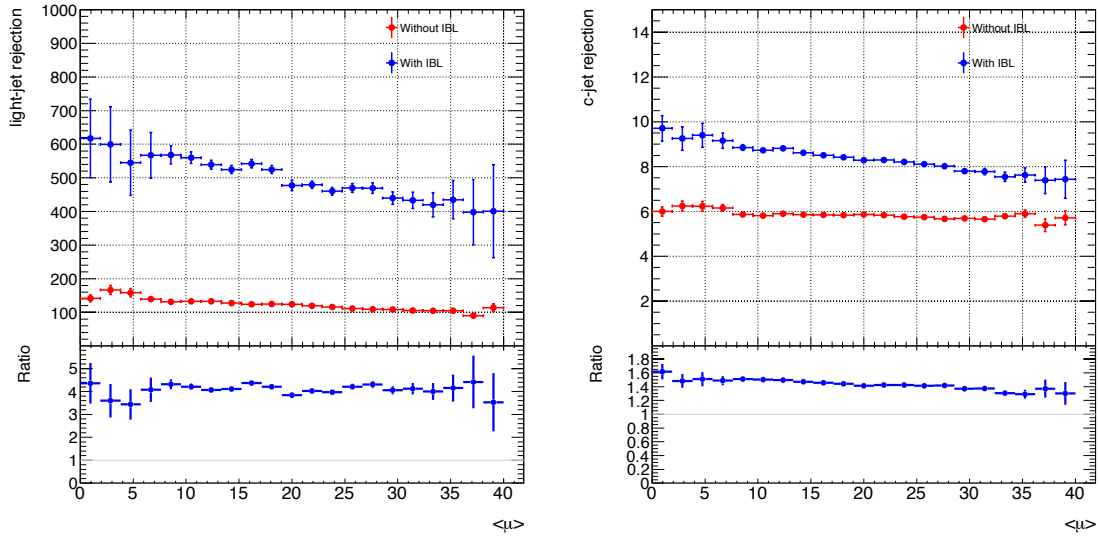


Figure 3.5: Performance of the b -tagging algorithm MV2c20 expressed in terms of light (on the left) or c -jet (on the right) rejection as a function of the average pile-up level μ , while keeping the b -tagging efficiency fixed at 70% in each μ bin. The performance of the Run 1 and Run 2 detector layouts are compared, where the latter includes IBL. The rejection is defined as the inverse of the tagging efficiency.

deal with such an environment [29] has allowed to counteract such degradation effectively and keep the performance of the new Run 2 geometry at least at the same level of Run 1 even for very high p_T jets.

The dependence on the average level of pile-up μ is presented in Figure 3.5. While the overall performance is much improved with the addition of IBL, the dependence on pile-up in terms of relative degradation versus μ is almost unchanged. This study is performed on top pair events, where the distinction of the primary vertex from pile-up vertices is not a major concern.

3.3 IBL Layout Overview

The IBL is located at a nominal distance of 33.5 mm from the beam axis, where this distance refers to the sensors position and it is the closest layer to the interaction point of the ATLAS detector as shown in Figure 3.6. Given the small sensor distance from the beam axis (compared to 50.5 mm for the Pixel B-Layer), the sensors and front-end electronics must cope with a much higher hit rate and radiation with respect to the other layers. To address these requirements, a new front-end read-out chip has been developed, the FE-I4 [38] and two silicon sensor technologies were developed.

The most important layout parameters of the IBL detector are listed in Table 3.2 and a picture of the layout is shown in Figure 3.7. The detector consists of 14 mechanical support (staves) equipped with pixel silicon modules surrounding the beam pipe, providing full azimuthal coverage. Each stave hosts the electrical and cooling services to 20 pixel modules that are attached to the stave and provide a $|\eta|$ coverage up to 3. Two module types are installed on each stave based on two different silicon sensor technologies: Planar and 3D.

	Value
Number of staves	14
Number of physical modules per stave	20 (12 planar, 8 3D)
Number of FEs per stave	32
Coverage in η , no vertex spread	$ \eta < 3.0$
Coverage in η , 2σ (122 mm) vertex spread	$ \eta < 2.58$
Active $ z $ stave length	330.15 mm
Geometrical acceptance in z min, max	97.4%, 98.8%
Stave tilt in ϕ	14°
Overlap in ϕ	1.82°
Center of the sensor radius	33.5 mm
Radiation length at $z = 0$	$1.9\% X_0$

Table 3.2: Main layout parameters for the IBL detector. The quoted radiation length is averaged over the stave width and includes the IBL support and positioning tubes.

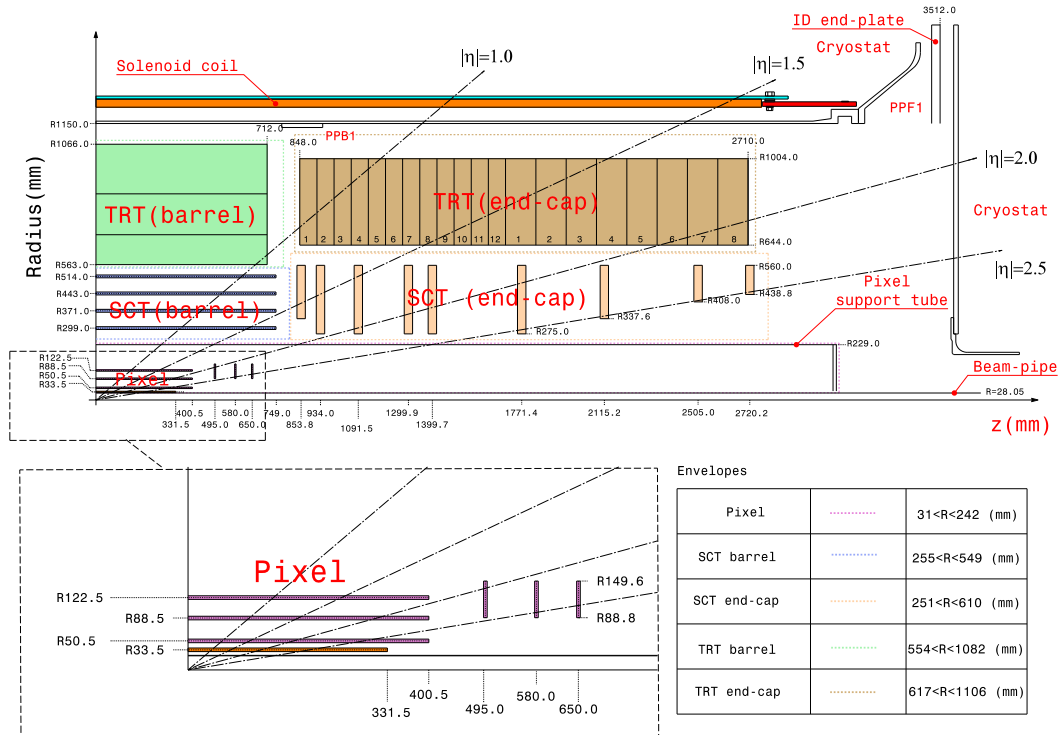


Figure 3.6: The layout of the ATLAS tracking system with the additional layer of IBL.

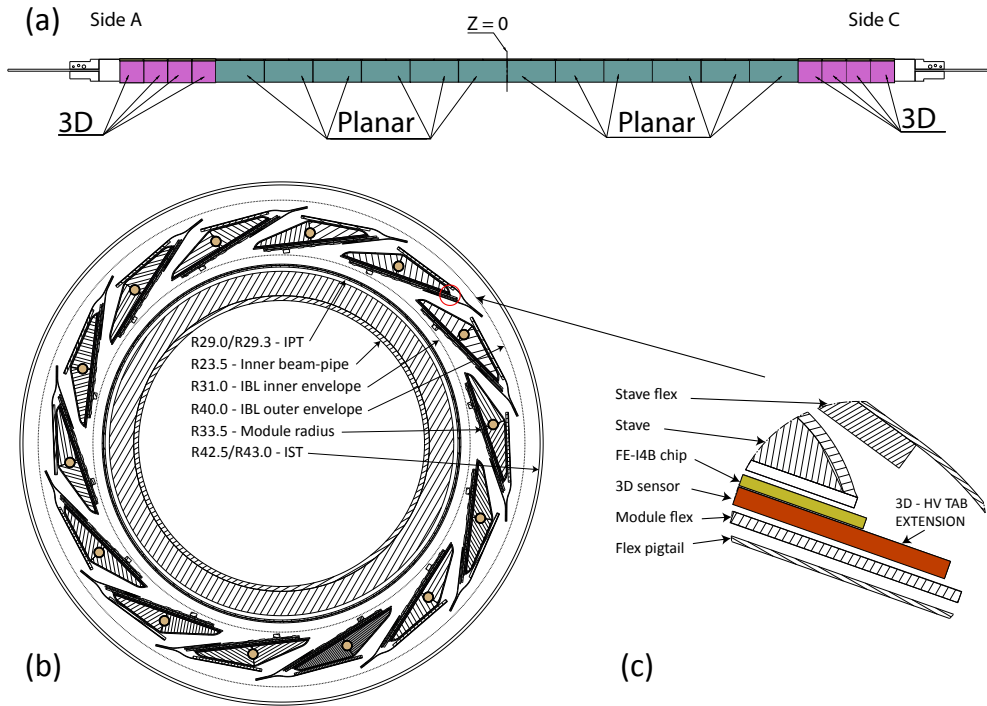


Figure 3.7: IBL layout: (a) Stave layout showing the position of Planar and 3D modules. (b) An $r-\phi$ section showing the beam pipe, the Inner Position Tube (IPT), the staves of the IBL detector and the Inner Support Tube (IST). (c) An exploded $r-\phi$ view of the corner of a 3D module fixed to the stave.

	Pixel	IBL
Active Surface [m ²]	1.73	0.15
Number of channels [$\times 10^6$]	80.36	12.04
Pixel size [μm^2]	50 \times 400	50 \times 250
Pixel array [pixels]	18 \times 160	80 \times 336
Chip size [mm ²]	7.6 \times 10.8	20.2 \times 19.0
Active Fraction [%]	74	89
Analog current [$\mu\text{A}/\text{pixel}$]	26	10
Digital current [$\mu\text{A}/\text{pixel}$]	17	10
Analog voltage [V]	1.6	1.4
Digital voltage [V]	2.0	1.2
Data out transmission [MBit/s]	40	160
Sensor type	Planar	Planar / 3D
Sensor thickness [μm]	250	200 / 230
Layer thickness [% X_0]	2.8	1.9
Cooling fluid	C ₃ F ₈	CO ₂

Table 3.3: Comparison of the main parameters of the Pixel detector and the IBL detector.

Planar sensors populate the central stave region, while 3D sensors the side region, as shown in Figure 3.7(a). The forward region of the staves are populated by 3D sensors where due to the electrode orientation they can guarantee a better z -resolution in the track reconstruction after heavy irradiation. The details about the sensors are given in Section 3.4.2. The staves are inclined by 14° with respect to the radial direction in order to achieve an overlap of the active area between staves. This tilt also compensates for the Lorentz angle of drifting charges in the case of Planar sensors, and the effect of partial column inefficiency for normal incidence tracks in the case of 3D sensors. Due to space constraints, the sensors are not overlapped along the stave (in z). However to minimize the dead region, modules are glued on the stave with a physical gap of $200\mu\text{m}$.

A comparison between the IBL and the 3 layer Pixel Detector technical parameters is reported in Table 3.3.

The IBL volume, which contains the staves and the services, is the space between an external Inner Support Tube (IST) fixed on the Pixel structure and a precision mechanical support called the Inner Positioning Tube (IPT). The central part of the ATLAS beam pipe is slid into the IPT tube and attached to it. A key feature of this design approach is that independent volumes are generated and the fast removal of either the beam pipe with respect to the IBL package, or of the IBL and beam pipe with respect to the Pixel package, are allowed. As the Pixel Detector was extracted in 2013 for repair and service refurbishment, the IST was inserted. The IBL package, including the beam pipe, was then slid inside the IST once the Pixel detector was re-installed and fully re-connected.

The reduction of the material budget leads to an optimization of the tracking performance. The average IBL radiation length is $1.88 X_0$ for normal incidence tracks at $z = 0$ and it corresponds to $\sim 70\%$ of that for the Pixel B-Layer¹. A lower radiation length with respect

¹The estimated IBL radiation length has been confirmed in collision data. The difference with respect to the estimate reported in the IBL TDR [36] is mainly due to an initial underestimated of the module material and to the addition of the IPT.

Item	Value [% X_0]
Beam pipe	0.32
IPT	0.12
Module	0.76
Stave	0.60
Services	0.19
IST	0.21
IBL total	1.88

Table 3.4: Averaged IBL material budget over the azimuthal angle ϕ for normal incident tracks at $z = 0$. The beam pipe material is excluded from the IBL total.

to the Pixel has been achieved by: a new low-mass module design; local support structures (staves) made of low density carbon foam; the use of CO₂ evaporative cooling that optimizes the mass flow and the pipe size; the use of aluminium conductors for the electrical power services. Table 3.4 reports the main contributions to the IBL material budget. Figure 3.8 shows the material traversed by a track of origin $z = 0$ as a function of η , smeared over the azimuthal angle.

3.4 Module Layout

The basic building block of the IBL is the module. Due to the two sensor concepts used, the IBL modules differ in size. For Planar sensors the module consists of two FE-I4 chips connected to one sensor. For 3D sensors the module consist of one FE-I4 chip connected to one sensor. A module consists of the following parts:

- the Planar or 3D sensor.
- one or two FE-I4 chips each containing 26880 pixel cells with amplifying circuitry.
- a double-sided, flexible printed circuit (referred to as module flex).

The FE-I4 chip is described in section 3.4.1, the two sensors concepts are treated in section 3.4.2 and the module flex is presented in section 3.4.3.

3.4.1 The FE-I4 redout chip

The FE-I4 is designed in a IBM CMOS 130 nm feature size technology using thin gate oxide transistors to increase the radiation hardness. The large chip (20.2 mm \times 18.8 mm) has an active area holding 26880 pixels, allocated in 80 columns (50 μ m pitch) and 336 rows (250 μ m pitch), and an approximately 2 mm wide periphery, as shown in Figure 3.9.

One of the main advantage of the FE-I4 chip with respect to the FE-I3 is the lower power consumption, as reported in Table 3.3. The design of the analog and of the digital circuitry was optimized with a power consumption per pixel of 26 μ W, while it is 75 μ W for the FE-I3. The analog part is made by a two stage charge sensitive amplifier and a discriminator, as shown in Figure 3.10(a). The basic working principle of the two is described in Chapter 2. The first amplifier stage (Preamp) is a cascode amplifier while the second stage (Amp2) is

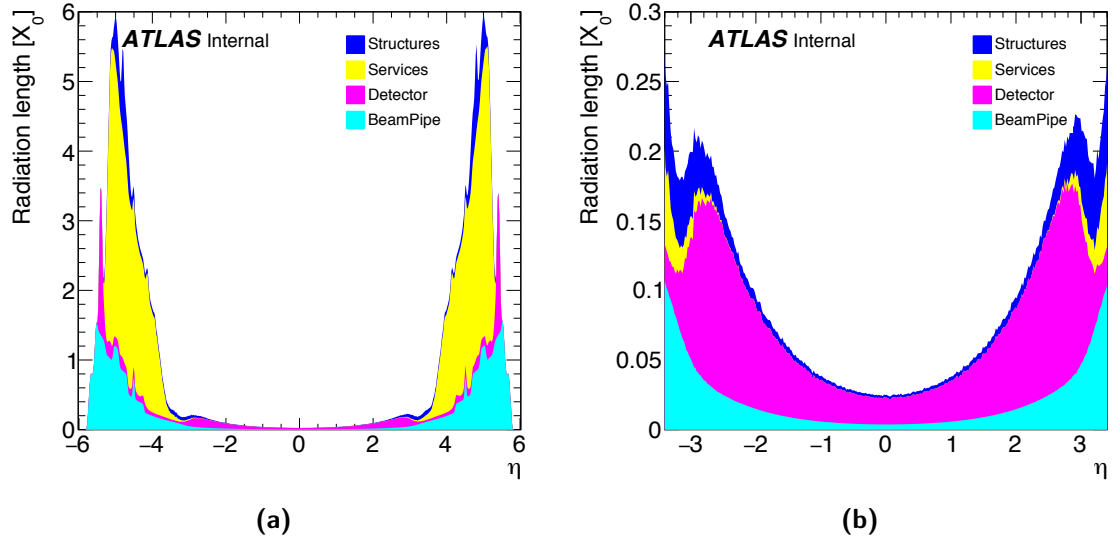


Figure 3.8: (a) Radiation length as a function of η for different components of the IBL detector as implemented in the ATLAS geometry model. Different components are shown: the beam pipe, the detector (IBL staves, modules and IPT), the services (cooling and cables) and the structures (IST, stave rings, endblocks, sealing ring area). (b) A zoomed view of the central $|\eta|$ distribution.

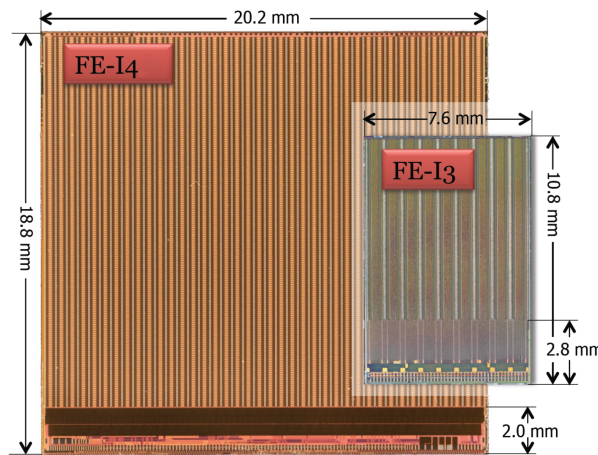
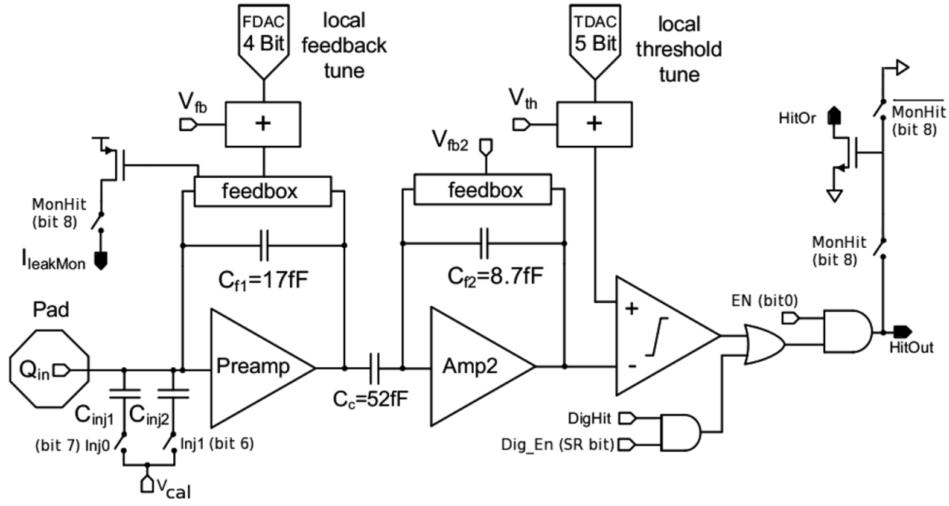
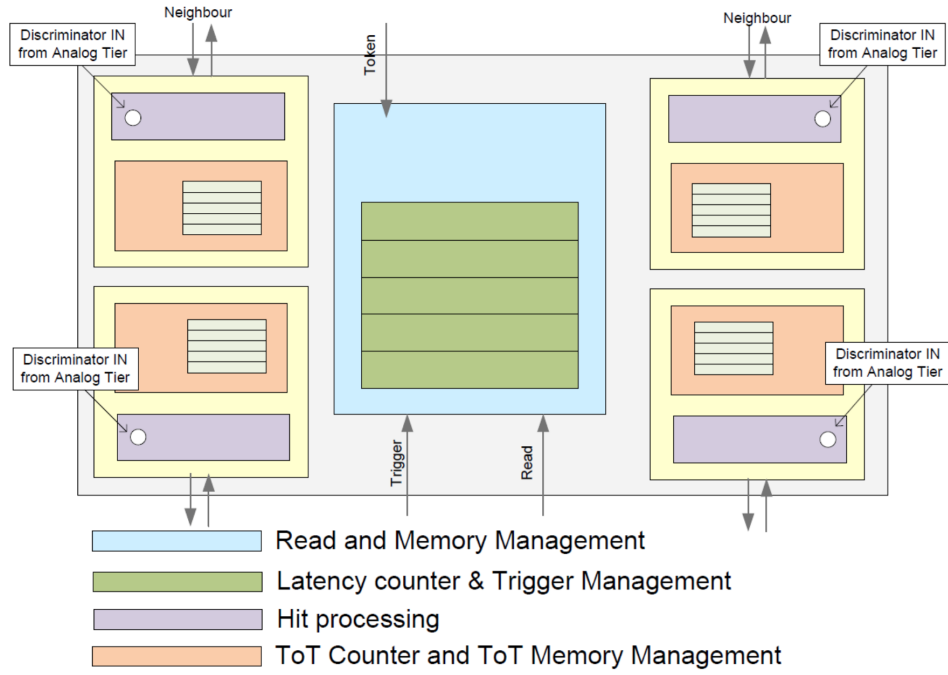


Figure 3.9: Picture of a FE-I4 chip and a to-scale picture of an FE-I3 chip. The pixel matrix and the approximately 2 mm wide periphery can be seen.



(a) Schematic view of the analog pixel cell



(b) Block diagram of the digital 4-pixel region.

Figure 3.10: Analog and digital schemes of the FE-I4 chip.

a folded cascode AC coupled to the Preamp. The two-stage choice allows to provide enough gain before the discriminator while permitting the optimization in the choice of the preamp feedback capacitor (C_{f1}). The feedback current of both amplifiers can be adjusted. These adjustments are implemented globally (V_{fb} and V_{fb2}), so that all pixels of the matrix are affected simultaneously. For the preamplifier feedback an additional current adjustment using the 4-bit FDAC allows the fine tuning of the Time Over Threshold (ToT) response for each pixel individually. The output of the Amp2 is compared to a threshold voltage (V_{th}) by the discriminator. The threshold voltage can again be adjusted globally as well as individually for each pixel.

The discriminator is built with a two-input voltage comparator and a threshold voltage generator. Signal shaping is only done by the preamp with an adjustable return to the baseline, while the second stage provides only the voltage gain, given by the ratio $\frac{C_c}{C_{f2}}$. The return to the baseline and the discriminator threshold are individually adjustable in each pixel, with dedicated local and global pixel registers. Two selectable capacitors are provided for analog calibration injection.

Additionally, each pixel contains test hit injection circuitries. Analog test signals are injected using a voltage step defined by the calibration voltage (V_{cal}) and two test charge injection capacitances ($C_{inj1/2}$), which can be selected independently. Digital test hits are injected to an OR element at the output of the discriminator. The output of the analog readout chain of each pixel can be disabled using an AND connected to the discriminator output and the enable bit (EN) on each pixel. The feedback current of the preamplifier can be adjusted in function of the leakage current coming from the sensor, in order to compensate the latter after the irradiation.

Four pixels share a common digital logic cell for further hit processing as shown in Figure 3.10(b). Detailed studies show that the transfer of the hit information to the chip periphery is the main inefficiency source at the expected IBL hit occupancy [39]. The FE-I4 hit processing architecture therefore stores the hits in the pixel array close to the analog readout chain and the hits are processed only if a trigger signal is received. Detailed information on this architecture can be found in [38]. Four pixels share a set of five latency counters, while each pixel holds his own set of five ToT counters. A hit in one of the analog pixel cells allocates and starts the first unallocated latency counter to count down from the programmed latency (in units of 25 ns). The charge information belonging to this specific time stamp is stored in the buffers for all pixels connected to the 4-pixel digital region. An incoming Level-1 trigger in coincidence with the latency value of zero initiates the transfer of the hit data to the end-of-chip logic, and deallocates the latency counters and buffers. If no corresponding Level-1 trigger arrives, the hit information is deleted and the counter and buffers are deallocated as well.

Each of the readout chips holds two on-chip LDO (Low Drop Out) regulators ([40, 41]) to generate the analog and digital supply voltages. These are linear regulators, which keep a constant output voltage independently of the input voltage and the load current. A minimum difference between the input voltage and the output voltage (dropout voltage) is used to achieve a high power efficiency. The on-chip LDOs are operated in partial shunt mode. This means that they are operated as usual LDO as long as the current consumption is above an adjustable minimum input current. If below, an additional current is shunted to ground by the regulators. This operation mode does not increase the power consumption of the FE-I4 chip as long as its current consumption in working conditions is above the shunt

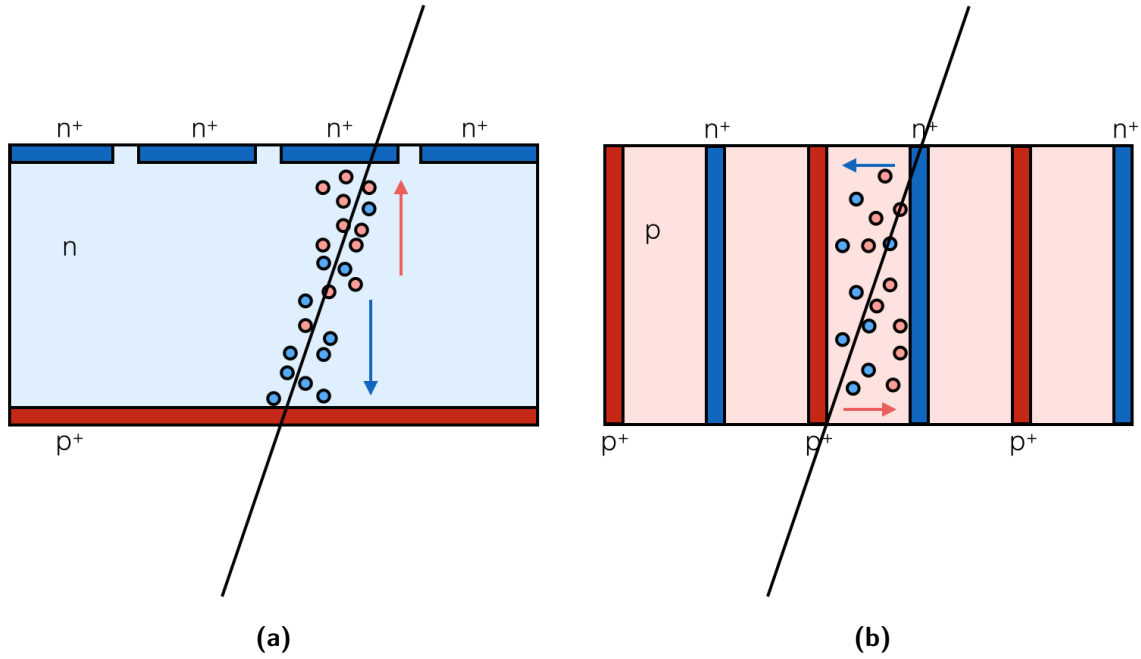


Figure 3.11: Charge collection mechanism in Planar (a) and 3D (b) sensors

current. The advantage of this mode is the reduction of the transients in comparison to the pure LDO mode in case of load current fluctuations. This will happen in case during the setting of the FE-I4 register (configuration) or accidental configuration loss. The reference voltages needed for the operation of the two LDOs are generated on-chip.

3.4.2 Sensors

Two sensor technologies are used in the IBL detector: the first is an improved version of the one used in the other layer of Pixel Detector, the Planar [42] architecture; the second is the novel 3D[43] technology. Both sensor types showed satisfactory performance in terms of noise, hit reconstruction efficiency and uniformity before and after irradiations to the fluence level of $5 \times 10^{15} \text{ n}_{\text{eq}}/\text{cm}^2$ NIEL, as required for the IBL operation [44].

Planar sensors In the Planar technology the electrode are obtained on the surfaces of the Planar sensors bulk, the equipotential lines are then parallel to the surface of the device. When the sensor is biased and a charge particle crosses it, the holes and the electrons created by ionization drift towards the electrodes, moving across the bulk width as shown in Figure 3.11a.

The design of the Planar sensor derives from the design of the sensor of the ATLAS Pixel Detector, which employs an n^+ -in- n technology, where the n -side segmentation matches in size the front-end read-out electronics connected via bump-bonds. A guard-ring structure is placed on the p -side. To be compatible to the newly developed FE-I4 chip, the pixel dimensions have been shrunk to $250 \times 50 \mu\text{m}^2$.

A key feature of the IBL Planar sensors is the slim-edge design which features enlarge edge

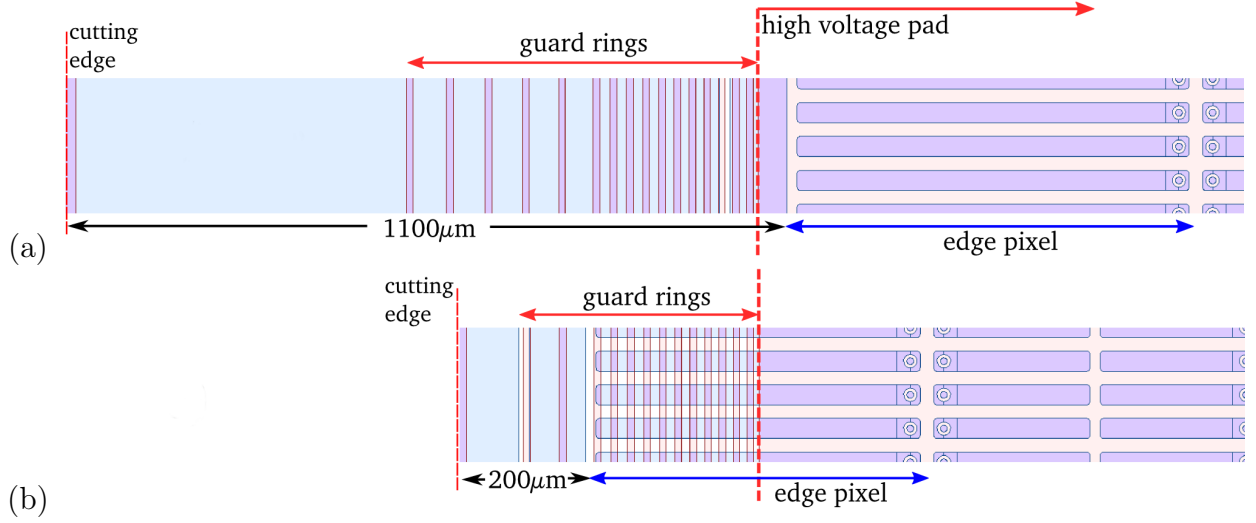


Figure 3.12: Comparison of the edge designs of the ATLAS Pixel sensor (a) and Planar IBL pixel sensor (b). The inactive edge has been reduced from 1100 μm to 200 μm in the IBL sensor. In the guard-ring area the blue horizontal areas represent the n-implantation on the front-side of the sensor, while the red vertical areas the p-implantation on the back-side. The figure is a modified version of the Figure at [45].

pixels opposite to the guard-rings, see Figure 3.12, as it is possible for n^+ -in- n sensors thanks to the double sided processing. This design decision was based on an extensive study which analyzed the efficiency of the sensor in the guard ring area [46]. No changes in the breakdown behavior have been observed as the voltage drops take place on the p-side. The number of guard-rings was optimized based on a complementary study, which evaluated the breakdown behavior after partial guard-ring removal [47]. Compared to the original ATLAS Pixel sensor the number of guard-rings has been reduced from 16 to 13. Also the cutting edge has been shifted nearer to the guard-rings. In Figure 3.12 the improvement of the slim-edge design for the IBL sensor in comparison to the design of the ATLAS pixel sensor is shown. The combination of the three modifications (moving the cutting edge as safety margin, reducing the number of guard-rings and extending the edge pixels beneath the guard-rings) allows the reduction of the inactive edge from 1100 μm for the ATLAS Pixel design to approximately 200 μm for the slim-edge IBL design [45]. The substrate material is float zone enriched with oxygen with a $\langle 111 \rangle$ bulk crystal orientation and a resistivity from 2 kΩ cm to 5 kΩ cm. The production of Planar sensor for the IBL was done at CiS². All details of the sensor design can be found in [45].

The pixels of the two central columns of the double-chip sensor are extended to 450 μm to keep the necessary gap between the two adjacent front-end chips. The pixels at the outer edges of the sensor are enlarged to 500 μm length. The nominal outer dimensions of the sensor layout are 41 300 μm × 18 600 μm. The positions of high-voltage contact pads on the p-side matches the flex design openings to allow wire bonding to the sensor. Fiducial marks on the p-side of the sensor allow proper alignment of the modules during stave loading. Those marks are placed outside the guard-ring area within the dicing streets in the inactive area of the sensor. Metallized scratch patterns are placed on the p-side of the IBL sensor close to the dicing street. In combination with the four identifying sensor numbers implemented in

²CiS: Forschungsinstitut für Mikrosensorik GmbH, Erfurt, Germany

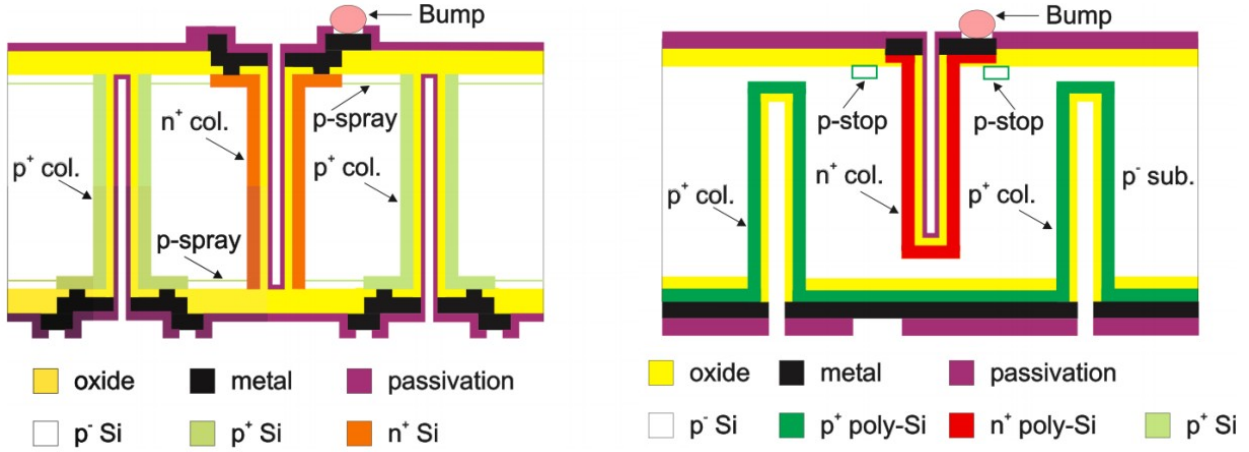


Figure 3.13: Design of the columns of the FBK (left) and CNM (right) 3D sensors. This sketch is for illustration only and is not to scale.

the metal mask on the n- and p-side of the sensor, this allows a unique identification of the sensor throughout the whole quality assurance, assembly and mounting processing of IBL sensors and modules. Further details of the sensor design can be found in [45].

3D sensors In the 3D technology the electrodes penetrate the bulk in depth perpendicularly to the sensor surface. The electrode shape is columnar and the depletion region grows around the columns. In this configuration the holes and electrons drift parallel to the sensors surface. The drift distance is not related to the width of the device, but only to the pitch between electrodes of different type. Since the inter-electrodes pitch is of the order of $50\text{ }\mu\text{m}$, the average distance that the electrons and holes travel in the silicon bulk is reduced in 3D sensors with respect to Planar. The possibility of recombination after irradiation is then reduced. Given the 3D electrodes geometry, full depletion is reached for lower voltage than the Planar technology, which results in a lower power consumption. Given these characteristics the 3D geometry is a very good candidate for high radiation environment, being less demanding in terms of cooling and bias voltage. The fabrication process of 3D sensors is more complex and the production yield is lower than for the Planar. 3D sensors do not need to compensate for the Lorentz drifting angle, since the orientation of the electric field is parallel to the ATLAS solenoid magnetic field. Test-beam investigations have shown that even if the overall efficiency was measured to be the same of that of the Planar sensors, the region of the columns was slightly inefficient.

In 3D pixel sensors, the column-like electrodes penetrate the substrate, instead of being implanted on the wafer surface and the depletion region grows coaxially to the columns. The $\approx 10\text{ }\mu\text{m}$ diameter columns are alternately n- and p-type doped defining the pixel configuration. The electrode spacing can be five to ten times smaller than the detector thickness (typically a few hundred microns), thereby dramatically reducing the charge-collection distance and depletion voltage. The 3D sensors for IBL have been fabricated at FBK³ and CNM⁴. Starting wafers were Float Zone, p-type, with 100 mm diameter, $\langle 100 \rangle$ crystal orientation,

³FBK: Fondazione Bruno Kessler, Trento, Italy

⁴CNM: Centro Nacional Micro-electronica, Valencia, Spain

Parameter	planar	3D CNM	3D FBK
Tile dimension [μm^2]	41315×18585	20450×18745	20450×18745
Sensor thickness [μm]	200	230	230
Pixel size (normal) [μm^2]	250×50	250×50	250×50
Pixel size (tile edge) [μm^2]	500×50	250×50	250×50
Pixel size (tile middle) [μm^2]	450×50	-	-
Edge isolation	Guard-rings	3D guard-ring, fences	Fences
Pixel isolation	p-spray	p-stop on n-side	p-spray
Operating bias voltage [V]			
unirradiated	80	20	20
irradiated $5 \times 10^{15} n_{eq}$	1000	160	160
Power Consumption [mW cm^{-2}]			
at -15°C after $5 \times 10^{15} n_{eq}$	90	15	15

Table 3.5: Summary of the main design specifications of Planar and 3D sensors.

230 μm thickness, and a very high resistivity (10 to 30 $\text{k}\Omega\text{ cm}$). Columnar electrodes, 12 μm wide, were obtained by Deep Reactive Ion Etching (DRIE) and dopant diffusion from both wafer sides (n+ columns from the front side, p+ columns from the back side), without the presence of a support wafer. By doing so, the substrate bias can be applied from the back side, as in Planar devices. Figure 3.13 shows details of the 3D column layout. The sensor design is detailed in [48] and also reported in [44]. Each of the 80×336 pixels has a size of $250 \mu\text{m} \times 50 \mu\text{m}$, and contains two read-out (n^+) columns (two-electrode configuration), with an inter-electrode spacing between n^+ and p^+ columns of $\approx 67 \mu\text{m}$. For yield reasons, it was decided to have single-sensor tiles (8 per wafer). A 200 μm wide region separates the active pixel area from the physical edge of the tile. The nominal dimension of the 3D sensors are $20\,400 \mu\text{m} \times 18\,700 \mu\text{m}$. The main differences between FBK and CNM productions are the following:

- FBK sensors have traversing columnar electrodes, i.e., 230 μm deep; on the contrary, for CNM sensors, electrode etching is stopped $\approx 20 \mu\text{m}$ before reaching the opposite surface;
- FBK sensors have surface isolation between n+ electrodes is obtained by a p-spray layer on both wafer sides, whereas in CNM sensors, p-stops are used on the front side only;
- FBK sensors have the edge isolation based on a multiple ohmic column fence able to stop the lateral spread of the depletion region, whereas in CNM sensors a 3D guard-ring, surrounded by a double row of ohmic columns, is used to sink the edge leakage current.

More details on FBK and CNM 3D technologies used for the IBL production can be found in [49] and [50], respectively.

Table 3.5 summarises the main parameters of the IBL sensors.

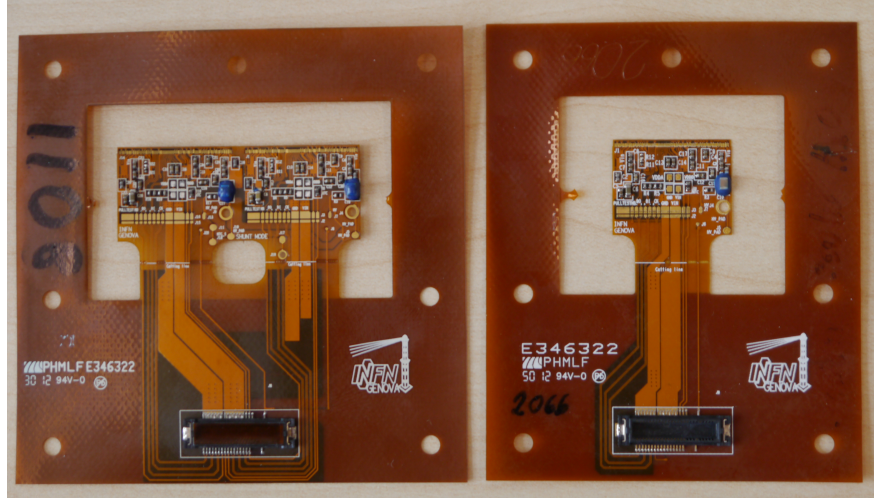


Figure 3.14: Photographs of a double-chip (left) and a single-chip module flex hybrid (right). The frame and flex extension allows testing of the module before loading on stave. The flex extension is cut during the stave loading procedure at a cutting line indicated as white line slightly outside the bare module envelope.

3.4.3 Module Flex Hybrid

The module flex hybrid is a double-sided, flexible printed circuit board which routes the signal and power lines between the stave flex (described later in this chapter) and the FE-chips and provides the bias voltage for the sensor via copper traces. Since both types of modules are on each stave, single-chip (SC) 3D modules and double-chip (DC) Planar modules, two types of module flexes were needed. From the layout and schematic point of view the DC module flex is a pair of SC module flexes. The envelope of the module flex is defined by the sensor dimensions and it is slightly narrower than the sensor width. Figure 3.14 shows a picture of single-chip and double-chip module flex hybrids.

The module flexes are glued to the sensors's backside and are connected to the longitudinal stave flex which is located at the backside of the stave via thin transversal wings, one per read-out chip. The layer stack is 130 μm consisting of two copper layers, each 18 μm thick, and the dielectric kapton layers, which are all glued together with acrylic adhesive layers. Passive components are mounted on the module-flex for decoupling and filtering of the read-out chips and for terminations of the signal traces. The module temperature is remotely monitored via a Negative Temperature Coefficient (NTC) thermistor mounted on the module-flex. All passive components are soldered on the top layer of the flex. Special emphasis is given to high voltage (HV) routing and filtering since the flex hybrid has to be functional up to 1000 V. To avoid HV discharges, sufficient space between HV, signal and low voltage (LV) traces are introduced. The HV capacitor is encapsulated with a polyurethane resin and 27 μm thick kapton cover layers are used on the top and bottom of the flex.

All signal and power traces of the module flex are routed to a 50-pin connector outside the module area used during production to test of the modules. Underneath the connector a stiffener is added to make the frame more rigid. Both module flex hybrid types use the same connector, and an intermediate wire bond connection is necessary to connect all signal and power lines from the flex to the connector on the frame. Prior to the loading of the module to the staves this connector area is cut away. The cutting line is about 1.5 mm away from

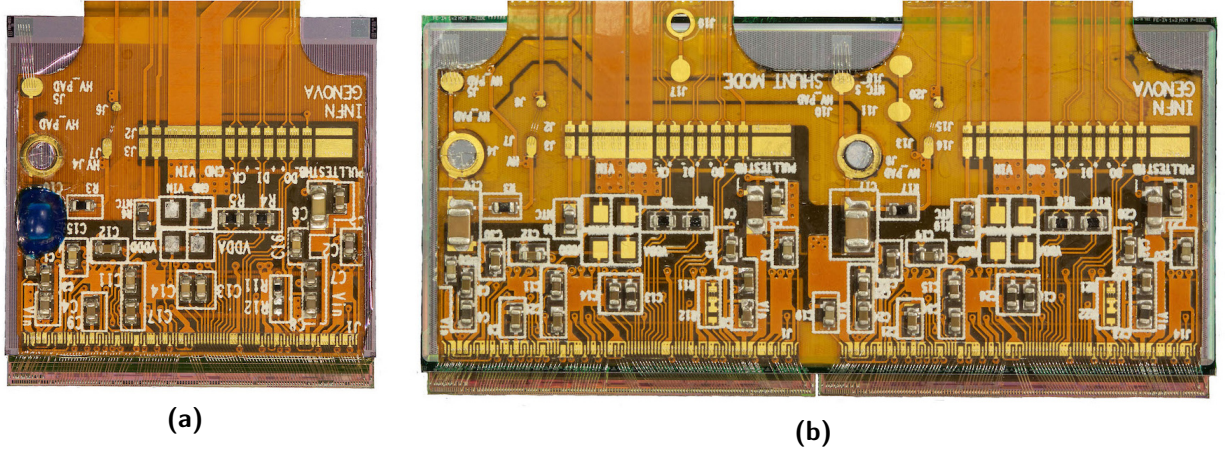


Figure 3.15: Photographs of a dressed IBL single chip module (a) and a double chip module (b). The flex extension visible on the top allows testing of the module before loading on stave. It is cut during the stave loading procedure at a cutting line slightly above the bare module.

the sensor. The cutting area of the module flex hybrid is smaller in width than the stave flex hybrid wings to avoid any part of the residual cut area touching other components of the detector. Intermediate wire bond pads are then used to connect the modules flex hybrid to the stave flex hybrid wings.

The module flex hybrids were produced at Phoenix⁵ and surface mounted device (SMD) component loading, including encapsulation, was performed at Mipot⁶. Basic quality assurance (QA) like testing of line integrity for open and shorted connections were done by the vendors and was followed by more detailed QA tests at the two module assembly sites. These QA procedures include HV standoff tests at 1.5 kV, visual inspection and dedicated cleaning to allow for high-quality wire bonding.

3.4.4 Dressed modules

Figure 3.15 shows pictures of a fully dressed single chip and a double chip module. The modules are cut out of the handling frame. The entire design of the module is optimized for low material budget. The FE chips are thinned to 150 μm and the sensor thickness is reduced to 200 μm for Planar sensors and 230 μm for 3D sensors. The thickness of the double sided flex has been chosen to be only 130 μm and the number of SMD components is reduced to a minimum. Table 3.6 summarizes the thickness of the IBL modules and its parts in units of the radiation length X_0 for perpendicular particle penetration. The contributions of the different materials are averaged over the module size. The total thickness of a Planar IBL module is 0.58 % X_0 and 0.61 % X_0 for a 3D module.

⁵Phoenix S.r.l., Via Burolo 22, 10015 Ivrea (Torino), Italy

⁶Mipot S.p.A., Via Corona 5, 34071 CORMONA, Italy

	$\%X_0$
FE chip	0.21
Planar sensor	0.24
3D sensor	0.27
Module flex incl. SMD components	0.13
Total for Planar module	0.58
Total for 3D module	0.61

Table 3.6: Breakdown of material budget for the IBL modules in percent of radiation length, for particles crossing perpendicularly the module.

3.5 Stave Layout

The IBL modules are supported and cooled by means of fourteen mechanical supports, the staves, cylindrically arranged around the beam-pipe. In this section a description is given of the support stave and of the flexible printed circuits used as services for the stave.

3.5.1 The support stave

The support stave design is motivated by several important requirements:

- Low radiation length to improve physics performance,
- Excellent thermal performance to cool down silicon sensors to maximize signal to noise and to prevent thermal runaway,
- Good mechanical stability for most efficient tracking performance,
- Low thermal expansion coefficient of materials to reduce stress and increase stability.

As shown in Figures 3.16 and 3.17 the stave is an assembly of four main components: the cooling pipe; the carbon foam to drain the heat flux; carbon laminates to increase the stave stiffness (the face plate where module will be loaded and the back stiffener on the opposite side); the fixation pin to assemble the stave around the beam-pipe. These complex materials require specific manufacturing techniques. For example: the carbon laminate requires fabrication in high pressure ovens to obtain the required transverse thermal conductivity; the assembly process require accurate gluing for material minimization; the titanium cooling pipes require accurate machining and minimal wall thickness (0.12 mm) compatible with high pressure CO₂ operation.

Minimizing materials is one of the most important requirements for the IBL detector to guarantee the required physics performance. For the support stave, this has led to a very aggressive design and choice of materials while maintaining a high level of reliability. The total material budget of the support stave structure is 0.62 $\%X_0$ and the contribution of each part is detailed in Table 3.7.

An important design element of the stave is to remove the dissipated heat from the sensors and the read-out electronics. The target temperature of IBL sensor during operation is below -15°C in order to minimize the effects of the reverse annealing and avoid the thermal runaway. An additional requirement due to the beam pipe proximity is to cool

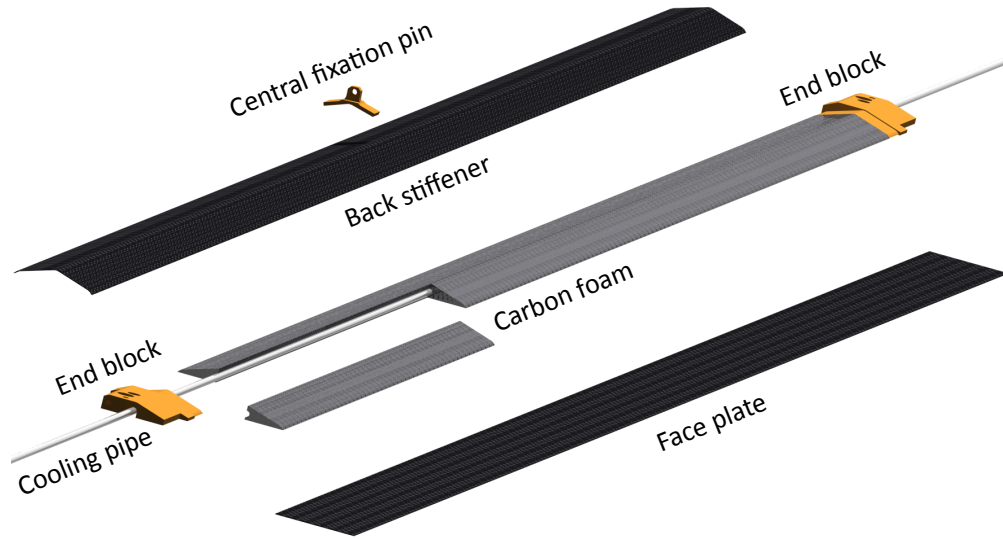


Figure 3.16: Sketch of the IBL support stave structure.

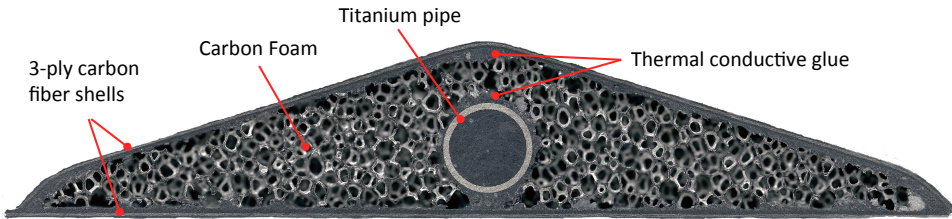


Figure 3.17: IBL stave section.

Component	Material	Volume/stave (cm ³)	Eq. Thickness (cm)	X ₀ (cm)	X/X ₀ (%)
Back stiffener	K13C/RS3	2.02	0.144	21.1	0.068
Glue layers	Stycast 2850FT	3.29	0.234	8.97	0.261
Foam	K9	21.60	1.536	213	0.072
Cooling pipe	Titanium T40	0.411	0.029	3.56	0.082
Face plate	K13C/RS3	1.903	0.0135	21.1	0.064
End of Stave fixation	Peek CA 40	2.51	0.178	25	0.071
Central fixation	Peek CA 40	0.075	0.005	25	0.002
Total:					0.621

Table 3.7: Support stave radiation length budget. Values are stave averages.

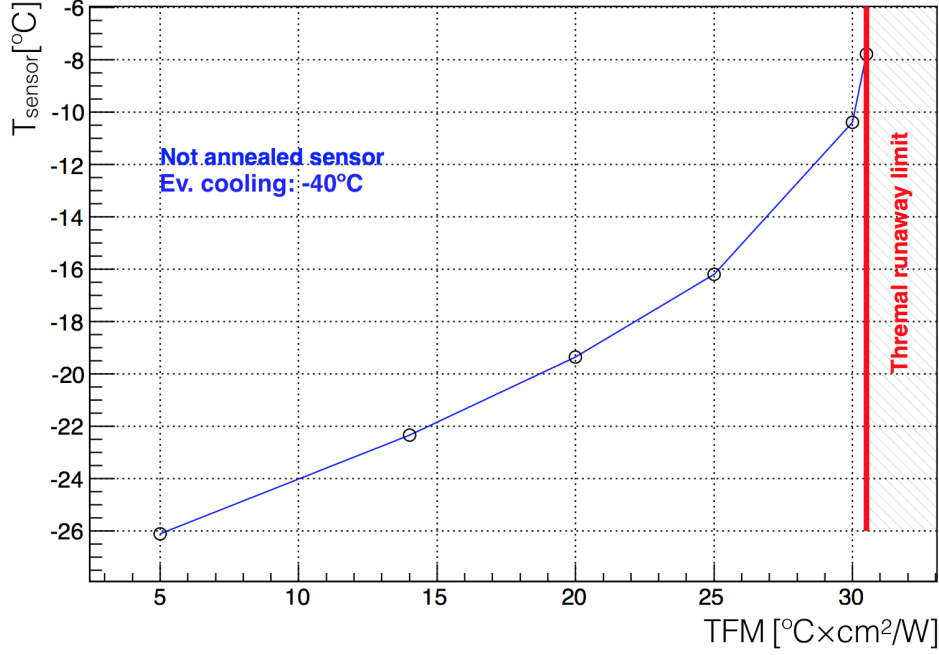


Figure 3.18: Sensor maximum temperature with respect to the stave thermal figure of merit TFM at -40°C evaporative cooling temperature.

down safely the modules during the beam-pipe bake-out phase that is meant to de-gas the beam pipe prior routine circulation of the beams. The CO_2 cooling liquid is chosen to achieve the required low temperature module operation while minimizing the pipe diameter and the associated radiation length. Because of the high CO_2 critical pressure (73.8 bar(a) at 31°C), the thin wall titanium tubes must fulfill stringent pressure requirements. Several simulations were performed to estimate the ultimate stave thermal performance (called Thermal Figure of Merit, TFM), i.e. the thermal resistance between the cooling fluid and the sensor surface. In the IBL detector conditions, the maximum sensor temperature can be expressed as follow:

$$T_{\text{sensor}} = T_{\text{coolant}} + \frac{TFM}{A_{\text{sensor}}} \times (P_{\text{chip}} + P_{\text{flex}} + P_{\text{sensor}}) \quad (3.1)$$

where P_{chip} is the chip dissipated power; P_{flex} the dissipated power in the module flex; P_{sensor} the dissipated power in the sensor calculated in worst case conditions; A_{sensor} the active sensor area and T_{coolant} is the temperature of the refrigerator liquid. In such condition the thermal runaway can be determined and was estimated to occur for the $TFM > 30^{\circ}\text{Ccm}^2/\text{W}$, as shown in Figure 3.18.

The simulation results are graph reported in Figure 3.19a that shows the thermal results obtained on a stave prototype during the final design qualification. The TFM measured is $14^{\circ}\text{Ccm}^2/\text{W}$ for $T_{\text{coolant}} = -22^{\circ}\text{C}$ which is conservatively two times below the 'admissible' value. To qualify the stave thermal performance during the production, the temperature uniformity has been measured after module loading. All installed staves show a temperature dispersion within 0.48°C , as shown in Figure 3.19b, which is a good indication of the production uniformity.

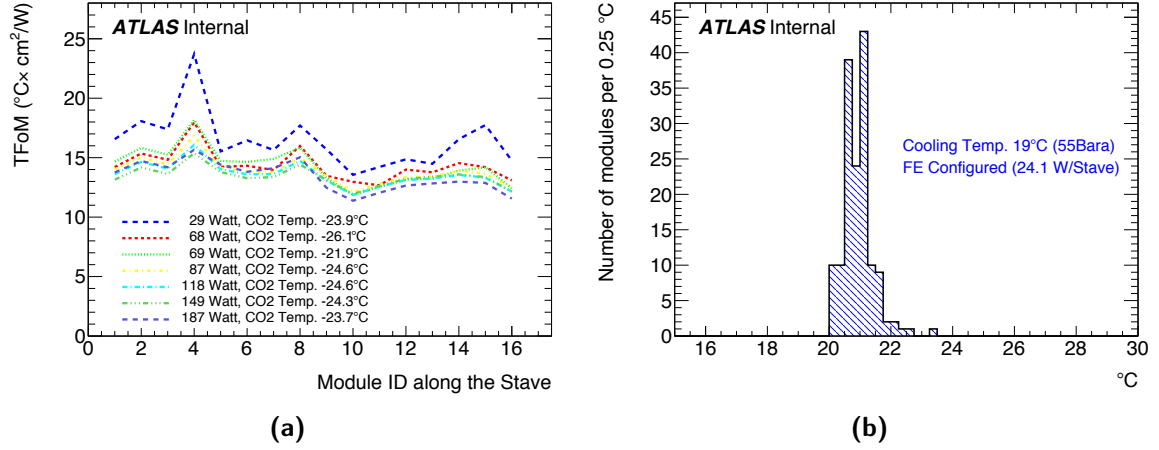


Figure 3.19: a) *TFM* of 1.5 mm stave cooling tube diameter along the cooling line. b) Module temperature distribution on produced staves with a cooling temperature of 19 °C and read-out electronics configured. The histogram has 152 entries, a mean value of 20.9 °C and a RMS of 0.5 °C.

3.5.2 Stave Flex

Two symmetric multi-layer flexible circuits, the stave flexes, are glued on the back of the mechanical support structure and route electrical services to the end of stave regions. A stack of the different layers of the stave flex is shown in Figure 3.20. Each stave flex has 16 lateral extensions, one per front-end chip, so-called wings, that mechanically and electrically connect the module and the stave flex. The glueing required a positional accuracy of 0.3 mm in the longitudinal direction and of 0.1 mm in the transverse direction of the stave in order to fit the IBL envelope requirement. The harsh radiation environment, the thermo-mechanical constraints and the minimization of the material budget are fundamental conditions for the choice of the glue to be used. After an intensive campaign of tests, the Araldite 2011 was selected as the best option. Both thermal and radiation loads were applied to the stave assembly during tests with a 10 MeV electron source. After an irradiation of 380 Mrad and 110 thermal cycles between 40 °C and -40 °C no critical damage was observed on the stave-flex glue joint[51].

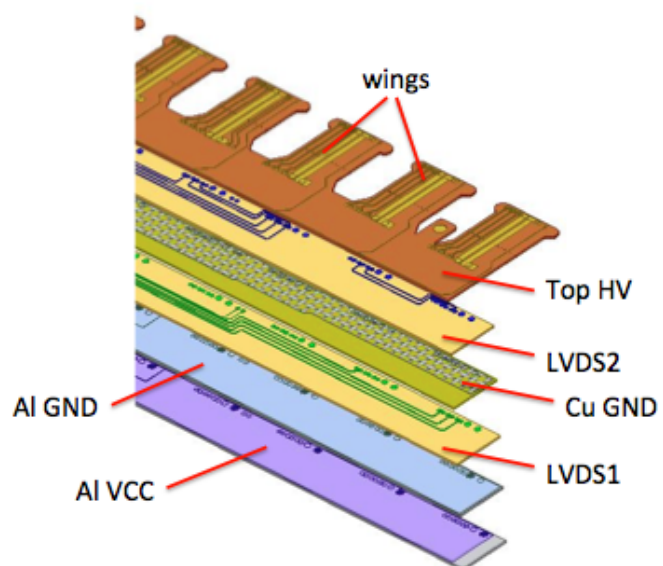


Figure 3.20: Stack of the different layers of the stave flex.

Chapter 4

The IBL construction

The construction of the IBL, shared among different sites, lasted around three years. It consisted of several steps as it can be seen in Figure 4.1. The loading of the modules onto stave and the detector commissioning are described in detail in the following since they are the main subject of this thesis. A brief description of the other phases of the IBL construction is also given. Each of the construction step was followed by a quality assurance; each component was monitored after every production step.

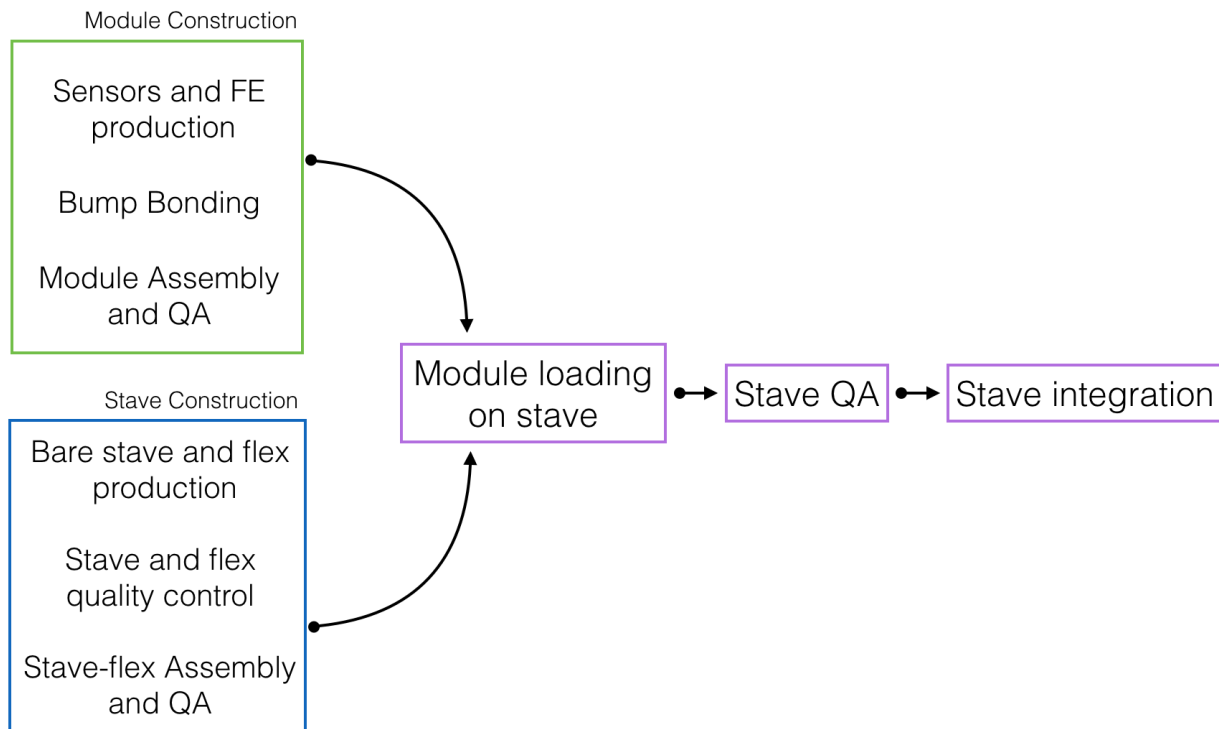


Figure 4.1: Schematics of the IBL construction

4.1 Module electrical test

During the whole production chain a key element was the check of the electrical functionality of the modules. A subset of a large variety of scans was systematically repeated at each

construction step to monitor the correct performance of the sensors and of the FE-I4s. Three different read-out systems were used for the FE-I4 testing at the different stages of the production.

- **USBpix:** this was a modular custom built system developed by the ATLAS Pixel Collaboration to test hybrid pixel detectors based on a multi-purpose FPGA card (Multi-IO board). This system was used for the test of single modules before the loading on the stave. Because of the limited bandwidth of the USB port it was not used for parallel testing of multiple modules.
- **RCE:** the acronym stands for Reconfigurable Cluster Element, and it was a readout system that uses standard commercial ATCA, therefore allowing for a faster data transfer with respect to the a USB system. The RCE was used for the FE-I4 testing after modules loading onto stave, allowing simultaneous operation of 16 FEs in combination with an High Speed Input/Output board (HSIO) dealing with the communication by means of optical fibers.
- **ROD-BOC:** it was a system composed by two card, the Read-Out Driver (ROD) and the Back Of Crate (BOC). The first card was responsible for driving the calibration scan and data-taking, while the second converts the electrical signal into an optical one and viceversa. The ROD-BOC is the system developed for data-taking; although it was under development at the time of the IBL construction, it was used for the calibration of the IBL. It is a VME-based system very similar to the one used for the other sub-detectors of ATLAS.

Even though the three readout systems were different the electrical tests of the FE-I4 were very similar and they shared a common C++ library which was driving the communication with FE-I4.

The most important electrical tests performed during the IBL construction are described below.

I-V scan Silicon sensors are diodes used in reverse bias polarization. During the IBL construction it was important to monitor that no damages occurred to the silicon sensors. A way to monitor these was the check of the I-V characteristic at the different steps of the process. To select the best modules particular attention was payed to the breakdown voltage value and the stability of the breakdown voltage points, which could reveal the presence of damages. The scan was performed by measuring the leakage current at different values of the bias voltage applied (V).

Digital test The digital test consisted in injecting pulses at the output of the discriminator. In this way the digital part of the electronics was tested without being affected by the analog part. A number of signal injections was performed, with 100% efficiency channel response expected. The number of injection was depending on the aim of the test. During the characterization of the module 200 injections per pixel were performed, while in the following steps the number was reduced to 50. The pulse injected had the same amplitude of the discriminator output.

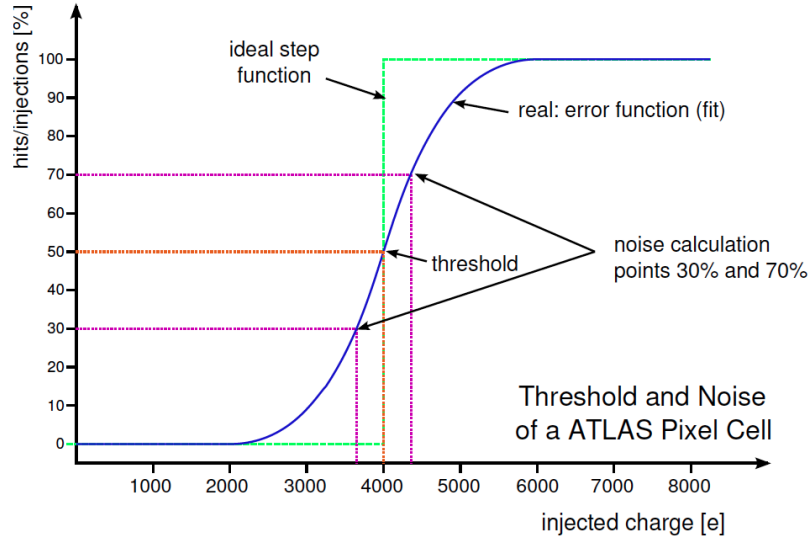


Figure 4.2: Example of the S-Curve for one pixel, X axis shows the injected charge

Analog test The analog test was similar to the digital test, with the difference that the injections happened at the preamplifier input stage. A voltage pulse, V_{cal} , was injected in the calibration capacitance, C_{inj} , of each pixel, generating a signal at the input of the preamplifier equivalent to the one generated by a charge $V_{cal} \cdot C_{inj}$ (see Figure 3.10a). For the analog test it was important whether the sensor was depleted or not, since this determines the noise at the pre-amplifier. The combined information from the analog and the digital tests indicate if failures were present in the analog part of the circuitry. Typically a charge of $16000e^-$ was injected. The number of injections was the same as for the digital test. An analog test was also used to check the ToT response, checking the average ToT corresponding to a charge injection. It was also possible to inject a charge in a pixel and check for response in the neighbor one, this scan was very useful to identify merged bump bondings and it was known as crosstalk scan.

Threshold scan The main goal of the threshold scan was to define the threshold and measure the Equivalent Noise Charge (ENC) for each pixel. A set of pulses was generated for each different value of the injected charge, spanning over a range going from no hits detected to full efficiency. One would expect to have a sharp transition from no hits, when the signals are under threshold, to full efficiency, when the signals are always above threshold. In reality the transition is not sharp, due to the noise contribution, and the number of collected hits versus the injected charge is well represented by "S-curve", the convolution of the step function that describes the threshold activation and a gaussian that describes the contribution of the noise. The S-curve function used for the fits is the product of a_0 , the number of injection executed for each charge value, and the cumulative distribution function

$$\frac{1}{2}(1 + \text{Erf}(\frac{Q-\mu}{\sqrt{2}\sigma})):$$

$$a_0[\frac{1}{2}(1 + \text{Erf}(\frac{Q-\mu}{\sqrt{2}\sigma}))] \quad (4.1)$$

$$\text{Erf}(x) = \frac{2}{\sqrt{\pi}} \int_0^x e^{-t^2} dt \quad (4.2)$$

where Q is the injected charge, μ is the threshold, defined as the 50% of detection probability, and σ is the width of the gaussian noise contribution. The ENC is defined as 2σ of the fit. An example of S-curve is shown in Figure 4.2

This test allows for an identification of disconnected bumps. For a depleted sensor the ENC is lower then for a un-depleted one because the lower capacitance when the sensor is depleted, as explained in Chapter 2. Bumps that are disconnected from the silicon sensors are expected to have no difference in the ENC in the depleted and un-depleted cases[52]. This method works well for planar sensors, which largely increases their capacitance when the sensor is not powered, but it is not enough to guarantee a qualification of 3D modules, so that a the determination of disconnected bumps was done with source tests.

Tuning The threshold and ToT response could be changed acting on the following FE-I4 parameters (see Figure 3.10a):

- V_{th} , a 8-bit global register for the control of the threshold;
- TDAC, a 5-bit local register for the control of the threshold;
- V_{fb} , a 8-bit global register for the control of the feedback current of the pre-amplifier;
- FDAC, a 4-bit local register for the control of the feedback current of the pre-amplifier.

where a global register controls the entire pixel matrix and the local register controls a single pixel. The optimization of the parameters required a dedicated tuning procedure. Since the level of the threshold affects the ToT response by definition, at least two iterations of the tuning procedure were required. The tuning consisted in four main scans, each one dedicated to one register type, in the order of the list above. Each step consisted in a binary search across the register range of the target threshold or ToT.

4.2 FE-I4 production and QA

The production of the FE-I4 chip was carried out at IBM for a total of 3060 chips. Each FE-I4 had to pass a selection process testing the analog and digital functionality of each pixel, the global chip parameters and the chip calibration. The selection was based on the characterization performed on the first 600 chips. A detailed description of the selection process can be found in [45]. In particular the FEs were accepted if less than 0.2% of the pixels were failing with less than 20 pixels per column. In total 61% of the tested FE-I4 qualified for the IBL. The test results of the fully probed chips leading to a disqualification for IBL usage are shown in Figure 4.3.

An important step of the FE-I4 production was the chip calibration which was carried out by using dedicated pads that cannot be bonded after the module assembly. No failure

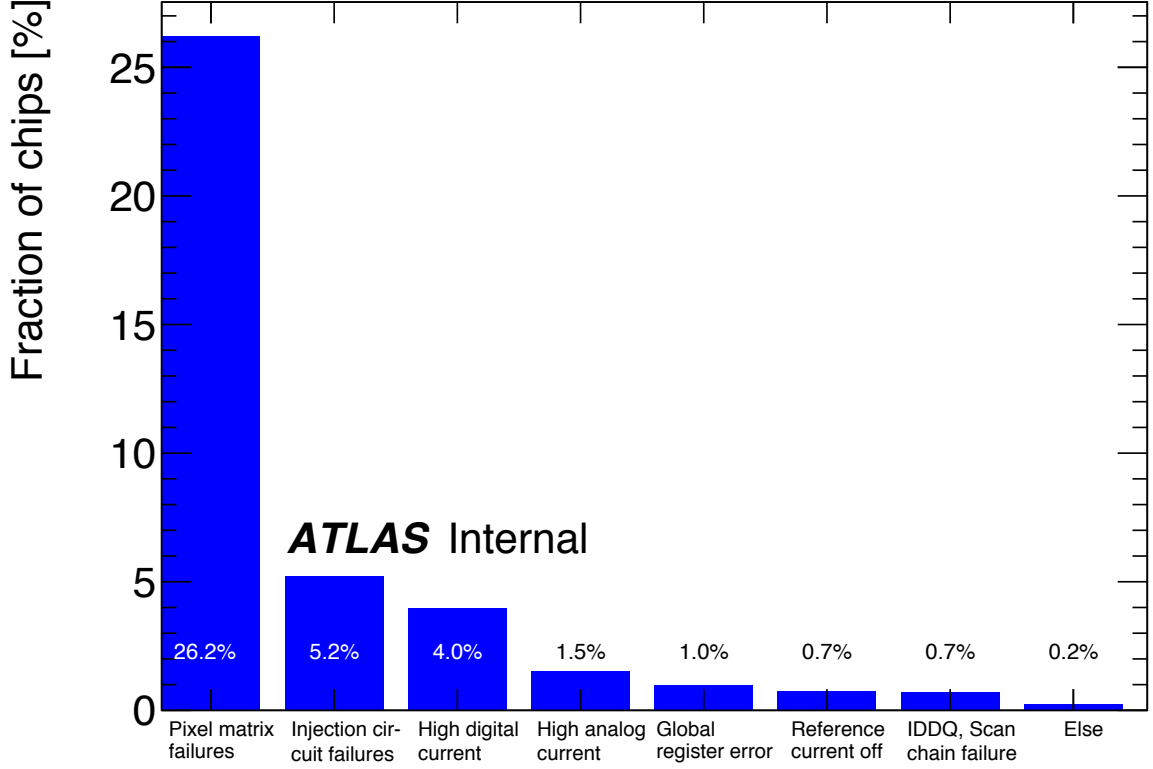


Figure 4.3: Failure modes leading to a disqualification of the FE-I4s for IBL operation. All 2814 fully probed chips are taken into account. Each bin shows the failure mode in percent. The bin *Pixel matrix failures* indicates FEs where the number of bad pixels were too high ($>0.2\%$ failing pixels or >20 pixels per column). The bin *Injection circuit failures* sums up all failures related to this circuit (low maximum voltage, injection delay not configurable, etc.). The bins *High analog/digital current* combine current measurements at different chip states (unconfigured, configured, high digital activity). The next three bins give the rate for chips failing the global register tests, the reference current generation and the scan chain tests. All failure modes that were not explicitly mentioned contribute with only 0.2% and were summed up in the bin *Else*. A total of 1,821 chips passed all tests giving a production yield of 61% .

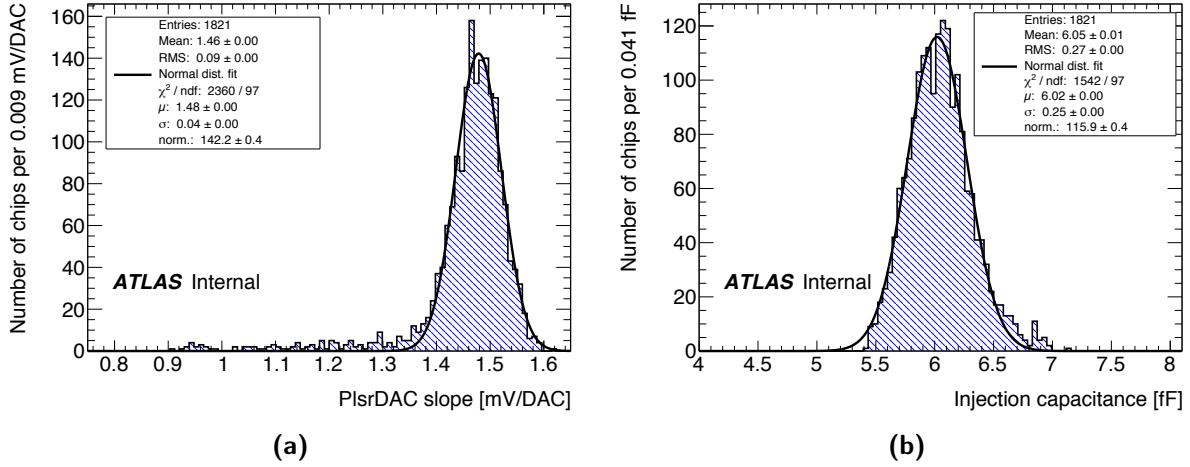


Figure 4.4: Calibration constants of the internal charge injection circuit. The circuit distributes a voltage step to injection capacitors present in each pixel. (a) The slope of the transfer function of the voltage DAC (*PlsrDAC*). (b) Distribution of measured values of injection capacitors of the 1821 selected good chips.

was allowed at the chip calibration stage.

The chip calibration consisted in the measurement of the voltage corresponding to the DAC of the pulser and in the measurement of the injection capacitance. These two parameters allows to determine which charge was injected in the FEs circuitry with the injector. The calibration constants for the entire IBL production is shown in Figure 4.4.

The on-chip power regulators of the FE chips were not tested during the probing, but only after the modules had been assembled completely, see section 4.4.2.

4.3 Sensor Production

Planar sensors The planar sensor production was carried out at CiS. A total of 150 wafers of planar sensors were produced, each of them was four inch in diameter and 200 μm thick, for an overall production of 600 sensors. Each wafer was tested and had to fulfill both electrical and metrology requirements. The planar design includes a grid structure that allows biasing of the entire sensor by means of a punch-through technique. This bias grid was used to evaluate the quality of the tiles at wafer level, before the dicing and the assembly to the FE-I4. The sensors were polarized in reverse bias voltage. For the sake of simplicity the voltage value will be reported in absolute value. The depletion voltage (V_{dep}) had to be in the range 15 V to 75 V and the current at the operative voltage ($V_{dep}+30$ V) had not to exceed 2 μA . The ratio between the current at the operative voltage and the current at the depletion voltage had to be lower than 1.6. The wafer thickness had to be in the range 180 μm to 220 μm , with a planarity better than 40 μm . A total number of 119 wafers was qualified, the rest of them was either damaged during the processing itself or did not pass the selection criteria.[45]

3D sensors The 3D sensor production was carried out by two different vendors, FBK and CNM. In total 118 wafers were produced, 58 at FBK and 60 at CNM. Each wafer was 4

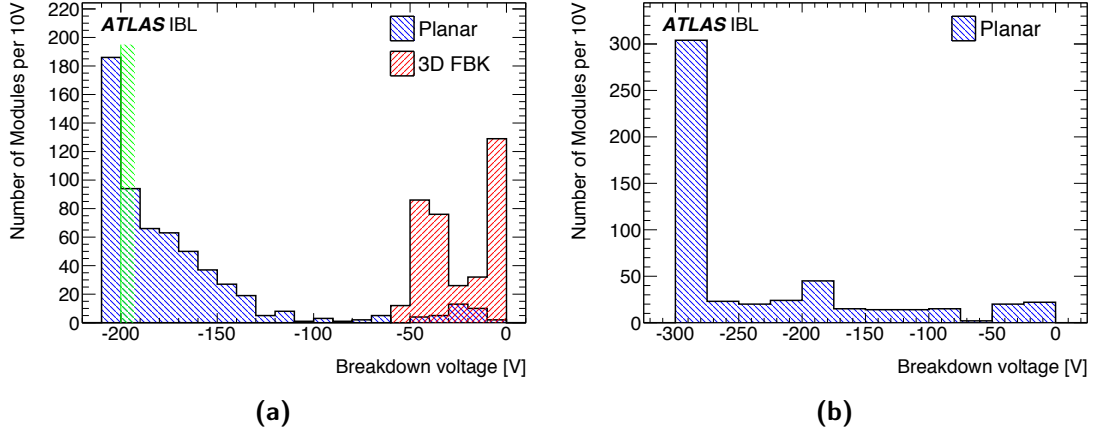


Figure 4.5: The breakdown voltages of planar and FBK 3D sensors measured at the wafer level were presented in (a). The entry behind the vertical line indicates the planar sensors with breakdown voltage beyond 200 V. The breakdown voltage of the planar sensors after under-bump metallization and dicing was shown in (b).

inches in diameter for a 230 μm thickness. For the testing, a different approach was used in the IV characterization, since it was difficult to implement a bias grid similar to the one used for the planar sensors. FBK sensors used a temporary metal grid that was shorting all the pixels in the same column to a pad located in the periphery of the active region. The I-V curves of the 80 columns were measured with a probe card. The metal layer was removed before the dicing by chemical etching.

The depletion voltage had to be lower than 15 V and the current at the operative voltage ($V_{dep}+10\text{ V}$) had not to exceed 2 μA . The ratio between the current at the operative voltage and the current at the depletion voltage had to be lower than 2. Wafers with 3 or more qualified tiles were selected for the bump-bonding process and dicing[48].

The CNM sensor selection criteria were based on the leakage current measured through the 3D guard ring structure that surrounds the pixelated area. The CNM sensors were required to had a breakdown voltage higher than 25 V, the depletion voltage lower than 15 V, and guard ring current lower than 200 nA at the operative voltage, which was set 10 V above the depletion voltage. The ratio of the current in between the operative and the depletion voltage was also constrained to be less than 2. Wafers with at least 3 sensors that passed the selection criteria were sent to IZM for under-bump metallization and dicing [48].

During module assembly several CNM 3D modules showed a low breakdown voltage due to the poor correlation between the breakdown voltage measured on the wafer. Studies on initial batches indicated a good correlation between the breakdown voltage measured through the 3D guard ring structure and the breakdown voltage after detector assembly [44]. However, during module assembly, the correlation proved to be poor, with several CNM 3D modules showing a low breakdown voltage. At this stage, all the sensors that were not assembled were re-tested on a probe station. The n-side of the sensor was placed in contact with a grounded chuck via the under-bump metallization (see Section 4.4.1), while the p-side was connected to the bias potential. The sensors that showed a voltage breakdown larger than 25 V were selected for hybridization. The yield of the CNM production on selected wafers as measured with the 3D guard ring method, was 72 %. However, after re-testing, the final

production yield was similar to the FBK one.

4.4 Module assembly and QA

This section gives a description of the module assembly and of the qualification performed on the modules.

4.4.1 Module assembly

The first step of the module construction consisted in the channel-by-channel connection of the sensor with the FE-I4, the so called bump-bonding process. It was done at IZM¹ and consisted of the following steps.

- The FE-I4 thickness was reduced to 150 μm .
- Under-bump metallization: a metal stack of TiW and Cu was sputtered on sensor and FE-I4 aluminum pads, which otherwise would not be solderable.
- Deposition of the SnAg solder bumps on the FE-I4 wafer via electroplating technique.
- Dicing of the sensor wafer and flip chip.
- Bump soldering.

Given the high temperature of the soldering process and the thin thickness of the FE-I4 IBL readout chip, a 500 μm thick glass carrier chip was temporarily mounted to the read-out chip and removed again after the soldering. This prevented any deformation of the chip. The glass was then removed by means of a UV excimer laser with a wavelength of 248 nm, the glass carrier material was optimized for the UV transmittance and the laser light was fully absorbed in the polyimide bonding layer.

The first batches of module production showed a high bump-bonding failure rate due to large areas of disconnected bumps and isolated shorts between neighbor pixels. The disassembled sensors and FE-chips of defective modules revealed polymerized flux residuals. The residuals acted as a spacer during the reflow preventing a proper bump connection between sensor and FE pixel. The disassembled modules revealed flux residuals in areas with larger number of shorts too, with the short vanishing after the disassembling. The flip-chip procedure was then changed, in particular the solder flux was replaced with glycerin [53].

The step following the bump-bonding procedure was the module dressing, which consisted of the loading of the flex service and the wire-bonds connection for the FE and sensor pads. The module dressing consisted in the following operation.

- Preparation and cleaning of the module flex hybrid, including visual inspection: here the flex hybrid was treated with special cleaning fluids² in an ultrasonic bath.
- Preparation and visual inspection of the bare module.
- Alignment of the module flex hybrid to the module, deposition of the glue and curing.

¹Fraunhofer IZM, Gustav-Meyer-Allee 25, 13355 Berlin, Germany

²Vigon A200

- Activation of the wire-bonds pads via plasma cleaning.
- Wire bonding of the FE-chip to the module flex hybrid and of the wire bond bridge to the test connector.

4.4.2 Module QA

The modules were subject to a QA which included tests of the electrical and functional performance of both the FE-I4 the and sensors. This characterization was performed at room temperature and at -15°C , the latter in order to test the module in the environmental condition of IBL operation. During the module QA the power regulators were tested for the first time and also calibrated; digital and analog circuitries of the FE-I4 were also tested. An aging test was performed as well, which consisted of ten thermal cycles of the module from -40°C to 40°C , when the module was not operative. A detailed description of the module QA and chip calibration can be found in [54]. The module selection for the stave loading was done according to the results of these performance tests. Only modules passing all tests were considered as candidates for IBL. The number of failing pixel of each test was summed up without counting the pixels twice if they were failing more than one test. For any module, nonconformities like rework, sensor scratches or chip penalties in terms of additional bad pixels were put in the bad pixel count. Only modules with a total number of bad pixel count below 1 % were selected. This mean that less than 540 (270) bad pixels were tolerated for double (single) chip modules.

Of particular interest for this was the characterization of module performance in terms of the sensor breakdown voltage, the fraction of failing pixels and the timing performance³ of modules production. In particular the breakdown voltage and the fraction of failing pixels were used for determining the position of the module into the stave, while the timing performance became crucial in the commissioning phase of the detector.

The breakdown voltage differs for the three module flavors (Figure 4.6a). The operation voltage of the two 3D module types was -20 V , hence all 3D modules with a breakdown voltage below -20 V were rejected. The sensor test procedure at wafer level was significantly different for the CNM and the FBK modules as explained in section 4.3. As a consequence, the correlation between the breakdown voltage measurement at wafer level and at dressed-modules level was poor for CNM modules. This was the reason for the increased number of dressed modules failing the minimum breakdown voltage cut of the CNM compared to the FBK modules. Additionally, the value of the measured current was dominated by surface current effects on the sensor. This makes the breakdown voltage determination difficult and thus the distribution broader than for the FBK modules. The dominance of the surface current was expected to disappear with the increased leakage current due to radiation damage in the silicon bulk. The planar modules were accepted if there was a difference of more than 70 V between the breakdown voltage and the operational voltage of 80 V . All dressed modules with a planar sensor, but four, fulfilled the sensor breakdown voltage criteria. After the test of each individual failure mode, the pixels failing any test were counted. Individual pixels were not double counted. The fraction of pixels that fails in any test is shown in Figure 4.6b for all modules. The mean number of failing pixels of the accepted planar modules was about 0.56 % with an RMS of 1.67 %. As expected, the fraction of failing pixels distribution of the CNM and FBK modules was comparable to the planar module distribution with a

³the capability of assign the signal coming from the sensors to the correct bunch crossing

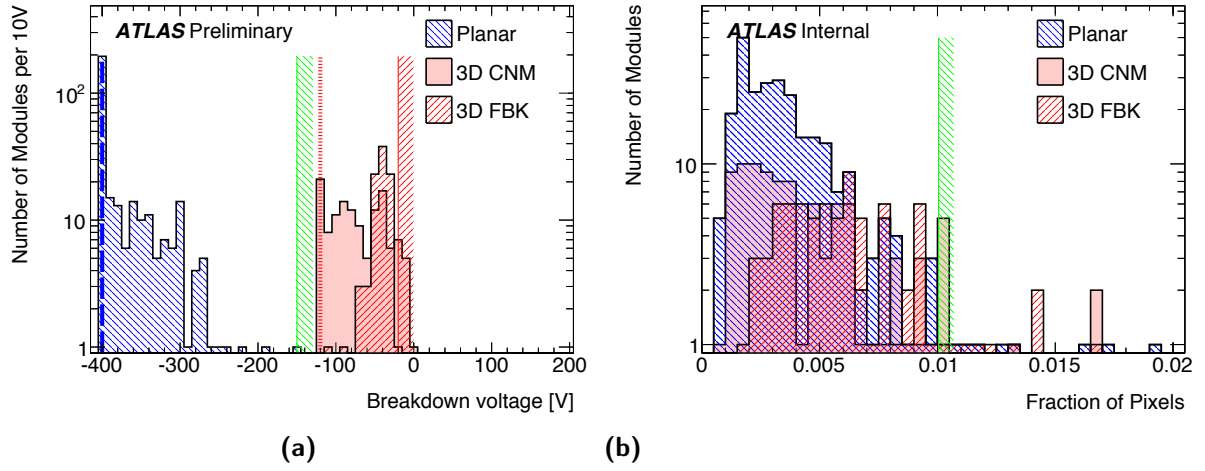


Figure 4.6: (a) Breakdown voltage for the three types of modules. The dashed vertical line indicates the maximum measurement point of -400 V for the planar modules and the red dotted vertical line the maximum measurement point of -120 V for the 3D CNM and FBK modules. Additionally, the acceptance criteria for the planar modules above -150 V (green band) and -20 V (red band) were indicated by the shaded areas. The mean value of the distribution of 313 planar sensors was -375 V. The 3D CNM distribution of 128 CNM sensors had a mean value of -73 V. The distribution of 93 FBK sensors showed a mean value of -43 V. A percentage of 42% of the modules fails the indicated minimum acceptance level for planar and 3D CNM and FBK sensors. (b) The distribution of the fraction of pixels failing in any of the test. The green vertical band shows the acceptance criteria of the fraction of bad pixels, which was 1% .

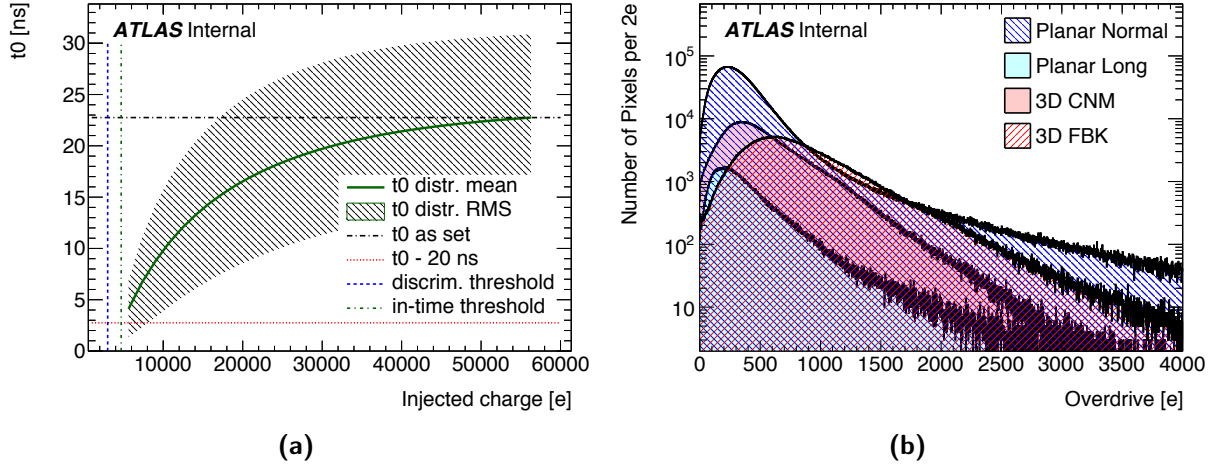


Figure 4.7: (a) The pixel-to-pixel distribution of the in-time threshold and (b) The overdrive distribution (explained in the text). All modules matching IBL quality criteria were shown. The 3D CNM distribution had a mean value of $3519 e^-$ and a RMS of $357 e^-$. The 3D FBK distribution mean value was $3820 e^-$, the RMS was $483 e^-$. Pixels failing the measurement were not included in the distributions.

mean of about 0.52 % and an RMS of 0.44 % in the CNM case, and a mean of 0.68 % and a RMS of 0.39 % in the FBK case.

During the detector operation, IBL modules will be read using only a one bunch-crossing-wide Level-1 trigger. This mode translates into a sensitive time of only 25 ns. Thus the hit timing is of major importance for IBL operation. The mean turn-on time of the full pixel array was measured and the injection time (t_0) was fixed to the mean turn-on time plus a safety margin of 5 ns.

Measuring the t_0 time as a function of the injected charge reveals the time-walk effect: the smaller the injected charge, the earlier was the t_0 measured and this could lead a signal to be associated to the previous bunch crossing. Figure 4.7a shows the t_0 as function of the injected charge.

A useful quantity for the characterization of the time-walk was the overdrive, i.e. the charge above the discriminator threshold that was needed for the hit to be detected within one bunch crossing. All hits with a charge above the discriminator threshold plus the overdrive are associated to the right bunch crossing. This threshold was commonly called in-time threshold. The overdrive distribution of the planar modules ($355 e^-$ mean with $250 e^-$ RMS) was lower than the distribution of the CNM modules ($530 e^-$ mean with $351 e^-$ RMS), while the FBK modules had the highest overdrive ($828 e^-$ mean with $478 e^-$ RMS). These time-walk values were well-below the time-walk correction capability of the read-out chip (approximately $1500 e^-$, see [54]). Figure 4.7b shows the overdrive distribution for the modules matching the IBL selection criteria.

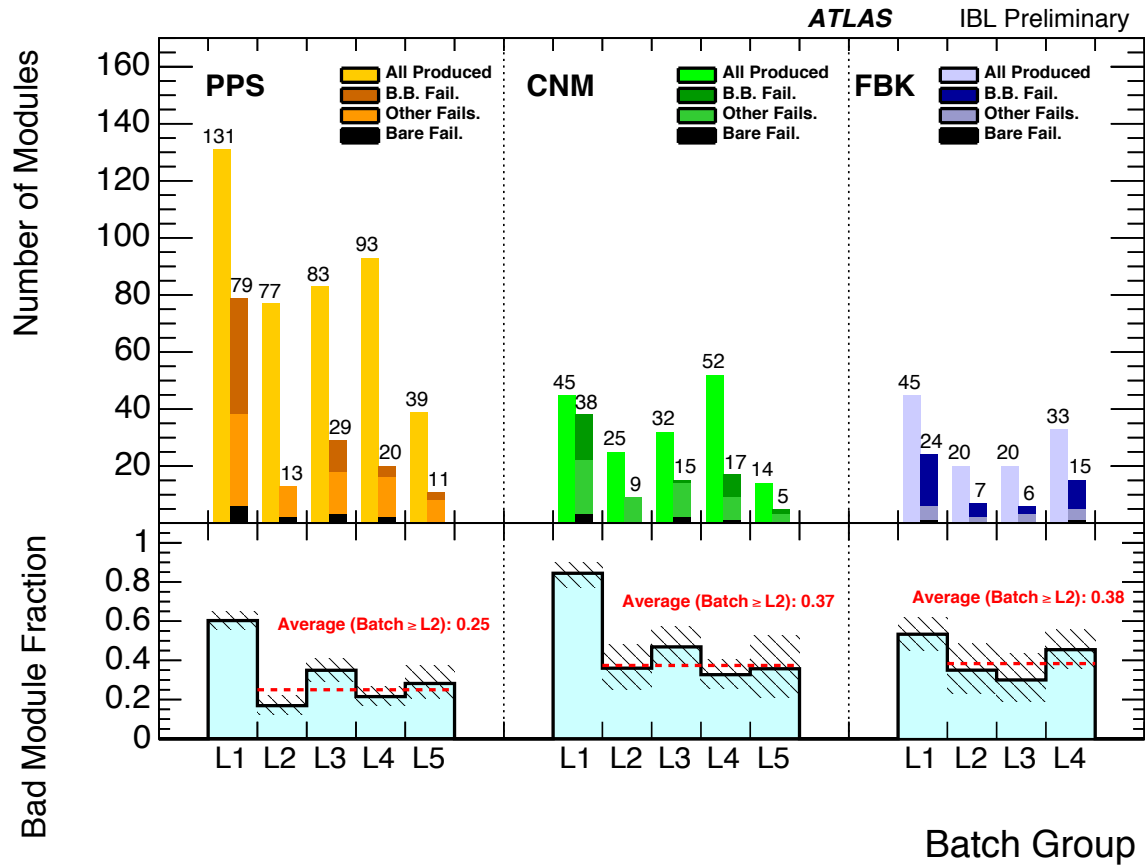


Figure 4.8: Yield of IBL module production for planar (PPS) and 3D (CNM, FBK) sensor types per production batch. In the top panel *B.B. Fail.* designates large bump-bonding failure, *Bare Fail.* for the modules not assembled due to mainly mechanical damages, and *Other Fails.* were both electrical and sensor failures discovered after assembly. Within the same batch group, similar configuration of the laser condition and the bump bonding was applied. In the bottom panel, the first batch group was excluded from the average yield in the plot because they were largely affected by bump bonding problems. The average bad module fraction of all batches for PPS, CNM, FBK was 0.36, 0.50, 0.44, respectively, excluding the first batches

4.4.3 Production Yield

Figure 4.8 summarizes the IBL module production yield. In the figure the yield was expressed in terms of bad modules and distinguishes between the three different types of IBL modules. The yield was divided into different production batches with similar laser de-bonding and flip chip method applied.

The production yield of the first batch group L1 of all modules was very poor due to the problems with the bump bonding[53]. Only 40 % of the planar modules, 20 % of the CNM and 35 % for the FBK 3D modules passed the acceptance criteria. For the other batches the yield improved to an average of 75 % for the planar modules, 63 % for CNM and 62 % for FBK modules. Other main defects observed during the module production were either of mechanical or electrical origin. During the entire production a roughly constant defect rate of about 15 to 20 % was observed which included all kind of electrical failures. Main contributions were failures of the on-chip regulators which were not tested during wafer probing of the read-out chip wafers. Also other electrical problems appeared, such as failing double columns of the FE and communications issues; since the rates were quite low, no special effort was applied to improve this. A number of CNM modules in L2 and L3 showed problems with low breakdown behavior of the sensor. The reason for this was an insufficient testing procedure during the sensor wafer quality insurance. CNM sensors used for the batches L4 and L5 were retested after under bump metallization deposition and dicing and therefore the yield improved slightly. However, re-testing required the removal of the sensor from the clean room environment and the placing of the sensor pixel side to a metal chuck. Thus additional dust and scratches were introduced, which could not be cleaned properly prior to the flip chip. Therefore the bump bonding failure rate increased for these batches with respect to the previous ones.

4.5 Bare stave and flex assembly

The assembly of the stave with the flex was entirely performed in clean room. A visual inspection was performed as soon as the components were received from the respective production sites, each component was cleaned to prevent contamination of the flex services and the stave surfaces. Before the loading, an electrical test was performed on the flex, which had to stand 1000 V for the HV lines dedicated to planar modules and 500 V for the HV lines dedicated to the 3D ones. The resistivity measurements indicated a value compatible with the design value of $0.196\,\Omega$. After this electrical test the wings were bent and a second electrical test was performed. The flex was then loaded on the stave and glued to one of the stave back sides. After the hardening of the glue the stave joints were checked with an endoscope. The stave was then loaded on dedicated designed handling frame and final glueing steps performed, which involved the carbon fibre clamping.

As a first step of the qualification, the staves were visually inspected and the stave flexes were electrically tested to verify that the services were not damaged during the loading. Then the staves were thermally stressed: a program was defined with an initial phase at 35 °C for 1 h followed by 10 cycles of 1 h from 40 °C to -40 °C. The program ended with a stabilization phase of 3 h at 20 °C [55].

A metrology survey was systematically done before and after thermal cycling to study how

	stave 1	stave 2	stave 3	stave 4	stave 5	stave 6	stave 7
planarity before [μm]	218	178	176	217	108	219	177
planarity after [μm]	244	205	223	235	189	290	222
Dif. [μm]	26	27	47	18	81	71	45
	stave 8	stave 9	stave 10	stave 11	stave 12	stave 13	stave 14
planarity before [μm]	157	195	194	230	280	186	181
planarity after [μm]	193	229	243	298	314	224	218
Dif. [μm]	36	34	49	68	34	38	37
	stave 15	stave 16	stave 17	stave 18	stave 19	stave 20	
planarity before [μm]	135	283	-	282	220	257	
planarity after [μm]	325	329	114	336	266	237	
Dif. [μm]	190	46	-	54	46	-20	

Table 4.1: Production staves planarity before and after thermal cycling for the 20 staves selected for the module loading. Measurement of stave 17 before the thermal cycling was accidentally lost.

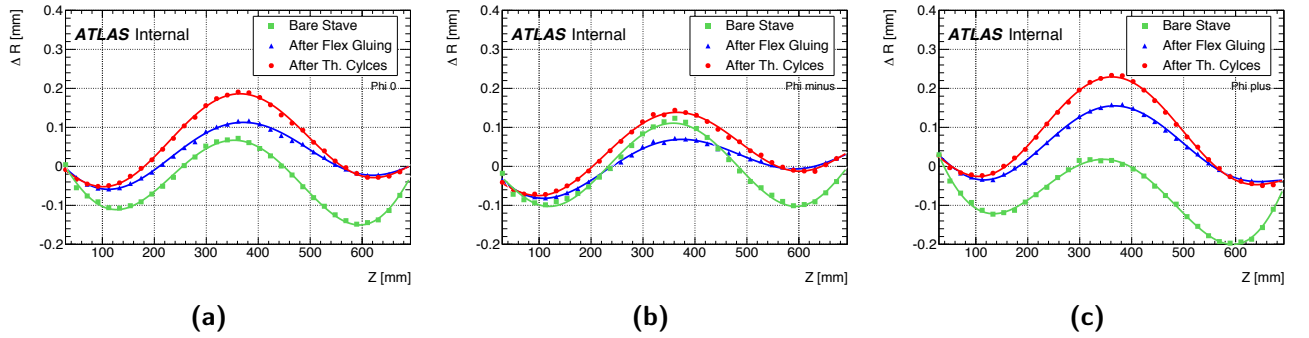


Figure 4.9: Stave profiles before stave flex gluing, after flex gluing and after thermal-cycling as a function of the position along the stave. 4.9a measurements at the center of the stave (Phi 0); 4.9b measurements at the edge of the stave where the stave flex is glued (Phi -) 4.9c measurements at the other edge of the stave (Phi +)

Type	#
Staves accepted for flex assembly	24
Staves used for system test prototypes	2
Staves assembled with flex	22
Staves rejected after flex assembly	1
Staves qualified for module loading	21
Staves loaded with modules	20

Table 4.2: Allocation for the produced and qualified bare staves.

the mechanical supports were deformed by the flex glued on top of them and to verify that the assembly was still respecting the required envelope. The most important measurement of the metrology check was the planarity, defined as the maximal excursion from an ideal plane of the stave faceplate surface. The planarity of the stave was of importance because of the mechanical envelope of the IBL structure, which allows a clearance of 500 μm during the integration steps of the IBL stave around the IPT. A safe limit for the planarity of 350 μm was imposed as a selection criteria. The planarity results of production staves (before and after thermal cycling) are summarized in Table 4.1 [55]. The profile of the stave was measured across the cooling pipe direction, three set of measurement were taken, at the center of the stave (ϕ_0) and at both the edges (ϕ_+ and ϕ_- , where the latter refers to the side where the stave flex was glued). An example of one of the stave profile is shown in Figure 4.9, showing the measurements for each loading step. Although the shape of the mechanical supports was changed by the flex assemblies they were measured to remain within the envelope. During the prototyping phase one stave flex started to delaminate after several thermal cycles. A carbon clip was added to the design in order to prevent this problem. This was the only stave which had a critical problem due to glue mixture mistake and polymerization failure. None of the 20 staves used for the module loading presented this issue. A summary of allocation for the staves is reported in Table 4.2.

4.6 Stave Loading

The stave loading was a procedure which consisted in the mechanical loading of the modules on the stave and of electrical, functional and mechanical checks of all the stave assembly components. Reception tests were carried out in the clean room facility of University of Geneva for the modules and the staves, as soon as they were received from the productions sites. then the modules were loaded onto the staves by mean of dedicated gigs and handling frames. After module loading the modules were wire-bonded to the stave flex. After this operation, an electrical check of the modules was performed, then the stave was thermally cycled and the electrical integrity checks repeated. This entire procedure, as it will be explained in the following sections, was followed up to the stave number 12, then the last two steps were removed. A module-replacement procedure was also available in case of failures of modules. A detailed description of each part of the stave loading activity follows.

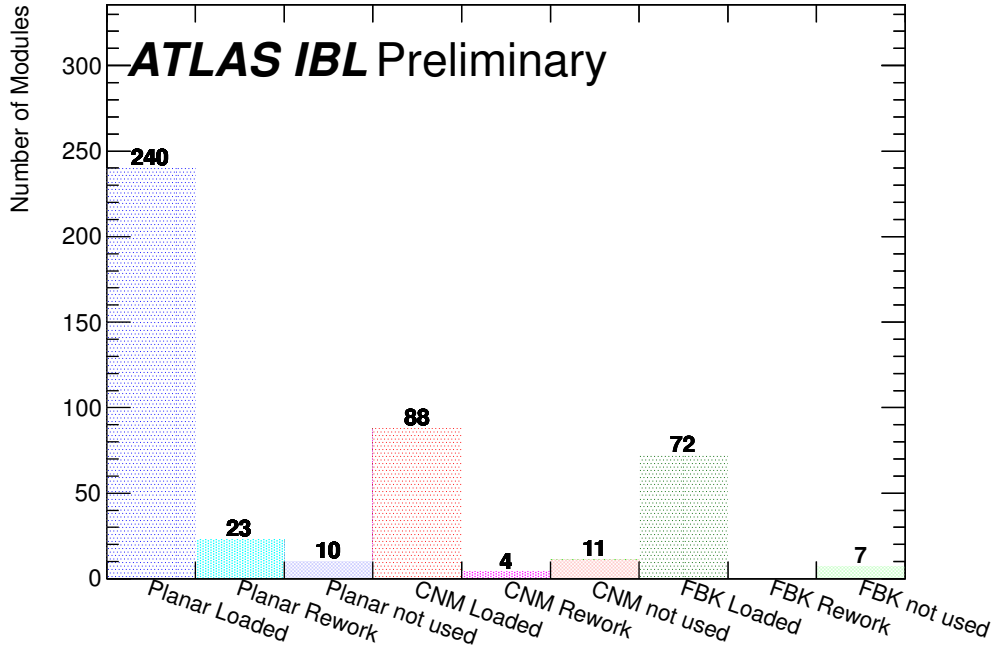


Figure 4.10: Total number of modules tested (planar, 3D CNM and 3D FBK) organized in categories.

4.6.1 Module reception tests

The module reception test procedure consisted of two steps: optical inspection and electrical check.

The optical inspection was a thorough visual examination in which the modules were inspected by means of an optical microscope with a total magnification of up to 500 \times and a digital camera. The purpose was to check the modules integrity after the transportation to the loading site, especially wire bonds integrity and cracks in the sensor area. Particular attention was payed to the wire-bondings: each one was checked to make sure there were no shorts that may happened due to a shock, nor any weakened or faulty connection. The visible part of the sensors was also inspected for cracks and any other damage that may affect the operation of the module. Pictures were taken during the optical inspection, checking systematically:

- the fiducial marks, one on each corner of the sensor, since these were the references used during the metrology survey to know the position of a module with respect to the stave fixation reference;
- the HV pads, to make sure that the pads were well glued and bondings were good, as a failure at this level could prevent the module to be operated.

A total of 456 modules was received and tested for stave production. The number of modules loaded on the staves and of the ones used for reworkings is shown in Fig. 4.10.

No module was rejected at the optical inspection stage.

The electrical and functional checks of the modules consisted in the repetition of some of the tests already performed during the module quality assurance. In this test the func-

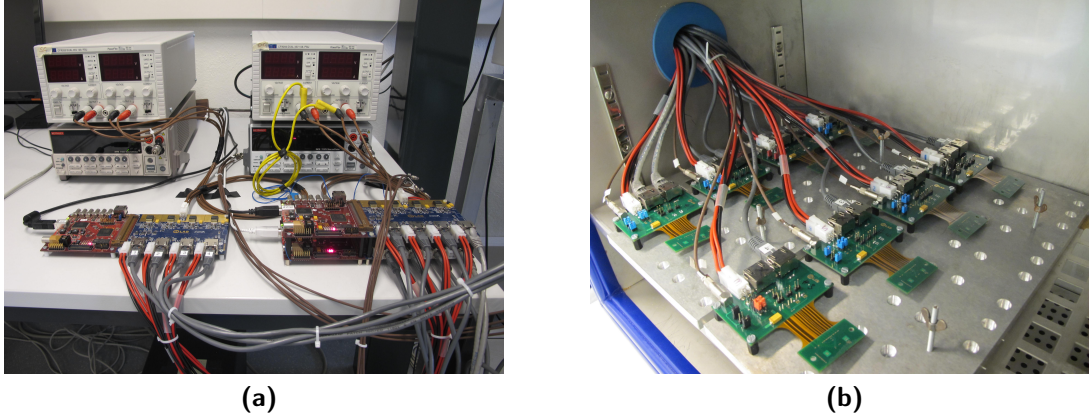


Figure 4.11: (a) The USBpix setup used for the electrical qualification of modules for single (left) and double (right) chip modules. (b) The USBpix adapter cards used for the electrical qualification of the modules.

tionality of the readout chip had been retested, checking the performance of both the digital and the analog parts of the chip. Threshold scans were as well performed, and a tuning of the chip repeated. Those steps were not meant to qualify the module, but just to check that the FE was not damaged during the transportation and it was still showing the same behavior measured at the production site. Pictures of the setup for electrical tests are shown in Figure 4.11

The electrical characteristics of the sensor were checked by means of an I-V scan, monitoring the voltage breakdown, defined as in the production site and the operational current. Fig. 4.12 shows the distribution of the measured breakdown voltage values, (V_{bd}), for the complete IBL modules population received at the loading site. The minimum V_{bd} observed for the planar sensors was 130 V and 95% of them had values greater than 200 V. For what concerns the 3D sensors, the sensors from the two producers present different performances: the breakdown distribution of the FBK production had a mean value of 42.5 V and a root mean square value of 7 V, while the CNM sensors present a flat distribution between 20 V and 105 V. The measurement of the I-V curve done at CNM consisted in biasing only the guard ring of the sensor and not the pixel array. This method did not allow to properly extrapolate the breakdown voltage value at the tile level as was done in the FBK case, where the measurement was performed on the full device, leading to a broader distribution. Fourteen CNM sensors presented a linear (ohmic) increase of current as a function of the increasing bias voltage in the explored range: in these cases the breakdown was most probably larger than the maximum voltage (100 V). No significant discrepancies had been found with respect to the production sites in terms of operational currents and breakdown voltages. In the very few cases where a lower V_{bd} value was observed, the modules were rejected.

The modules loaded on the staves were selected according to the ranking of the modules assigned at the production site and to the V_{bd} measurement.

For the reception test and for a quick check of the stave functionality, an analysis framework was developed at the loading site. The software, which includes the ROOT libraries, was largely used for example to compare the results at each stages of the staves production (before/after loading, before/after thermal cycle, etc.), to find failing pixels or just to investigate problems in a faster way.

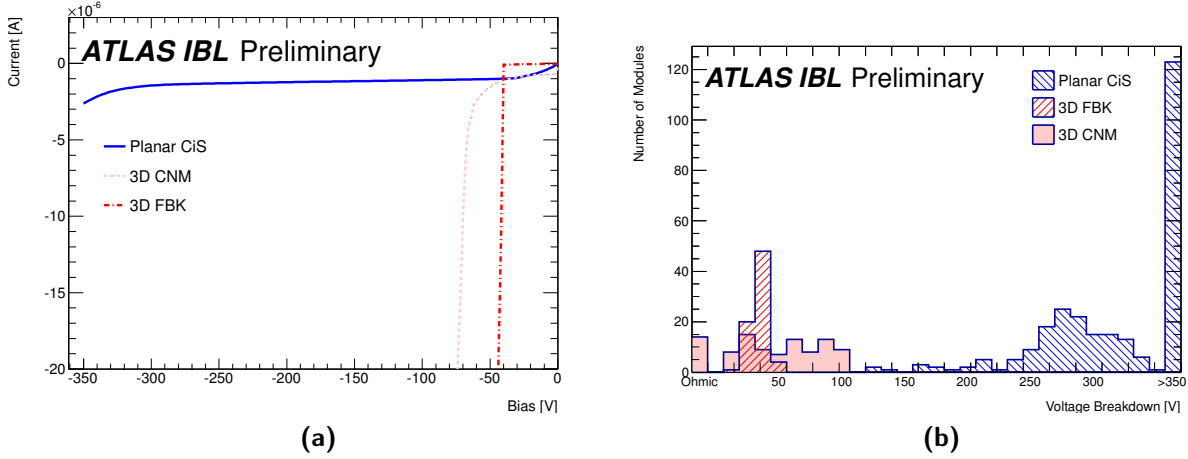


Figure 4.12: (a) Typical I-V behavior for planar and 3D sensors. A current limit of $-20 \mu\text{A}$ was used to protect the modules. (b) Breakdown values measured for all the modules.

4.6.2 Module loading procedure

The first step in the loading procedure was the selection of the 12 planar and the 8 3D sensor modules to be loaded on one stave out of the ones available in stock at that moment. Due to the fact that different sensor are powered in parallel for the HV, e.g. two planar sensors share the same HV line, modules with similar breakdown performance were chosen for the same HV sector. FBK and CNM 3D modules were not mixed in the same HV group. The strategy adopted was to choose the modules with best ranking available for the more central positions, both for planar and 3D modules.

At first the stave was positioned and aligned on the loading tool (Fig. 4.13), which provided the support and the reference points for the loading procedure, thus protecting the stave. The reference points were used for a precise positioning of the stave in the tool itself.

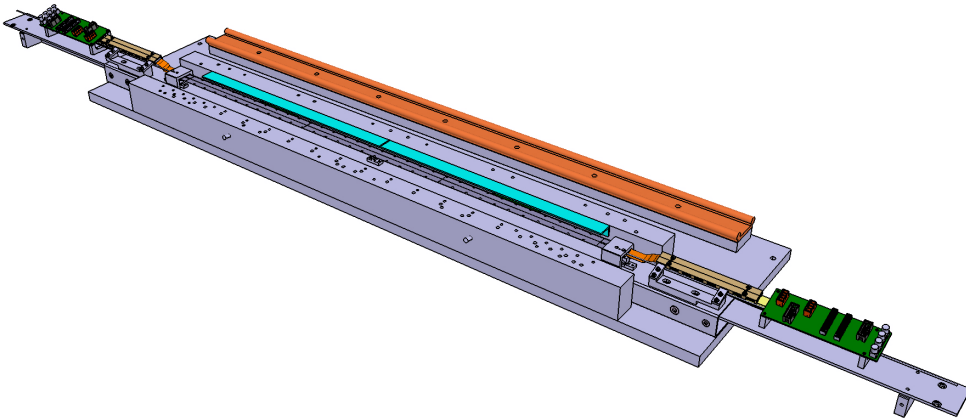


Figure 4.13: 3D CAD model of a stave and its handling frame positioned on the loading tool.

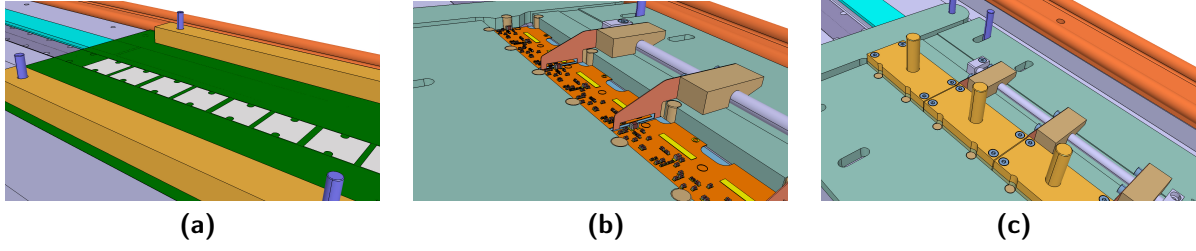


Figure 4.14: 3D representations of each of the main stave module loading steps. (a) Positioning of the aluminum mask (in green) and thermal grease application. (b) Installation of the last positioning stopper. (c) Installation of the module weights.

Once the stave alignment was performed, a 70 μm thick stainless steel mask was positioned on the stave face-plate⁴, which allowed the deposition of a ~ 70 μm thick layer of thermal grease⁵, ensuring good thermal contact between the face-plate and the module. In order to obtain sharp edges, the stainless steel shim was previously sprayed with a universal adhesive for large surface bonding produced by UHU and temporarily glued to the face-plate. The use of a mask (see Figure 4.14a) allowed two points per FE-I4 to be left clean in order to apply glue drops which will bond the modules to the face-plate.

A positioning jig with plastic stoppers was then installed to constrain the module to be loaded in the correct position. Two Araldite 2011⁶ glue drops per FE-I4 chip were then applied with a needle on the thermal grease template openings. The first module was then loaded and pushed against the stoppers while a 205 μm thick spacer was placed with a holder block. This spacer set the module-to-module distance, allowing a later insertion of an electric insulator, but also preventing any tilt angle of the module. The same procedure was then repeated for all the modules in the same half of the stave. An extra positioning tool, equipped with plastic stoppers, was used at this point, Fig. 4.14b.

Weights of 20 g were positioned on top of the modules, one for each FE-I4 readout chip, during the glue curing process (24 hours at room temperature), helping the module to properly settle on the grease layer and the glue dots contacts (Fig. 4.14c). In order to prevent any damage to the module the weight was equipped with three Teflon feet in order to leave space for the wire-bonds and the loaded SMDs. The weight and positioning tools were then removed and an optical inspection was performed for each FE-I4 electronic chip with a built-in sliding camera.

The full process was then repeated on the other side of the stave.

After the glueing of the modules to the support stave, the stave flex was glued to the module flex. A layer of Araldite 2011 was deposited in correspondence of the stave flex wings through a mask, in order to apply the glue only in the desired area. The wings were then released and positioned on the module flex (Fig. 4.15a) before installing the wing positioning tool. This tool locked the stave in its position by means of a wedge which pushed against the stave, allowing the wings to stay in their nominal position by using two clamps. All the wings were retracted and bent away to leave access to spray the glue. A weight of 16 g was

⁴Due to the tool design, the loading was done one side at a time, without any preference between A or C side. This side-to-side sequential loading was mainly due to the needed alignment tools in the central region that will overlap in the case of a parallel loading.

⁵HTCP, Electrolube.

⁶Araldite 2011, Meury Enterprises TY LTD.

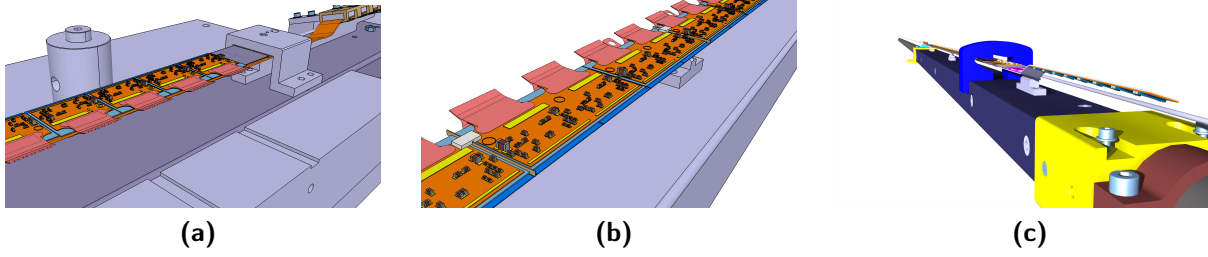


Figure 4.15: 3D representations for each of the main stave-flex wing gluing steps. (a) Wing positioning for each FE. (b) HV insulator placement and bridge gluing. (c) Stave envelope check.

then positioned on top of the wing during the glue curing process. In order to avoid any glue excess or damage to the module nor to the wing pads, the weight contact surface was covered with Teflon. Several modules in a stave are powered in parallel, dividing the stave in each powering sectors for both the HV and LV lines. This was a design choice, devoted to the optimization of the services. Once the stave was fully loaded and cured, a Kapton insulator of $\sim 100\ \mu\text{m}$ was inserted in between modules that were not sharing the same HV line for electrical insulation purposes (Fig. 4.15b). The insulator was constrained to an holder (Fig. 4.15b) glued to the module flexes, avoiding any leak of glue in the space between the module. This operation prevented to have shorts in between the modules. In order to avoid any glue between the modules, a holder was glued to two consecutive module flexes which hold the insulator. As a last step, the stave envelope was checked to fulfill the mechanical constraints of the IBL, as shown in Fig. 4.15c

For the wire-bonding operation (see Figure 4.16a), the stave and its handling frame were installed into the wire-bonding cradle. To ensure a good support and stiffness of the wire-bonded region, a shim block was positioned underneath the stave. The bond-loop height was limited to a maximum value of $250\ \mu\text{m}$. Wire Modules HV, clock, command, data output lines and powering pads were wire-bonded to the respective wing pads with $25\ \mu\text{m}$ AlSi wires. For redundancy, four wire-bonds were performed for each Low Voltage Differential Signaling (LVDS) and HV pad (see Figure 4.16b). Ten wire-bonds were dedicated to the LV and the ground to cope with the expected $0.5\ \text{A}$ current per FE. -bonds quality was tested by pull tests, performed every 2 FE on empty pads. The results of the pull tests are reported in Tab. 4.3.

Module replacement procedure A module replacement procedure was developed during the stave production period, in order to replace any failing module that was already loaded on a stave. Table 4.4 shows how many modules were reworked and for which reason. In total, fifteen reworks were performed due to modules being accidentally damaged during the module loading procedure, thus compromising the integrity of the sensor, the FE-I4 or the module flex ; five modules were replaced due to failures of the FE-I4 chip and two more modules were replaced because they had failed the QA tests performed before final integration. In addition, due to the cleaning and re-bonding intervention performed at CERN-DSF and discussed in Section 4.7.5, six more modules were replaced on the twelve re-bonded staves.

	stave 1	stave 2	stave 3	stave 4	stave 5
Mean pull force [g _F]	6.23 ± 0.78	5.70 ± 0.59	6.13 ± 0.63	5.75 ± 0.62	5.94 ± 0.43
	stave 6	stave 7	stave 8	stave 9	stave 10
Mean pull force [g _F]	6.22 ± 0.74	6.30 ± 0.64	6.23 ± 0.51	5.85 ± 0.53	6.09 ± 0.58
	stave 11	stave 12	stave 13	stave 14	stave 15
Mean pull force [g _F]	6.19 ± 0.56	6.00 ± 0.69	7.20 ± 0.29	7.26 ± 0.33	6.80 ± 0.50
	stave16	stave 17	stave 18	stave 19	stave 20
Mean pull force [g _F]	-	7.11 ± 0.41	7.03 ± 0.42	6.32 ± 0.66	5.85 ± 0.76

Table 4.3: Mean and RMS values of the wire-bonds pull tests performed on the 20 staves produced. Values for stave 16 were lost.

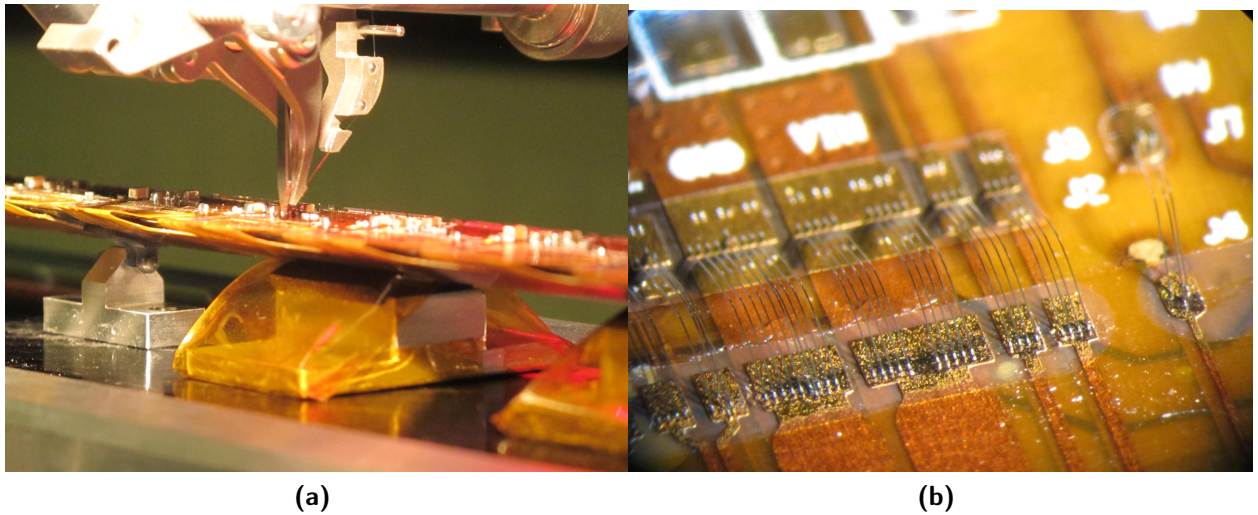


Figure 4.16: (a) Stave flex wings under wire-bonding showing the wire-bonding head and the shims placed under the stave to increase its mechanical stability. (b) Stave-to-module wire-bonds

Reason of the rework	Number of reworked modules
Failure in the loading proedure	15
Rework after wire-bonds substitution at DSF	6
FE failure	5
Failed QA	2

Table 4.4: Number of modules for each category of rework. Reworks were mainly motivated by accidents during the loading or modules re-bonds and FE failures during the early testing. A minority were replaced after the stave QA due to some failing registers.

The module replacement procedure⁷ started with the installation of two 100 μm thick Kapton spacers between the module that needed to be removed and its neighbors. Spacers of only 100 μm were placed during the module rework instead of 205 μm in order to add some margin to the module placement. The spacers maintained the distances between the modules and protected the neighboring modules. The failing module was then removed by inserting a plastic spatula in between the module and the face-plate, breaking the glue drop bonds. The face-plate was then cleaned to remove any thermal grease and glue. A new thermal grease layer was applied by using an individual mask. Once the mask was removed, glue drops were applied and the new module was placed thanks to a dedicate individual positioning tool. A weight of 20 g for the 3D modules or 40 g for the planar modules was then put on top during the glue curing process.

After the module placement, the wing gluing, the optical inspection, the envelope check and the HV insulator insertion were performed following the same procedure as for the standard loading.

4.6.3 Stave quality check at the loading site

A stave quality check was performed for each stave, aiming to spot possible damages occurred to the instrumented stave after the loading procedure and to perform aging tests. The stave quality check consisted of a metrological checks of the module position and electrical and functional tests of the loaded modules.

Both the metrical, electrical and functional tests were performed before and after the thermal cycle procedure.

The position of the modules was checked by means of a metrology machine. A pattern recognition of the sensors was performed and the x , y and z coordinates were obtained by probing the fiducial marks. The envelope checks were also repeated after the thermal cycle. The profile of each stave was as well measured during the metrological test, in order to have a complete monitoring. The results on the staves z -axis profiles are shown in Fig. 4.17 for the test performed before the thermal cycle procedure, divided between ϕ^+ and ϕ^- . During this tests the references of the metrology were the fiducial marks printed at the corner of the sensors; as a result of this two data points are taken at each module edge for each stave profile (ϕ^+ and ϕ^-).

The position of each module, measured during the process, was compared to the nominal design position. The RMS of the residual distribution was of ~ 50 μm for planar modules in both axes and ~ 34 μm in x and ~ 57 μm in y for 3D modules.

The aim of the electrical check was to spot any possible damage that may had occurred during one of the assembly, wire-bonding or metrology survey steps. A full electrical qualification of the module followed after the stave being delivered at the integration site.

The stave testing setup is schematized in Fig. 4.18a and a photo is presented in Fig. 4.18b.

During those tests the staves were powered and cooled for the first time, the stave temperature was set to 19°C. For the stave cooling, a two phase CO₂[56] system was used, in order not to contaminate the cooling pipes with other coolant liquids. The system was able to cool the staves between -35°C and 20°C , providing a maximum cooling power of about 250 W. A custom Detector Control System (DCS) was developed for the monitoring

⁷In order to avoid any repetition, only the instructions that differ from the standard module loading procedure were mentioned in this section.

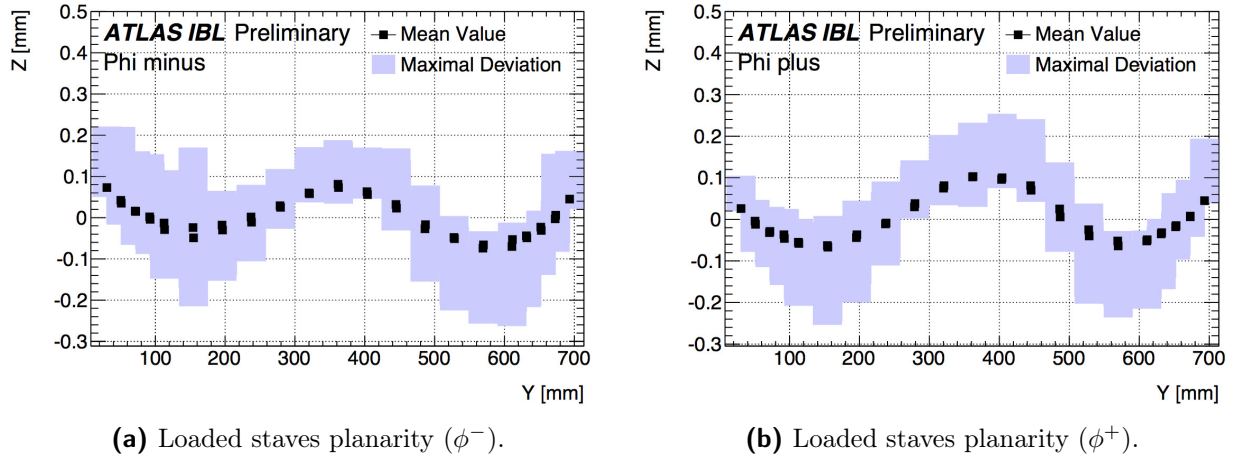


Figure 4.17: Average profiles of the 20 staves produced (black dots) along the z -axis and divided between ϕ^+ and ϕ^- . The filled boxes represent the range of values measured for the profiles.

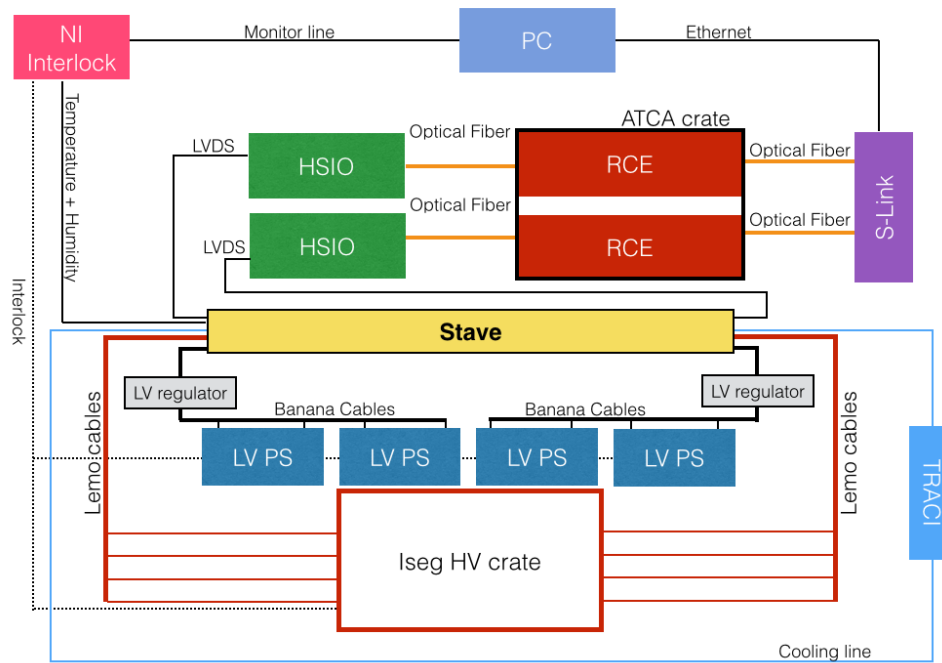
of temperature and humidity of the stave environment. This DCS was based on a National Instrument board, instrumented with humidity and temperature sensors, and LabView software. An interlock was set to prevent modules to reach temperatures above 40°C . The DCS system was capable as well of monitoring the module temperatures thanks to the NTC located on the module flex. An external Low Voltage regulator system was developed to ensure that the LV regulation does not accidentally exceed the limit of 2.4 V , in order not to damage the LDOs on the readout chip. An ISEG⁸ crate was used for the HV power of the silicon sensors. A dedicated Labview program was developed for monitoring and for interlock purposes. The software interrupted the power on a channel if the current got higher than $100\text{ }\mu\text{A}$.

The DAQ setup was made of two RCEs and two HSIO boards which communicate through optical fibers.

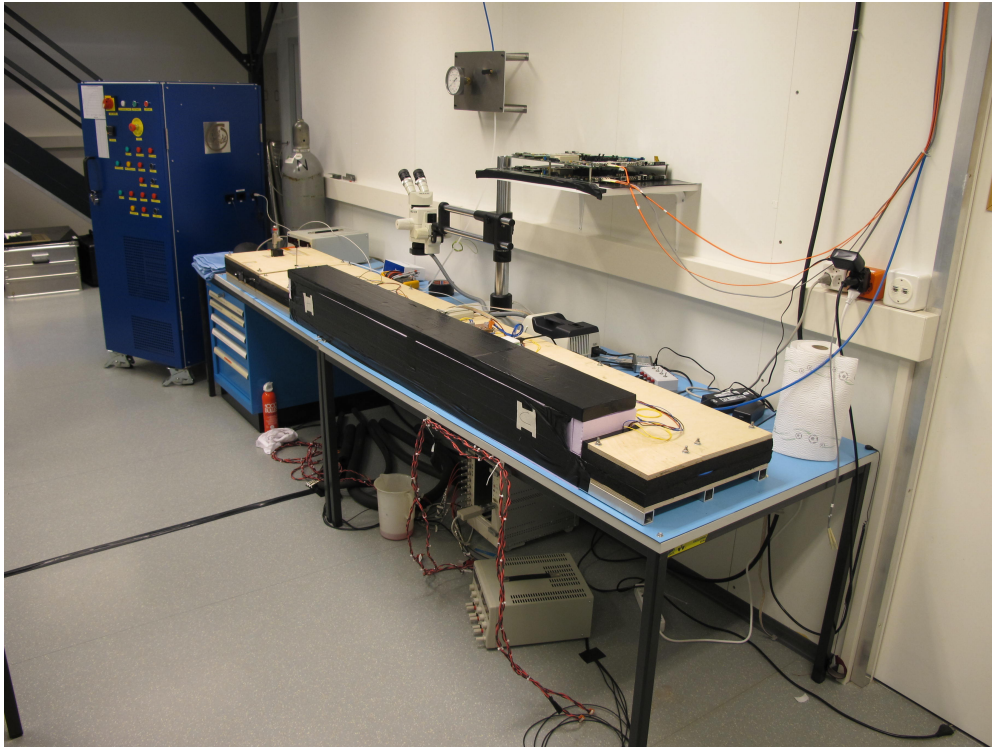
The basic electrical functionalities of the staves were verified by checking the power-up, the voltage set, the current consumption of the readout front-ends and I-V curves of the sensors. The power-up procedure was initiated after the staves were cooled to 19°C . FEs were powered with 2.2 V and then configured. The increase of the temperature and of the current consumption were monitored through the DCS. Each powering sector groups four FE-I4 readout chips, so that the current consumption of the LDOs was monitored in each of the sectors. The LV currents were monitored at the powering up of the modules and after the configuration of the FE-I4 registers. The latter operation typically increased the current consumption. The typical LDOs current consumption for a powering group was about 1.4 A at an operative voltage of 2.2 V . Part of the procedure was to perform a digital scan and an analog scan, for checking both the digital part of the FE-I4 circuitry and the analog one. For further tests on the analog part of the circuitry threshold scans were as well performed; this scan allowed also to have information on the disconnected bumps.

A threshold scan measured the equivalent noise charge per pixel (if a bump was not connected the equivalent noise had to be similar whether the sensor was powered or not). No

⁸ISEG system crates, ISEG Spezialelektronik GmbH.

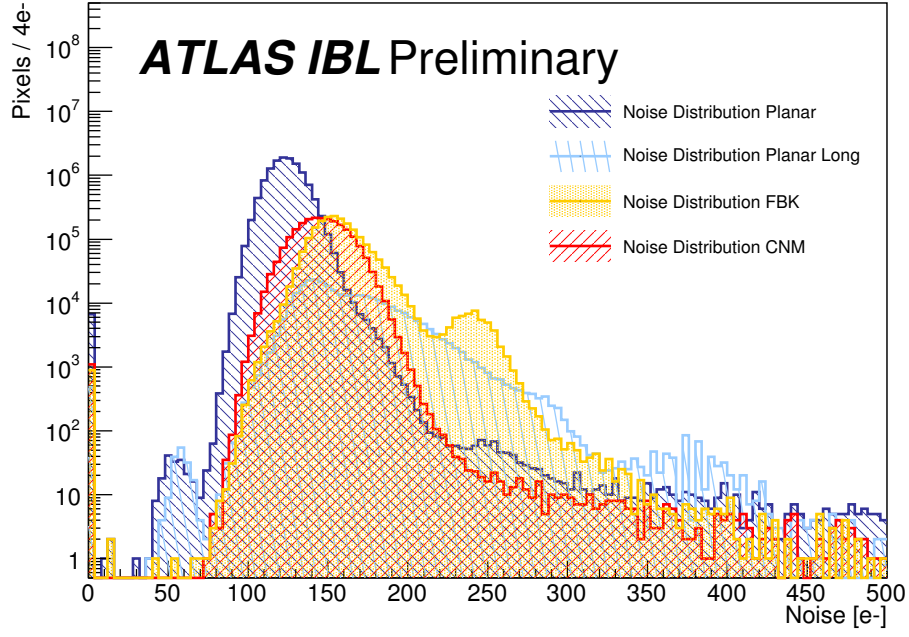


(a)

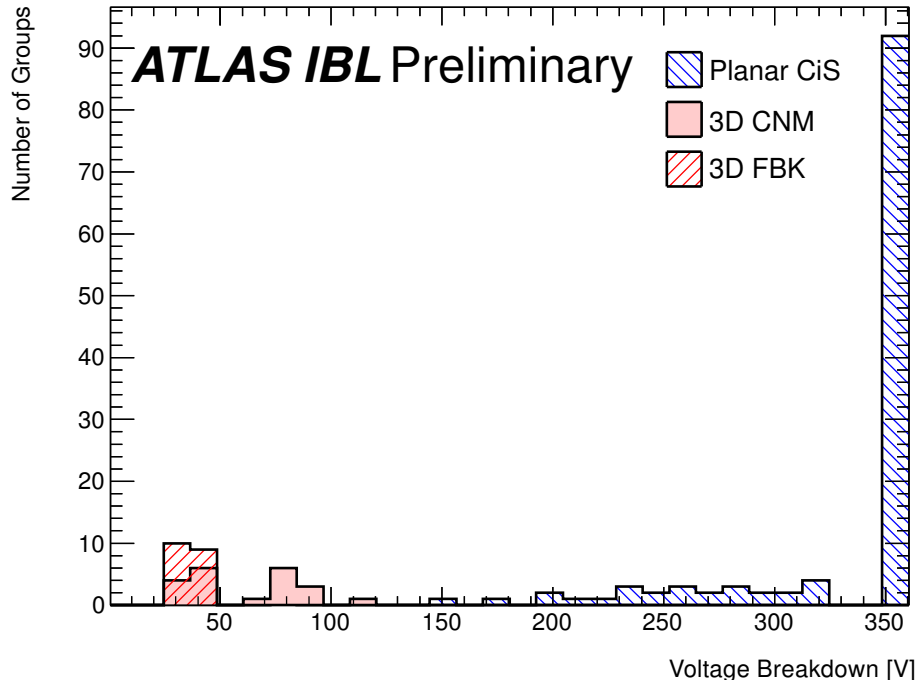


(b)

Figure 4.18: (a) Sketch of the stave testing setup, (b) Picture of the stave testing setup.



(a) Modules ENC distributions.



(b) Modules breakdown distribution.

Figure 4.19: Stave quality results: (a)Equivalent Noise Charge, ENC, of the modules loaded on the staves for each pixel technology and producer; (b) voltage breakdown values for each HV sector of the production staves, the last bin contains breakdown values higher than 350 V.

additional large area of disconnected bumps was observed with respect to the module production site measurements. This was intended to be just a check after the loading procedure, while a complete qualification with source was performed during the quality assurance.

The readout system communicated with a single FE-I4 within a module thanks to a geographical address assigned with special wire-bond logic. Most of the scan could happen as well in broadcast mode, without checking the proper address of the front-end. Setting the FE-I4 register required the proper geographical address, so that to check the proper communication a tuning of the FE-I4 chip was performed. This checks allowed also the functionality of most of the FE-I4 register to be checked [38].

In Fig. 4.19a, the Equivalent Noise Charge, ENC of the modules after tuning is shown. In this conditions the ENC mean value for planar sensors was about 130 e^- for the normal pixels, while for 3D sensors the mean noise value was slightly higher: it was 160 e^- for FBK sensors and 145 e^- for CNM sensors. The higher noise value of the 3D modules with respect to the planar ones was due to the larger coupling pixel capacitance given by the design of the 3D sensors themselves. The noise value was not affected by the loading procedure and it was consistent with the measurement made at the reception tests and in the module assembly laboratories. The I-V performance of the modules after the loading were consistent with those measured during the module reception tests. For any stave, the HV output was shared among different sensors due to the stave flex design, so the only sensor breakdown observable was the lowest in the sector. The distribution of the voltage breakdown at the stave level was shown in Fig. 4.19b.

4.7 Stave Quality Assurance at the IBL integration site

A QA at the integration site for all the produced staves was performed in order to select the best staves for being integrated on the IBL support structure. In the following text a description of the quality assurance tests and the selection criteria for the stave integration is presented.

4.7.1 Reception tests

In the stave QA test [57], loaded staves were connected to the necessary services and read-out components to be as close as possible to operation conditions in the ATLAS detector. The setup had the capability to operate two staves concurrently. The staves were installed in an environmental box, which was flushed with dry air to control the humidity to stay at less than 3%. The cooling system, as at the loading site, was CO_2 based. Most of the DCS components were Pixel Detector DCS components located in a rack close to the setup modified for the IBL operation. The DAQ was the same as the one used in the loading site. A detailed optical inspection of each stave was performed. As a first step, photographs of each module were taken with a high resolution camera and then a microscope investigation was performed. The full two-step optical inspection procedure was repeated after all remaining QA tests were completed to ensure that nothing was damaged during the QA process.

Before running calibration measurements, the basic electrical functionality of a stave was verified. This included power-up studies, verification of voltage settings and consumed currents in un-configured and configured states of the chip, as well as I-V characteristics of the sensors.

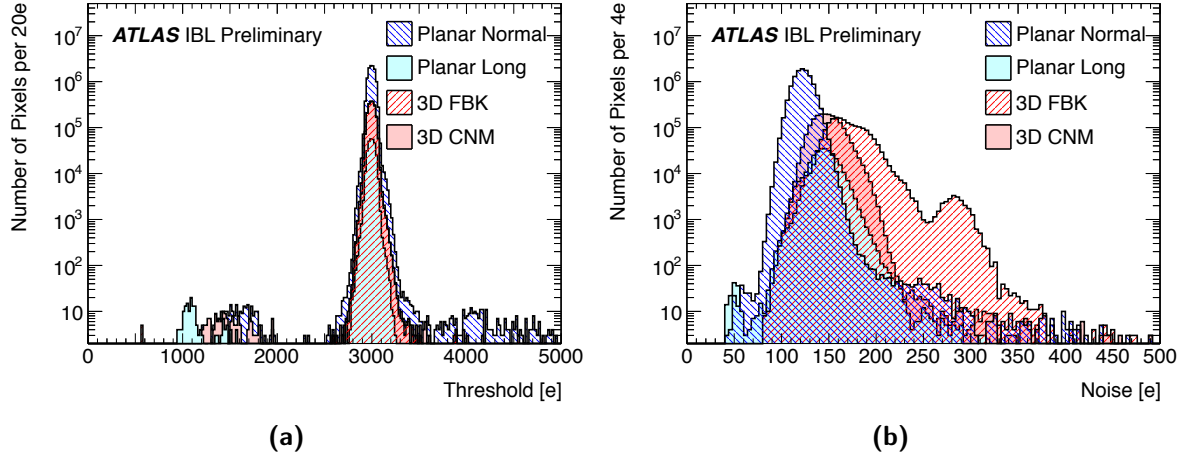


Figure 4.20: Threshold (4.20a) and noise (4.20b) of pixels for $3000 e^-$ threshold tuning at 22°C module temperature. No constraints on timing were set for the threshold measurement.

The powering behavior of the modules was tested by execution of ten LV power cycles. In the case of faulty modules, the current consumption varied significantly between cycles. The modules passed the test if the currents absorbed were below 2 A and above 0.8 A.

An I-V scan was performed for all the powering sectors. The sensor HV was ramped in 20 steps from 0 V to 100 V for 3D sensors and from 0 V to 200 V for planar sensors. The current limit for all the IV acceptance tests was $20 \mu\text{A}$.

4.7.2 Calibration and radioactive-source scan

The discriminator threshold and the Time-over-Threshold (ToT) parameters of the IBL chips needed to be calibrated and tuned to distinguish between a charged particle hit and electronic noise as well as to ensure that the signal response was uniform over all IBL pixels. The calibration is required many times over the course of the IBL lifetime to compensate for the effects of radiation damage and for changes in operating conditions. For example, the threshold had to be lowered as the charge collection efficiency decreases with increasing radiation damage. While the majority of the QA tests were performed at a room temperature of 22°C , the staves were also cooled to the Pixel Detector operating temperature of -12°C to test the calibration capabilities of the IBL chips in operation conditions. The module tunability was tested for reference thresholds of $3000 e^-$ at 22°C and $1500 e^-$ at -12°C . The ToT was tuned to 10 units of 25 ns for a reference minimum ionizing charge of $16\,000 e^-$.

Figure 4.20 shows the threshold and noise distributions of pixels for the $3000 e^-$ threshold tuning at 22°C module temperature. The $1500 e^-$ distributions, not shown, look similar. The higher noise of FBK pixels was primarily due to two modules located on staves 14 and 20 at the highest η position, the worst of which formed a small occupancy peak near $300 e^-$ noise. These staves were not chosen for the IBL and remained as backups in case of problems during integration. In both cases, the staves were tested on the bench of the QA setup and the HV bias supply line serving the 3D modules on the A-side presented a noise of 0.2 V. In general, sensitivity to such external noise is observed for all 3D modules.

The threshold-over-noise distributions of pixels for $3000 e^-$ and $1500 e^-$ tunings are presented in Figure 4.21. A threshold over noise value higher than 5 ensured that the noise

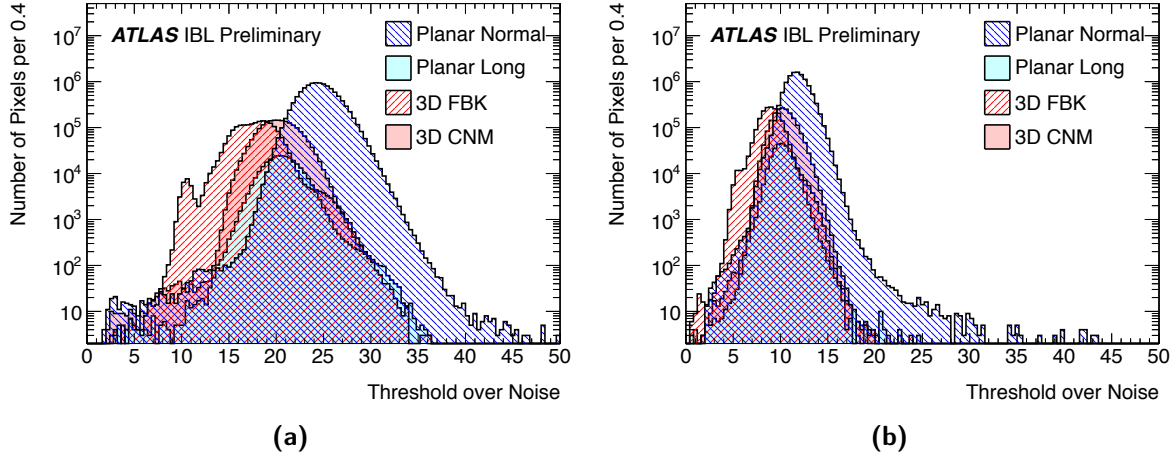


Figure 4.21: Threshold-over-noise distribution of pixels for $3000 e^-$ (a) and $1500 e^-$ (b) threshold tunings at 22°C and -12°C module temperatures.

contamination in physics hits from IBL would be less than 0.1 %. A pixel was classified as noisy when it has a noise occupancy higher than 10^{-6} , the observed fraction of noisy IBL pixels is less than 0.03 % for the $1500 e^-$ reference tuning at -12°C module temperature. The expected physics occupancy for the IBL is 10^{-3} hits per pixel per units of 25 ns in early operation and higher in later years.

The source scans were performed with two ^{90}Sr sources of 28.8 MBq each, emitting 2.28 MeV electrons, at 22°C . The FE-I4 chip was using an internal self trigger mechanism, so that no external trigger system was required. The FE-I4s were tuned at $3000 e^-$ threshold and a ToT response of 10 counts in units of 25 ns at $16000 e^-$ signal. As the source was moved over the stave, data were taken for 400 s for each chip to collect reasonable statistics for identifying disconnected bumps (~ 200 hits per pixel).

4.7.3 Pixel defects

Pixel defects can be categorized into three main “bad pixel” classes: defects pertaining to the front-end, sensor or bump bonding. A combined analysis of the calibration and source scan results makes it possible to classify each failing pixel. The failure classification is exclusive, which means that only one category of failure is used per pixel. All failure categories are listed in order of exclusion in Table 4.5, showing the category name, the scan used for identification and the specific criteria for each class.

Most of the failures rely on the module showing a hit excess or deficit. The digital and analog functionality can be directly tested with digital and analog scans, respectively. Digital and analog dead pixels are common electronic failures, while the digital and analog bad categories only appear in high numbers in case of a poor ohmic connection between pixels. The latter mainly occurred in the early prototype production of modules and was subsequently now fixed. An exception to a failing analog functionality is the identification of a merged bump. It is defined as two solder bumps connecting the sensor to the read-out chip being merged together and manifests itself in an analog failing pixel which still gives a response in a crosstalk scan. A pixel was classified as untunable if the threshold or ToT cannot be tuned at all. However a high discrepancy from the tuning target is allowed as

Failure Name	Scan Type	Criteria
Digital Dead	Digital Scan	Occupancy < 1 % of injections
Digital Bad	Digital Scan	Occupancy < 98 % or > 102 % of injections
Merged Bump	Analog Scan	Occupancy < 98 % or > 102 % of injections
	Crosstalk Scan	Occupancy > 80 % of 25 keV injections
Analog Dead	Analog Scan	Occupancy < 1 % of injections
Analog Bad	Analog Scan	Occupancy < 98 % or > 102 % of injections
Tuning Failed	Threshold Scan	s-curve fit failed
	ToT Test	ToT response is 0 or 14×25 ns
Noisy	Noise Scan	Occupancy > 10^{-6} hits per 25 ns
Disconnected Bump	Source Scan (^{90}Sr)	Occupancy < 1 % of mean Occupancy
High Crosstalk	Crosstalk Scan	Occupancy > 0 with 25 ke $^{-}$ injection

Table 4.5: Classification of pixel failures.

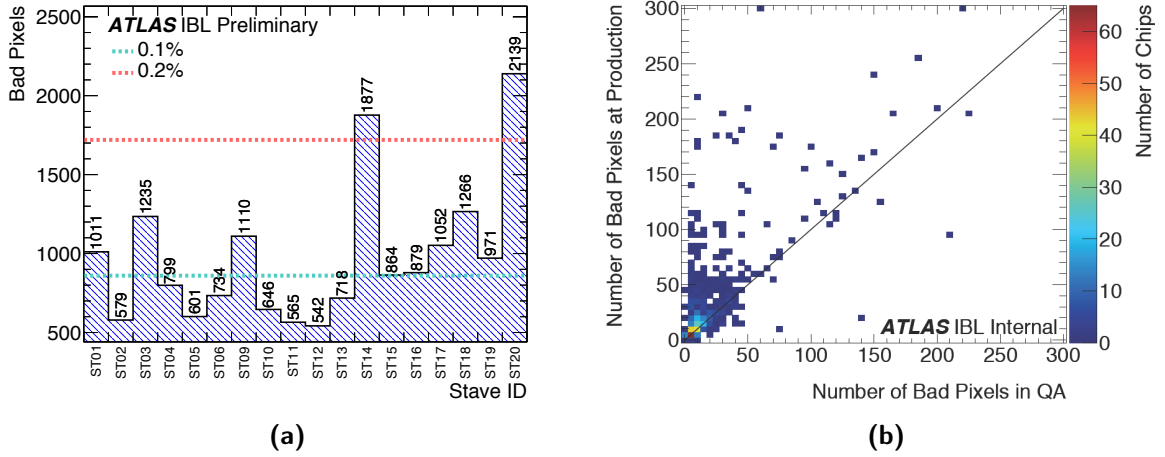


Figure 4.22: (a) Total number of bad pixels per stave for all 18 qualified staves. (b) Number of bad pixels per chip after module assembly at the module production site and after stave loading in the stave QA. In general the number of bad pixels is lower in the stave QA, which can be related to a more strict set of scans performed in the module production. A very small amount of chips have a higher amount of bad pixels in the stave QA which can be accounted for by differences in the calibration

these kinds of pixels can still be used for operation even if just to a limited extent. The noise occupancy, which shows how many hits per BC are produced due to noise, is a very important quantity for operation. A pixel gets masked for operation and classified as a bad pixel if the noise occupancy exceeds 10^{-6} hits per units of 25 ns.

All tests mentioned so far are aimed at probing the electrical functionality of the pixel. In addition, it is necessary to ensure that the read-out electronics is properly connected to the sensor, in other words to make sure that the bump connection in-between is intact. The easiest way to identify a disconnected bump, is to analyze the response from a source-scan. If a pixel shows zero or only very few hits in the source scan data, the bump is assumed to be disconnected. The last bad-pixel category, called high crosstalk, is not directly related to the performance of the pixel although a sensor pixel showing a high amount of charge sharing to its neighbors can influence the precision of the offline reconstruction.

The total number of failing pixels per stave is shown in Figure 4.22a. The two dashed lines indicate 0.1 % and 0.2 % marks; the specification requires a stave to be below 1 %. All staves are well below this cut, 80 % of staves are below the 0.2 % mark and 50 % of those staves are even below 0.1 %. About 50 % of all failures are due to disconnected bumps, the other 50 % are distributed between a pixel being analog dead or its tuning being impossible. Figure 4.22b presents the correlation of the number of bad pixels per FE detected in the module production and stave QA. A correlation can be observed. Although similar requirements to classify a pixel as bad have been used in the two test stages, during the module production the more intense tuning procedure was applied. This explains why more bad pixels are detected per FE in the module production.

4.7.4 Stave ranking

Among the 18 qualified loaded staves there was not a unique way to select and map the 14 staves to be used for the IBL. We chose the geometrical acceptance loss due to bad pixels as the main concern to select staves.

The quality of a loaded stave with respect to geometrical position inefficiency due to bad pixels can be scored with the η -weighted bad pixel fraction V defined as

$$V = \frac{\sum_{i \in \text{bad pixels}} \cosh^{-1}(\eta_i)}{\sum_{i \in \text{all pixels}} \cosh^{-1}(\eta_i)} \quad (4.3)$$

where the weight factor $\cosh(\eta_i)^{-1}$ is the geometrical acceptance of the pixel i measured in the η - ϕ ATLAS coordinate system.

A criterion was developed to select which stave select for a given position[57]. Two constraints were applied:

- the first and the last integrating staves have to have the best planarity
- the reworked and non-reworked staves for corroded wire bonds at the DSF are mapped alternately.

Table 4.6 summaries the position in the IBL loading map, the rank and other characteristics of the staves considered in the selection. Figure 4.23a compares the average bad-pixel ratio distribution as a function of η for the 14 installed staves and for the four staves not installed. The total bad pixel ratio of the integrated IBL staves is 0.07 % for $|\eta| < 2.5$ and

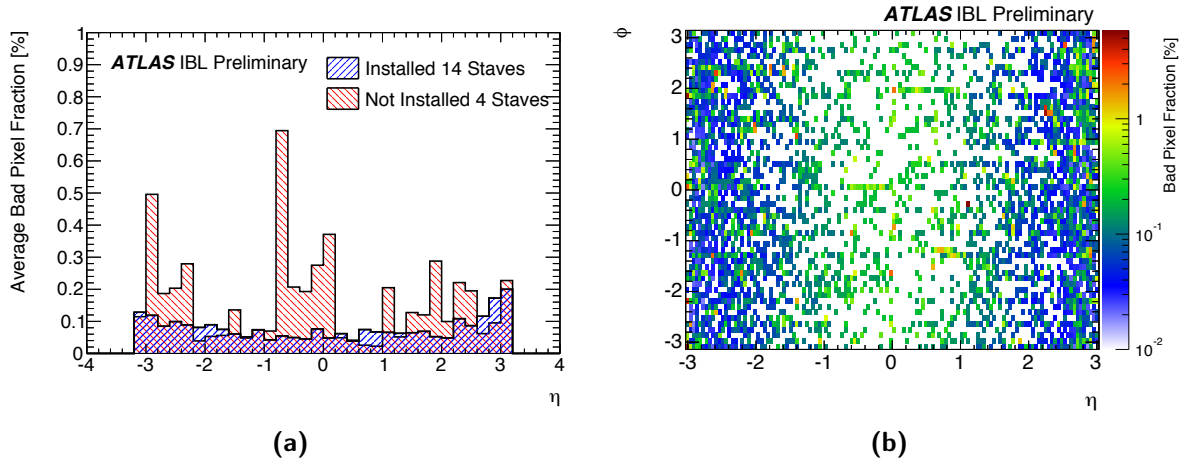


Figure 4.23: Average bad pixel ratio distribution (a) as a function of η for installed and not installed staves and (b) in the $\eta - \phi$ plane for the 14 IBL staves.

0.09% when considering the full η range. For comparison, the corresponding numbers for the four staves not installed are 0.16% and 0.18%, respectively. Figure 4.23b shows the two-dimensional distribution of bad pixel ratio as a function of η and ϕ . Stave overlap is taken into account in this plot and the ratio is computed as the number of bad pixels per total number of pixels in a unit cell.

4.7.5 Wire bond corrosion issue

During the IBL production an incident occurred with the Quality Assurance setup, for which two production staves that were under test got damaged. While the two staves were cooled at -20°C some electrical disfunctions were discovered, caused by ice building-up around the coldest part of the staves. Investigations revealed some defects and leaks of the environmental box, which was later upgraded and improved. An optical inspection was performed with a microscope on both staves and it was observed that most of the aluminum wire bonds got corroded (see Figure 4.24a) and for some of them the corrosion led to the rupture of the wire bond. The white residues or powder seen around the bond feet could be barely seen with normal incident light while it was easier to observe it with ring or raising lights. The setup used for the stave quality assurance was reviewed and qualified with prototype staves before releasing it for testing the reworked and the newly produced staves. The two staves that were damaged in the quality assurance setup were not considered for the loading on the IBL. The other staves were inspected with the same type of illumination under the microscope. A similar kind of damage was found, even though less severe. The decision was to stop the production until the origin of the problem was understood. Out of the 12 staves already produced, 11 were affected by the corrosion; the decision was to cure and rework them.

The corrosion was originated by the presence of water on the wire-bond pad of the flexes. The water was produced during the thermal cycles at the loading site and for two of the stave by an accident during the stave QA procedure. The thermal cycle was performed in a climate chamber of 1.6 m^3 . Here each of the staves underwent 10 cycles from -40°C to 40°C . The temperature and the humidity of the climate chamber volume were constantly monitored during the thermal cycle. After the discovery of the corrosion phenomenon on

Position	Stave	Number of bad pixels	Score	Planarity [μm]	Reworked
01	ST17	1052	1.01	114	no
02	ST02	579	0.44	205	yes
03	ST19	971	1.13	266	no
04	ST09	1110	1.00	229	yes
05	ST18	1266	0.94	336	no
06	ST04	799	0.69	235	yes
07	ST13	718	0.56	224	no
08	ST10	646	0.62	243	yes
09	ST11	565	0.58	298	no
10	ST12	542	0.62	314	yes
11	ST16	879	0.82	329	no
12	ST06	734	0.79	290	yes
13	ST15	864	0.84	325	no
14	ST05	601	0.68	189	yes
n/a	ST01	1011	1.04	224	yes
n/a	ST03	1235	2.48	223	yes
n/a	ST14	1877	1.11	218	no
n/a	ST20	2139	2.01	237	no

Table 4.6: Ranking and loading order overview of the 14 IBL staves. The position is sequential around the beam-pipe. The cooling pipe of the stave in position 01 is at $\phi = -6.1^\circ$, subsequent staves are displaced by 25.7° in ϕ . The score is determined by the number of bad pixels, each of which is weighted according to the position on a stave. A lower score thus translates into a higher quality stave. The planarity shows the difference between the minimum and maximum height of a stave. The last column indicates whether a stave has been reworked at the CERN DSF lab. For completeness, the bottom four lines show the data for the staves that were not chosen for installation. For the stave loading around the beam-pipe, not only this score but a uniform $\eta - \phi$ bad pixel distribution and engineering constraints were also taken into account.

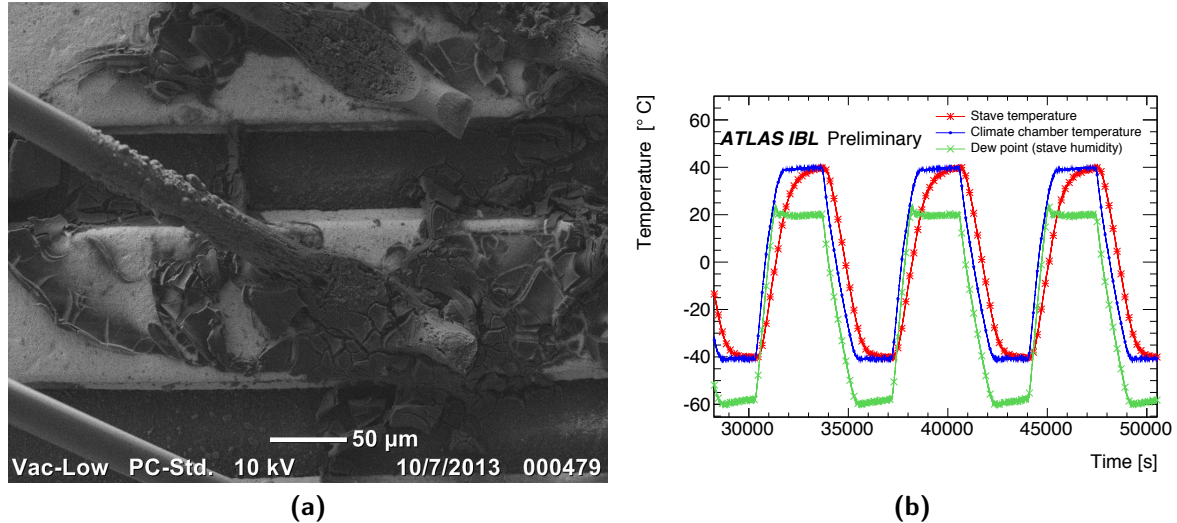


Figure 4.24: (a) Scanning Electron Microscopy (SEM) image of corroded wires and residues. (b) Temperature and dew point monitoring in the stave modules vicinity during the thermal cycling in the 1.6 m³ climate chamber.

the staves the thermal cycle procedure underwent a thorough revision. During the thermal cycle procedure each stave was embedded in a plexiglass handling frame, to protect from any accidental damage. During the revision it was observed that the temperature in the handling frame volume was different from the one measured in the climate chamber. This because of the large volume of the chamber and the fast ramp of the temperature, from -40°C to 40°C in about 10 minutes. As a consequence the dew point was reached for a couple of minutes during the fast temperature ramp-up (see Figure 4.24b). Even if the volume was flushed with dry air during the cycles and the humidity control activated, this was not enough to guarantee the absence of water condensation.

Apart from the corrosion the stave electrical and mechanical integrity was not affected, which was confirmed by electrical characterizations and metrology surveys. For the rest of the production the loaded staves were not thermal cycled. All the corroded staves underwent the quality assurance procedure after having being reworked.

Further studies were performed on module prototypes and their components to understand the chemical origin of the corrosion. IBL modules used Ni/Au pad for hosting the wire-bonds, respectively 3 μm and 100 nm thick, while the IBL wire-bond are made of Al. Au and Al form a galvanic coupling and electro-chemistry that cause ions from the anode (aluminum is the most electro-negative) to migrate to the cathode (the gold on the pad). During the ultrasonic wire bonding the friction generates elevated temperatures which remove locally the thin gold layer and the final metal contact is made between aluminum and nickel which is more stable with a lower galvanic coupling. In addition the aluminum wire is normally protected by a thin oxidation layer that is quickly formed after hours to stabilize at a thickness of about 5 nm. However this layer can be damaged in presence of water or due to mechanical or chemical attack. The corrosion residues and Al-wires were analyzed (see Figure 4.25) with an Energy Dispersive X-Ray Spectroscopy technique which revealed a level of C, O, Ca, Na, Cl, F atoms of up to few % which alone or in a molecular form can be the compounds that chemically attack the aluminum. The presence of ionic compounds suggested to improve the cleaning of the module flex after SMD assembly. The corrosion process could be reproduced

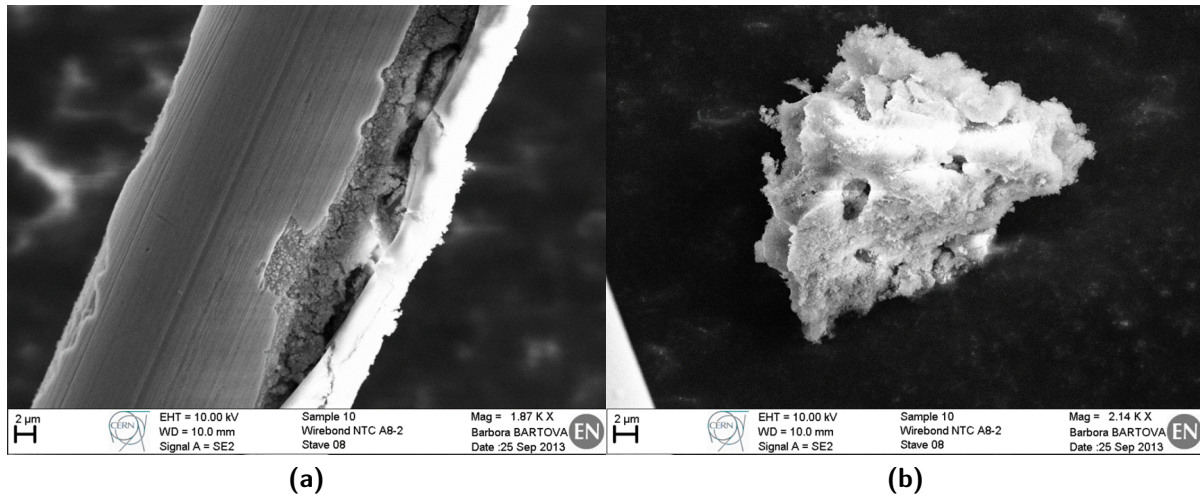


Figure 4.25: Images of a corroded Al-wire (a) and powder (b) taken from one of the corroded stave. The image was taken with an Energy Dispersive X-ray spectroscopy set-up.

easily in the laboratory in presence of deionized water on wire bonded samples. However, further investigations revealed that this process can even be observed on ultra-clean bare flex assembly. Additional cleaning process like plasma cleaning did not help to stop the observation of the corrosion phenomenon on the flex. The susceptibility to corrosion activity while the bond feet were in immersion could depend upon the cleaning and upon the origin of the flex but never disappeared. An ultimate sample analysis was done with an X-ray Photoelectron Spectroscopy and alternating the measurements and the sputtering of the gold layer with argon-ion. This method allows removing a defined and calibrated gold layer which depends upon the exposition time (0.6 nm min^{-1}). This allows measuring the atomic spectrum at the gold surface removing layers by step until reaching the Ni interface. This measurement was made for several flex circuits and for two different producers. On one sample, Fluorine was detected at a significant level (up to 14 % at 7 nm), and which could not be understood and reproduced from other flex circuits from the same producer.

4.8 Summary of the IBL construction

The construction of the IBL lasted three years and it consisted of assembly steps that involved several institutes of the ATLAS collaboration. A total of 709 FE-I4 modules were produced, 400 of them were loaded onto staves. 20 staves were produced and qualified, 18 of them were selected for the loading and 14 of them were successfully used for the IBL detector. The stave loading phase lasted one year, as shown in Figure 4.26, in which two stops happened for the investigations of the bump-bonding failure, not highlighted in the Figure, and the wire-bond corrosion. Both issues were solved and at the end of the production of an IBL detector with only 0.2% failing pixels was achieved, which was installed in ATLAS in May 2014.

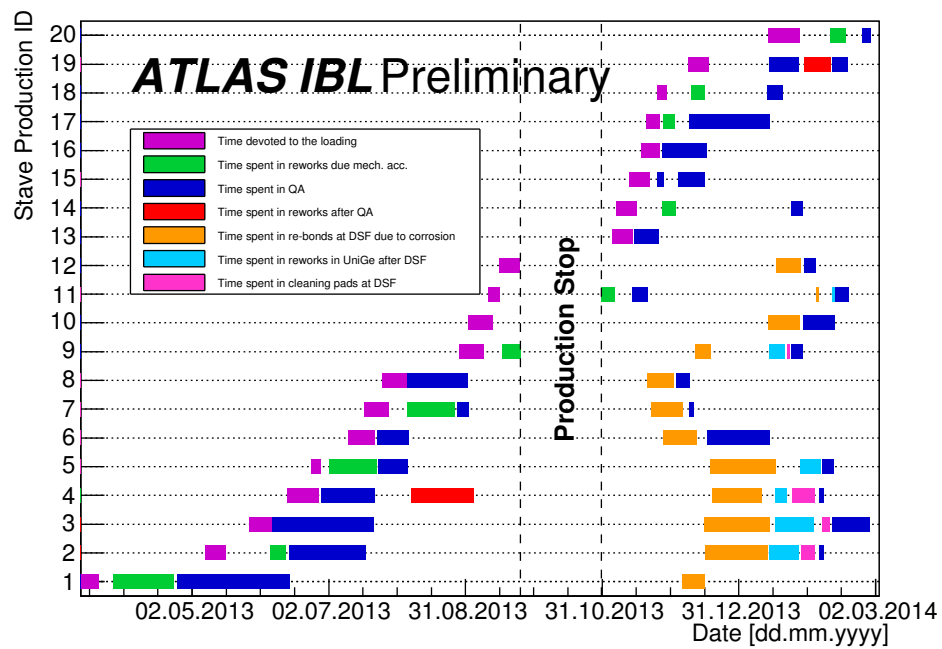


Figure 4.26: Work flow of the stave loading activity

Chapter 5

The IBL commissioning

In the following text we will refer to commissioning as the subset of tests devoted to the characterization of the full IBL detector and the optimization of its performance, including the first period of data-taking. The commissioning of the IBL can be divided in two phases the on-surface test after the assembly and the calibration after the IBL installation in the ATLAS volume.

5.1 The IBL on-surface testing

The IBL detector went through an on-surface commissioning, which consisted of two main parts: the commissioning of the services and a further test of the staves after the installation around the IPT.

As a benchmark apparatus a system test was built in order to assess an estimation of the detector behavior in operation. Prior to loading around the IST, each of the 14 selected staves was tested by means of the so-called connectivity test. This was done to verify the electrical and functional integrity of the stave components after integration onto the IPT.

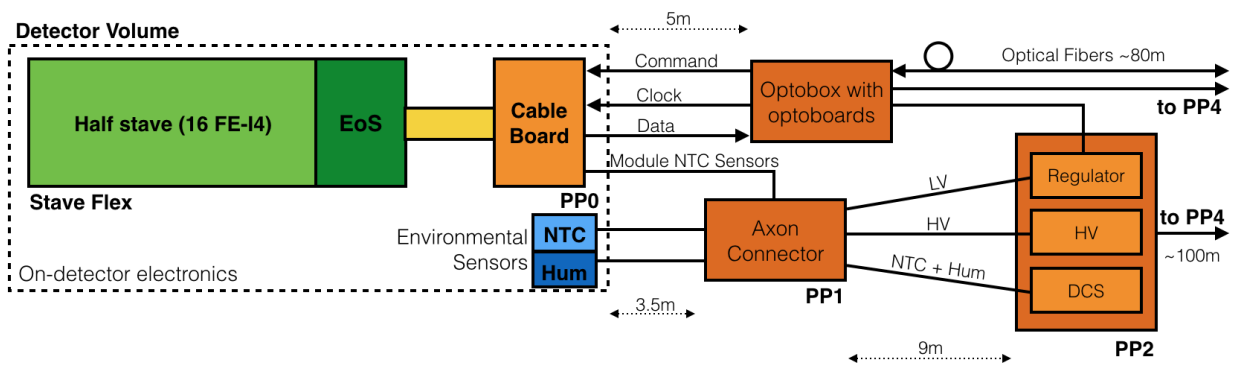


Figure 5.1: Scheme of the IBL connectivity test

5.1.1 The IBL system test

The IBL system test had the target of replicating on-surface the powering chain as close as possible to the one to be used for operation in the ATLAS detector. It was needed to

verify that the tests performed at the QA were not affected by the length of the cables or by electrical cross-talk among two adjacent staves. For this purpose functionality test and data-taking were performed mounting two staves around the IPT support. It was as well an occasion to test the full IBL readout chain before the insertion.

For this setup the two staves that were damaged during the stave QA were used, stave 7 (ST07) and 8 (ST08). Those staves were rejected for the insertion at the QA because of the accident described in the Section 4.7.5. Nevertheless these were still partially functional and they suited for the testing purpose of the setup. All services connected to the staves were production parts in order to have a realistic model of the final system as in ATLAS. Differently from the real data taking the test made use of a RCE-based readout system.

The IBL connectivity consisted of several cables and patch panels, as schematized in Figure 5.1, where patch panels are dedicated boards that rearranged the cables wrapping and in which interlocks and regulators can be embedded. Each stave was connected to the electrical services through the End of Stave (EoS) card, located at the first patch panel (PP0). Two cables come out the PP0: a 5 meter electrical cable with the FE-I4 communication and a 3.5 meter cable which took care of the Humidity and NTC information. The first cable delivered the data, the clock and the command lines of the FE-I4 chips to the boards that took care of the electrical-to-optical signal conversion, the opto-boards. These opto-boards were located in a dedicated rack, the opto-box, which took care of the cooling of the opto-boards and as well their powering. 80-meters long optical fibers connected the optobox to the readout system. The LV control lines were connected either to the second patch panel (PP2) or to the final one (PP4).

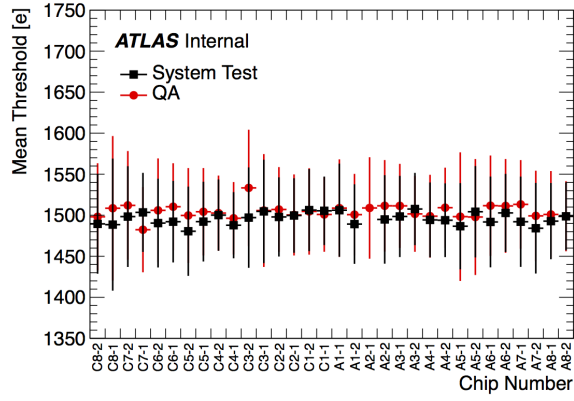
The second cable took care of the NTC and humidity sensors located in the stave volume, feeding an Axon Connector¹ which took care of the wrapping of the lines coming from the stave flex and the ones associated to environmental measurements. The HV, LV and sensor lines were then connected to the PP2. At this the stage LV lines went through regulators, to minimize the voltage drop. PP2 is crucial for the IBL monitoring, because is the closest stage to the detector in which detector monitoring can happen.

From PP2 all the electrical cables are connected to PP4, where all the power supply and the interlock system for the HV are hosted.

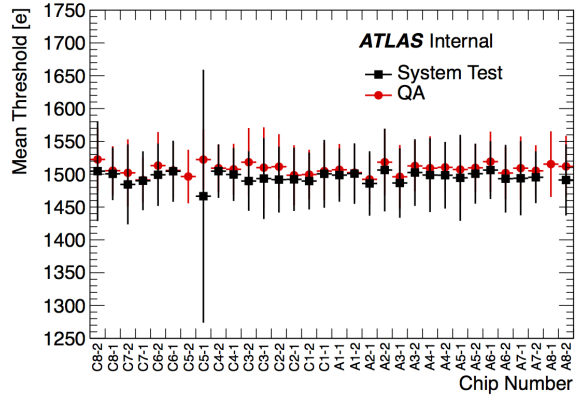
As a first step in the commissioning of the setup, a complete test of the electrical services was carried-out. This was performed by using a stave dummy load, a test board to mimic the stave power consumption and allows probing of all inputs and outputs, which was connected to PP0. This test was essential for the development of the final protocol for the commissioning of the services for both the system test and the final detector installed in the experiment. The same CO₂ cooling system as for the stave QA was used in the system test. Several measurements of the analog behavior of the modules were performed during the system test: in a first instance measurements with the existing configuration from the stave QA and then with the configuration retuned at the same threshold target of $1500 e^-$ by the system test. The main difference between the two test-stands (QA and system test) was just in the service chain. Figures 5.2a-5.2f compare the threshold values and ToT values obtained in the system test and during QA for a temperature of 0°C for staves 7 and 8. Given the 40 MHz clock in data-taking the ToT is measured in units of 25 ns, also referred as Bunch Crossing units (BC).

In Figure 5.2c and 5.2d the threshold noise distributions of both staves are showed. It can

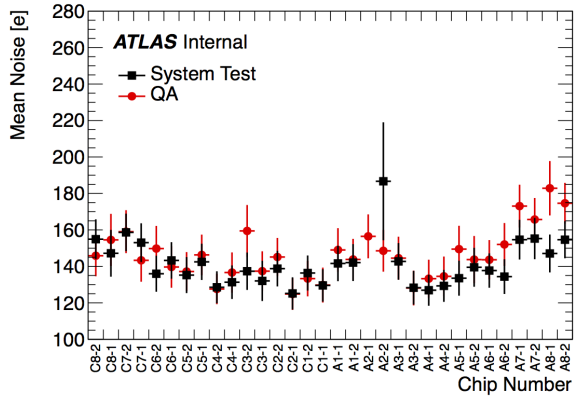
¹<http://www.axon-cable.com/>



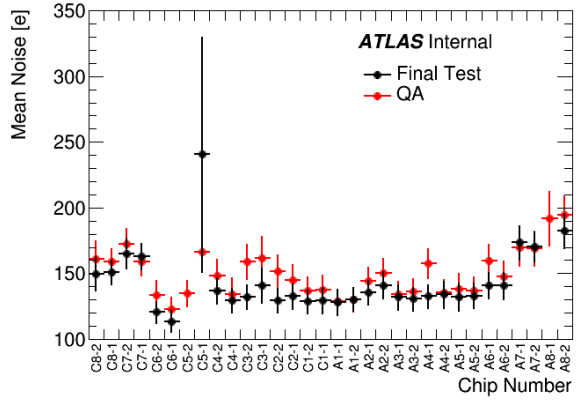
(a)



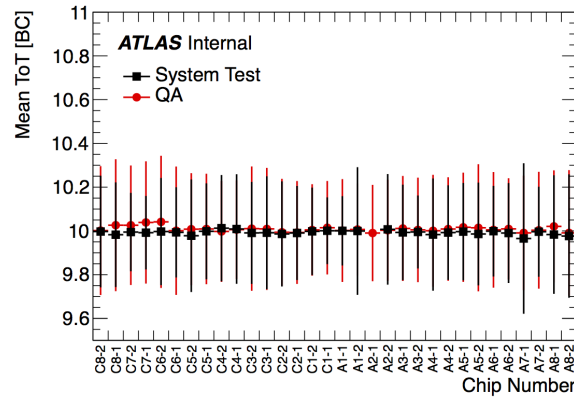
(b)



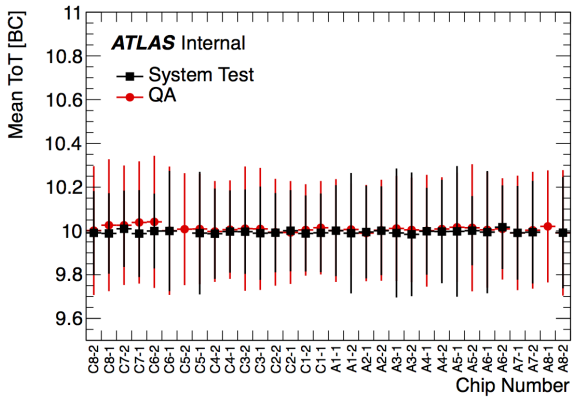
(c)



(d)



(e)



(f)

Figure 5.2: Stave ST07 (left) and ST08 (right) threshold (a,b), noise (c,d) and ToT (e,f) results. ToT measurements are reported in Bunch Crossing units (BC), which correspond to 25 ns each. It should be noted that on ST07 the FE chip A2-1 was not working due to a short between Reset and GND pads and on ST08 the FE chips A8-1 and C5-2 were not working due to broken power regulators. Therefore, they were disabled during the system test operation and only QA data are shown for them in the comparison plots.

be seen that the noise is low except for two modules that are neighboring the broken ones. The results obtained for different tunings showed excellent performance with a slightly lower and more homogeneous noise level compared to the QA, as a more sophisticated powering and grounding scheme was used in the system test.

A noise scan was performed directly after tuning, after several steps of noisy pixel masking and while running a threshold scan simultaneously on the other stave. The results show no increased noise on ST07 while a scan was running on ST08. This test confirmed that no crosstalk happened at the service level in two neighboring staves.

The system test was also used to confirm functionality of the interlock system. Both staves showed no problems during the complete duration of the system test.

5.1.2 The IBL stave-connectivity test

The purpose of the stave connectivity test was to verify the electrical and functional integrity of each stave after its integration onto the IPT and test of the services chain. Once a stave was integrated onto the IPT two sets of the electrical and functional tests was performed: one right after the stave integration and one just after having integrated its neighbor stave. In both cases, the test results were directly compared to the stave QA measurements.

Since the integrated staves were not cooled, all the scans needed to check the electrical and functional integrity were performed in a very short time (10s maximum) to prevent module-temperatures higher than 30 °C. For that purpose, the read-out system and the LV power-supply were operated by using fully automatic processes in order to minimize the time of the LV powering.

Similarly to the stave QA, the readout system of the connectivity test was based on the RCE system. The FE chips and sensors were powered by commercial and portable power-supplies, while the temperature of the environment and modules and the humidity were read out by a dedicated DCS system with an interlock on the LV power-supplies for module temperatures higher than 30 °C. All the connectivity test components were housed into a mobile rack for allowing easy movement of the system around the IBL package.

The connectivity test consisted in:

- Digital and analog tests and read-out checked of the FE-register values to check the FE functionality;
- Threshold scan without powering the sensor bias voltages to look for disconnected bumps between the sensor and the FE;
- I-V sensor measurements to cross-check the sensor voltage breakdown;
- Digital and analog-tests, threshold and ToT scans with biased sensors to cross-check the stave quality.

To operate at temperatures lower than 30 °C, threshold and ToT scans were performed with only 16 % of the FE channels on.

Figure 5.3 shows the comparison of the results of the threshold, noise and ToT values between the stave QA and connectivity test. Since cooling was not operated during the connectivity test, the noise and threshold values are larger in the connectivity test than the stave QA. In

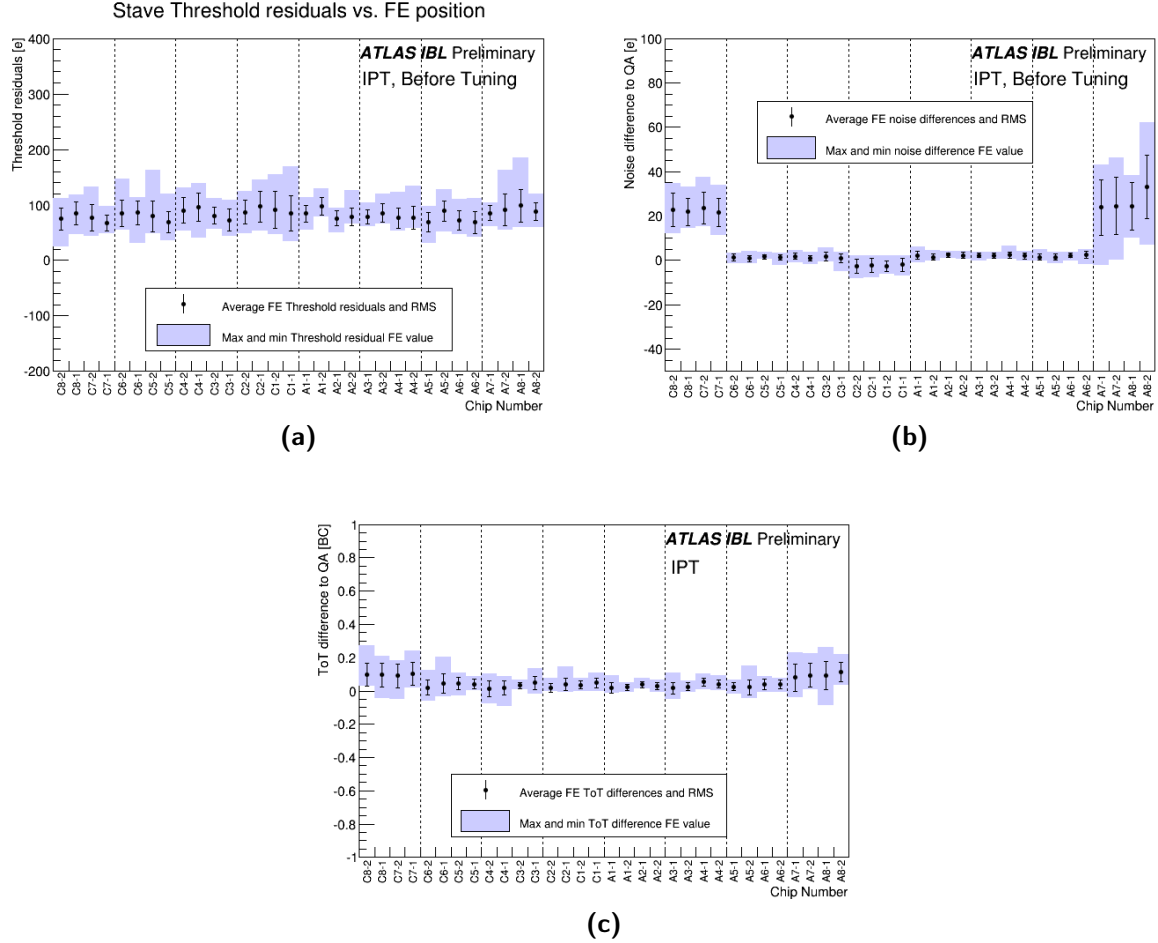


Figure 5.3: Average of the chip-to-chip FE threshold (a), noise (b) and ToT (c) difference between the obtained results with the Connectivity Test minus the quality-assurance (QA) values for the 14 integrated staves after integration around the Inner Positioning Tube. ToT measurements are reported in Bunch Crossing units (BC), which correspond to 25 ns each. Data taking was performed using the quality-assurance configuration file targeted to $3000 e^-$ and 10 ToT at $16 ke^-$. The average value and the maximum and minimum FE threshold mean values of the 14 staves are represented for each chip position by the filled area.

particular, the modules with the 3D sensors are more sensitive to the difference in temperature than the modules with the planar sensors. These deviations were not an issue since they were within the expected levels. Furthermore, no significant change in the performance was observed in the other scans.

Together with the electrical performance, the connectivity test also revealed hardware problems, such as the disconnection of a wire and a broken NTC in the type-I cable and the merged solder with the neighboring lines in the intermediate flex. They were fixed soon after the problems were found except for the broken NTC which was difficult to access after closing the IBL with the dummy IST, and it was therefore decided to leave it un-repaired.

5.2 Detector calibration after insertion in ATLAS

In order to be ready for the data-taking period, the IBL needed to go through a dedicated phase of calibration. This phase was divided in two main operations:

- the charge calibration, i.e. the tuning of the FE parameters related to the threshold and the charge to ToT conversion;
- the timing calibration, i.e. the optimization of the timing response for each front end pair, needed to maximize the efficiency in one single bunch crossing readout window.

A description of the two calibrations follows.

5.2.1 Charge calibration

Given the effects of radiation damage induced by the circulating beams, the threshold and charge-to-ToT settings of the FEs need to be constantly monitored and periodically adjusted. As discussed in Section 2.2.4, the maximum signal pulse height of a silicon sensor decreases with the integrated luminosity, while the equivalent noise charge increases, so that the threshold needs to be lowered to keep the IBL operating at high efficiency.

While lowering of the threshold allows detecting of low charge signals, it also increases the possibility that noise passes the discriminator and be treated as a real signal. Figure 5.4 shows the noise occupancy per bunch-crossing per pixel for different threshold settings. The measurement was done for the two different sensors technology: planar (PPS) and 3D sensors. The measurement was performed averaging over 3×10^8 triggers.

At the beginning of the data-taking a conservative value of 2500 electrons was chosen as target threshold; this is a starting value that will be lowered with time as the integrated luminosity will increase.

The FE-I4 threshold is controlled through the voltage generator, supplied by two different Digital to Analog Converter (DAC), the TDAC, a 5 bit register for local threshold tune, and a 16-bit DAC (GDAC) register, for the control of the global voltage V_{th} provided to the generator. The latter register is not linear, and there are two 8-bit values for the coarse and the fine threshold adjustment. The characterization of the threshold control parameter was performed before the assembly. Figure 5.5a shows the threshold as function of the GDAC parameter with the typical non-linear behavior, while Figure 5.5c shows the threshold as function of the TDAC.

Threshold is measured taking as reference the charge injected with the pulser circuitry. A

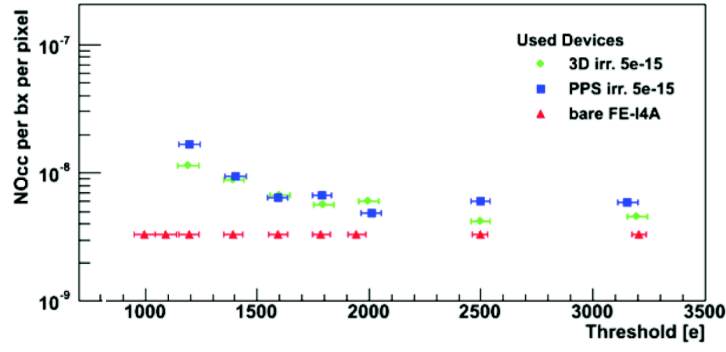


Figure 5.4: Noise occupancy per bunch crossing per pixel vs. the FE-I4 threshold. The noise occupancy measured for planar (PPS) and 3D assemblies after irradiation to $5 \times 10^{15} n_{eq}/cm^2$ and cooled to $-15^\circ C$. Dead pixels were excluded from the measurement. The measurements are compared to the noise of a stand-alone FE-I4 [Rubinskiy]

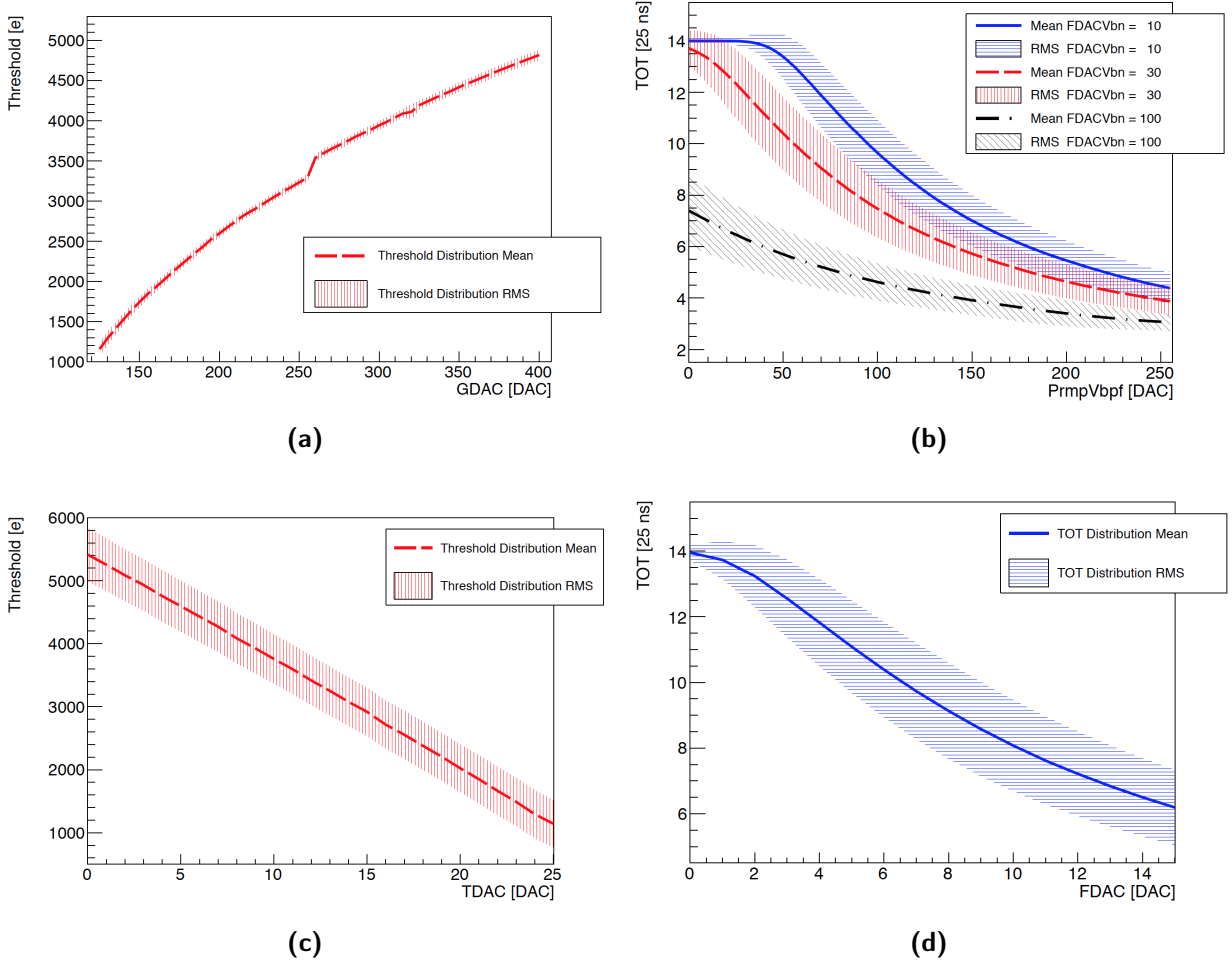


Figure 5.5: (a) Threshold as function of the global settings. (b) TOT response as function of the global feedback current. (c) Threshold as function of the pixel level threshold setting. (d) TOT response as a function of the pixel level feedback current setting. Plots are taken from [54]

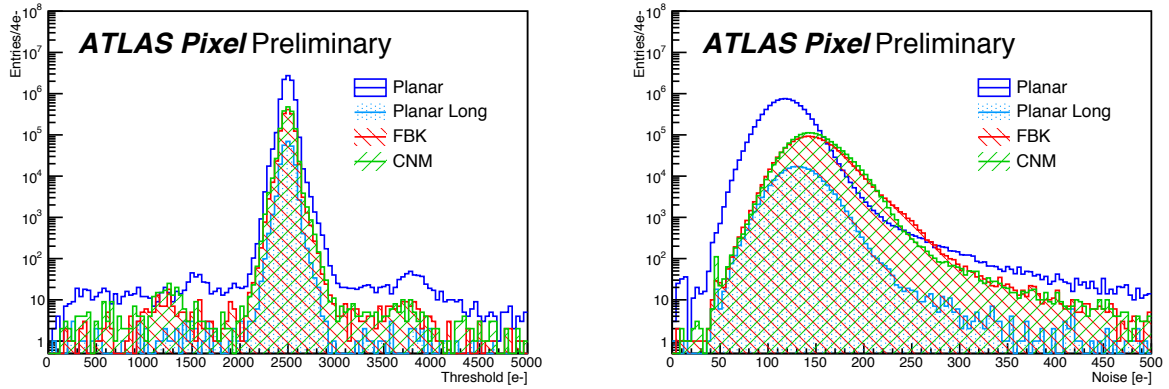


Figure 5.6: Noise and the Threshold distribution of the IBL detector pixels.

precise measurement of each injected capacitance was performed and the values obtained was stored in the module configuration file for each FE chip. Details about the calibration of the pulser injection circuitry can be found in [54]. For the ROD-BOC system used for operating the detector in the ATLAS environment the binary search algorithm for the GDAC tuning needed to be developed.

The binary search algorithm begins by comparing the target value to the value of the middle element of the range of a specific FE register. If the target value is equal to the middle element's value, then the register is set and the search is finished. If the target value is less than the middle element's value, then the search continues on the lower half of the array; while if the target value is greater than the middle element's value, then the search continues on the upper half of the array. This process continues, eliminating half of the elements, and comparing the target value to the value of the middle element of the remaining elements, until the target value is found. The new method reduce of a factor 15 the time spent for the procedure with respect to the old method which was scanning the GDAC parameter with a fixed step size. Figure 5.5a shows the Threshold as a function of the GDAC parameter. Figure 5.6 shows the map of the mean value of the noise and of the threshold at the pixel level. It can be noticed that the 3D modules have a larger noise; this is due to the larger capacitance of the electrode structure of the 3D sensors have a larger capacitance. It should be noted that capacitance is the main source of noise for not irradiated sample, while after irradiation the leakage current will be the dominant contribution. The 3D detectors therefore will have a smaller leakage current contribution and will be less noisy after large irradiation fluences.

The control of the ToT is provided by the feedback current of the PreAmp. When a negative charge is deposited at the input, a positive charge appears at the output of the Preamp. In an ideal system, the voltage amplitude of this pulse would be $\frac{Q_{in}}{C_{f1}}$ (see Figure 3.10a), but because of the fast shaping (i.e. fast return to baseline) the amplitude will be less. The faster is the shaping the smaller the pulse amplitude will be for the same input charge. The return to baseline is implemented by a feedback system which discharges the capacitor C_{f1} with an almost constant current source. The negative pulse at the output of the second amplification stage feeds the negative input of the comparator, with a threshold voltage at the positive input. The time that the signal will spend over

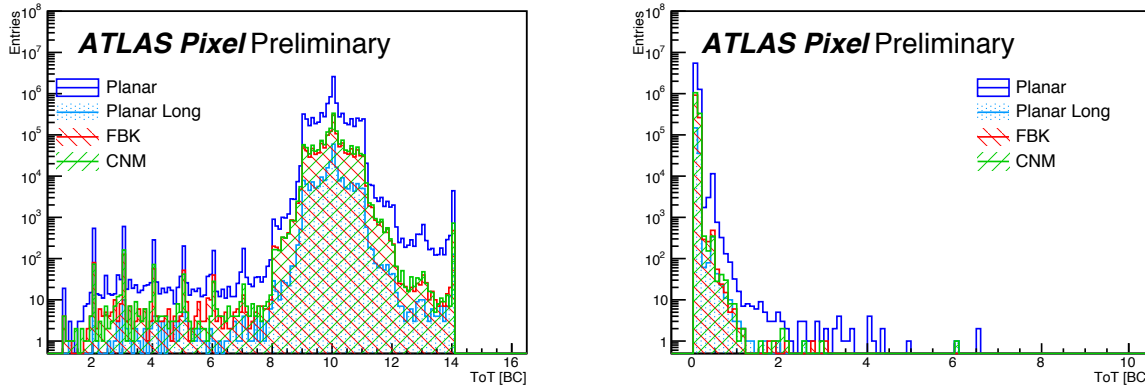


Figure 5.7: ToT and RMS of ToT distribution for the IBL detector with an injection charge of $16000e^-$

threshold is then controlled by the feedback current of the PreAmp, which sets the fall time of the preamp output. This can be tuned with a local 4-bit register (FDAC) and 8-bit global register (PrmpVbpf). The ToT characterization with respect to the PreAmp feedback current is shown in Figure 5.5b for different values of the local settings. The step width of $FDACV_{bn}=30$ was chosen as starting point for all the IBL modules. During the IBL commissioning a campaign of tuning was performed targeting for a uniform threshold of 2500 electrons and a correspondence of 10 ToT for an injected charge of 16000 electrons, the results of the tuning are shown in Figure 5.7.

The radiation damage not only affects the sensor performance, but also, the operation of the several transistors in the FE-I4 chip. In particular the leakage current and the intrinsic threshold of each transistor are affected as described in Chapter 2. The net effect is an influence on the FE-I4 threshold and ToT. The mean threshold of each FE will increase with irradiation and the ToT will lower, as shown in Figure 5.8. Given this effect, the detector needs to systematically go through the tuning procedure. The effect is expected to saturate after few Mrad of total ionizing dose.

5.2.2 Timing optimization

A tuning of the FE settings was required to operate the IBL in one bunch-crossing time window. The data-taking system of the IBL uses a double-chip module logic, so it considers a module as composed of 2 FE chips, regardless the distinction done in the previous chapters. This choice was done to simplify the data-taking chain, in terms of software and firmware. In the following text such choice will be referred to as DAQ module. The response of each of the FE needed then to be synchronous with the other FE in the same DAQ module. As the data-taking chain cannot apply a correction for a single FE, the timing adjustment needed to be done at the level of the readout chip electronics. The response time of the analog part of the chip can be modified through the 8-bit discriminator bias register, $DisV_{bn}$. Figure 5.9a shows the FE latency as function of the $DisV_{bn}$ parameter for two readout chips in the same DAQ module. The tuning strategy was then to fix the $DisV_{bn}$ for one of the FE and to adjust the value for the other chip in order to minimize the latency among the two. The

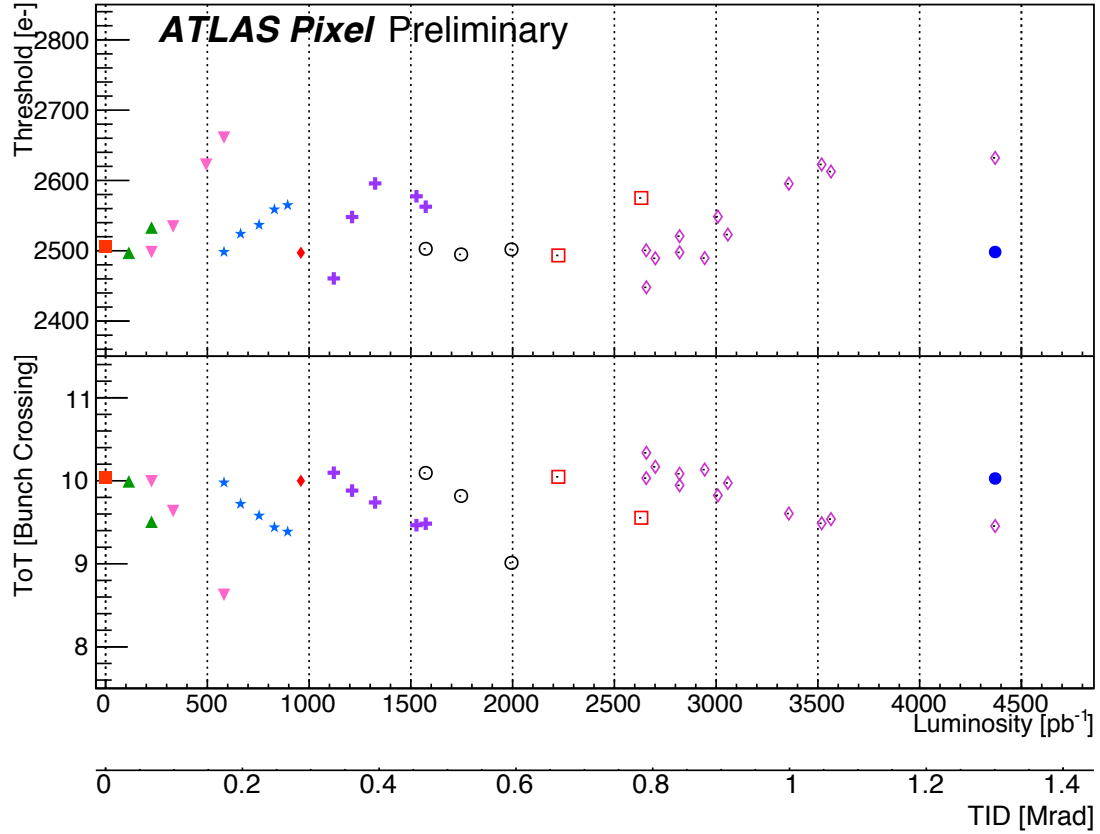


Figure 5.8: The evolution of the mean threshold and the mean ToT measured for all pixels in the IBL detector as a function of the integrated luminosity and the corresponding total ionizing dose (TID) in 2015. The measurement was obtained in calibration scans. The threshold was tuned to 2500 electrons. Radiation effects caused the measured threshold to drift upward with integrated luminosity, but short periods of annealing and regular re-tuning brought the mean threshold back to the tuning point. Each series of the measurements indicated by the same symbol shows consecutive measurements, while the change of the symbol indicates a re-tuning.

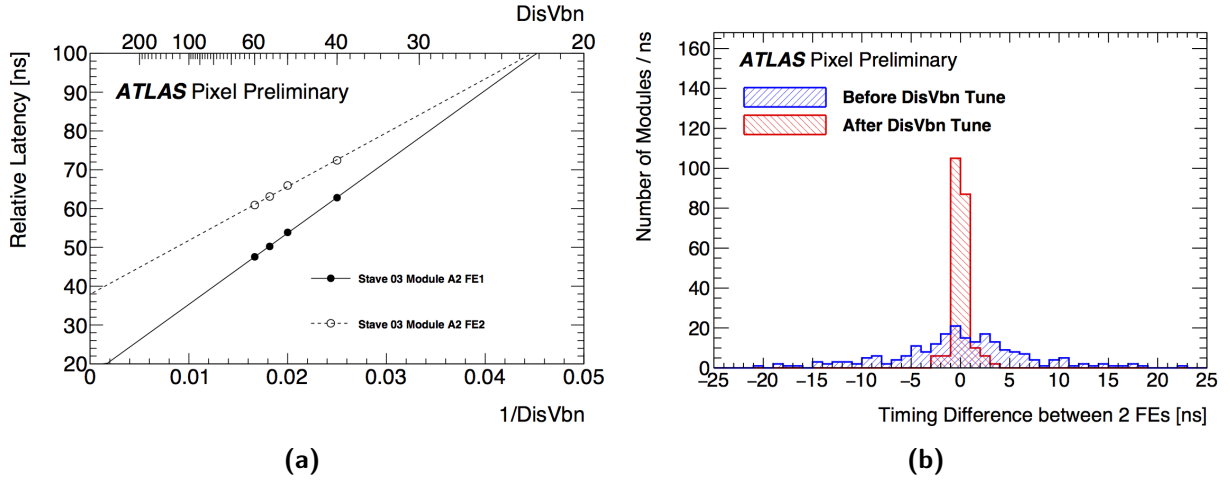


Figure 5.9: (a) Variation of the latency of the two FE chips of a particular DAQ module of the IBL as a function of the FE-I4 configuration parameter DisVbn to change the discriminator bias.(b) Timing difference between the 2 FEs in the common module of the IBL before and after the discriminator bias (DisVbn) adjustment.

timing difference between two FE chip in the same DAQ module is shown in 5.9b before and after the DisVbn adjustment. The maximum time difference for a DAQ module is 4 ns after the tuning.

The FE time response is not constant with respect to the signal charge, due to time-walk of the analog amplifier in the readout chip. Even if the signal coming from the sensor has usually a rise time of the order of a nano-second, in case of low charge signals the output of the amplifier could take few dozens of nanosecond to reach the threshold of the discriminator. In the case of the FE-I4 this happens for signals just above the threshold of the discriminator. Figure 5.10a shows the time-walk for a single pixel, tuned at 1485 electrons threshold and with a correspondence of 9 ToT for a charge of 16000 electrons; it can be seen that a signal just above threshold require up to 35 ns to pass the threshold. This led to a small efficiency in the low ToT regime even after a DisVbn tuning, as shown in Figure 5.10b. The FE-I4 can discriminate hits of different sizes in order to associate low ToT hits with the correct bunch crossing in spite of time-walk. This feature is controlled by the HitDiscCnfg register. When HitDiscCnfg is set to zero, this disables any small/large hit discrimination and any time the comparator fires this is counted as a hit occurring in the bunch crossing that the comparator fires. As Figure 5.10a shows, for hits close to the threshold the firing of the comparator is delayed due to time-walk and therefore such hits will appear in the wrong bunch crossing. Setting the HitDiscCnfg to 1 (2) means that only hits with ToT greater than 1 (2) clocks are counted as stand-alone hits in the bunch crossing the the comparator fires. Because those signals are significantly above threshold, they are hardly affected by time-walk and so they appear in the correct bunch crossing. Signals with TOT less than 1 (2) are only discarded if they occur in isolation (no other signals in their vicinity). Otherwise, they are counted in the same bunch crossing as any neighbor big hits, within an association window 2 bunch-crossing wide. Figure 5.10b and 5.10c show the efficiency for different ToT values. Two situations are considered, HitDiscCnfg set as 0, for which the short signals efficiency is very low, and HitDiscCnfg set as 2, for which the efficiency is above 90% . The tests were performed in different period, and at the time of the test with HitDiscCnfg = 2 there were

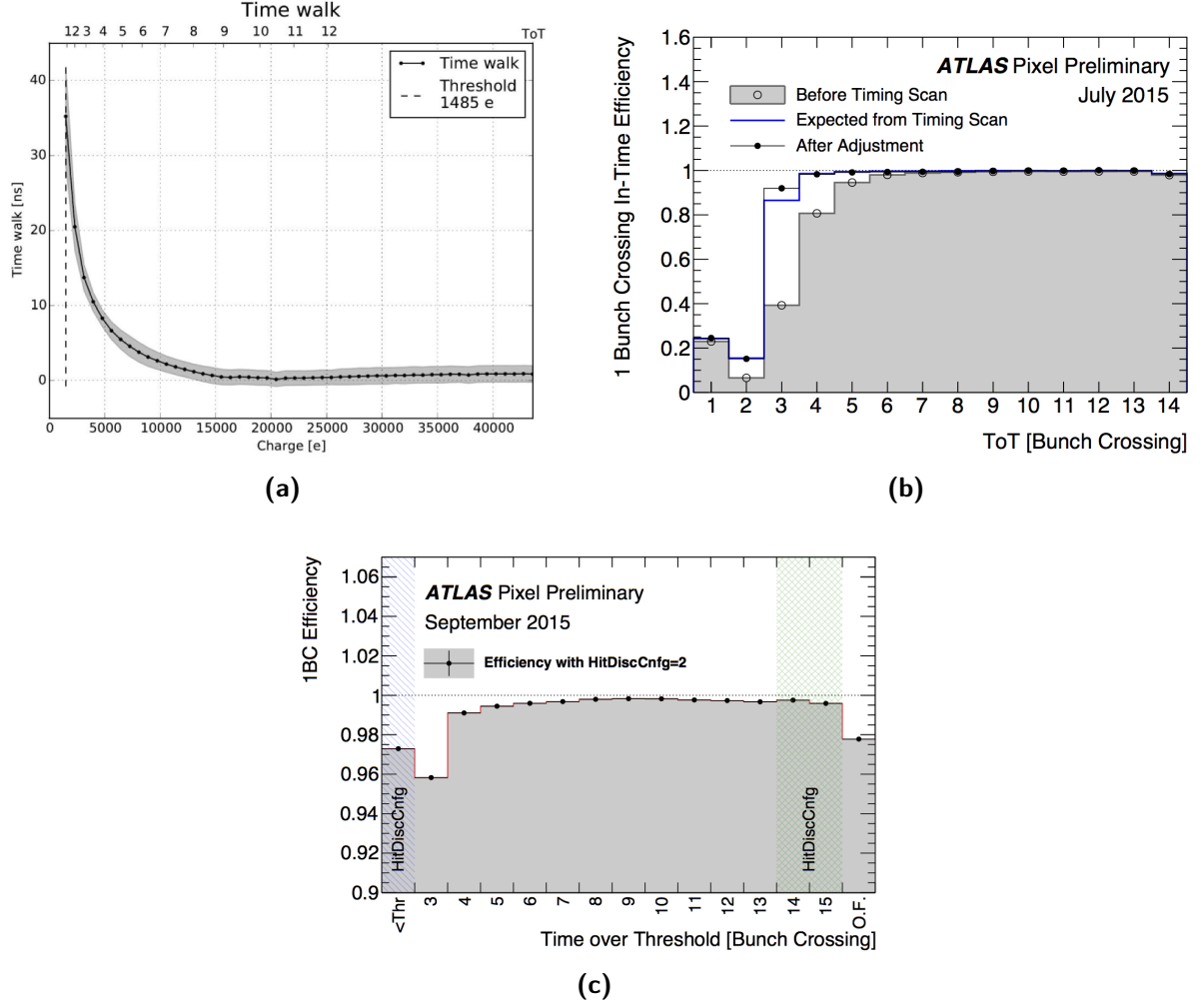


Figure 5.10: (a) Timewalk for a single pixel tuned at a threshold of 1485e⁻ and a correspondence of 9 ToT for an injected charge of 16000 electrons [58]. (b) 1 BC In-Time efficiency of the IBL as a function of ToT before (open dots), and after the timing adjustment (bullet) where HitDiscCnfg is set to 0. (c) In-time efficiency of the IBL as a function of time-over-threshold (ToT) with setting HitDiscCnfg to 2. The measurement of the in-time hit efficiency shown in this plot was performed using a special condition run with expanding the readout window from 1 BC to 3 BCs in September 2015. In this HitDiscCnfg mode, low time-over-threshold (ToT) hits of ToT=1,2 is combined in "< Thr" bin (blue band) with also copying the hits in the next bunch crossing to the triggered bunch crossing. As a by-product of HitDiscCnfg switch, the ToT dynamic range is expanded from 13 to 15 (green band). The "O.F." bin represents the overflowed hits with ToT greater than 15.

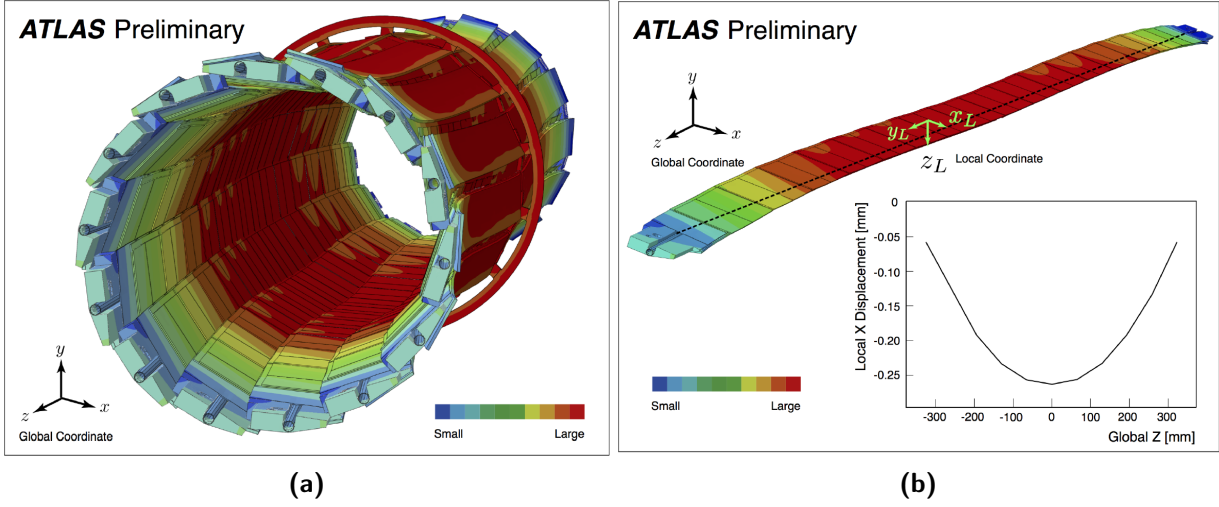


Figure 5.11: 5.11a Full package of the IBL staves with the central ring simulated by the 3D FEA representing the distortion. The size of the distortion is magnified for visualization. The color represents the relative size of the local displacement. The temperature is set at $T = -60^\circ\text{C}$ uniformly from the nominal temperature. The distortion is magnified by a factor 20. 5.11b Visualization of the distorted stave with magnified distortion size. The size of the distortion is magnified for visualization. The color represents the magnitude of the displacement. The right bottom graph shows the relative displacement size in local-x direction as a function of the global z position at the face plate of the stave.

also improvements in the transmission-line fine-delay setting that led to an improvement in the efficiency even for $\text{ToT} \geq 3$.

5.3 The IBL mechanical stability

During the commissioning and alignment of the IBL using cosmic-ray data, a mechanical distortion of the IBL was observed. This distortion is caused by a difference in the coefficients of thermal expansion (CTE) of the IBL stave components. In particular a difference between the flex services bonded to the stave and the stave itself. A three-dimensional finite element analysis (FEA) was performed to understand the observed large distortion of the IBL staves. The model is 14-fold symmetric around the beam pipe and considers the detailed structure of the staves. The FEA implements the constraint due to the central ring and mechanical boundary conditions at screws, alignment pins and glues. A uniform temperature is assumed over the full package of the IBL in the calculation. The FEA simulation shows that the stave bows to the negative direction in the ATLAS global coordinate system when it is cooled down (Figure 5.11). The CTE of the bare stave is almost zero ppm, while the polyimide flex bus line (Stave Flex) glued on one side of the bare stave is several tens ppm. The Stave Flex shrinks more than the bare stave, generating the bowing of the stave in the azimuthal direction. The FEA simulation also predicts radial distortions other than the region around the central ring. The FEA simulation calculates that the magnitude of the bowing is expected to be approximately parabolic in the azimuthal direction with the maximum at the center of the stave (Figure 5.11b). At $T = -60^\circ\text{C}$ the magnitude of the displacement is calculated

to be about 270 μm at the center of the stave.

5.3.1 Measurement of the bowing and thermal stability

In order to study the correlation to the temperature of the size of the IBL distortion, cosmic-ray events were collected in March 2015 at different temperatures: 15 °C, 7 °C, 0 °C, −10 °C, −15 °C and −20 °C. To quantify the size of the IBL distortion, track-based alignment corrections [59] were applied to determine the positions of the IBL modules as well as their geometrical distortions relative to the nominal geometry. More than 5×10^5 cosmic-ray events were taken at each temperature with both the toroid field and the solenoid field on. The trigger for cosmic-ray events was the Fast-OR trigger of the TRT, a hardware-based logical OR of the TRT wires having a hit along a likely muon-track path. The trigger efficiency was above 90% [60] and the average acquisition rate 4.84 Hz. Tracks were reconstructed from hits measured by three subdetectors: the Pixel Detector (including the IBL), the SCT, and the TRT. 17% of Fast-OR triggered events were used in the distortion studies after a series of track quality cuts:

- $N_{Pixel} + N_{SCT} \geq 4$: at least four silicon hits;
- $N_{TRT} \geq 25$: at least 25 hits in the TRT;
- $p_T^{trk} \geq 2 \text{ GeV}$: 2 GeV threshold of the transverse momentum.

The $p_T^{trk} \geq 2 \text{ GeV}$ is applied in order to reduce the impact of multiple scattering in the traversed material. The unbiased track-to-hit residual vector, $\vec{r}_{res} = \vec{r}_{hit} - \vec{r}_{exp}$, is used to quantify the distortion of the IBL, where \vec{r}_{hit} is the vector of measurements of the hit position in the module and \vec{r}_{exp} is the expected position according to the track fit. Both are defined in the local coordinate system² of the module registering the hit. The residuals were unbiased, since the hits on a certain module were removed from the track fit before computing the track-to-hit residual. To demonstrate the distortion effect due to temperature variation, a set of initial alignment constants with the ideal geometry for flat staves was used as the reference constant set for the track reconstruction. There was also a global alignment for the whole IBL as a rigid body, to account for global displacements of the IBL with respect to the other ID sub-detectors; there were a total of 3 degrees of translation and 3 degrees of rotation for the IBL. This initial alignment corrections [59] were derived from the cosmic-ray data collected in February 2015. Using cosmic-ray data collected in March 2015, the magnitude of the distortion was found to depend linearly on the operating temperature of the IBL, with a gradient of 10 $\mu\text{m K}^{-1}$. For a quantitative estimate of the temperature gradient, a set of module-level alignment correction was calculated using the data collected at −20 °C. The module-level alignment takes each individual IBL module as the basic element for the geometry correction. Three possible translations, and one rotation around the local-z axis are allowed. The measured residual after this alignment correction at −20 °C is shown in Figure 5.12. It is consistent with zero, which shows that the distortion of the IBL can be corrected by the alignment algorithm. The y-residual shows no temperature dependence within 20 μm uncertainty. The FEA simulation calculates that the averaged local-x residuals,

²In the IBL module frame, the x and y axes are defined in the detector plane with the x-axis pointing along the most precise measurement direction. The x-axis is oriented along the transverse plane in the ATLAS coordinate system. The y-axis points along the beam direction.

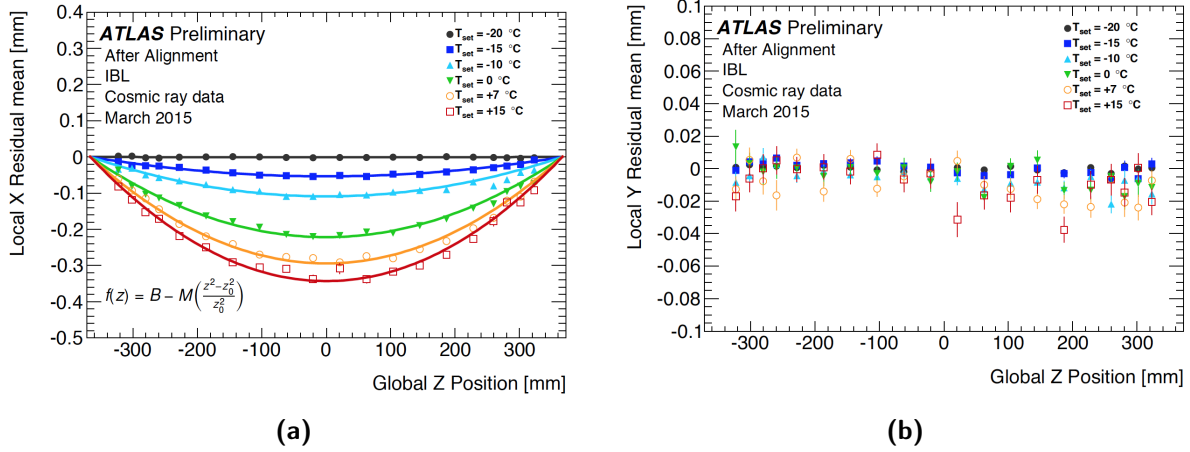


Figure 5.12: The track-to-hit residual mean in the (a) local-x and (b) the local-y direction. The residual mean is averaged over all hits of modules at the same global-z position. The alignment corrections derived at -20°C are applied to the local positions in the module frames. For local-x, each data set is fitted to a parabola which is constrained to match to the baseline $B = 0$ at $z = z_0 = 366.5$ mm.

x_L , is expected to be parabolic. Therefore a fitting function to describe x_L , is parametrized with the following parabolic function:

$$\Delta x_L(z) = B - \frac{M}{z_0^2}(z^2 - z_0^2) \quad (5.1)$$

where z is the global z position of the module, $z_0 = 366.5$ mm is the fixing point of the stave at both ends, B is the baseline which describes the overall translation of the whole stave and M is the magnitude of the distortion at the center of the stave. B is set to a common constant for all temperature points because the end-blocks of each stave are fixed mechanically. M is the free parameter in the fit and it can be used to quantify the size of the distortion. The above parametrization function describes the distortion shape of each temperature, as presented in Figure 5.12a. Figure 5.13 shows the magnitude of the distortion as function the operating temperature. A linear dependence on the temperature of the magnitude of the distortion is observed. The temperature gradient of the magnitude of the distortion, M , is fit as:

$$\frac{dM}{dT} = -10.6 \pm 0.7 \mu\text{m K}^{-1} \quad (5.2)$$

The uncertainty on the above gradient is estimated by comparing to a fit performed without constraining the baseline B in addition to the statistical uncertainty. The observation supports the hypothesis that the distortion is driven by the mismatch of the coefficient of thermal expansion.

For a correct operation of the IBL detector a stable temperature is therefore required. The sources of temperature instability are the intrinsic stability of the cooling system as well as the environment and the variation in power consumption of the FEs. Since the thermal capacity of the cooling system is much larger than the module's power consumption, the cooling pipe temperature stability is assumed to be decoupled from the variation of the power consumption. The stability of the temperature of the IBL cooling system was investigated

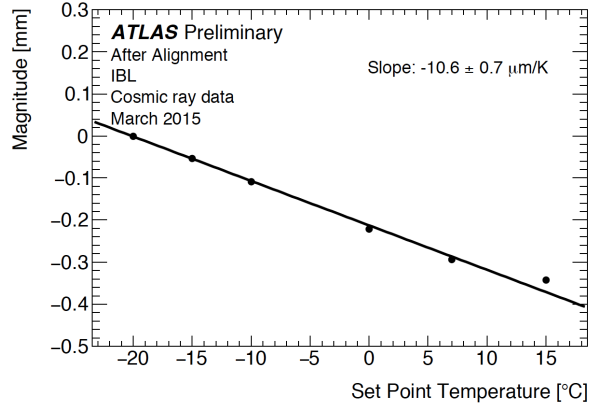


Figure 5.13: The magnitude of the distortion as a function of the temperature. Each data point is a best fit of a parabola to the local- x residual mean as a function of the global- z of the module position. The alignment corrections derived at -20°C are applied to the local positions in the module frames.

using the temperature sensor monitoring system during the same cosmic-ray run studied in the previous section. There are 10 negative temperature coefficient (NTC) thermistors for each stave. They are composed of one NTC for every four FE chips (eight in total per stave) and one NTC for each of the inlet and outlet sides of the cooling pipe at $z \simeq \pm 700$ mm. The precision of the NTC sensors on modules and the sensors on the cooling pipe is estimated to be $\sim 0.02\text{K}$. The IBL employs a bi-phase CO_2 cooling system [61]. The coolant, CO_2 , is liquid at the inlet and it transits to bi-phase (gas and liquid) as it absorbs the heat dissipated in the stave. The actual position of transition varies by staves. Therefore the outlet side is considered to represent a more accurate reference for the temperature of the coolant than the inlet side. On the other hand, the NTC sensors on modules are used to evaluate the temperature stability at the modules. For each sensor i of each run k , the temperature value is read out $N_i^{(k)}$ times in the detector control system, while each run is a block of the data-taking period. The standard deviation and the peak-to-peak values of each sensor i of each run k are defined as:

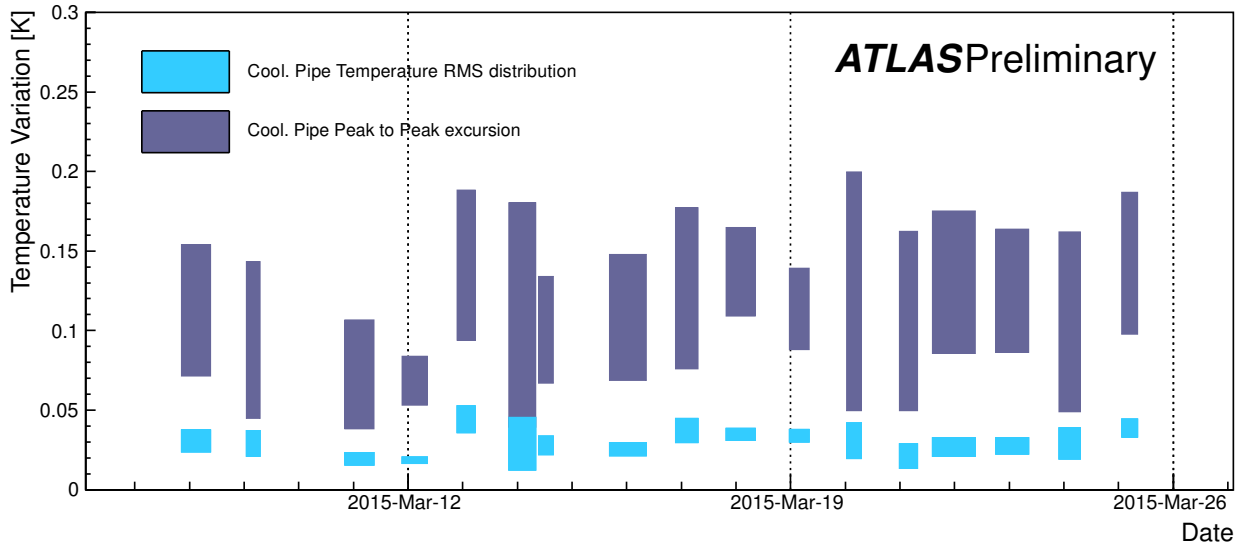
$$\begin{aligned} \text{Standard deviation: } \delta T^{(k)}_i &= \sqrt{\frac{1}{N_i^{(k)}} \sum_j (T_i^{(k)}[j] - \langle T_i^{(k)} \rangle)^2} \\ \text{Peak to peak: } \Delta T_i^{(k)} &= \max_j(T_i^{(k)}[j]) - \min_j(T_i^{(k)}[j]). \end{aligned} \quad (5.3)$$

where $T_i^{(k)}[j]$ is each temperature readout and $\langle T_i^{(k)} \rangle$ represents the average temperature readout. For the cooling pipe outlet, there are 14 sensors in total. The standard deviation of $\delta T_i^{(k)}[j]$ over 14 sensors, denoted as:

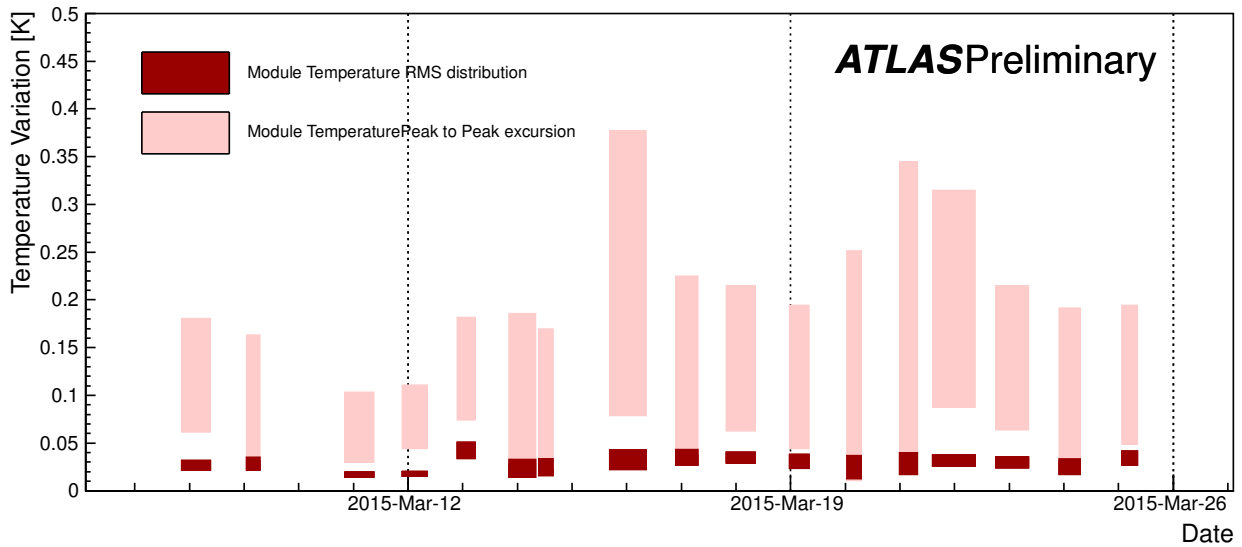
$$\delta(\delta T^{(k)}) = \sqrt{\frac{1}{14} \sum_i (\delta T_i^{(k)} - \langle \delta T^{(k)} \rangle)^2}, \quad (5.4)$$

where $\langle \delta T^{(k)} \rangle$ represents the average of $\delta T_i^{(k)}$ over 14 sensors. Figure 5.14a shows the results of the stability study using the cooling outlet-pipe temperature sensors. Each bar represents a run. There are two kinds of bars denoted as *RMS* and "peak-to-peak". The vertical range of the RMS bar for each run k is defined as:

$$\text{RMS: } [\langle \delta T^{(k)} \rangle - \delta(\delta T^{(k)}), \langle \delta T^{(k)} \rangle + \delta(\delta T^{(k)})], \quad (5.5)$$



(a)



(b)

Figure 5.14: Stability of the outlet of the (a) cooling pipe temperature and (b) module temperature sensors of the IBL during the comic-ray data-taking in the commissioning phase. Each bar represents the block of data taking period called runs. The width of each bar represents the duration of the data-taking of the run. For each module temperature sensor, the RMS and the peak-to-peak values of the temperature readout during the run are calculated. The "RMS" bar in the figure represents the variance of the RMS values of the 112 temperature sensors with indicating ± 1 RMS range around the average RMS. The "peaktopeak" bar represents the variance of the peak-to-peak values of the 112 temperature sensors indicating the maximum and the minimum peak-to-peak values among the 112 temperature sensors.

and the vertical range of the peak-to-peak bar is defined as:

$$\text{peak to peak: } [\min_i(\Delta T_i^{(k)}), \max_i(\Delta T_i^{(k)})]. \quad (5.6)$$

The width of each bar represents the duration of the corresponding run. As seen in the plot, the RMS bar of the temperature during a run is well within $0.05K$ while the peak-to-peak bar is within $0.2K$.

The same description of the stability is performed for 112 NTC sensors on the modules, and the result is shown in Figure 5.14b. For most of the runs the peak-to-peak value is within $0.25K$, which is not significantly larger than the stability of the outlet cooling pipe of $0.2K$. The maximum peak-to-peak values in some of the runs are close to $0.4K$. These excess values are recorded by the sensors which are the closest to the inlet cooling pipe. It is considered that the temperature fluctuation at this position is caused by the bi-phase transition of the CO_2 coolant. Such a local temperature fluctuation is expected to have small impact to the global distortion of the stave. The fact that the variation of module temperature is not very deviated from the cooling output pipe temperature stability indicates that the dominant source of the module temperature variation could be considered to be from the stability of the cooling system and environment.

5.3.2 Effect on the performance

In order to assess the effect of track reconstruction under varying temperature conditions, a set of alignment constants is produced to mimic the IBL stave distortion in the local- x axis. It is assumed that a certain amount of displacement of module positions, generated by the temperature fluctuation under stable collision data-taking, is not corrected by the alignment procedure. The magnitude of the distortion is calculated for a $\delta T_{flex} = 0.2\text{ K}$, corresponding to $2\mu\text{m}$ displacement at the center of the stave. It is expected that the transverse impact parameter (d_0) of a charged track is the most sensitive track parameter to the distortion of the IBL. Figure 5.15 shows the d_0 distribution of muon tracks with respect to the beamspot using the MonteCarlo simulation of $Z \rightarrow \mu^+ \mu^-$ events in $\sqrt{s} = 13\text{ TeV}$ proton-proton collisions based on the nominal geometry and the distorted geometry. For each event, only a pair of opposite sign reconstructed muons with the invariant mass of $60 < m_{\mu\mu} < 120\text{ GeV}$ and with the opening angle of two muons greater than 0.2 radian is selected. The track quality selection is similar to the one used for the alignment except for the minimal threshold of the transverse momentum, increased to 15 GeV . The bias to the transverse impact parameter (d_0) is $\sim 1\mu\text{m}$, small in comparison to the expected d_0 resolution, $O(10\mu\text{m})$.

Further investigations were performed to assess the impact on b-tagging performance for different scenarios, with a $\delta T_{flex} = 0.2\text{ K}, 0.5\text{ K}, 1\text{ K}, 2\text{ K}$, in the MonteCarlo simulation of $t\bar{t}$ events at $\sqrt{s} = 13\text{ TeV}$. In the case of $\delta T_{flex} = 0.2\text{ K}, 0.5\text{ K}$ b-tagging performance does not deteriorate. An impact in b-tagging performance was observed for $\delta T_{flex} = 1\text{ K}$ and 2 K , as shown in Figure 5.16a, with light-jet rejection decreasing respectively to the 90% and the 50% of the nominal value for a 70% b-tagging efficiency working point. Figure 5.16b shows the light-jet rejection at 70% b-tagging efficiency working point as a function of the jet- p_T . The higher the jet- p_T is, the more the tracks are collimated. As it will be explained in Chapter 7, for high- p_T jets is crucial a good reconstruction of the impact parameter significances ($\frac{d_0}{\sigma_{d_0}}$ and $\frac{z_0}{\sigma_{z_0}}$). At p_T higher than 350 GeV tracks within a jet are more collimated than in the low- p_T case, so the impact parameter is usually lower. On the other hand the

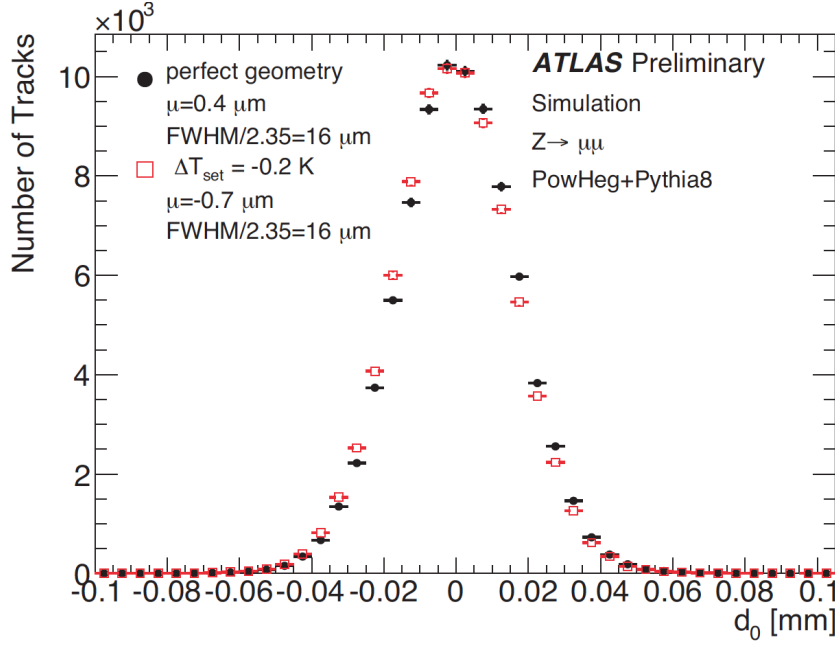


Figure 5.15: Distribution of the transverse impact parameter d_0 of muon tracks with respect to the beamspot from $Z \rightarrow \mu^+ \mu^-$ events simulated in $\sqrt{s} = 13$ TeV proton-proton collisions. Solid circles show the nominal geometry and the open red squares the distorted geometry corresponding to a temperature variation of the IBL of $\delta T_{flex} = 0.2$ K (2 μm displacement at the center of the stave)

multiple scattering contribution to the error is less significant, so that the impact parameter significance is mostly biased by the systematic so that the effect of the bowing affects more the b-tagging performance. This can be seen in the fact that for the 2 K scenario and jet with p_T higher than 350 GeV the light-jet rejection is just the 30% of the default case.

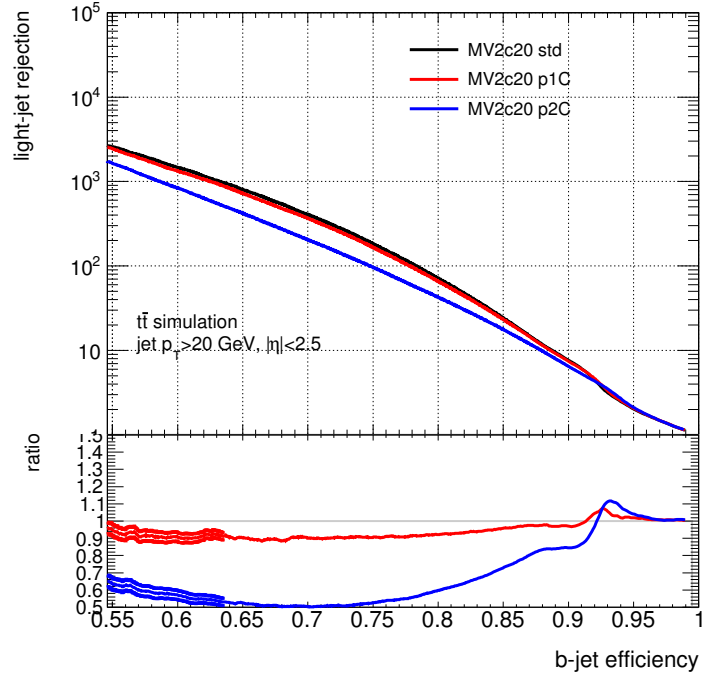
5.4 Measurement of the Lorentz angle

During the cosmic data-taking phase, occurred in the commissioning of the ATLAS detector, a study of the silicon detector properties was carried out. In particular a measurement of the Lorentz angle was carried out.

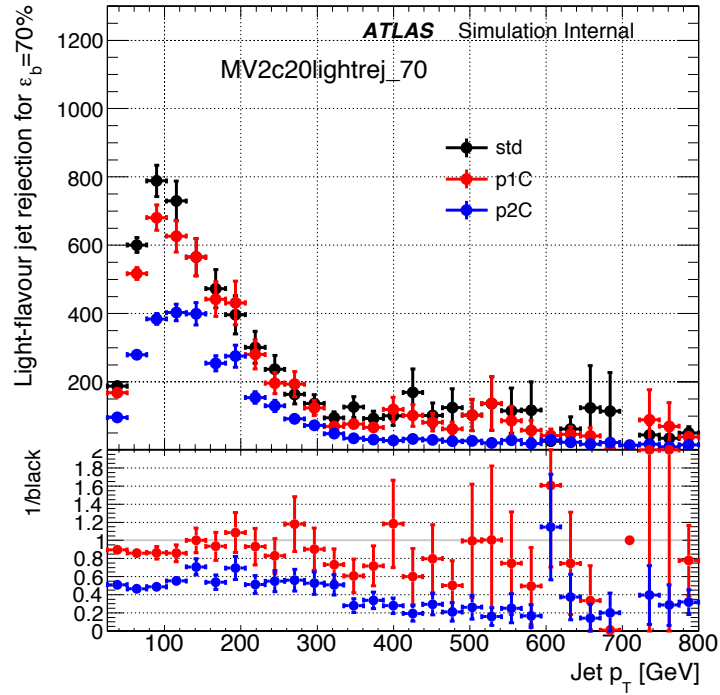
As described in Chapter 1, the Inner Detector operates in a constant magnetic field of 2 T generated by the ATLAS solenoid magnet. The presence of magnetic field has to be considered for the study of the electron/hole pairs drift in the silicon bulk, as introduced in Chapter 2, with the concept of the Lorentz angle.

For the IBL two different technologies of silicon sensors have been used, the Planar and the 3D. As previously described the main difference of the two technologies is the geometry of electrodes and the consequent orientation of the electric field. In Planar devices the electric field is perpendicular to the solenoidal magnetic field and so the Lorentz mechanism is present. In 3D technology, instead, the electric field is almost colinear to the magnetic field which minimize considerably the Lorentz force and only a small effect is expected [62].

This is what can be seen in Figure 5.17 which shows the average transverse dimension of



(a)



(b)

Figure 5.16: Light-jet rejection evaluated with the MV2c20 algorithm with respect to (a) b-tagging efficiency and in function of (b) jet- p_T for a nominal b-tagging efficiency of 70% . Three different bowing scenarios are shown: the nominal geometry and the foreseen effect for a temperature stability of 1K and 2K. For 1K (2K) temperature stability the mechanical stability is expected to be 1 μm (2 μm)

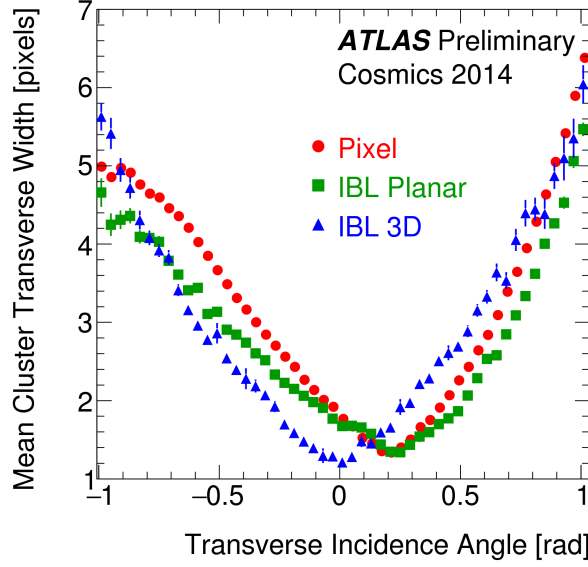


Figure 5.17: Variation of the mean cluster transverse width with transverse incidence angle for pixel layers and IBL sensors.

Technology	a [pixels]	α_L [mrad]	b [pixels]	σ [mrad]	$\chi^2/\text{d.o.f}$
Pixel Layers	3.28 ± 0.02	201 ± 1	1.14 ± 0.01	80 ± 4	64/23
IBL Planar	2.35 ± 0.06	224 ± 4	1.18 ± 0.03	112 ± 21	41/23
IBL 3D	2.90 ± 0.07	-10 ± 5	1.08 ± 0.03	64 ± 20	19/23

Table 5.1: Lorentz angle fit for the three sensor technologies of the Pixel and IBL detectors with cosmic data in 2014. Errors are statistical only.

the clusters as a function of the particle transverse incident angle ϕ_{inc} for the IBL sensors and the ones used in the other 3 layers of the Pixel barrel detector. In planar sensors, the minimal cluster width is reached when the particle incidence angle coincides with the drift angle of the charge carriers. This angle is the Lorentz angle and is a property of the silicon bulk for a given magnetic field. We can see that pixel layers and IBL planar sensors have their minimum for the same ϕ_{inc} , while 3D sensors are compatible with the expected zero value of the Lorentz angle.

The curve of Figure 5.17 can be fitted with the following function of incident angle α :

$$F(\alpha) = [a(\tan \phi_{inc} - \tan \alpha_L) + \frac{b}{\sqrt{\cos \phi_{inc}}}] \otimes G(\phi_{inc}) \quad (5.7)$$

where \otimes indicates the convolution operator and G is the Gaussian function. The free parameters of the fit are the values of a and b , the standard deviation of the Gaussian function, and the Lorentz angle value α_L . In the formula, the term $a(\tan \phi_{inc} - \tan \alpha_L)$ represents the geometrical projection of the charge carriers liberated by the particle on the sensor surface. The parameter a depends on with how rapidly the cluster size increases with the incident angle. The term $\frac{b}{\sqrt{\cos \phi_{inc}}}$ describes the cluster size, where b is the mean cluster size for tracks at the Lorentz angle. Fit results are shown in Table 5.1. The parameter a varies as expected with the sensor thickness, while the minimal cluster size b is obtained for 3D sensors, confirming the small amount of charge sharing at normal incidence for this

technology. The deviation from 0 of the 3D Lorentz angle amounting to 10 mrad can be considered as a fair estimation of the systematic error on the Lorentz angle. This error includes the temperature difference between modules, track and cluster selection, cluster position estimation, alignment uncertainty and fit range. More statistics is needed to study separately each of these sources.

Chapter 6

The b -tagging performance in Run II

6.1 Physics motivation

The identification of jets originating from bottom quarks, denoted as b -tagging, is an important ingredient for the physics program of the ATLAS experiment for any search that involves top physics, Higgs boson searches and new phenomena studies.

b -quarks are the heaviest quarks in the Standard Model which still form hadrons before undergoing a weak decay, contrary to what happens for the top quark which can be detected only indirectly by analyzing their decay products (in most cases a bottom quark and an additional W). Indeed also many interesting physics process contain bottom quarks in the final state, while the most abundant backgrounds contains mostly up, down and strange quarks or gluon jets. As a results most interesting physics cases involve events with final states containing more than one b -jet.

The aim of the b -tagging is therefore to extract the b -quark with high jet efficiency, while rejecting most of the background contamination from jets originating from fragmentation and hadronization of light (u , d and s) quarks, gluons and c -quarks.

From the physics point of view the hadronization of b -quarks has several unique properties, which can be exploited by b -tagging. A b -quark, once produced, forms necessarily a b -flavored hadron, like a B^* or a B^{**} , which decays immediately, strongly or electromagnetically, into a ground state b -hadron plus one or more further particles, while in the remaining cases a ground state b -hadron is produced which have typically a lifetime of the order of the 1 ps. From an experimentalist perspective, one is however only interested in the transition

b-hadron	Branching fraction
B^+	$(40.0 \pm 1.2)\%$
B^0	$(40.0 \pm 1.2)\%$
B_S^0	$(11.4 \pm 2.1)\%$
$b - baryon$	$(8.6 \pm 2.1)\%$

Table 6.1: Branching fraction of b -hadrons produced out of the fragmentation of b -quarks, taken from [63]

from a b -quark into the final ground state b -hadron, since the timescale typical for electromagnetic and strong interactions is so small that the B^* and the B^{**} decay vertices are not

significantly displaced with respect to the primary vertex. The various different fractions of ground state b -hadrons produced out of the fragmentation of an original b -quark are presented in Table 6.1. The fragmentation function describes the distribution of the fraction of energy of the original b -quarks which is kept by the b -hadron. Due to the b -quark fragmentation function being very hard, most of the original b -quark energy is transmitted to the final b -hadron: this fraction is for example on average $\simeq 70\%$ for b -quarks with a momentum of $\simeq 45$ GeV. This property can be exploited during b -tagging, since the fragmentation function for light-quarks into light hadrons or c -quarks into hadrons is softer.

The effective distance traveled in the detector by the b -hadron before decaying depends on the b -hadron momentum, which enters the relativistic boost factor $\beta\gamma$. This means that a b -hadron with a momentum of 50 GeV will travel approximately 3 mm, which is a visible flight length in the detector. Due to the combination of the b -hadron lifetime and its relatively high mass ($m_B \simeq 5$ GeV), the charged particles produced at the decay vertex will be on average significantly displaced with respect to the primary vertex position and the b -hadron decay products will be characterized by a non-negligible decay angle with respect to the b -hadron flight direction.

This is the main signature which is exploited by lifetime-based b -tagging algorithms, which are based either on the presence of significantly displaced tracks, as in impact-parameter-based b -tagging algorithms, or on the explicit reconstruction of the b -hadron decay vertex, as in secondary-vertex-based b -tagging algorithms. Weak decays are governed by the CKM matrix mechanism [64] and [65]: since $|V_{cb}|^2 \gg |V_{ub}|^2$ b -hadrons decay preferably into a c -hadron plus additional particles. These c -hadrons can be again excited states, like D^* and D^{**} , but these again decay with negligible lifetime to weakly decaying c -hadrons. The c -hadrons can still travel for a significant path in the detector and form with its decay products a visible tertiary vertex, displaced with respect to both secondary and primary vertices. There are several possible strategies to deal with such tertiary from c -hadron decays. In the case of the b -tagging algorithms based purely on impact parameter information from the charged particle tracks, the presence of tracks with a more significant displacement does not require an explicit strategy: these tracks will in general just improve the b -tagging performance.

Another property which is usually exploited by b -tagging is the fraction of b and c -hadron decays into leptons, a lepton from the semi-leptonic decay of a b -hadron or from the subsequent decay of the c -hadron turns out to be produced in a b -quark in the $\simeq 21\%$ of the cases. This is valid for muons and electrons, which brings the overall fraction to $\simeq 42\%$. Due to the b or c -hadron mass, the lepton will be emitted with an average transverse momentum comparable with the mass of the b -hadron (m_{bHad}) or the mass of the c -hadron (m_{cHad}). By identifying either an electron or a muon originating from a jet and by requiring it to have a sufficiently high transverse momentum with respect to the jet axis, it is possible to identify b -jets, rejecting light jets.

6.2 The Run 2 b -tagging algorithm for the ATLAS experiment

The basic b -tagging algorithms use charged particle tracks to produce a set of variables which discriminate between different jet flavor. Tracks are first associated to a jet and are then required to pass a quality selection. ATLAS uses three distinct basic b -tagging algorithms, which provide complementary information

- Impact parameter based algorithm
- Inclusive secondary vertex reconstruction algorithm
- Decay chain multi-vertex reconstruction algorithm

The output of these b -tagging algorithms are later combined into a multivariate discriminant which provides the best separation between the different jet flavors.

6.2.1 Track Selection

Tracks are associated to calorimeter jets based on their angular separation ΔR between the track and the jet. The ΔR association requirement varies as a function of the jet p_T , resulting in a narrower cone for jets at high p_T which are more collimated. A given track is associated with only one jet; if it satisfies the association criterion with respect to more than one jet, the jet with the smallest ΔR is chosen. The track selection depends on each specific b -tagging algorithm. For the impact parameter based algorithm, a tight selection is applied. The most important requirements include a requirement on the track p_T above 1 GeV, the transverse and longitudinal impact parameters to be limited to $|d_0| < 1$ mm and $|z_0| \sin \theta < 1.5$ mm, and at least two hits in the pixel detector. For the secondary vertex based algorithms a looser selection is used, relying on the secondary vertex reconstruction to provide additional purity. This includes requiring track p_T to be above 700 – 800 MeV and significantly looser requirements in terms of impact parameter and track quality.

6.2.2 Impact Parameter based Algorithms: IP2D, IP3D

The IP2D and IP3D algorithms [66], make use of the signed impact parameter significances of the tracks matched to the jet. Transverse impact parameter significance is defined as $\frac{d_0}{\sigma_{d_0}}$ where d_0 is the transverse impact parameter and σ_{d_0} is the error on d_0 . Longitudinal impact parameter significance is defined as $\frac{z_0}{\sigma_{z_0}}$ where z_0 is the longitudinal impact parameter and σ_{z_0} is the error on z_0 . While IP2D only considers the information of the transverse plane with respect to the beam axis, IP3D makes use as well of the longitudinal impact parameter. In both cases the sign of the impact parameter is a lifetime information associated to the impact parameter, replacing the sign of the geometrical definition of the impact parameter. The sign is defined positive (negative) if the point of closest approach of the track to the primary vertex is in front (behind) the primary vertex with respect to the jet direction.

Both cases are illustrated in Figure 6.1, together with the variables needed to define the lifetime sign.

The vector $\Delta \vec{r}_{IP} = \vec{r}_{IP} - \vec{r}_{PV}$ defines a three-dimensional impact parameter of the track

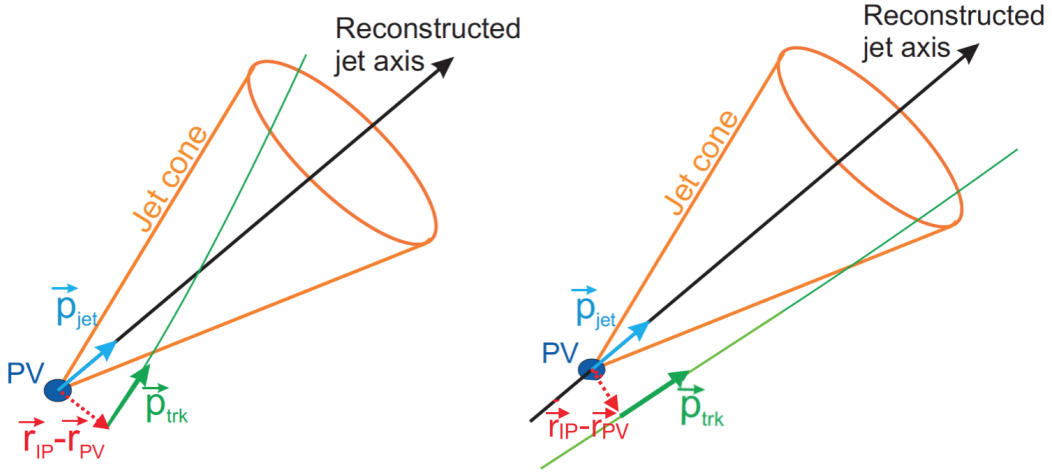


Figure 6.1: Definition of variables needed to compute the lifetime sign of a track in the three-dimensional space. In addition a positive (left) and negative (right) lifetime track are shown.

momentum defined at the point of closest approach to the primary vertex. The lifetime sign can then be defined in the three-dimensions, according to the variables \vec{p}_{jet} , \vec{p}_{trk} and $\Delta\vec{r}_{IP}$:

$$sign_{3D} = sign([\vec{p}_{trk} \times \vec{p}_{jet}] \cdot [\vec{p}_{trk} \times \Delta\vec{r}_{IP}]) \quad (6.1)$$

or it can be alternatively defined on the transverse plane ($x - y$) or on the longitudinal plane ($r\phi - z$) by considering the projection of the three-dimensional impact parameter on those planes. In these cases the formula simplifies and the lifetime signs can be expressed as:

$$sign_{r\phi} = sign(\sin(\phi_{jet} - \phi_{trk}) \cdot d_{0,trk}), sign_z = sign(\sin(\eta_{jet} - \eta_{trk}) \cdot d_{0,trk}). \quad (6.2)$$

The computation of the lifetime sign assumes that the jet direction reproduces, up to a good approximation, the b -hadron direction: from the physical point of view this assumption can only be fulfilled in an approximate way, since the jet momentum is supposed to reproduce the momentum of the initial quark, which is given by the sum of the momentum of the b -hadron and of the remaining tracks arising directly from fragmentation. Under this assumption and up to resolution effects both on jet direction and on the impact parameter and momentum of the track, the lifetime sign for tracks originating from b -hadron decays is positive. The extension of the impact parameter significance distribution to high values for K_S^0 decays and conversions are limited by applied impact parameters cuts.

The impact-parameter significances of all N tracks associated to the jet need to be combined into a single discriminating variable. It is assumed that the tracks are uncorrelated, so that their probability density functions (PDF) are uniquely defined as a function of the jet flavor. Using a likelihood function defined according to the product of these PDFs, under the hypothesis of uncorrelated tracks, the following likelihood ratio provides optimal separation, according to the Neyman-Parson lemma:

$$LR(IP_1, IP_2, \dots, IP_N) = \frac{\prod_{i=1}^N PDF_b(IP_i)}{\prod_{i=1}^N PDF_l(IP_i)} \quad (6.3)$$

Where the PDF_b represents the PDF of b -quarks and PDF_l that of light quarks and IP_i the i^{th} coordinate information. For convention the discriminating variable used for b -tagging is then defined as:

$$\text{weight}(IP_1, IP_2, \dots, IP_N) = \log(LR(IP_1, IP_2, \dots, IP_N)). \quad (6.4)$$

Using such a formalism, the impact parameter based b -tagging algorithms are constructed based on the definition of $\text{PDF}(IP_i)$;

$$IP2D : \quad \text{PDF}(IP_i) = \text{PDF}(IP_{i,r\phi}), \quad (6.5)$$

$$IP3D : \quad \text{PDF}(IP_i) = \text{PDF}(IP_{i,r\phi}, IP_{i,z}). \quad (6.6)$$

In the first case the track PDF is one-dimensional, based on the transverse impact parameter significance. In the second case it is a two-dimensional PDF, based on the transverse and longitudinal impact parameter significance. The impact-parameter-based algorithm permit to obtain a very good b -tagging performance and at the same time allow keeping the method fairly simple, with a single track based PDF to be calibrated for each quark flavor. One of the reason for the good performance is that the likelihood method based on the impact parameter significance contains implicitly, as a prior knowledge in the PDF for b -jets, the fraction of tracks expected to arise from fragmentation and the fraction expected to arise from b and c -hadron decays. However, this method has also some drawbacks. One is that the fraction of tracks from fragmentation depends on the energy of the initial quark, the second is that, while the impact parameter significance of prompt tracks is independent of the jet p_T and η , the impact parameter from secondary decays is not; indeed, while the impact parameter as such is nearly invariant under Lorentz boosts of the b -hadron, the error decreases with increasing track p_T and smaller η . The track-based PDF is thus not invariant neither under a boost of the b -quark nor under a boost of its emerging charged particles tracks. This can be cured both by making track-PDF category-dependent, where the categories correspond to different intervals either in jet kinematics or in the track errors. Using a category dependent PDF brings a significant improvement in performance, but it has the disadvantage of increasing the number of free parameters of the likelihood model [67]. In Run 2, the categorization of tracks has been significantly refined with respect to the version used in Run 1. Table 6.2 describes the different track categories and shows the rate at which tracks from b -, c - and light-flavor jets populate them. Alternative Log Likelihood Ratio (LLR) discriminants can be constructed based on ratios of the b - and c -jet, or c - and light-flavor jet hypotheses. IP3D uses both the transverse and longitudinal impact parameters taking into account their correlations, while IP2D only uses the transverse impact parameters. Compared to IP3D, IP2D is more robust against the effects of pile-up, as it does not take account of the longitudinal impact parameter significance, which will typically be large for tracks from pileup jets. Figure 6.2 shows the transverse and longitudinal impact parameter distributions for tracks from b -, c - and light-flavor jets. In the distribution of transverse impact parameter significances for light-flavor jets a clear exponential tail at high positive values is seen, corresponding to tracks from K_S or Λ decays, from photon conversions and interactions in the detector material. In the case of the longitudinal impact parameter significance, an additional component is seen in the tail, symmetric around zero, corresponding to tracks from pileup. The final discriminants for both the IP2D and IP3D algorithms are illustrated in Figure 6.3

#	Description	<i>b</i> -jets	<i>c</i> -jets	light jets
0	No hits in first two layers; exp. hit in L0 and L1	1.5	1.6	1.6
1	No hits in first two layers; exp. in L0 and not exp. in L1	0.1	0.1	0.1
2	No hits in first two layers; not exp. in L0 and exp. in L1	0.03	0.03	0.03
3	No hits in first two layers; not exp. in L0 and L1	0.03	0.03	0.02
4	No hit in L0; exp. hit in L0	2.4	2.3	2.1
5	No hit in L0; no exp. hit in L0	0.9	0.9	0.9
6	No hit in L1; exp. hit in L1	0.5	0.5	0.5
7	No hit in L1; no exp. hit in L1	2.4	2.4	2.3
8	Shared hit in both L0 and L1	0.01	0.01	0.04
9	Shared pixel hits	2.1	1.6	1.8
10	Two or more shared SCT hits	2.4	2.2	2.2
11	Split hits in both L0 and L1	1.2	1.1	0.8
12	Split pixel hit	2.1	1.6	1.1
13	Good: a track not in any of the above categories	84.3	85.5	86.6

Table 6.2: Description of the track categories used by IP2D and IP3D algorithms along with the fraction of tracks in each category for the $t\bar{t}$ sample. The categories are constructed with respect to the track quality, which is defined by the clusters (hits), from the silicon layers of the Inner Detector, used in the track reconstruction. The clusters in the innermost (L0) and next-to-innermost (L1) layers of the pixel detectors are of particular importance, as is the knowledge of whether a cluster was expected (exp.) or not, based on the detector coverage and dead module maps. Shared hits are clusters which are shared among more than one track, degrading track quality, while split hits are clusters which have been identified as originating from overlapping tracks and have therefore be split into sub-clusters.

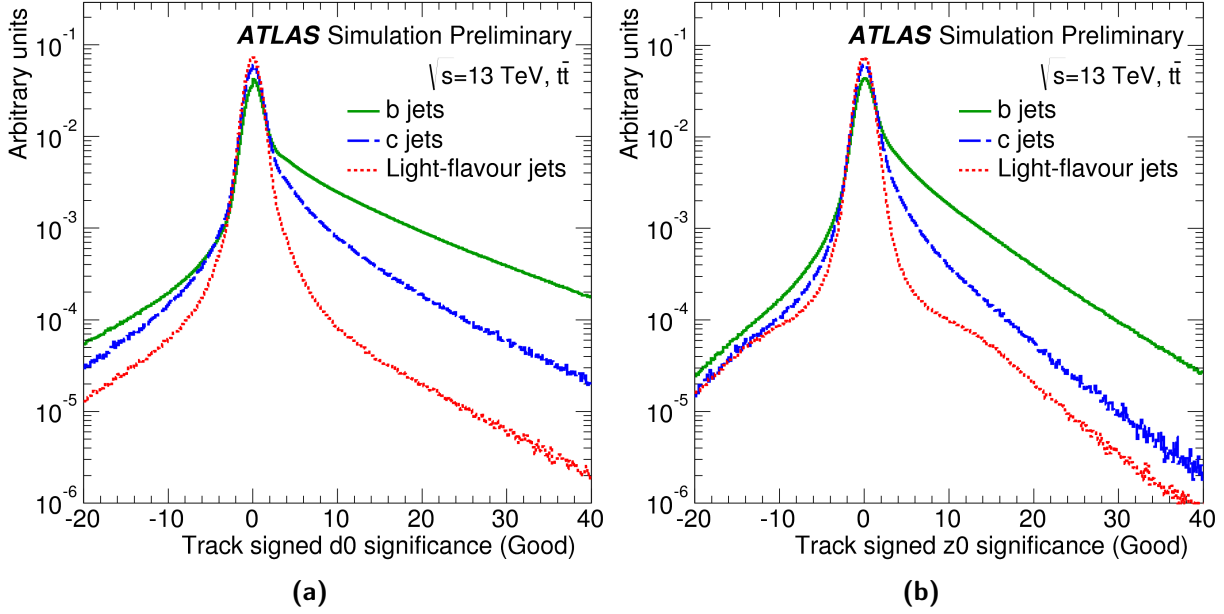


Figure 6.2: The transverse (a) and longitudinal (b) signed impact parameter significance of tracks in $t\bar{t}$ events associated with b (solid green), c (dashed blue) and light-flavor (dotted red) jets for the "Good" category defined in Table 6.2.

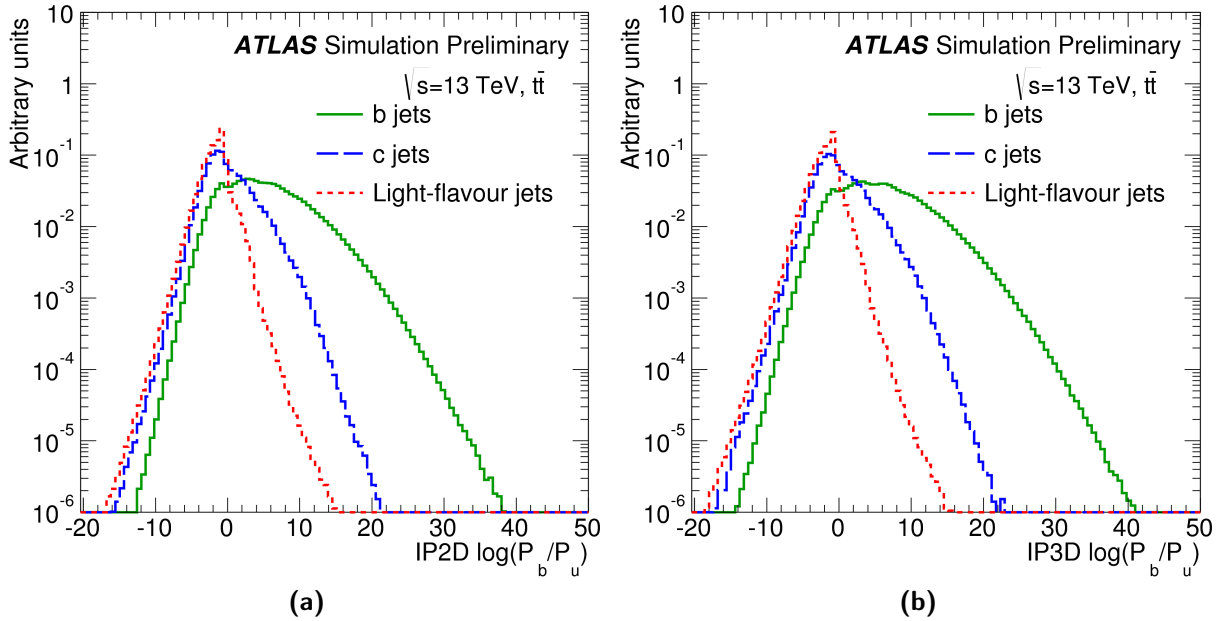


Figure 6.3: The log likelihood ratio for the IP2D (a) and IP3D (b) b -tagging algorithm for b (solid green), c (dashed blue) and light-flavor (dotted red) jets in $t\bar{t}$ events. If no tracks are found in the jet, a large negative value is assigned as the algorithm output. This happens for less than 0.5% of b and c-jets, and for about 2% of light-flavor jets.

6.2.3 Secondary-vertex reconstruction of b -jets

The explicit reconstruction of secondary vertex of b -jets can significantly improve the b -tagging performance of the impact parameter based algorithms. An exclusive reconstruction of the different possible b -decay modes cannot be performed with high efficiency: many of these decays modes involve neutral particles, which are not reconstructed by the Inner Detector, and the set of selection cuts needed to reconstruct all the different decay modes would severely limit the reconstruction efficiency. The reconstruction of secondary b and c -hadron decay vertices in jets thus has to be done in an inclusive way, where the number of charged particle tracks originating from b and c hadron decay is not known a-priori.

Trying to resolve the b and c hadron vertices of the decay cascade is challenging for the following reasons:

- The probability to have at least two reconstructed charged particle tracks both from the b and c hadron decay is limited. This is due to the small charged-particle multiplicities involved in this decay, to the fact that some of the particle coming from b and c -hadron decay are compatible with the primary vertex and to the limited track reconstruction efficiency.
- The resolution of the relevant track parameters, especially at low transverse momenta, are not sufficient to separate the two vertices efficiently.

Two strategies to detect a secondary vertex in b -jets are available in ATLAS. The first one is based on a fit of single geometrical vertex. Even if this is not correct, this approximation works well for a large fraction of cases. The second algorithm is based on a kinematic approach, which assumes that the primary event vertex, the b -vertex and the c -vertex lie approximately on the same line, the flight path of the b -hadron.

6.2.4 The secondary vertex finding algorithm: SV

The secondary vertex finding algorithm (SV) reconstructs the vertex formed by the decay products of the b -hadron, including the products of the possible subsequent charm hadron decay. The algorithm starts from all tracks that are significantly displaced from the primary vertex and associated with the jet, forming vertex candidates for track pairs with vertex fit $\chi^2 < 4.5$. Vertices compatible with long-lived particles or material interactions are rejected; the invariant mass of the track four-momenta is used to reject vertices that are likely to originate K_s , Λ decays and photon conversions, while the position of the vertex in the r - ϕ projection is compared to a simplified description of the two innermost pixel layers to reject secondary interactions in the detector material. All tracks from the remaining two-track vertices are combined into a single inclusive vertex using an iterative procedure to remove the track yielding the largest contribution to the χ^2 of the vertex fit until this contribution passes a predefined threshold. SV is based on the secondary vertex finding infrastructure employing a likelihood ratio formalism as the one described for the impact-parameter algorithm. Six of the vertex properties are exploited:

- the vertex mass, i.e. the invariant mass of all tracks used to reconstruct the vertex under the assumption that all the tracks are pions;
- the number of the tracks at the vertex;

- the number of two-track vertices reconstructed within the jet;
- the 3D decay length significance;
- the transverse decay length;
- the energy fraction, defined as the energy from the tracks in the displaced vertex relative to all tracks reconstructed within the jet.

In addition, the ΔR between the jet direction and the direction of the line joining the primary vertex and the secondary vertex is used in the logarithmic likelihood ratio.

6.2.5 The JetFitter algorithm

Jet Fitter is an inclusive secondary vertex reconstruction algorithm which exploits the topological structure of weak b and c -hadron decays inside a jet. Differently to the SV algorithm, described in the previous section, the JetFitter assumes that b and c -hadrons decay on the same line defined by the b -hadron flight path. All charged-particle tracks stemming from either the b and c -hadron decay thus intersect this b -hadron flight axis. There are several advantages of this method:

- Incomplete topologies can also be reconstructed (in principle even the topology with a single track from the b -hadron decay and a single track from the c -hadron decay is accessible).
- The fit evaluates the compatibility with the given set of tracks with a $b \rightarrow c$ -hadron like cascade topology, increasing the discrimination power against light quark jets.
- Constraining the tracks to lie on the b -hadron flight axis reduces the degrees of freedom of the fit, increasing the chance to separate the b and the c -hadron vertices.

From the physics point of view this hypothesis is justified through the kinematics of the particles involved as defined through the hard b -quark fragmentation function and the masses of the b and c -hadrons. The lateral displacement of the c -hadron decay vertex with respect to the b -hadron flight path is small enough not to violate significantly the basic assumption within the typical resolutions of tracking detectors. In JetFitter the vertexing task is mathematically implemented as an extension of the Kalman Filter (Section ??) formalism for the vertex reconstruction. While a conventional Kalman Filter iteratively update the vertex position variables \vec{x} , the JetFitter algorithm is described through the following variables:

$$\vec{d} = (x_{PV}, y_{PV}, z_{PV}, \phi, \theta, d_1, d_2, d_3, \dots, d_N) \quad (6.7)$$

with:

- (x_{PV}, y_{PV}, z_{PV}) : the primary vertex coordinates;
- (ϕ, θ) : the azimuthal and the polar directions of the b -hadron flight axis;
- (d_1, \dots, d_N) : the distances of the fitted vertices, defined as the intersections of one or more tracks and the b -hadron flight axis, to the primary vertex position along the flight axis (N representing the number of vertices).

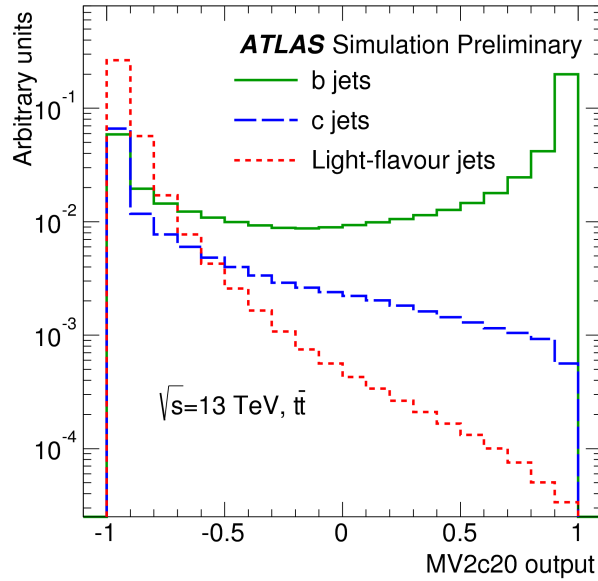


Figure 6.4: The MV2c20 output for b - (solid green), c - (dashed blue) and light-flavor (dotted red) jets in $t\bar{t}$ events.

Before starting the fit, the variables are initialized with the information of the primary vertex position, provided by the primary vertex finding algorithm, and the b -hadron flight direction, approximated by the direction of the jet axis. After this initialization a first fit is performed under the hypothesis that each track represents a single vertex along the b -hadron flight axis, until χ^2 convergency is reached, obtaining a first set of fitted $(\phi, \theta, d_1, d_2, d_3, \dots, d_N)$. A clustering procedure is then performed, where all the combinations of two vertices (picked among the vertices lying on the b -hadron flight axis plus the primary vertex) are taken into consideration, using the vertex probability estimation techniques, described in details in [.] The vertex-probability estimation technique provides the probability of a certain vertex to be compatible with the fitted decay chain and the probability for two initially separated vertices along the flight axis to be compatible with a single vertex and with the overall new resulting decay chain. The vertices with the highest compatibility are merged, a new complete fit is performed with the new decay-chain structure. This procedure is then iterated until no pairs of vertices with a probability above a certain threshold exist anymore. The result of this clustering procedure is a well defined decay-chain topology with a certain association of tracks to vertices along the b -hadron flight axis, where each vertex possesses at least one track.

6.2.6 Multivariate Algorithm: MV2

The b -tagging Run 2 final algorithm is called MV2 and it is a boosted-decision tree that takes as input the output of the algorithms previously described. For a comprehensive description of a boosted decision tree it is worth to describe the concept of decision tree. A decision tree is a sequence of conditions that needs to be verified, each of the condition verified is called *node* and it can be either true or false. Indeed, the final statement of a decision can be either true or false.

In boosted-decision trees, the selection is done on a majority vote on the result of several

decision trees, which are all derived from the same training sample by supplying different event weights during the training. Successive decision nodes are used to categorize the events out of the sample as either signal or background. Each node uses only a single discriminating variable to decide if the event is signal-like or background-like. The training starts with the root node. Here one takes the full training event sample and selects the variable and corresponding cut value that gives the best separation between signal and background at this stage. Using this cut criterion, the sample is then divided into two subsamples, a signal-like (right) and a background-like (left) sample. Two new nodes are then created for each of the two sub-samples and they are constructed using the same mechanism as described for the root node. The division is stopped once a certain node has reached either a minimum number of events, or a minimum or maximum signal purity. The latter are then called "signal" or "background" if they contain more signal or background events from the training sample. The idea behind boosting is, that signal events from the training sample, that end up in a background node (and vice versa) are given a larger weight than events that are in the correct leave node. This results in a re-weighted training event sample, with which then a new decision tree can be developed. The boosting can be applied several times (typically 100-500 times) and it ends up with a set of decision trees (a forest). Only one tree is modified at a time, while the other trees stay fixed. The input variables obtained from the three basic algorithms are combined to discriminate b -jets from light (u,d,s-quark or gluon jets) and c -jets. The training is performed on a set of approximately 5 million $t\bar{t}$ events. The MV2c20 algorithm is defined as the output of such a boosted decision tree with the training performed assigning b -jets as signal and a mixture of 80% light-flavor jets and 20% c -jets as background. The list of input variables used for the training is summarized in Table 6.3. The kinematic properties (p_T and η) of the jets are included in the training to take advantage of correlations with the other input variables. In order to avoid any difference in the kinematic spectra between signal and background jets being interpreted as discriminant by the training, the signal jets are re-weighted to match the spectrum of the background jets.

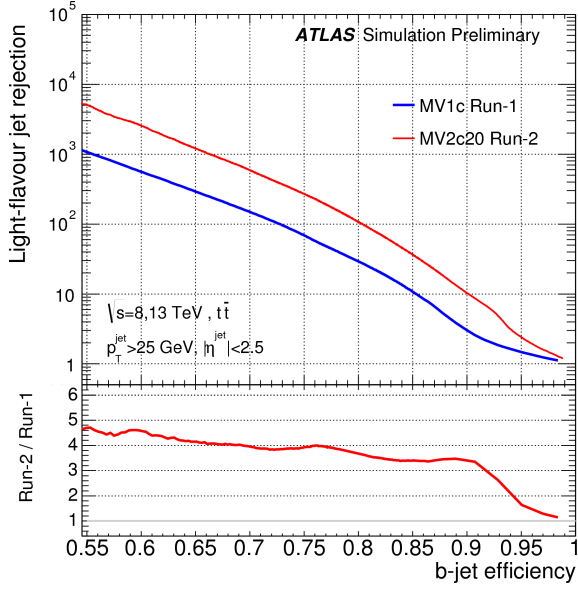
The MV2c20 output distribution is shown in Figure 6.4 for b , c and light-flavor jets.

6.3 The b -tagging performance

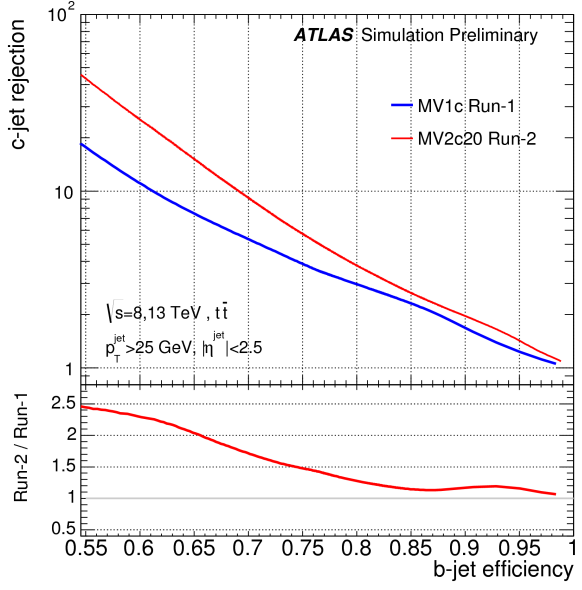
The Run 2 baseline algorithm for b -tagging was completely renewed during the long shut-down, and with the insertion of the IBL it will improve the b -tagging performance. In Section 3.2.2 the impact of the IBL on b -tagging performance has been shown. That study used a Run 2 based algorithm comparison. A study over a MonteCarlo sample of $t\bar{t}$ events has been performed to compare the b -tagging performance in Run1 and at the beginning of Run2. This requires a comparison to be made between samples produced using the Run 1 simulation and reconstruction software to those using the Run 2 setup. It is therefore necessary to slightly alter the selection and simulation setup to ensure a meaningful comparison. The minimum jet p_T requirement is raised from 20 to 25 GeV. The Run 1 and Run 2 samples have been produced with different centre of mass energies (8 and 13 TeV) and different pile-up conditions. In order to get an unbiased comparison, the distributions of jet p_T , jet η and of the average number of interactions μ for the Run 2 sample are re-weighted in such a way to reproduce the corresponding Run 1 distributions. Figure 6.5a shows the light-jet

Input	Variable	Description
Kinematics	p_T (jet)	Jet transverse momentum
	η (jet)	Jet pseudo-rapidity
IP2D, IP3D	$\log(\text{Pb}=\text{P}_{\text{light}})$	Likelihood ratio between the b- and light jet hypotheses
	$\log(\text{Pb}=\text{P}_c)$	Likelihood ratio between the b- and c-jet hypotheses
	$\log(\text{Pc}=\text{P}_{\text{light}})$	Likelihood ratio between the c- and light jet hypotheses
SV	m (SV)	Invariant mass of tracks at the secondary vertex assuming pion masses
	f_E (SV)	Fraction of the charged jet energy in the secondary vertex
	NTrkAtVtx(SV)	Number of tracks used in the secondary vertex
	N2TrkVtx (SV)	Number of two track vertex candidates
	L_{xy} (SV)	Transverse distance between the primary and secondary vertices
	L_{xyz} (SV)	Distance between the primary and secondary vertices
	S_{xyz} (SV)	Distance between the primary and secondary vertices divided by its uncertainty
	R(jet;SV)	R between the jet axis and the direction of the secondary vertex relative to the primary vertex
Jet Fitter	N2TrkVtx (JF)	Number of 2-track vertex candidates (prior to decay chain fit)
	m (JF)	Invariant mass of tracks from displaced vertices assuming pion masses
	S_{xyz} (JF)	Significance of the average distance between the primary and displaced vertices
	f_{EV} (JF)	Fraction of the charged jet

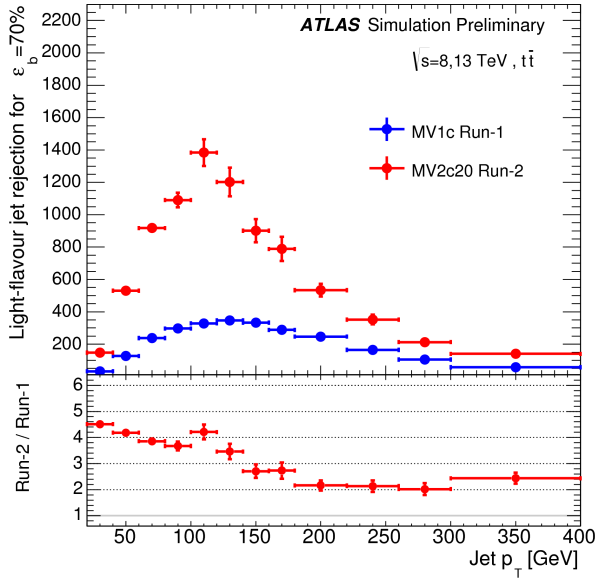
Table 6.3: The 24 input variables used by the MV2c00 and MV2c20 b -tagging algorithm.



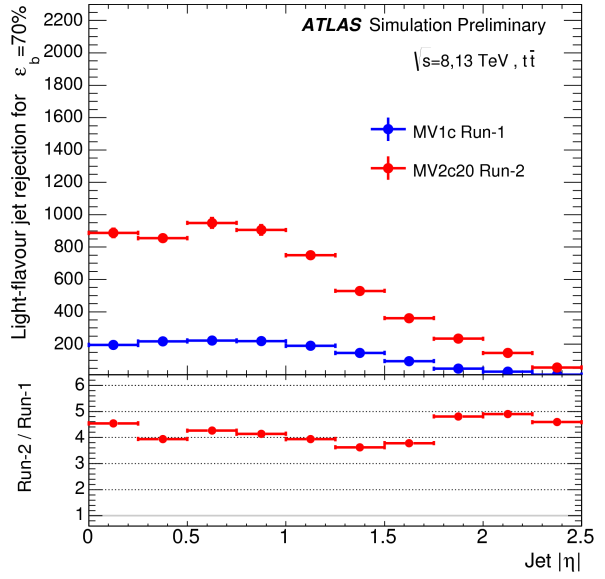
(a)



(b)



(c)



(d)

Figure 6.5: The light (a) and c-jet rejection (b) versus b -jet efficiency for the MV1c b -tagging algorithm using the Run 1 detector and reconstruction software (blue) compared to the MV2c20 b -tagging algorithm using the Run 2 setup (red). The light-flavour jet rejection in bins of jet p_T (c) and $|\eta|$ (d) for the MV1c b -tagging algorithm using the Run 1 detector and reconstruction software (blue) compared to the MV2c20 b -tagging algorithm using the Run 2 setup (red). In each p_T or $|\eta|$ bin the b -tagging cut value has been chosen in such a way to yield a constant b -jet efficiency of 70%.

rejection¹ with respect to the b -tagging efficiency, for a working point of 70% b -tagging efficiency an improvement of factor 4 for the light-jet rejection can be seen. Figure 6.5b shows the c-jet rejection as function of the b -jet efficiency. ²Figures 6.5c and 6.5d show respectively the light-jet rejection as function of the jet- p_T and the jet- $|\eta|$, performance was improved by at least a factor 2.

6.4 Optimization of the IP3D tagger at high- p_T

The b -tagging algorithm uses MonteCarlo samples as reference to discriminate b -jets from light-jets and c-jets. This happens in the training of the algorithms, in which the flavor of the jet is defined a priori and then the characteristics of each jet family can be recognized. Normally the training is performed with $t\bar{t}$ events samples. This choice is motivated by the decay of the top quark. The only known way that a top quark can decay is through the weak interaction producing a W-boson and a down-type quark (down, strange, or bottom). Because of its enormous mass, the top quark is extremely short-lived with a predicted lifetime of only 5×10^{-25} s [8]. As a result top quarks do not have time to form hadrons before they decay, as other quarks do. In particular the branching ratio $\Gamma(W + b)/\Gamma(W + q(q = b, s, d)) = 0.91 \pm 0.04$ [8]. The Standard Model also allows more exotic decays, but only at one loop level, meaning that they are extremely suppressed. For this reason $t\bar{t}$ samples are extremely good to study the b -tagging properties, since most of the time there are at least two b -quarks in the final state, and often associated with light-jet produced in the W decay, which has $69.91 \pm 0.06\%$ probability to decay hadronically.

Although $t\bar{t}$ samples work well for the training of the b -tagging algorithms, they are not predictive of b -jet at high- p_T and in an extremely boosted scenario which is of interest for the search of new physics. For example one can study the performance of the MV2c20 algorithm over a sample with high- p_T b -jets, as shown in Figure 6.6. A good candidate for this study is a sample of MonteCarlo describing the production and decay of a particle not foreseen by the Standard Model, called the Z' [68], which has the same characteristics of the Z boson, but with higher mass. In particular the decay of the Z' in $t\bar{t}$ have a topology very similar to the $t\bar{t}$ channel described before, but more boosted. These samples allow the investigation of the performance at high- p_T and where the b -jets are often collimated to the jets coming from the W decay, if this decays hadronically. Figure 6.6b shows the distribution of the jet p_T for both b -jets and light-jets in a Z' sample, where the Z' is expected to have a mass of 4 TeV. In this sample there is a considerable population of b -jets with a p_T higher than 500 GeV.

The deterioration of the performance seen in Figure 6.6 at high- p_T has different causes:

- tracks within the jet are more collimated,
- the number of tracks coming from the fragmentation of b -hadrons increase with the jet- p_T .
- the secondary vertex is in general more displaced with respect to the low- p_T scenario.

¹light-jet rejection is defined as $\frac{1}{\epsilon_b^l}$, where ϵ_b^l is the efficiency for a light jet to be tagged as a b -jet

²c-jet rejection is defined as $\frac{1}{\epsilon_b^c}$, where ϵ_b^c is the efficiency for a c-jet to be tagged as a b -jet

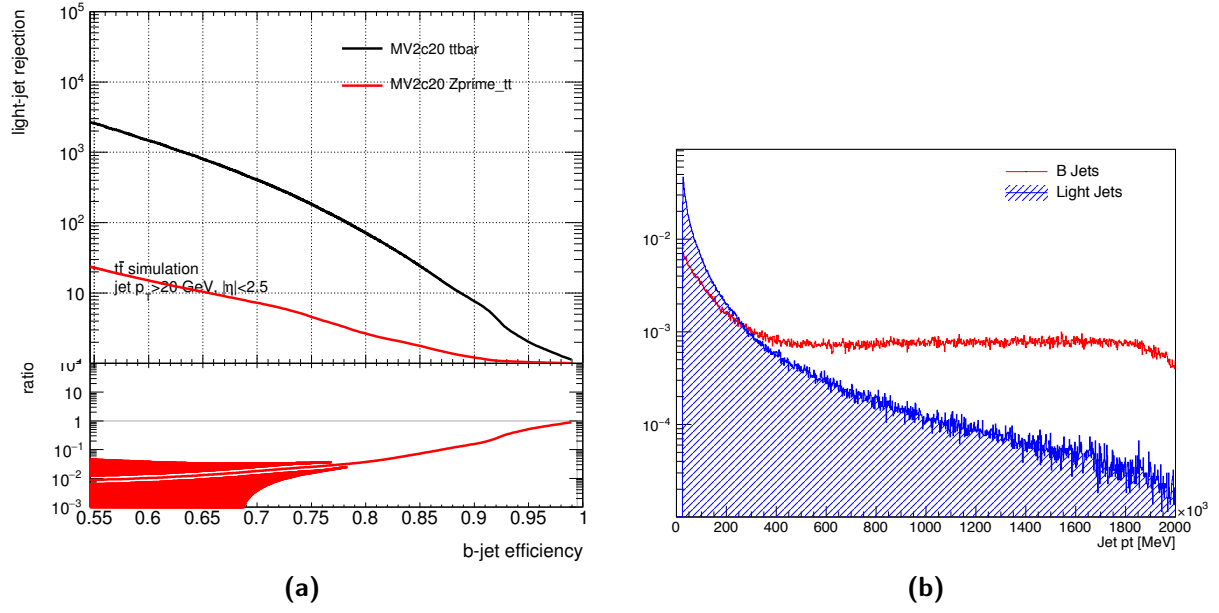


Figure 6.6: MV2c20 performance over a Z' samples trained while trained with $t\bar{t}$ events

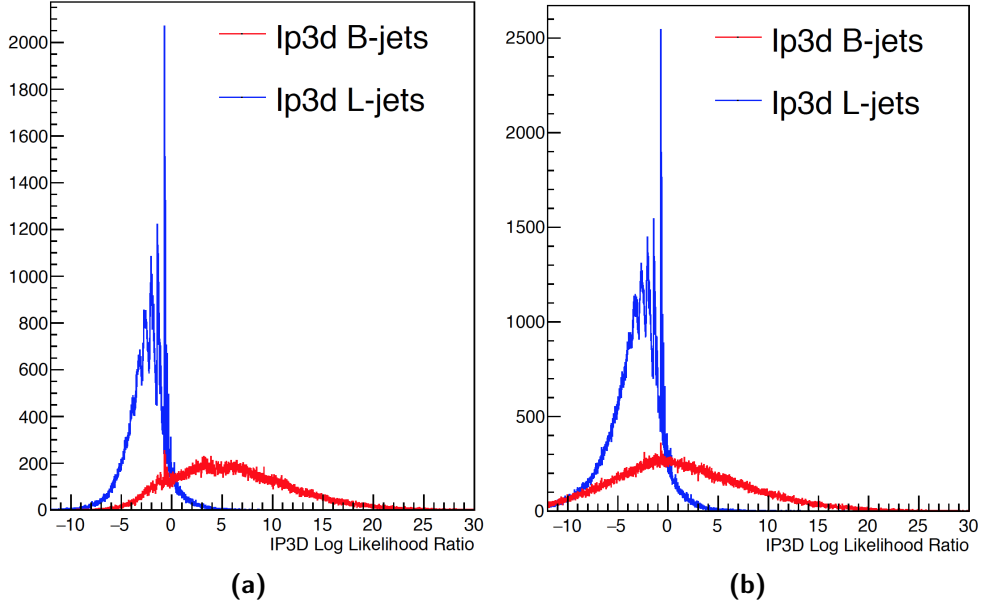


Figure 6.7: IP3D log likelihood ratio distributions of $t\bar{t}$ (6.7a) and $Z'(4 \text{ TeV}) \rightarrow t\bar{t}$ (6.7b) samples, for b -jets and light jets.

As Figure 6.7 shows, while in the $t\bar{t}$ sample there is a good separation between the b -jet distribution and the light jet one, for the $Z'(4\text{ TeV}) \rightarrow t\bar{t}$ the separation is poor, so that it becomes more difficult to discriminate the b -jets. In particular the higher is the p_T of a b -jet, the lower is the value of the IP3D log likelihood ratio. The standard 70% b -tagging efficiency IP3D cut is derived on a $t\bar{t}$ sample, if the same cut is applied on a $Z'(4\text{ TeV}) \rightarrow t\bar{t}$ this will result in a lower efficiency, given the dependency of the IP3D Log Likelihood ratio distribution from the jet- p_T , in particular for the effect of the increase of number of tracks from b -hadron fragmentation. An optimization of the tagger algorithm is then required to deal with the different topology of the b -jet. The optimization of the IP3D tagger was one of the goal of this thesis. This optimization could be provided with a tuning on high- p_T samples and with additional requirements on the track selection.

6.4.1 Tuning over a mixed sample

With the increase of the jet p_T , tracks originated by the b -hadron decay change their characteristics. For jet- p_T of $\sim 100\text{ GeV}$ more than 90% of the originated tracks are considered Good, according to the description of Table 6.2. When the jet- p_T is higher than 400 GeV less than 30% of the tracks are Good. The trend as function of the jet- p_T is shown in Figure 6.8a. Two concurrent effects are responsible of this behavior:

- at high- p_T the b -hadron could travel for some centimeter, flying over the IBL and the B-layer. This will result in missing hits in those layers.
- the jets are more collimated and the number of tracks from fragmentation increases. These two effects will produce a high density track environment, in which more than one track could be associated to the same hit.

Figure 6.8b shows the distribution of the b -jet tracks with respect to track categories for a $t\bar{t}$ sample and a Z' decaying in $t\bar{t}$ one, where the Z' has a mass of 4 TeV. In the high- p_T sample the number of Good tracks drastically reduces, while the categories with missing hits in the first two layer and the ones with split and shared hits are more populated. The effect is not only statistical, since the impact parameters distributions differs from one sample to the other, due to the topology of the jet-tracks changing with the p_T .

Figure 6.9 shows the impact parameter significance $\frac{d_0}{\sigma_{d_0}}$ distribution of b -hadron tracks for the two samples. The high- p_T sample shows in general a broader distribution, with higher tails for negative impact parameter significance. The b -hadron p_T doesn't increase linearly with the jet p_T , as shown in Figure 6.10. This is because of the increase of the fragmentation itself and the reconstruction of the jet coming from the W-decay within the b -jet cone. As a result of this effect the direction of the b -hadron could slightly differ from the direction of the jet, leading to a poor reconstruction of the lifetime sign. The high- p_T behavior needs to be considered in the tuning of the IP3D algorithm. Indeed the $t\bar{t}$ sample alone is not descriptive of the impact parameter significance for some of the tracks categories, in particular the ones with missing hits in the first two layers. Therefore new tuning procedure was developed, using a mixed sample of $t\bar{t}$ and $Z'(4\text{ TeV})$, in order to preserve the low- p_T performance and improve the performance at high- p_T . Categories with missing hits in the first two layers were populated with contribution from both the samples, while for the other categories only the $t\bar{t}$ events were considered. This method guarantees to keep the same performance at low- p_T while improving at high- p_T . Figure 6.11 summarizes the b -tagging and light-jet rejection

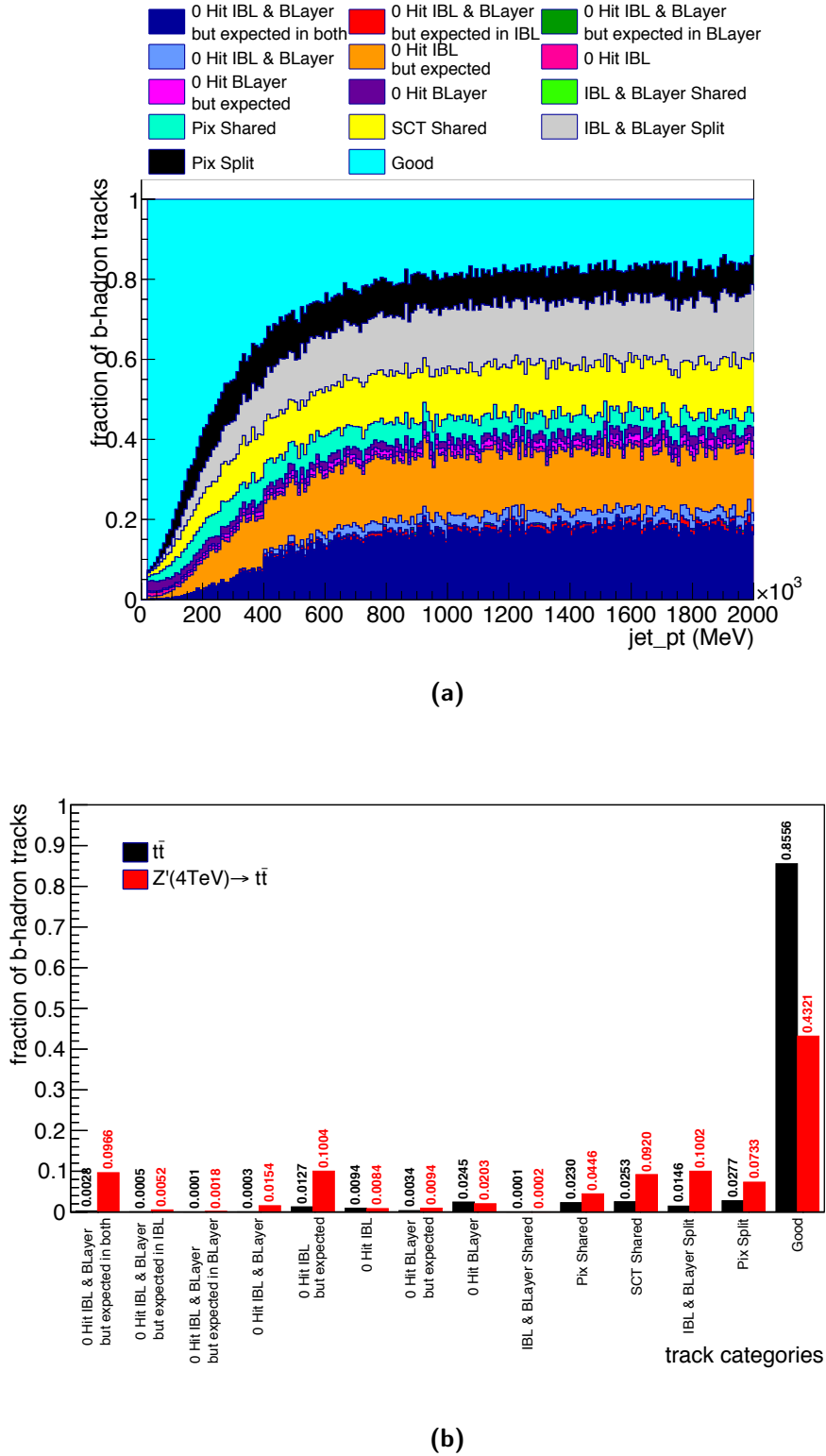


Figure 6.8: (a) Distribution of the b -jet tracks with respect to track categories for a $t\bar{t}$ sample and a Z' decaying in $t\bar{t}$. (b) Relative population of the track categories as a function of the jet- p_T for the tracks coming from the decay of the b -hadron and the eventual decay of the c -hadron

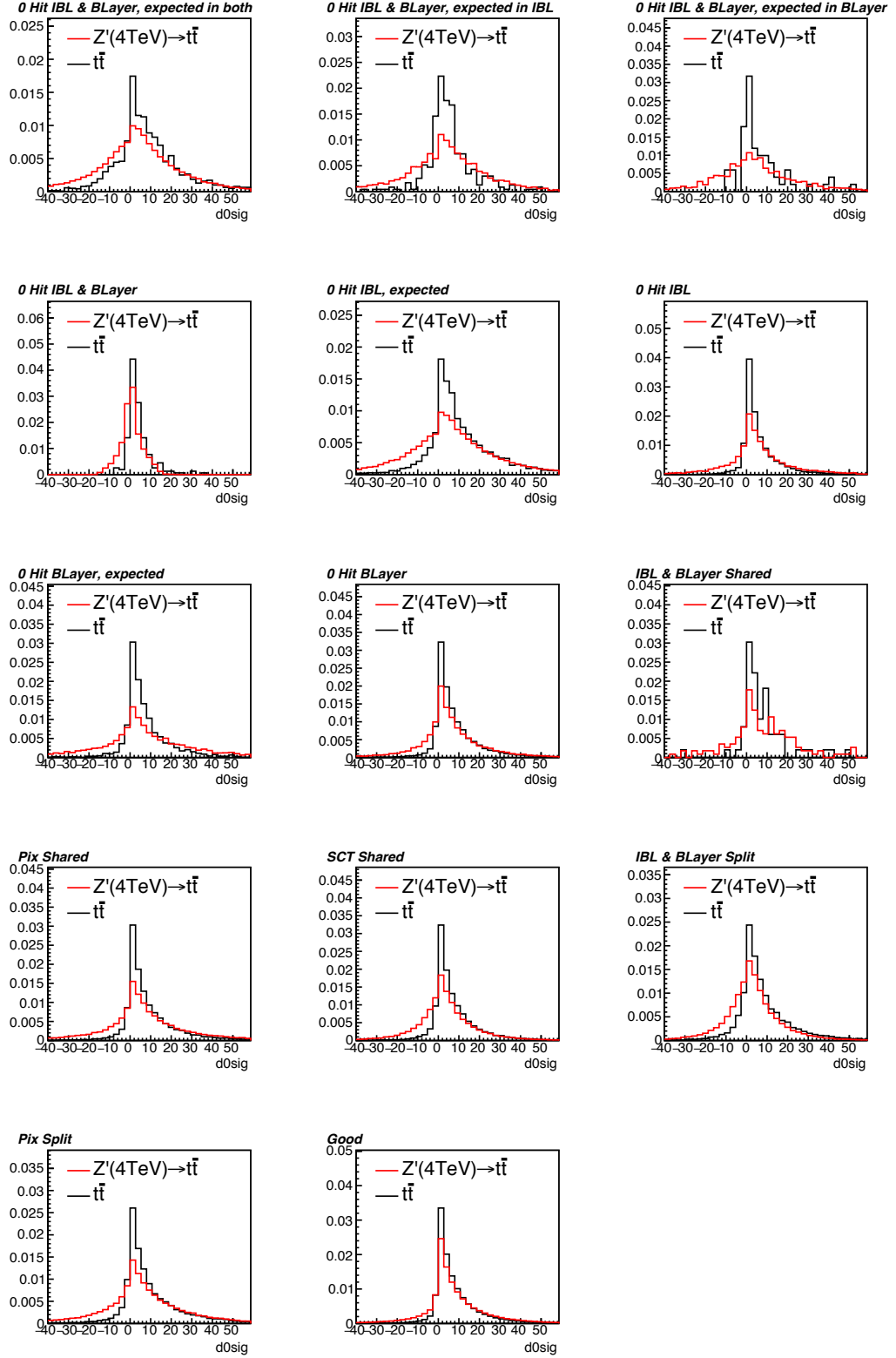


Figure 6.9: Transverse impact parameter significance $\frac{d_0}{\sigma_{d_0}}$ distribution of b -hadron tracks for different track categories. The red histograms represent the result for the $Z'(4 \text{ TeV}) \rightarrow t\bar{t}$, while the black histogram the results for $t\bar{t}$ production.

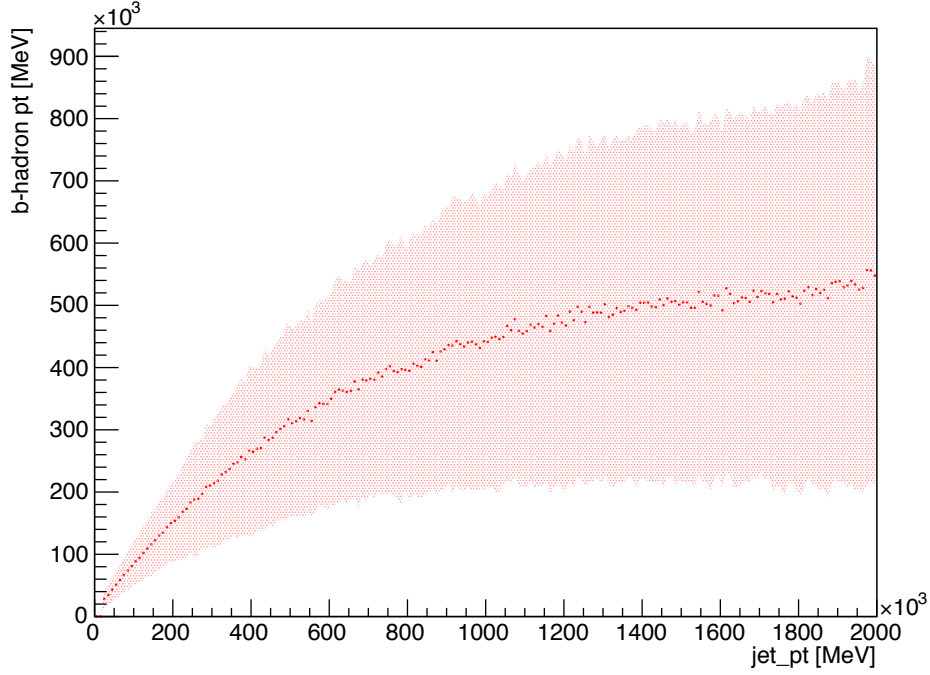


Figure 6.10: b -hadron p_T as a function of the jet p_T for a $Z'(4 \text{ TeV}) \rightarrow t\bar{t}$ sample. The vertical width of the band represents the RMS.

performance as a function of the jet p_T for a b -tagging efficiency of 70% over a $Z'(4 \text{ TeV}) \rightarrow t\bar{t}$ sample. In particular Figure 6.11a shows respectively the b -tagging efficiency as a function of the jet- p_T and Figure 6.11b shows the light-jet rejection as a function of the jet- p_T , both evaluated for a fixed cut on the IP3D log-likelihood ratio variable. It can be seen that the b -tagging efficiency is not constant as a function of the jet- p_T due to the dependance of the IP3D log-likelihood ratio from the jet- p_T itself. This has an impact on the interpretation of Figure 6.11b since the different values of the b -tagging efficiency, at each jet- p_T bin, should be considered when evaluating the light-jet rejection. A better way to estimate the light-jet rejection is to use a dynamic cut to the IP3D log-likelihood ratio, so that in each bin the b -tagging efficiency is 70% (flat cut). This removes the issues coming from the IP3D log-likelihood ratio dependancy. Figure 6.11c shows the light-jet rejection for the new and the standard tuning. The new tuning provides $\sim 10\%$ improvement at high- p_T . The light-jet rejection was evaluated for both a fixed cut on the IP3D log-likelihood ratio variable, and a dynamic cut which gives a flat efficiency of 70% for each jet p_T bin.

6.4.2 New track selection

Figure 6.12b shows the number of tracks that passes the IP3D selection for b -jets in the case of the $Z'(4 \text{ TeV}) \rightarrow t\bar{t}$ sample. The contributions of tracks coming from b -hadron and fragmentation are shown. It can be seen that the number of tracks coming from fragmentation increases with the jet- p_T , while the number of tracks coming from the b -hadron are almost constant with respect to the jet- p_T . A slight decrease can be observed due to bad track reconstruction at high- p_T .

Ideally one would like to remove the contribution from fragmentation, with a tighter track

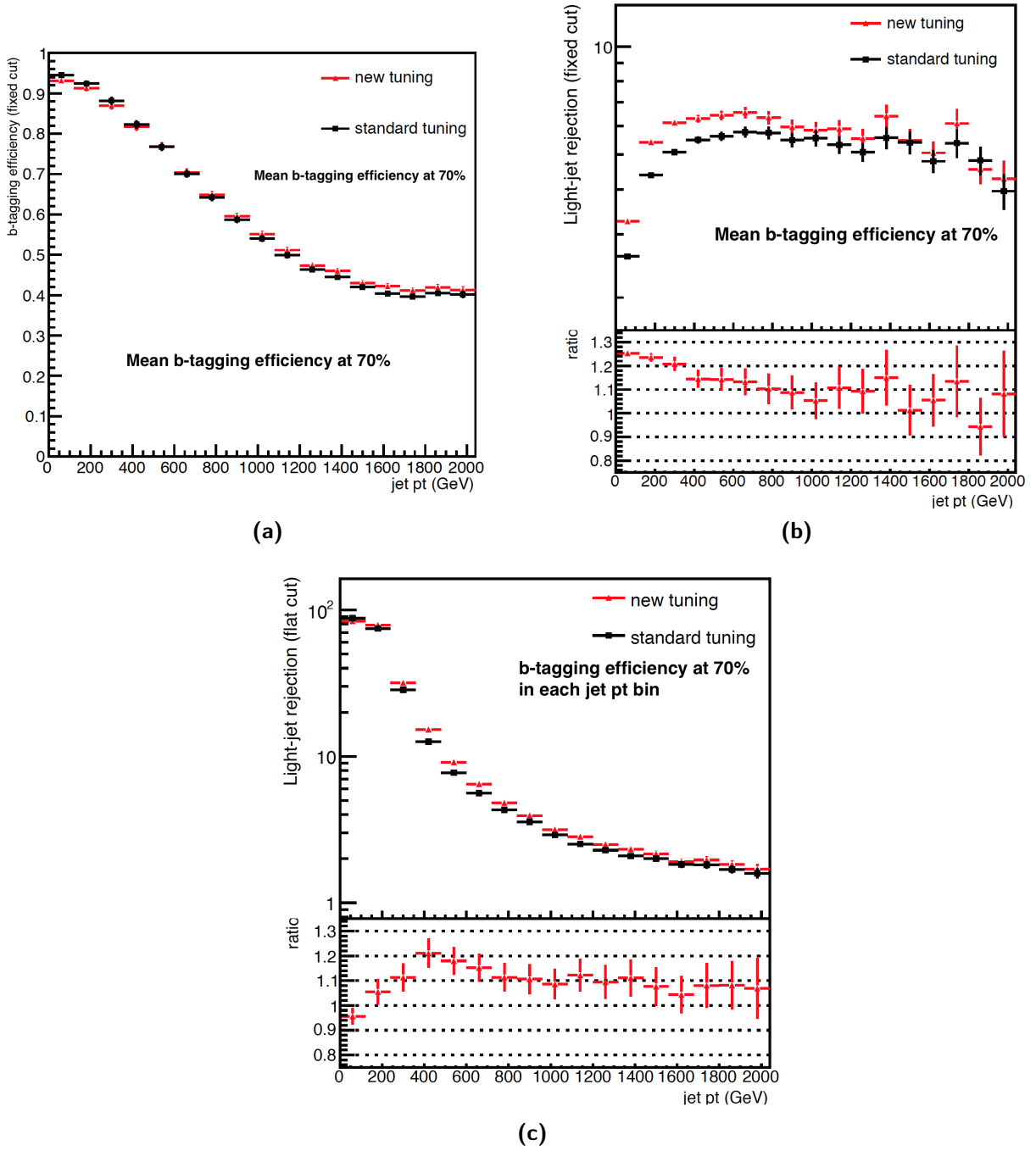
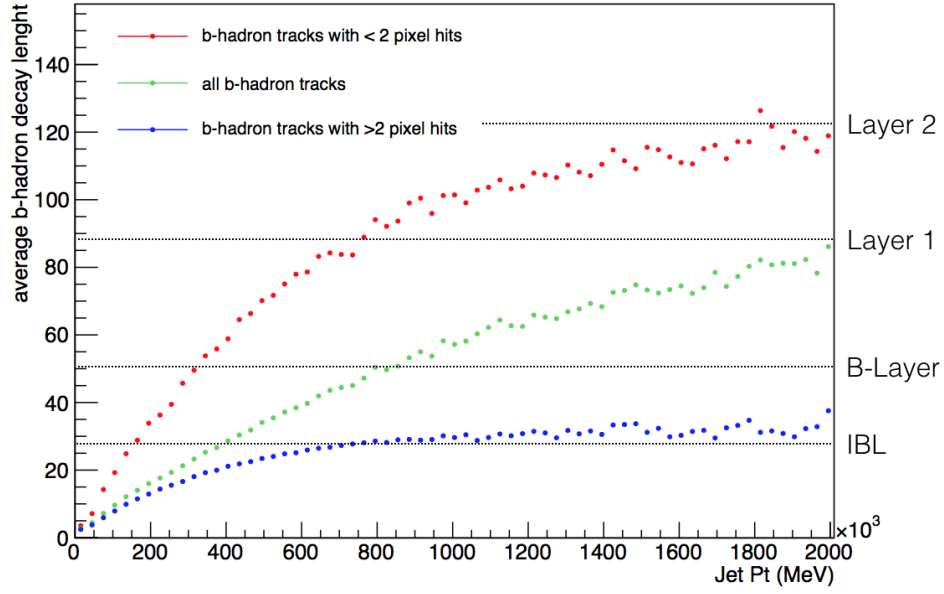
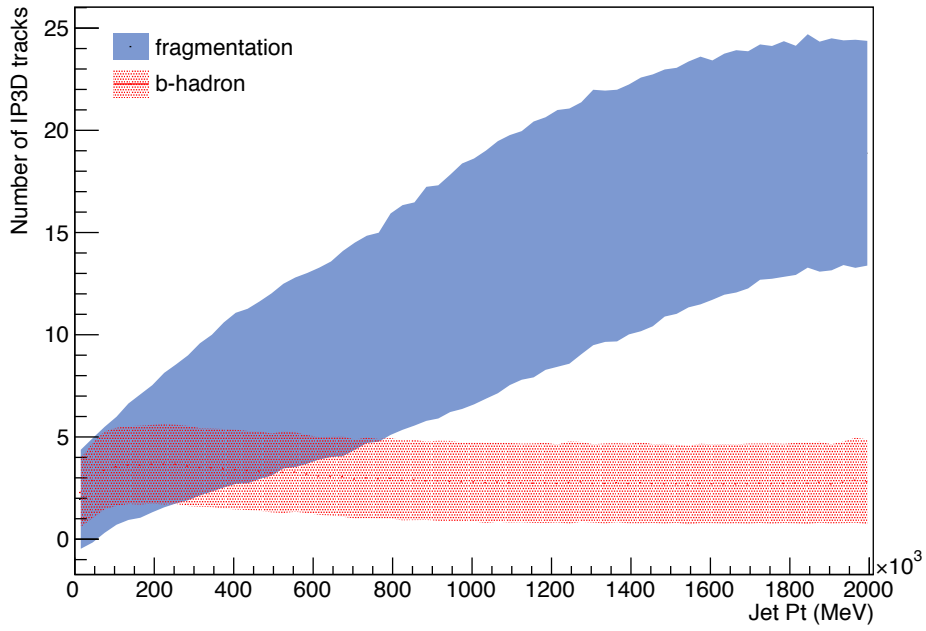


Figure 6.11: b -tagging efficiency (a) and light-jet rejection (b) as function of the jet- p_T for a 70% b -tagging efficiency IP3D log likelihood ratio fixed cut calculated for the standard tuning (black) and the new tuning (red). Light-jet rejection as function of the jet- p_T for a 70% b -tagging efficiency IP3D log likelihood ratio dynamic (flat) cut calculated for the standard tuning (black) and the new tuning (red).



(a)



(b)

Figure 6.12: (a) Average b -hadron decay length as function of the jet p_T , tracks with less than 2 pixel hits are related to a b -hadron which decays over the the B-Layer. (b) Number of tracks that passes the standard IP3D track selection for the b -jet as function of the jet- p_T . Contributions from the b -hadron tracks and the fragmentation are shown.

selection. New selection mechanisms of the IP3D tracks were studied, aiming to reject the tracks coming from fragmentation in the b -jets.

Figure 6.12a shows the average b -hadron decay length as a function of jet p_T . It can be seen that tracks with a number of pixel hits less than 2 often correspond to a b -hadron which decay after the first two layers. As first action the minimum number of hits in the Pixel Detector was relaxed from 2 to 1. This action has been proven not to deteriorate the b -tagging performance at low- p_T . In order to better reject tracks from fragmentation one could select just those tracks with highest p_T or impact parameters.

Figure 6.13 shows the average values of the $\frac{\text{track } p_T}{\text{jet } p_T}$ and the $\sqrt{d_{0sig}^2 + z_{0sig}^2}$ as a function of the jet p_T . It can be seen that the track p_T information is not providing a good rejection of fragmentation tracks (Figure 6.13a), while a better separation can be appreciated for the $\sqrt{d_{0sig}^2 + z_{0sig}^2}$ variable (Figure 6.13b).

Impact on b -tagging performance was evaluated for two selections:

- keep the 8 tracks with highest track p_T ;
- keep the 8 tracks with the highest value of $\sqrt{d_{0sig}^2 + z_{0sig}^2}$.

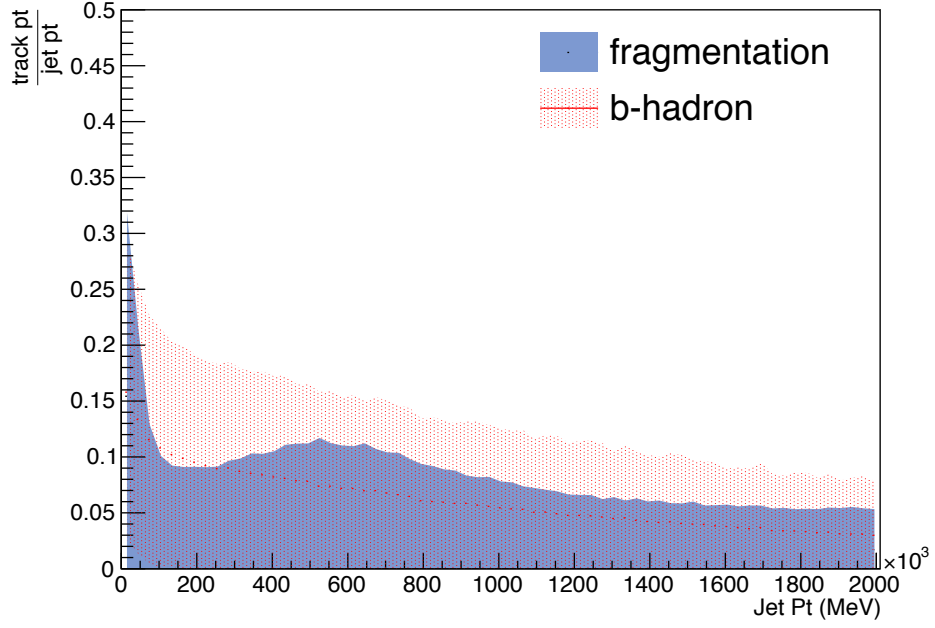
The choice of keeping the first 8 tracks was done because of Figure 6.12b, one would expect to exceed this number for jet with a p_T higher than ~ 200 GeV. Even if 5 tracks are in average expected from the b -hadron decay, some of the tracks from fragmentation may have a large transverse momentum or impact parameter, so that the selection was relaxed to 8 tracks.

The performance of both selections were evaluated on $Z'(4 \text{ TeV})$ sample. Figures 6.14a and 6.14b show the effect of the selection of the 8 largest p_T tracks, compared with the standard IP3D track selection, when a fixed cut for a 70% b -tagging efficiency is applied. The efficiency over the jet p_T range becomes flatter when a fixed cut on b -tagging 70% efficiency is applied. As a result the light-jet rejection will improve for the low p_T region. A dynamic cut could be applied as well, to have a 70% efficiency for each jet p_T bin. Figures 6.14a and 6.14b shows that this selection has the same performance of the standard selection for $p_T < 300$ GeV, while an improvement for higher jet- p_T can be appreciated.

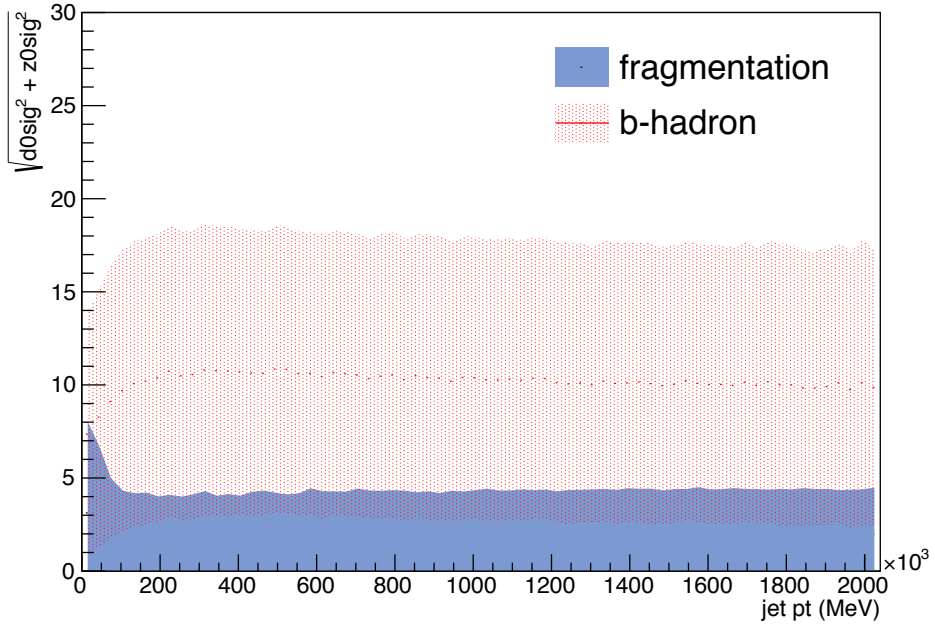
Figure 6.15a and 6.15b shows the effect of the selection of the 8 largest impact parameter tracks ($\sqrt{d_{0sig}^2 + z_{0sig}^2}$). This method makes the efficiency flatter all over the jet p_T . Anyhow the flat efficiency cut (see Figure 6.15c) reveals lower performance in the range 200 GeV to 1000 GeV, while an improvement for higher p_T . This is due to the bias induced on the selection of light jets, which will have a higher IP3D Log Likelihood Ratio then the standard calculation.

Ideally one would like to combine the benefit of the two different methods. For example using the selection of the 8 largest tracks for jet p_T lower than 800 GeV and a of the 8 largest $p_T \sqrt{d_{0sig}^2 + z_{0sig}^2}$ tracks for the higher jet p_T . Figure ?? shows the performance of the latter track selection.

Figures 6.17a, 6.17b and 6.17c show the effect of the combination of the new tuning method with the latter track selection. A better rejection can be measured on the entire p_T spectrum.

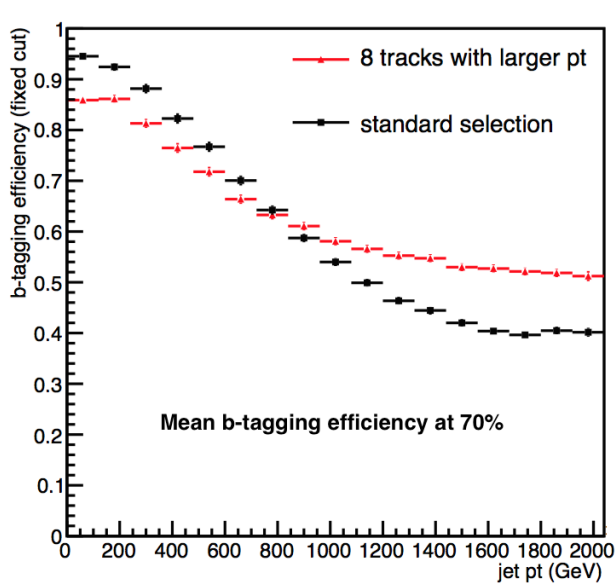


(a)

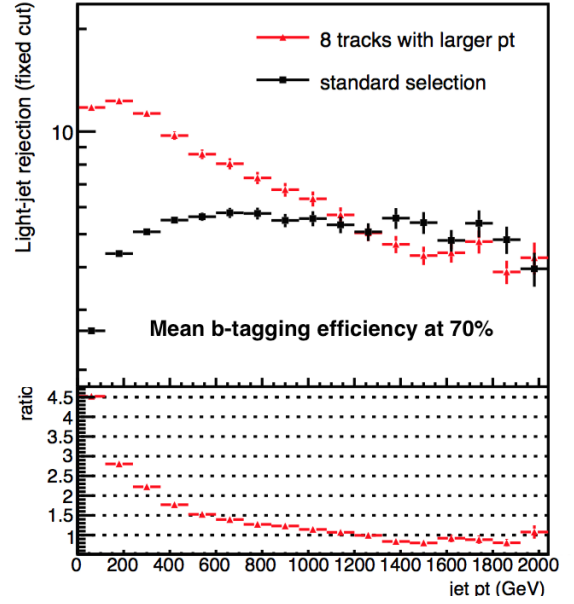


(b)

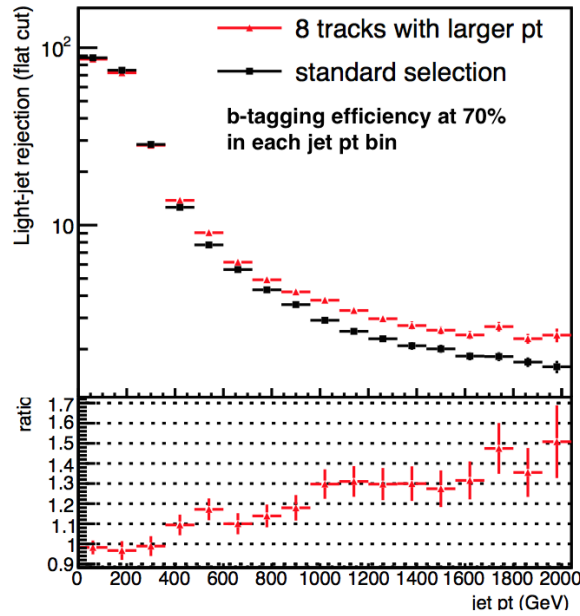
Figure 6.13: (a) $\frac{\text{track } p_T}{\text{jet } p_T}$ with respect to the jet p_T for b -hadron and fragmentation tracks. (b) $\sqrt{d_{0sig}^2 + z_{0sig}^2}$ with respect to the jet p_T for b -hadron and fragmentation tracks.



(a)

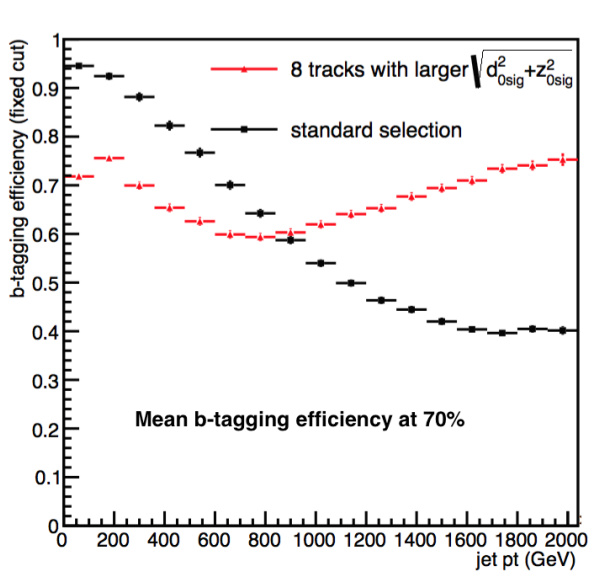


(b)

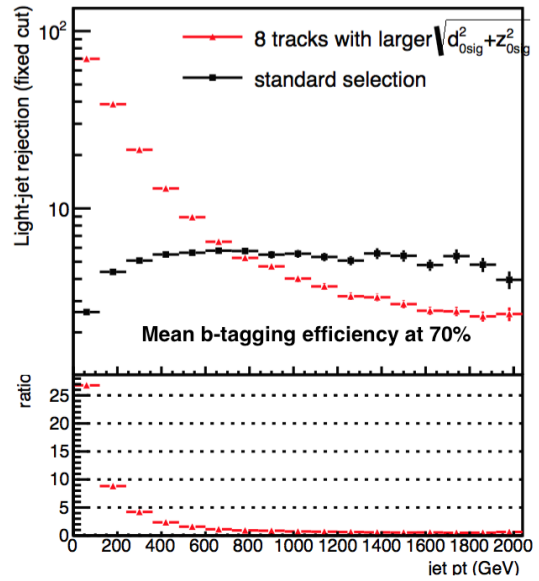


(c)

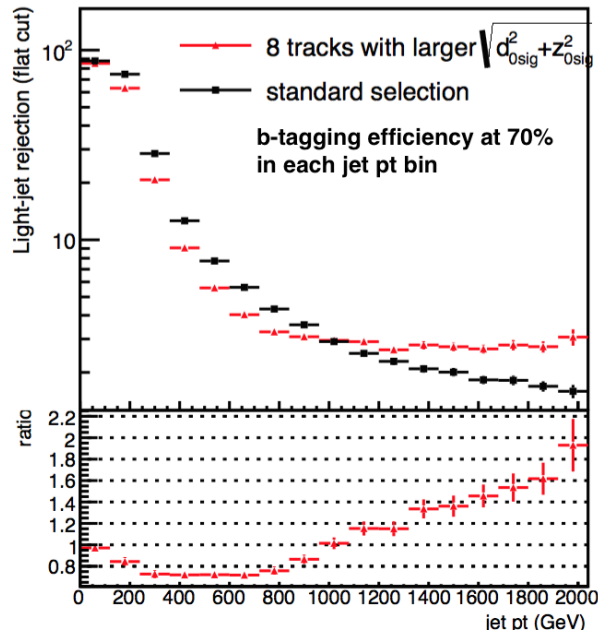
Figure 6.14: b -tagging efficiency (a) and light-jet rejection (b) as function of the jet- p_T for a 70% b -tagging efficiency IP3D log likelihood ratio fixed cut calculated for the standard selection (black) and the the 8 tracks with larger p_T (red). (c) Light-jet rejection as function of the jet- p_T for a 70% b -tagging efficiency IP3D log likelihood ratio dynamic (flat) cut calculated for the standard selection (black) and the 8 tracks with larger p_T (red).



(a)

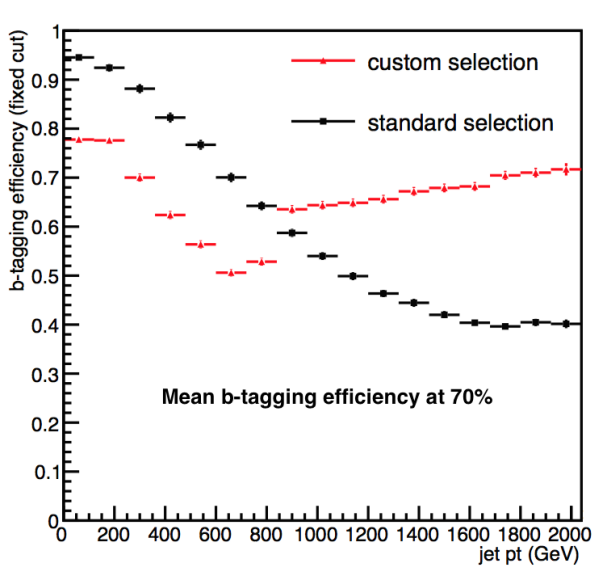


(b)

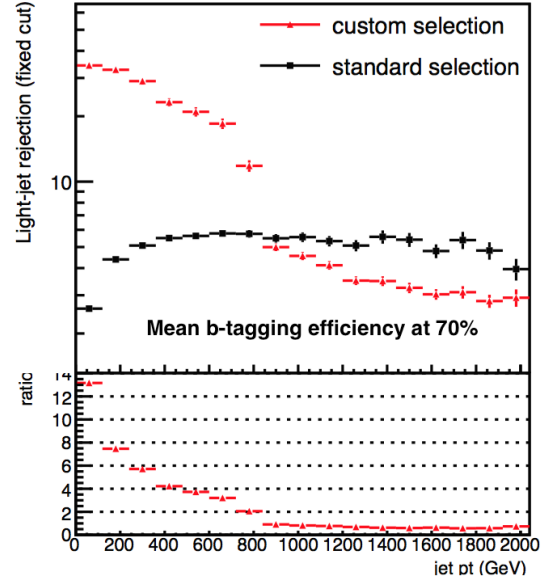


(c)

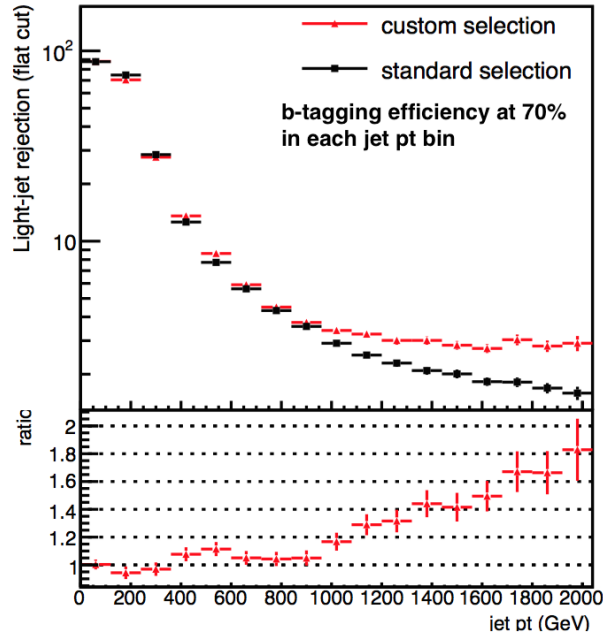
Figure 6.15: b -tagging efficiency (a) and light-jet rejection (b) as function of the jet- p_T for a 70% b -tagging efficiency IP3D log likelihood ratio fixed cut calculated for the standard selection (black) and the 8 tracks with larger $\sqrt{d_{0sig}^2 + z_{0sig}^2}$ (red). (c) Light-jet rejection as function of the jet- p_T for a 70% b -tagging efficiency IP3D log likelihood ratio dynamic (flat) cut calculated for the standard selection (black) and the 8 tracks with larger $\sqrt{d_{0sig}^2 + z_{0sig}^2}$ (red).



(a)

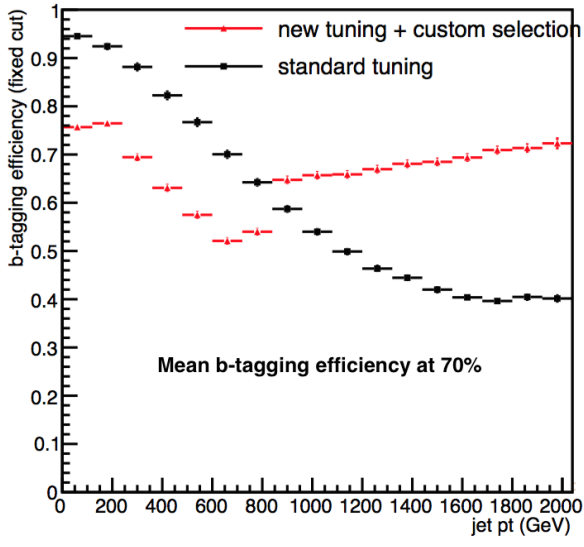


(b)

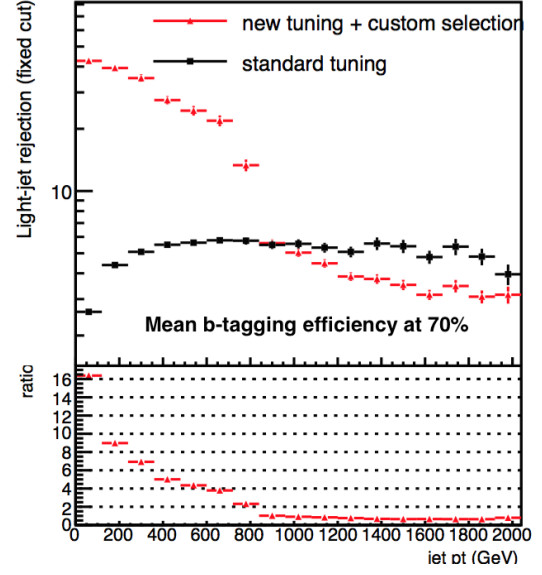


(c)

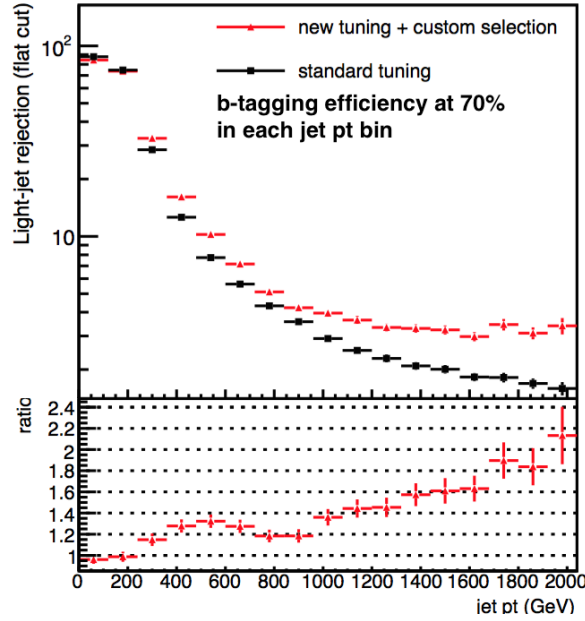
Figure 6.16: b -tagging efficiency (a) and light-jet rejection (b) as function of the jet- p_T for a 70% b -tagging efficiency IP3D log likelihood ratio fixed cut calculated for the standard selection (black) and the 8 tracks coming from the custom selection (red). (c) Light-jet rejection as function of the jet- p_T for a 70% b -tagging efficiency IP3D log likelihood ratio dynamic (flat) cut calculated for the standard selection (black) and the the 8 tracks coming from the custom selection (red). The custom selection consists in selecting the 8 tracks with largest p_T if the jet- p_T is lower than 800 GeV and in selecting the 8 tracks with largest $p_T \sqrt{d_{0sig}^2 + z_{0sig}^2}$ if the jet- p_T is higher than 800 GeV



(a)



(b)



(c)

Figure 6.17: b -tagging efficiency (a) and light-jet rejection (b) as function of the jet- p_T for a 70% b -tagging efficiency IP3D log likelihood ratio fixed cut calculated for the standard tuning (black) and for the new tuning and selecting the 8 tracks coming from the custom selection (red). (c) Light-jet rejection as function of the jet- p_T for a 70% b -tagging efficiency IP3D log likelihood ratio dynamic (flat) cut calculated for the standard selection (black) and the the 8 tracks coming from the custom selection (red). The custom selection consists in selecting the 8 tracks with larger p_T if the jet- p_T is lower than 800 GeV and in selecting the 8 tracks with larger $p_T \sqrt{d_{0sig}^2 + z_{0sig}^2}$ if the jet- p_T is higher than 800 GeV

6.4.3 Next steps

As next step of this work it will be important to verify the performance on different high- p_T samples involving b -hadrons decay, as: $Z' \rightarrow b\bar{b}$, $Z' \rightarrow c\bar{c}$ and $Z' \rightarrow u\bar{u}$. At the moment of this thesis $Z' \rightarrow t\bar{t}$ was the only official decay channel available in the official ATLAS simulation, and this provides a combination high- p_T and boosted scenario, while it will be important to evaluate and optimize the performance in the high- p_T case.

Another important study that could improve the b -tagging performance is the optimization of the lifetime sign derivation. At high- p_T the tracks within the jet are more collimated and the possibility of a wrong association of the lifetime sign becomes larger.

This study has proven that the $t\bar{t}$ sample is not predictive of high- p_T behaviors, in particular it is important to consider the different topology of the tracks involved in the jets and the larger contribution from fragmentation.

Conclusions

The LHC will investigate the nature of the elementary particles and their fundamental interactions, in particular a detailed study of the Higgs boson properties and the search for physics beyond the Standard Model will be the main goals for the next years.

The LHC underwent an upgrade during the first long shutdown period, in which a higher center of mass energy ($\sqrt{s} = 13$ TeV and eventually the design energy of 14 TeV) and a higher peak instantaneous luminosity ($10^{34} \text{ cm}^{-2} \text{ s}^{-1}$) were achieved.

The ATLAS collaboration made a significant effort to cope with the upgraded LHC luminosity, which will result in high pile-up, i.e. additional soft proton-proton collisions that overlap the signal of interest. In particular a new innermost layer of silicon pixel detector was built and installed, the Insertable B-Layer (IBL), to prevent from inefficiencies due to high pile-up. This was achieved thanks to the shorter pixel size of IBL ($250 \mu\text{m}$) with respect to the other layers of the Pixel detector ($400 \mu\text{m}$). The IBL improves the charged particle tracking performance and in particular it provides a better track impact parameter which is of extreme importance for the discrimination of b -quarks jets.

The work presented focuses on the construction and quality assurance of the IBL, and on the optimization of the impact parameter b -tagging algorithm for jets with high transverse momentum.

The IBL construction lasted for three years, taking into account the assembly, the quality assurance, the installation and the commissioning of the detector. The core of the IBL construction was the production of the staves, done in the laboratories of University of Geneva, which are the carbon fiber support structure instrumented with the pixel silicon detector sensors, the readout front-end chip and the services for the electrical connections. Twenty production staves were fully assembled, each of the staves fulfilled the mechanical constraints of $350 \mu\text{m}$ maximal excursion after the assembly. This requirement was driven by the stave-to-stave clearance in the integration of the staves around the support structure. All the twenty staves underwent a qualification in terms of mechanical and electrical performance, all of them fulfilling the production requirements.

Each of the staves went through a detailed quality assurance at CERN, where a functional characterization of each of the staves was performed. 14 staves were selected for the integration around the mechanical support with a fraction of 99.9% working pixels. The high efficiency was maintained after the loading of the staves around the IBL mechanical support. The IBL went through a commissioning phase in which the performance was checked before and after the installation in ATLAS; no variation has been observed at this stage. The detector was re-calibrated; a faster procedure for the threshold tuning was put in place, which uses a binary search algorithm. A tuning of the detector timing required to have $>99\%$ efficiency within 25 ns time-detection window.

During the commissioning a data-taking campaign for the acquisition of cosmic ray events

was held, in which the alignment of the detector and the study of the behavior in presence of 2 T magnetic field was done.

Due to a mismatch in the coefficient thermal expansion of components of the service and the carbon-fiber stave a deformation of the IBL structure has been observed with a magnitude of $10\,\mu\text{m K}^{-1}$ with respect to room temperature. A study was carried out to ensure the mechanical stability of the IBL during the data-taking. It was demonstrated that the alignment can correct the deformation as a function of the detector temperature. A temperature monitoring tool was developed, which measured a stability in temperature of 0.2 K during data-taking in cosmic-ray runs.

The IBL has a crucial impact on the b -tagging performance, leading to a factor 4 improvement for the light jet rejection. Since the region at higher transverse momentum is of interest for the searches of new particles not foreseen by the Standard Model, an optimization of the impact parameter algorithm has been performed. Two techniques have been suggested in this thesis, including an optimization of the track selection and optimization of the algorithm tuning. The combination of the two led to an improvement of the light jet rejection of $>20\%$ for jet of transverse momentum larger than 400 GeV at a b -tagging efficiency working point of 70% .

Bibliography

- [1] O. Bruening et al. *LHC Design Report*. Tech. rep. Geneva, 2004.
- [2] A. Airapetian et al. “ATLAS: Detector and physics performance technical design report. Volume 1”. In: *CERN-LHCC-99-14, ATLAS-TDR-14* (1999).
- [3] A. Airapetian et al. “ATLAS: Detector and physics performance technical design report. Volume 2”. In: *CERN-LHCC-99-15, ATLAS-TDR-15* (1999).
- [4] S. L. Glashow. *Partial-symmetries of weak interactions*. 1961.
- [5] A. Salam and J. C. Ward. “Electromagnetic and weak interactions”. In: *Phys. Lett.* 13, 168 (1964).
- [6] S. Weinberg. “A model of Leptons”. In: *Phys. Rev. Lett.* 19, 1264 (1967).
- [7] Cheng. *Gauge theory of elementary particle physics*. Oxford Oxfordshire New York: Clarendon Press Oxford University Press, 1984. ISBN: 0198519613.
- [8] K. A. Olive et al. “Review of Particle Physics”. In: *Chin. Phys.* C38 (2014), p. 090001. DOI: 10.1088/1674-1137/38/9/090001.
- [9] J. Schechter and J. W. F. Valle. “Neutrino Masses in SU(2) x U(1) Theories”. In: *Phys. Rev.* D22 (1980), p. 2227. DOI: 10.1103/PhysRevD.22.2227.
- [10] Roel Aaij et al. “Observation of J/ ψ Resonances Consistent with Pentaquark States in $B^0 \rightarrow J/\psi K^- p$ Decays”. In: *Phys. Rev. Lett.* 115 (2015), p. 072001. DOI: 10.1103/PhysRevLett.115.072001. arXiv: 1507.03414 [hep-ex].
- [11] Georges Aad et al. “Combined Measurement of the Higgs Boson Mass in pp Collisions at $\sqrt{s} = 7$ and 8 TeV with the ATLAS and CMS Experiments”. In: *Phys. Rev. Lett.* 114 (2015), p. 191803. DOI: 10.1103/PhysRevLett.114.191803. arXiv: 1503.07589 [hep-ex].
- [12] Ties Behnke et al. “The International Linear Collider Technical Design Report - Volume 1: Executive Summary”. In: (2013). arXiv: 1306.6327 [physics.acc-ph].
- [13] John R. Ellis and I. Wilson. “New physics with the compact linear collider”. In: *Nature* 409 (2001), pp. 431–435. DOI: 10.1038/35053224.
- [14] “ATLAS magnet system: Technical design report”. In: *CERN-LHCC-97-18* (1997).
- [15] “ATLAS inner detector: Technical design report. Vol. 1”. In: *CERN-LHCC-97-16, ATLAS-TDR-4* (1997).
- [16] “ATLAS inner detector: Technical design report. Vol. 2”. In: *CERN-LHCC-97-17* (1997).
- [17] *The Evaporative Cooling System for the ATLAS Inner Detector*. Tech. rep. ATL-INDET-PUB-2008-006. ATL-COM-INDET-2008-007. Geneva: CERN, 2008. URL: <https://cds.cern.ch/record/1100863>.

- [18] Alessandro La Rosa. “ATLAS Pixel Detector: Operational Experience and Run-1 to Run-2 Transition”. In: *PoS Vertex2014* (2015), p. 001. arXiv: 1410.6347 [physics.ins-det].
- [19] A. Ahmad et al. “The Silicon microstrip sensors of the ATLAS semiconductor tracker”. In: *Nucl. Instrum. Meth.* A578 (2007), pp. 98–118. DOI: 10.1016/j.nima.2007.04.157.
- [20] E. Abat et al. “The ATLAS Transition Radiation Tracker (TRT) proportional drift tube: Design and performance”. In: *JINST* 3 (2008), P02013. DOI: 10.1088/1748-0221/3/02/P02013.
- [21] H. A. Bethe. “Zur Theorie des Durchgangs Schneller Korpuskularstrahlen durch Materie”. In: *Ann. Physik* 397 (1930), p. 325.
- [22] L. Landau. “On the energy loss of fast particles by ionization”. In: *J. Phys.(USSR)* 8 (1944), pp. 201–205.
- [23] E. Rutherford. “The Scattering of α and β Particles by Matter and the Structure of the Atom”. In: *Philos. Mag.* 6 (1911).
- [24] E. Keil et al. “Zur Einfach- und Mehrfachstreuung geladener Teilchen”. In: *Z. Naturforsch.* 15A (1960).
- [25] Antonios Gonis. *Multiple scattering in solids*. New York: Springer, 2000. ISBN: 038798853X.
- [26] N.W. Ashcroft and N.D. Mermin. *Solid state physics*. Science: Physics. Saunders College, 1976. ISBN: 9780030493461. URL: <https://books.google.ch/books?id=FRZRAAAAMAAJ>.
- [27] L. Rossi. *Pixel Detectors: From Fundamentals to Applications*. Particle Acceleration and Detection. Springer, 2006. ISBN: 9783540283324. URL: <https://books.google.fr/books?id=Jbp73yTz-LYC>.
- [28] H. Spieler. *Semiconductor Detector Systems*. Series on Semiconductor Science and Technology. OUP Oxford, 2005. ISBN: 9780198527848. URL: <https://books.google.ch/books?id=MUMb3y37yqYC>.
- [29] *The Optimization of ATLAS Track Reconstruction in Dense Environments*. Tech. rep. ATL-PHYS-PUB-2015-006. Geneva: CERN, 2015. URL: <https://cds.cern.ch/record/2002609>.
- [30] M. Moll. “Radiation Damage in Silicon Particle Detectors”. PhD thesis. 1999.
- [31] E. Borchini et al. “Temperature and frequency dependence of the capacitance of heavily irradiated silicon diodes”. In: *Solid-State Electronics* 42.11 (1998), pp. 2093–2096. ISSN: 0038-1101. DOI: [http://dx.doi.org/10.1016/S0038-1101\(98\)00186-5](http://dx.doi.org/10.1016/S0038-1101(98)00186-5). URL: <http://www.sciencedirect.com/science/article/pii/S0038110198001865>.
- [32] A.S. Sedra and K.C. Smith. *Microelectronic Circuits*. Oxf Ser Elec Series. Oxford University Press, 1987. ISBN: 9780195323030. URL: <https://books.google.ca/books?id=wDQJQQAACAAJ>.
- [33] R. Fruhwirth. “Application of Kalman filtering to track and vertex fitting”. In: *Nucl. Instrum. Meth.* A262 (1987), p. 444. DOI: 10.1016/j.nima.2012.07.058.
- [34] T G Cornelissen et al. *Updates of the ATLAS Tracking Event Data Model (Release 13)*. Tech. rep. ATL-SOFT-PUB-2007-003. ATL-COM-SOFT-2007-008. Geneva: CERN, 2007. URL: <http://cds.cern.ch/record/1038095>.

- [35] Norbert Wermes and G Hallewel. *ATLAS pixel detector: Technical Design Report*. Technical Design Report ATLAS. Geneva: CERN, 1998. URL: <https://cds.cern.ch/record/381263>.
- [36] M Capeans et al. *ATLAS Insertable B-Layer Technical Design Report*. Tech. rep. CERN-LHCC-2010-013. ATLAS-TDR-19. Geneva: CERN, 2010. URL: <http://cds.cern.ch/record/1291633>.
- [37] Matteo Cacciari, Gavin P. Salam, and Gregory Soyez. “The Anti-k(t) jet clustering algorithm”. In: *JHEP* 04 (2008), p. 063. DOI: 10.1088/1126-6708/2008/04/063. arXiv: 0802.1189 [hep-ph].
- [38] Maurice Sciveres. *The FE-I4b manual*.
- [39] David Arutinov et al. “Digital architecture and interface of the new ATLAS pixel front-end IC for upgraded LHC luminosity”. In: *IEEE Trans. Nucl. Sci.* 56 (2009), pp. 388–393. DOI: 10.1109/TNS.2009.2015318.
- [40] M.A. Karagounis. *Analog integrated CMOS circuits for the readout and powering of highly segmented detectors in particle physics applications*. 2010. URL: <https://books.google.fr/books?id=26rimgEACAAJ>.
- [41] L Gonella et al. “The shunt-LDO regulator to power the upgraded ATLAS pixel detector”. In: *Journal of Instrumentation* 7.01 (2012), p. C01034. URL: <http://stacks.iop.org/1748-0221/7/i=01/a=C01034>.
- [42] P. Grenier. “Silicon Sensor Technologies for the {ATLAS} {IBL} Upgrade”. In: *Physics Procedia* 37 (2012). Proceedings of the 2nd International Conference on Technology and Instrumentation in Particle Physics (TIPP 2011), pp. 874 –881. ISSN: 1875-3892. DOI: <http://dx.doi.org/10.1016/j.phpro.2012.02.432>. URL: <http://www.sciencedirect.com/science/article/pii/S1875389212017865>.
- [43] Sherwood I. Parker, Christopher J. Kenney, and Julie Segal. “3-D: A New architecture for solid state radiation detectors”. In: *Nucl. Instrum. Meth.* A395 (1997), pp. 328–343. DOI: 10.1016/S0168-9002(97)00694-3.
- [44] J Albert et al. “Prototype ATLAS IBL Modules using the FE-I4A Front-End Readout Chip”. In: *JINST* 7 (2012), P11010. DOI: 10.1088/1748-0221/7/11/P11010. arXiv: 1209.1906 [physics.ins-det].
- [45] T. Witting. “Slim Edge Studies, Design and Quality Control of Planar ATLAS IBL Pixel Sensors”. PhD thesis. 2013.
- [46] S. Altenheiner et al. “Planar slim-edge pixel sensors for the ATLAS upgrades”. In: *JINST* 7 (2012), p. C02051. DOI: 10.1088/1748-0221/7/02/C02051.
- [47] C. Gossling et al. “Evaluation of the breakdown behaviour of ATLAS silicon pixel sensors after partial guard-ring removal”. In: *Nucl. Instrum. Meth.* A624 (2010), pp. 410–413. DOI: 10.1016/j.nima.2010.06.004.
- [48] Cinzia Da Via et al. “3D silicon sensors: Design, large area production and quality assurance for the ATLAS IBL pixel detector upgrade”. In: *Nucl. Instrum. Meth.* A694 (2012), pp. 321–330. DOI: 10.1016/j.nima.2012.07.058.
- [49] G. Giacomini et al. “Development of Double-Sided Full-Passing-Column 3D Sensors at FBK”. In: *Nuclear Science, IEEE Transactions on* 60.3 (2013), pp. 2357–2366. ISSN: 0018-9499.

- [50] G. Pellegrini et al. “3D double sided detector fabrication at IMB-CNM”. In: *Nucl. Instrum. Meth. A* 699 (2013), p. 27.
- [51] J Bilbao de Mendizabal et al. *Irradiation of an IBL stave in a 10MeV beta beam*. Tech. rep. ATL-INDET-PUB-2013-001. Geneva: CERN, 2013. URL: <https://cds.cern.ch/record/1557832>.
- [52] J Weingarten. “ATLAS IBL sensor qualification”. In: *Journal of Instrumentation* 7.01 (2012), p. C01039. URL: <http://stacks.iop.org/1748-0221/7/i=01/a=C01039>.
- [53] T. Fritzsche et al. “Flip chip assembly of thinned chips for hybrid pixel detector applications”. In: *JINST* 9 (2014), p. C05039. DOI: 10.1088/1748-0221/9/05/C05039.
- [54] Malte Backhaus. “High bandwidth pixel detector modules for the ATLAS Insertable B-Layer”. PhD thesis. 2014.
- [55] *IBL Module Loading onto Stave and Quality Check*. Tech. rep. ATL-INDET-PUB-2015-003. Geneva: CERN, 2015. URL: <https://cds.cern.ch/record/2110639>.
- [56] B. Verlaet et al. In: (). URL: http://www.nikhef.nl/pub/services/biblio/bib_PN/GL2012_Verlaet_208.pdf.
- [57] *ATLAS Pixel IBL: Stave Quality Assurance*. Tech. rep. ATL-INDET-PUB-2014-006. Geneva: CERN, 2014. URL: <https://cds.cern.ch/record/1754509>.
- [58] David Leon Pohl. personal communication. Jan. 13, 2014.
- [59] *ATLAS Inner Detector Alignment Performance with February 2015 Cosmic Rays Data*. Tech. rep. ATL-PHYS-PUB-2015-009. Geneva: CERN, 2015. URL: <https://cds.cern.ch/record/2008724>.
- [60] S Fratina et al. *The TRT Fast-OR Trigger*. Tech. rep. ATL-INDET-PUB-2009-002. Geneva: CERN, 2009. URL: <https://cds.cern.ch/record/1229213>.
- [61] Lukasz Zwalinski et al. “CO₂ cooling system for Insertable B Layer detector into the ATLAS experiment”. In: *PoS TIPP2014* (2015), p. 224.
- [62] P. Grenier et al. “Test beam results of 3D silicon pixel sensors for the {ATLAS} upgrade”. In: *Nuclear Instruments and Methods in Physics Research Section A: Accelerators, Spectrometers, Detectors and Associated Equipment* 638.1 (2011), pp. 33–40. ISSN: 0168-9002. DOI: <http://dx.doi.org/10.1016/j.nima.2011.01.181>. URL: <http://www.sciencedirect.com/science/article/pii/S0168900211003524>.
- [63] Claude Amsler et al. “Review of Particle Physics, 2008-2009. Review of Particle Properties”. In: *Phys. Lett. B* 667.1-5 (2008), pp. 1–6. URL: <https://cds.cern.ch/record/1124989>.
- [64] Nicola Cabibbo. “Unitary Symmetry and Nonleptonic Decays”. In: *Phys. Rev. Lett.* 12 (1964), pp. 62–63. DOI: 10.1103/PhysRevLett.12.62.
- [65] Makoto Kobayashi and Toshihide Maskawa. “CP Violation in the Renormalizable Theory of Weak Interaction”. In: *Prog. Theor. Phys.* 49 (1973), pp. 652–657. DOI: 10.1143/PTP.49.652.
- [66] *Commissioning of the ATLAS high-performance b-tagging algorithms in the 7 TeV collision data*. Tech. rep. ATLAS-CONF-2011-102. Geneva: CERN, 2011. URL: <https://cds.cern.ch/record/1369219>.

- [67] M. L. Mangano et al. “b anti-b final states in Higgs production via weak boson fusion at the LHC”. In: *Phys. Lett.* B556 (2003), pp. 50–60. DOI: 10.1016/S0370-2693(03)00078-9. arXiv: hep-ph/0210261 [hep-ph].
- [68] Thomas G. Rizzo. “Z’ phenomenology and the LHC”. In: *Proceedings of Theoretical Advanced Study Institute in Elementary Particle Physics : Exploring New Frontiers Using Colliders and Neutrinos (TASI 2006)*. 2006, pp. 537–575. arXiv: hep-ph/0610104 [hep-ph]. URL: <http://www-public.slac.stanford.edu/sciDoc/docMeta.aspx?slacPubNumber=slac-pub-12129>.